2015

High frequency combustion instability control through acoustic modulation at the inlet boundary for liquid rocket engine applications

John William Bennewitz

HIGH-FREQUENCY COMBUSTION INSTABILITY CONTROL THROUGH ACOUSTIC MODULATION AT THE INLET BOUNDARY FOR LIQUID ROCKET ENGINE APPLICATIONS

by

JOHN WILLIAM BENNEWITZ

A DISSERTATION

Submitted in partial fulfillment of the requirements
for the degree of Doctor of Philosophy
in
The Department of Mechanical and Aerospace Engineering
to
The School of Graduate Studies
of
The University of Alabama in Huntsville

HUNTSVILLE, ALABAMA

2015

In presenting this dissertation in partial fulfillment of the requirements for a doctoral degree from The University of Alabama in Huntsville, I agree that the Library of this University shall make it freely available for inspection. I further agree that permission for extensive copying for scholarly purposes may be granted by my advisor or, in his/her absence, by the Chair of the Department or the Dean of the School of Graduate Studies. It is also understood that due recognition shall be given to me and to The University of Alabama in Huntsville in any scholarly use which may be made of any material in this dissertation.

John William Bennewitz — 4/3/15

John William Bennewitz (date)

DISSERTATION APPROVAL FORM

Submitted by John William Bennewitz in partial fulfillment of the requirements for the degree of Doctor of Philosophy in Mechanical Engineering and accepted on behalf of the Faculty of the School of Graduate Studies by the dissertation committee.

We, the undersigned members of the Graduate Faculty of The University of Alabama in Huntsville, certify that we have advised and/or supervised the candidate of the work described in this dissertation. We further certify that we have reviewed the dissertation manuscript and approve it in partial fulfillment of the requirements for the degree of Doctor of Philosophy in Mechanical Engineering.

3/12/15 Committee Chair
Dr. Robert A. Frederick Jr. (Date)

3/12/2015
Dr. David M. Lineberry (Date)

3/12/2015
Dr. Sarma L. Rani (Date)

3/12/15
Dr. D. Keith Hollingsworth (Date)

3/12/15
Dr. A. Kader Frendi (Date)

3/12/15
Dr. Kunning G. Xu (Date)

3/12/15 Department Chair
Dr. D. Keith Hollingsworth (Date)

4/3/15 College Dean
for Dr. Shankar Mahalingam (Date)

4/13/15 Graduate Dean
Dr. David Berkowitz (Date)

ABSTRACT

School of Graduate Studies
The University of Alabama in Huntsville

Degree Doctor of Philosophy College/Dept. Engineering/Mechanical and Aerospace Engineering

Name of Candidate John William Bennewitz

Title High-Frequency Combustion Instability Control through Acoustic Modulation at the Inlet Boundary for Liquid Rocket Engine Applications

This research investigation encompasses experimental tests demonstrating the control of a high-frequency combustion instability by acoustically modulating the propellant flow. A model rocket combustor burned gaseous oxygen and methane using a single-element, pentad-style injector. Flow conditions were established that spontaneously excited a 2430 Hz first longitudinal combustion oscillation at an amplitude up to $p'/p_c \approx 6\%$. An acoustic speaker was placed at the base of the oxidizer supply to modulate the flow and alter the oscillatory behavior of the combustor. Two speaker modulation approaches were investigated: (1) Bands of white noise and (2) Pure sinusoidal tones. The first approach adjusted 500 Hz bands of white noise ranging from $0-500$ Hz to $2000-2500$ Hz, while the second implemented single-frequency signals with arbitrary phase swept from $500-2500$ Hz. The results showed that above a modulation signal amplitude threshold, both approaches suppressed 95+% of the spontaneous combustion oscillation. By increasing the applied signal amplitude, a wider frequency range of instability suppression became present for these two acoustic modulation approaches. Complimentary to these experiments, a

linear modal analysis was undertaken to investigate the effects of acoustic modulation at the inlet boundary on the longitudinal instability modes of a dump combustor. The modal analysis employed acoustically consistent matching conditions with a specific impedance boundary condition at the inlet to represent the acoustic modulation. From the modal analysis, a naturally unstable first longitudinal mode was predicted in the absence of acoustic modulation, consistent with the spontaneously excited 2430 Hz instability observed experimentally. Subsequently, a detailed investigation involving variation of the modulation signal from 0−2500 Hz and mean combustor temperature from 1248−1685 K demonstrated the unstable to stable transition of a 2300−2500 Hz first longitudinal mode. The model-predicted mode stability transition was consistent with experimental observations, supporting the premise that inlet acoustic modulation is a means to control high-frequency combustion instabilities. From the modal analysis, it may be deduced that the inlet impedance provides a damping mechanism for instability suppression. Combined, this work demonstrates the strategic application of acoustic modulation within an injector as a potential method to control high-frequency combustion instabilities for liquid rocket engine applications.

Abstract Approval: Committee Chair

Dr. Robert A. Frederick Jr.

Department Chair

Dr. D. Keith Hollingsworth

Graduate Dean

Dr. David Berkowitz

ACKNOWLEDGMENTS

My experience pursuing this degree has been a very long journey. Filled with many twists and turns, starts and stops. As this chapter is coming to a close and I look back on this experience, I can't help but appreciate how much I have grown as a researcher. Through it all, I have found that perseverance is essential to success and it is really true that the darkest hour is just before the dawn. Problem solving and overcoming obstacles are what we are trained to do as engineering researchers, and so often through shear determination can we accomplish our goals. If it were not for the assistance of the many individuals who have helped me along the way, I would not be here today.

I would first like to acknowledge the University of Alabama in Huntsville for providing me with the Von Braun Propulsion Scholarship for this project. It has been a honor to research under this very prestigious position and I am very thankful for the opportunities this award has provided me.

My advisor, Dr. Robert Frederick, needs to be commended for giving me the opportunity to research at the Propulsion Research Center. Through his guidance and consistent support, this work was possible. Ever since I started at UAH, he has done everything possible to set me up for success, and for that, I am forever grateful. I truly value all that I have learned working with you over the years.

I greatly appreciate the assistance of Dr. David Lineberry, who was vital in the experiment program for this work. I thank you for the many hours you spent helping perfect the data acquisition system and valve timing sequences for the combustor. Also, your assistance during the initial system check-out tests was crucial in allowing the experiments to be a success.

Dr. Sarma Rani also is to be acknowledged for his help in developing the analytical model within this work. With his direction, a complimentary analysis of the model combustor was able to be created. I appreciate our many discussions regarding combustion instability phenomena that took place during the development of the model. With your assistance, this research was advanced into a well-rounded blend of experiments and analysis.

I would also like to thank my other committee members, Drs. Hollingsworth, Frendi and Xu, for their recommendations regarding this research. Their insightful comments have been very helpful in shaping this work.

My fellow colleagues at the Propulsion Research Center also are to be recognized for all of their help. In particular, I am very grateful for the assistance of Tony Hall, who aided with the construction of the test facility and was instrumental with his insight regarding the hardware for the project. Also, I appreciate the feedback I received from fellow graduate students Chad Eberhart, Matthew Hitt and Brian Sweeney throughout the duration of this work. Finally, Logan Grumbach is to be acknowledged for his assistance with testing.

A huge debt of gratitude is owed to my research partner, Jacob Cranford, for all of his hard work. From the initial system check-out tests in which he played an unforgettable role, to the first successful instability suppression tests that were recognized by the engineering community, he has been there for all phases of this work. You have gone above and beyond what was asked time and time again, and I thank you for the countless hours we spent on this work. Your consistent effort and positive attitude has truly made for some great memories.

To my fellow friends in the computational modeling field, I thank you for your help. I greatly appreciate the assistance Vijaya Rani provided me during the Mathematica code development for the analytical model. With his help, the coding process became very streamlined and efficient. Working alongside Shreyas Bidadi my first semester in the Fluids Lab was also a very enriching experience. I have really enjoyed our discussions regarding fluid mechanics and propulsion topics through the years.

If it was not for my family, I would not be the person I am today. Without all of my family's support through the years, none of this would ever have been possible. I would like to thank my Uncle, John Gilbert, for encouraging me to continue my education at UAH. You have been very helpful to me during my time in Huntsville, and for that, I'm forever grateful. My parents and sister have been my personal support structure ever since I can remember. Blasting off rockets with my Dad since I was barely big enough to hold the launch controller, working on a water rocket experiment with my Mom in the eighth grade, even going through Pitt Engineering with my sister, they were all there every step of the way. I cannot thank you enough for

all the sacrifices you have made for me. My grandparents also need to be commended for their continued interest in both my and my sister's education; your support has given us both the strength to climb the academic summit.

Of course, my wife, Tara, is the reason I am able to accomplish my goals. Ever since I came to Huntsville, her support has given me strength I never knew existed. I thank you for everything you have done to allow me to finish my education. Your ability to see the larger picture has given me the proper perspective all throughout this work. I love you and I cannot wait to see what comes next for us.

TABLE OF CONTENTS

List of Figures **xvii**

List of Tables **xxiv**

List of Symbols **xxvi**

Chapter

1 Introduction **1**

1.1 Foreword 1

1.2 Historical Significance 2

1.3 Background 3

1.3.1 Liquid Rocket Engines 3

1.3.2 Combustion Chamber Processes 5

Injection 6

Atomization 9

Vaporization 10

Mixing 11

Combustion 12

1.4 Thermo-Acoustic Instabilities 14

1.4.1 Low-Frequency Combustion Instabilities 18

1.4.2 High-Frequency Combustion Instabilities 20

Longitudinal Instabilities 20
Transverse Instabilities 21
1.4.3 Coupling Mechanisms 26
Injection 28
Atomization 28
Vaporization 29
Mixing 29
Combustion 30

2 Background **32**

2.1 Historic Combustion Instability Control Techniques 32
2.1.1 Longitudinal Mode Control 33
2.1.2 Transverse Mode Control 33
Symmetric Injector Plate Baffle 34
Symmetric Fuel Injector Distribution 38
Resonance Absorbers 39
2.2 Advanced Combustion Instability Control Techniques 41
2.2.1 Asymmetric Injector Plate Baffle 41
2.2.2 Asymmetric Fuel Injector Distribution 44
2.2.3 Propellant Line Flow Modulation 48
Fast-Response Actuation Valve Study 48
Application of Acoustic Driving 51
2.3 Fundamental Combustion Instability Work 52

2.3.1 Flame-Acoustic Interaction under Controlled Acoustic Excitation . . . 52

2.4 Advancement to the State-of-the-Art . . . 56

3 Experimental Approach **57**

3.1 Overview . . . 57

3.1.1 Band-Limited White Noise Study . . . 58

3.1.2 Single-Frequency Acoustic Modulation Study . . . 58

3.2 Experiment Overview . . . 59

3.2.1 Single Element Model Rocket Combustor (SEMRC) . . . 59

3.2.2 Injector . . . 60

3.2.3 JBL 2446J Compression Driver . . . 61

3.2.4 Measurement Devices . . . 62

High-Speed Data Acquisition System . . . 62

Static Pressure Transducers . . . 63

High-Frequency Piezoelectric Pressure Transducers . . . 63

Thermocouples . . . 65

3.3 Test Campaign . . . 66

4 Data Analysis Methodology **68**

4.1 Acoustic Analysis Tools . . . 68

4.1.1 Analytical Acoustic Model for a Closed-Top Cylindrical Chamber . . . 69

4.1.2 Numerical Acoustic Model . . . 80

Model Validation . . . 82

4.2 Signal Analysis Tools 84

4.2.1 Time-Domain Characterization: Two-Way Butterworth Bandpass Filter 84

4.2.2 Frequency-Domain Characterization: Fast Fourier Transform 85

5 Experimental Results **90**

5.1 Instability Mode Determination 91

5.1.1 Numerical Acoustic Model: Non-Homogeneous Sound Speed Study 92

5.2 Experiment Testing: Phase One 97

5.2.1 Band-Limited White Noise: Principle Baseline Testing 97

5.2.2 Single-Frequency Acoustic Modulation: Principle Baseline Testing 105

5.3 Experiment Testing: Phase Two 113

5.3.1 Band-Limited White Noise: Signal Amplitude Study 113

5.3.2 Single-Frequency Acoustic Modulation: Signal Amplitude Study 123

5.4 Experiment Testing: Phase Three 132

5.4.1 Band-Limited White Noise: Pure Acoustic Testing 132

5.4.2 Single-Frequency Acoustic Modulation: Pure Acoustic Testing 135

6 Linear Modal Analysis Results **139**

6.1 Theory 140

6.2 Application to Combustor Geometry 141

6.2.1 Pressure Matching Condition 143

6.2.2 Velocity Matching Condition 143

6.2.3 Acoustically Closed Boundary Condition 144

6.2.4 Acoustic Speaker Boundary Condition 145

6.3 Speaker Constant Determination 146

6.3.1 Development of the Speaker Model Frequency Response Function (SMFRF) 147

6.3.2 Experimental Determination of the Speaker System Resonances 150

6.4 Assembly of the Boundary and Matching Conditions 153

6.5 Linear Modal Analysis Results and Discussion 154

7 Conclusions **159**

7.1 Summary 159

7.2 Recommendations and Future Work 163

APPENDIX A: Supplemental Acoustic Derivations **167**

A.1 Linear Homogeneous Acoustic Wave Equation 167

A.2 Linear Homogeneous Acoustic Wave Equation: Cylindrical Coordinate System Transformation 173

A.3 Cylindrical Chamber Acoustic Mode Pressure Distribution Solution Transformation 182

A.4 Linear Homogeneous Acoustic Wave Equation with Uniform Mean Flow 185

APPENDIX B: Supplemental Experimental Results **189**

B.1 Band-Limited White Noise: Principle Baseline Testing 189

B.1.1 Test 06-28-01: Waterfall Plot Supplement 189

B.1.2 Test 06-28-02: Waterfall Plot Supplement 190

B.2 Single-Frequency Acoustic Modulation: Principle Baseline Testing 191

B.2.1 Test 08-01-04: Waterfall Plot Supplement 191

B.2.2 Test 08-01-04: Maximum Normalized Instability Amplitude Response 193

B.2.3 Test 08-01-05: Waterfall Plot Supplement 194

B.2.4 Test 08-01-05: Maximum Normalized Instability Amplitude Response 196

B.3 Band-Limited White Noise: Signal Amplitude Study 197

B.3.1 $P'3$ Waterfall Plot Supplement 197

B.3.2 P'_{inj} Waterfall Plot Supplement 200

B.3.3 Maximum Normalized Instability Amplitude Response 203

B.4 Single-Frequency Acoustic Modulation: Signal Amplitude Study . . . 205

B.4.1 $P'1$ Waterfall Plot Supplement 205

B.4.2 P'_{inj} Waterfall Plot Supplement 208

B.5 Band-Limited White Noise: Pure Acoustic Testing 211

B.5.1 $P'1$ Waterfall Plot Supplement 211

B.5.2 $P'2$ Waterfall Plot Supplement 213

B.5.3 $P'3$ Waterfall Plot Supplement 215

B.5.4 P'_{inj} Waterfall Plot Supplement 217

B.6 Single-Frequency Acoustic Modulation: Pure Acoustic Testing 219

B.6.1 $P'1$ Waterfall Plot Supplement 219

B.6.2 $P'2$ Waterfall Plot Supplement 221

B.6.3 $P'3$ Waterfall Plot Supplement 223

B.6.4 P'_{inj} Waterfall Plot Supplement 225

REFERENCES **227**

LIST OF FIGURES

FIGURE PAGE

1.1 Propellant Delivery System for Typical Liquid Rocket Engines 4

1.2 Propellant Injection Stream Patterns for Typical Liquid Rocket Engines 7

1.3 Comparison Between Subcritical and Supercritical Propellant Injection 10

1.4 Pressure Oscillation Traces for Smooth Combustion and Combustion Instability Excitation 14

1.5 Unsteady Flame/Acoustic Interaction Schematic 16

1.6 Acoustic Pressure and Velocity Distributions for Common Transverse Instability Modes 22

1.7 Images Documenting One Cycle of the Spinning First Tangential Mode 24

1.8 Images Documenting One Cycle of the Standing First Tangential Mode 24

2.1 Example of a Symmetric Injector Plate Baffle System 34

2.2 Effect of a Symmetric Baffle System on the Acoustic Resonance Characteristics of a Liquid Rocket Engine Combustor 35

2.3 Schematic of a Symmetric Fuel Injector Distribution 38

2.4 Schematic of a Liquid Rocket Engine with an Acoustic Resonance Absorber 40

2.5 Asymmetric Baffle System for the Model Liquid Rocket Combustor 42

2.6 Instability Pressure Amplitude and Frequency Corresponding to Baffle Insertion Length 43

2.7 Asymmetric Fuel Injector Distribution System for the Model Liquid Rocket Combustor 45

2.8 Instability Amplitude vs. Air-Split Ratio (K_1) Plot 46

2.9 Combustion Instability Frequency Response Due to the Alteration in Fuel Flow Rate Actuation Frequency 49

2.10 Combustion Instability Amplitude Response Due to the Alteration in Fuel Flow Rate Actuation Frequency 50

2.11 Experiment Configuration with Acoustic Fuel Flow Modulation and Instability Suppression Plot through Acoustic Forcing 51

2.12 Schematic of the Single Injector Combustor with Transverse Acoustic Forcing 53

2.13 Perturbation Growth and Decay at the Fuel-Oxidizer Interface Due to the Alignment of $\bigtriangledown p$ and $\bigtriangledown \rho$ 54

2.14 Flame Perturbation Characteristics Due to Acoustic Forcing 55

3.1 View of the Single Element Model Rocket Combustor 59

3.2 Experiment Configuration Schematic with Acoustic Modulation . . . 60

3.3 Dimensioned Views of the SEMRC and Pentad Injector 64

4.1 Plot of the Bessel Function of the First Kind 76

4.2 Plot of the Bessel Function of the Second Kind 76

4.3 Plot of the Bessel Function of the First Kind with Mode Critical Points 78

4.4 Pressure Distributions of the First Four Longitudinal Acoustic Eigenmodes for Homogenous Sound Speed Conditions 83

4.5 Imposed Phase Shift Comparison between One-Way and Two-Way Filters 85

4.6 Time Histories and Frequency Spectra for Various Signal-to-Noise Ratio Cases 87

4.7 Signal Amplitude Percent Error Sensitivity Due to Signal-to-Noise Ratio 88

4.8 Example High-Frequency Pressure Data Taken from an Instability Baseline Test 89

5.1 Raw Time History and Frequency Spectra from an Instability Baseline Test 91

5.2 Model Geometries for the Non-Homogeneous Sound Speed Case Study 93

5.3 Alteration of the First Longitudinal Mode Frequency Due to Non-Homogeneous Sound Speed Conditions 95

5.4 Alteration of the First Longitudinal Acoustic Mode Pressure Distribution Due to Non-Homogenous Sound Speed Conditions 96

5.5 Instability Amplitude vs. Applied Bands of White Noise for Test 06-28-01 99

5.6 P'_{inj} Waterfall Plot for Test 06-28-01 101

5.7 Instability Amplitude vs. Applied Bands of White Noise for Test 06-28-02 102

5.8 P'_{inj} Waterfall Plot for Test 06-28-02 104

5.9 Baseline Normalized Instability Amplitude Response for Test 08-01-04 108

5.10 Baseline Normalized Instability Amplitude Response for Test 08-01-05 109

5.11 $P'2$ and $P'3$ Waterfall Plots for Tests 08-01-04 and 08-01-05 111

5.12 P'_{inj} Waterfall Plots for Tests 08-01-04 and 08-01-05 112

5.13 $P'3$ Waterfall Plots for the Band-Limited White Noise Signal Amplitude Study 116

5.14 P'_{inj} Waterfall Plots for the Band-Limited White Noise Signal Amplitude Study 118

5.15 Baseline Normalized Instability Amplitude Response in the Ascending Band-Limited White Noise Direction 120

5.16 Baseline Normalized Instability Amplitude Response in the Descending Band-Limited White Noise Direction 121

5.17 $P'1$ Waterfall Plots for the Single-Frequency Acoustic Modulation Signal Amplitude Study 126

5.18 P'_{inj} Waterfall Plots for the Single-Frequency Acoustic Modulation Signal Amplitude Study 127

5.19 Maximum Normalized Instability Amplitude Response in the Descending Single-Frequency Acoustic Modulation Direction 129

5.20 Maximum Normalized Instability Amplitude Response in the Ascending Single-Frequency Acoustic Modulation Direction 130

5.21 P'_{inj} Waterfall Plots for the Band-Limited White Noise Pure Acoustic Tests 134

5.22 $P'1$ Waterfall Plots for the Band-Limited White Noise Pure Acoustic Tests 135

5.23 P'_{inj} Waterfall Plots for the Single-Frequency Acoustic Modulation Pure Acoustic Tests 137

5.24 $P'1$ Waterfall Plots for the Single-Frequency Acoustic Modulation Pure Acoustic Tests 138

6.1 Schematic of the Combustor Model Geometry 142

6.2 Schematic of the Speaker Mass-Spring-Damper System 145

6.3 Schematic of the Speaker Mass-Spring-Damper System Used to Determine the SMFRF 147

6.4 Speaker Constant Determination Test Facility 151

6.5 Speaker Model Transfer Function for the JBL 2446J Speaker 152

6.6 Effect of Single-Frequency Application on the First Longitudinal Instability Mode Growth Rate with $f = 2300-2500$ Hz 156

6.7 Comparison Between Experiment Results and the Analytical Model Prediction 157

B.1 Enlarged Waterfall Plot for Test 06-28-01: P'_{inj} 189

B.2 Enlarged Waterfall Plot for Test 06-28-02: P'_{inj} 190

B.3 Enlarged Waterfall Plots for Test 08-01-04: $P'2$ and $P'3$ 191

B.4 Enlarged Waterfall Plot for Test 08-01-04: P'_{inj} 192

B.5 Maximum Normalized Instability Amplitude Response from Test 08-01-04 193

B.6 Enlarged Waterfall Plots for Test 08-01-05: $P'2$ and $P'3$ 194

B.7 Enlarged Waterfall Plot for Test 08-01-05: P'_{inj} 195

B.8 Maximum Normalized Instability Amplitude Response from Test 08-01-05 196

B.9 Enlarged $P'3$ Waterfall Plots for the Band-Limited White Noise Signal Amplitude Study: 13% and 30% RMS 197

B.10 Enlarged $P'3$ Waterfall Plots for the Band-Limited White Noise Signal Amplitude Study: 40% and 57% RMS 198

B.11 Enlarged $P'3$ Waterfall Plot for the Band-Limited White Noise Signal Amplitude Study: 62% RMS 199

B.12 Enlarged P'_{inj} Waterfall Plots for the Band-Limited White Noise Signal Amplitude Study: 13% and 30% RMS 200

B.13 Enlarged P'_{inj} Waterfall Plots for the Band-Limited White Noise Signal Amplitude Study: 40% and 57% RMS 201

B.14 Enlarged P'_{inj} Waterfall Plot for the Band-Limited White Noise Signal Amplitude Study: 62% RMS 202

B.15 Maximum Normalized Instability Amplitude Response in the Ascending Band-Limited White Noise Direction 203

B.16 Maximum Normalized Instability Amplitude Response in the Descending Band-Limited White Noise Direction 204

B.17 Enlarged $P'1$ Waterfall Plots for the Single-Frequency Acoustic Modulation Signal Amplitude Study: 16% and 32% RMS 205

B.18 Enlarged $P'1$ Waterfall Plots for the Single-Frequency Acoustic Modulation Signal Amplitude Study: 45% and 58% RMS 206

B.19 Enlarged $P'1$ Waterfall Plot for the Single-Frequency Acoustic Modulation Signal Amplitude Study: 82% RMS 207

B.20 Enlarged P'_{inj} Waterfall Plots for the Single-Frequency Acoustic Modulation Signal Amplitude Study: 16% and 32% RMS 208

B.21 Enlarged P'_{inj} Waterfall Plots for the Single-Frequency Acoustic Modulation Signal Amplitude Study: 45% and 58% RMS 209

B.22 Enlarged P'_{inj} Waterfall Plot for the Single-Frequency Acoustic Modulation Signal Amplitude Study: 82% RMS 210

B.23 Enlarged $P'1$ Waterfall Plots for the Band-Limited White Noise Pure Acoustic Tests: 0.387 and 0.996 kPa-rms 211

B.24 Enlarged $P'1$ Waterfall Plots for the Band-Limited White Noise Pure Acoustic Tests: 1.280 and 2.042 kPa-rms 212

B.25 Enlarged $P'2$ Waterfall Plots for the Band-Limited White Noise Pure Acoustic Tests: 0.387 and 0.996 kPa-rms 213

B.26 Enlarged $P'2$ Waterfall Plots for the Band-Limited White Noise Pure Acoustic Tests: 1.280 and 2.042 kPa-rms 214

B.27 Enlarged $P'3$ Waterfall Plots for the Band-Limited White Noise Pure Acoustic Tests: 0.387 and 0.996 kPa-rms 215

B.28 Enlarged $P'3$ Waterfall Plots for the Band-Limited White Noise Pure Acoustic Tests: 1.280 and 2.042 kPa-rms 216

B.29 Enlarged P'_{inj} Waterfall Plots for the Band-Limited White Noise Pure Acoustic Tests: 0.387 and 0.996 kPa-rms 217

B.30 Enlarged P'_{inj} Waterfall Plots for the Band-Limited White Noise Pure Acoustic Tests: 1.280 and 2.042 kPa-rms 218

B.31 Enlarged $P'1$ Waterfall Plots for the Single-Frequency Acoustic Modulation Pure Acoustic Tests: 0.485 and 0.972 kPa-rms 219

B.32 Enlarged $P'1$ Waterfall Plots for the Single-Frequency Acoustic Modulation Pure Acoustic Tests: 1.366 and 2.014 kPa-rms 220

B.33 Enlarged $P'2$ Waterfall Plots for the Single-Frequency Acoustic Modulation Pure Acoustic Tests: 0.485 and 0.972 kPa-rms 221

B.34 Enlarged $P'2$ Waterfall Plots for the Single-Frequency Acoustic Modulation Pure Acoustic Tests: 1.366 and 2.014 kPa-rms 222

B.35 Enlarged $P'3$ Waterfall Plots for the Single-Frequency Acoustic Modulation Pure Acoustic Tests: 0.485 and 0.972 kPa-rms 223

B.36 Enlarged $P'3$ Waterfall Plots for the Single-Frequency Acoustic Modulation Pure Acoustic Tests: 1.366 and 2.014 kPa-rms 224

B.37 Enlarged P'_{inj} Waterfall Plots for the Single-Frequency Acoustic Modulation Pure Acoustic Tests: 0.485 and 0.972 kPa-rms 225

B.38 Enlarged P'_{inj} Waterfall Plots for the Single-Frequency Acoustic Modulation Pure Acoustic Tests: 1.366 and 2.014 kPa-rms 226

LIST OF TABLES

TABLE PAGE

1.1 A Historical Example of a Liquid Rocket Motor that Experienced a Low-Frequency "POGO" Instability 19

1.2 A Historical Example of a Liquid Rocket Motor that Experienced a High-Frequency Longitudinal Instability 21

1.3 Historical Examples of Liquid Rocket Motors that Experienced a First Tangential Mode Instability 25

1.4 A Historical Example of a Liquid Rocket Motor that Experienced a First Radial Mode Instability 25

3.1 Technical Specifications for the JBL 2446J Compression Driver 61

3.2 Test Campaign Summary 66

4.1 Critical Point Locations for the First Sixteen Transverse Acoustic Modes 78

4.2 Longitudinal Eigenfrequency Comparison between the Numerical Acoustic Model and Analytical Solution 83

4.3 Analyzed Cases for the Signal-to-Noise Ratio FFT Amplitude Sensitivity Study 86

5.1 Analyzed Cases for the Non-Homogeneous Sound Speed Study 94

5.2 Flow Conditions and Average Instability Characteristics for the Band-Limited White Noise Principle Baseline Tests 97

5.3 Signal Specifications for the Band-Limited White Noise Principle Baseline Tests 98

5.4 Maximum Instability Suppression Characteristics for the Band-Limited White Noise Principle Baseline Tests 105

5.5 Signal Specifications for the Single-Frequency Acoustic Modulation Principle Baseline Tests 106

5.6 Flow Conditions and Average Instability Characteristics for the Single-Frequency Acoustic Modulation Principle Baseline Tests 106

5.7 Maximum Instability Suppression Characteristics for the Selected Single-Frequency Acoustic Modulation Principle Baseline Tests 110

5.8 Signal Specifications for the Band-Limited White Noise Signal Amplitude Study 113

5.9 Flow Conditions for the Band-Limited White Noise Signal Amplitude Study 114

5.10 Average Instability Characteristics for the Selected Band-Limited White Noise Signal Amplitude Tests 115

5.11 Maximum Instability Suppression Characteristics for the Band-Limited White Noise Signal Amplitude Study 123

5.12 Signal Specifications for the Single-Frequency Acoustic Modulation Signal Amplitude Study 124

5.13 Flow Conditions and Average Instability Characteristics for the Single-Frequency Acoustic Modulation Signal Amplitude Study . . . 124

5.14 Maximum Instability Suppression Characteristics for the Single-Frequency Acoustic Modulation Signal Amplitude Study . . . 131

5.15 Signal Specifications for the Band-Limited White Noise Pure Acoustic Tests 133

5.16 Signal Specifications for the Single-Frequency Acoustic Modulation Pure Acoustic Tests 136

6.1 Speaker Model Parameters and Technical Specifications for the JBL 2446J Speaker 152

6.2 Combustor Temperatures and Instability Characteristics for the Cases without Acoustic Modulation 154

LIST OF SYMBOLS

SYMBOL	DEFINITION
$A^{\pm}$	Amplitudes of the Longitudinal Mode Propagating in the Positive and Negative x Directions, Pa
A	Speaker Diaphragm Area, m^2
a	Characteristic Length in the r Direction, m
B	Electromagnetic Speaker B-field, T
b	Speaker Diaphragm Damping Coefficient, N-s/m
$\overline{c}$	Mean Speed of Sound, m/s
d_{dphgm}	Diaphragm Diameter, cm
d_{inner}	Inner Diameter of the Single Element Model Rocket Combustor, cm
$d_{\text{num,model}}$	Diameter of the Combustor Geometry within the Numerical Acoustic Model, cm
f	Frequency, Hz
$f_{\text{acous,sys}}$	Acoustic System Resonant Frequency of the Speaker Constant Determination Test Facility, Hz
f_{cutoff}	Cutoff Frequency of the Butterworth Filter for the High-Speed NI SCXI-1143 DAQ Module, Hz
$f_{\text{mech,spk}}$	Mechanical Resonance of the JBL 2446J Speaker, Hz
f_s	High-Speed Data Acquisition Sampling Frequency, Hz

F	Force, N
G_{amp}	Amplifier Gain
$H(f)$	Speaker Model Frequency Response Function, m/s-A
I	Current, A
K	Air-split Ratio
k	Total Wave Number, 1/m
k_r	Wave Number Along the r Direction, 1/m
k_z	Wave Number Along the z Direction, 1/m
$k^{\pm}$	Axial Wave Numbers of the Longitudinal Mode Propagating in the Positive and Negative x Directions, 1/m
$l_{\text{const,sys}}$	Length of the Speaker Constant Determination Test Facility, cm
l_{comb}	Length of the Single Element Model Rocket Combustor, cm
L_i	Analytical Model Duct Length of Region i, cm
$l_{\text{num,model}}$	Length of the Combustor Geometry within the Numerical Acoustic Model, cm
L_x	Characteristic Length in the x Direction, m
$\overline{M}$	Mean Flow Mach Number
m	Speaker Diaphragm Mass, kg
$\dot{m}_f$	Mass Flow Rate of Fuel (GCH_4), g/s
$\dot{m}_{ox}$	Mass Flow Rate of Oxidizer (GO_2), g/s

N	Number of Speaker Diaphragm Voice-Coil Turns
p	Pressure of a Fluid, Pa
p_c	Chamber Pressure (Ambient), Pa
p_{cr}	Critical Pressure of a Fluid, Pa
p'	Acoustic Pressure Fluctuations, Pa
$\overline{p}$	Mean Pressure of a Fluid, Pa
p'_{spk}	Acoustic Pressure at the Speaker Diaphragm, Pa
$P'1$	High-Frequency Pressure Transducer #1
$P'2$	〃 〃 〃 〃 #2
$P'3$	〃 〃 〃 〃 #3
$P'4$	〃 〃 〃 〃 #4
P'_{inj}	〃 〃 〃 〃 Located within the Injector Oxidizer Supply Line
P'_{sign}	Applied Signal within the Oxidizer Supply Line
$P'1_{\text{Bsl.}}$	$P'1$ Pressure Amplitude without Acoustic Forcing Present
$P'2_{\text{Bsl.}}$	$P'2$ 〃 〃 〃 〃 〃 〃
$P'3_{\text{Bsl.}}$	$P'3$ 〃 〃 〃 〃 〃 〃
$P'4_{\text{Bsl.}}$	$P'4$ 〃 〃 〃 〃 〃 〃
Q'	Unsteady Heat Release Rate Oscillations per Unit Volume, W/m^3

s	Entropy of a Fluid, J/kg-K
S_i	Analytical Model Duct Diameter of Region i, cm
T	Temperature of a Fluid, K
T_{cr}	Critical Temperature of a Fluid, K
$T'1$	Thermocouple #1
$T'2$	$''$ #2
$T'3$	$''$ #3
$T'4$	$''$ #4
T'_{inj}	$''$ Located within the Injector Oxidizer Supply
T_{comb}	Average Combustor Temperature Measured from the Four Thermocouples Located within the Chamber, K
$T_{\text{ox,sup.}}$	Average Temperature of the Oxidizer Supply Line, K
$\mathbf{u}$	Velocity of a Fluid, m/s
u'	Axial Acoustic Velocity Fluctuations, m/s
$\overline{u}$	Axial Mean Velocity of a Fluid, m/s
u'_{spk}	Acoustic Velocity at the Speaker Diaphragm, m/s
Z	Impedance, Pa-s/m

GREEK

SYMBOL	DEFINITION
β	Region Index
γ	Specific Heat Ratio of a Fluid
κ	Speaker Diaphragm Spring Constant, N/m
λ	Eigenvalue
ν	Kinematic Viscosity of a Fluid, m^2/s
π	Mathematical Constant: Ratio of the Circumference of a Circle to Its Diameter
ρ	Density of a Fluid, kg/m^3
$\overline{\rho}$	Mean Density of a Fluid, kg/m^3
ρ'	Acoustic Density Fluctuations, kg/m^3
ϕ_{avg}	Average Test Equivalence Ratio
ω	Angular Frequency of a Signal, rad/s
$\overline{\boldsymbol{\omega}}$	Vorticity of a Fluid, rad/s
Ω	Complex Frequency, rad/s

To my beloved wife, Tara

CHAPTER 1

INTRODUCTION

1.1 Foreword

The phenomenon of combustion instabilities has been a major issue in the development of liquid rocket engines (LRE's) all throughout their history. Thermo-acoustic combustion instabilities occur when the unsteady heat release generated from combustion couples with the acoustic pressure oscillations within the combustion chamber. When these oscillations couple in phase with each other, a feedback mechanism is created that promotes combustion instability growth. If the severity of these instabilities becomes large enough, the liquid rocket engine can fail due to a structural breakdown of the combustor through over-pressurization, extreme mechanical vibration or heat transfer. The exact reasons as to why combustion instabilities become excited within liquid rocket engine combustors is still not completely known, causing combustion instability research to be a topic of great interest to the propulsion community.

1.2 Historical Significance

Perhaps the most notable example of combustion instability issues pertaining to liquid rocket engines occurred during the design of the F-1 engine for the Saturn V in the 1950's and 1960's. During the development of the F-1 engine, the spontaneous excitation of thermo-acoustic combustion instabilities within its combustor was the main concern that plagued its early design. Starting in 1959, a seventeen month testing campaign for the first iteration of the engine was performed, consisting of forty four full-scale tests. Of these tests, high amplitude combustion instabilities occurred in approximately half (20/44 tests). With this critical design issue hindering the success of the engine, Project First was established to solve the instability issue of the F-1 [1].

Under Project First, the instability issues of the F-1 engine were heavily investigated to generate a stable combustor design. What began in 1962, the program carried out over 2000 full-scale engine tests with 108 various injector designs in an attempt to solve and explain these issues. From these tests, it was determined that certain types of instability (i.e., high-frequency transverse instabilities) were more detrimental to the engine's operation and overall stability than others. These thermo-acoustic instabilities were seen to be the most severe and had a large effect on the propellant interaction processes that take place within the combustor (i.e., injection, atomization, vaporization and mixing) and vice-versa. Thus, the focus of solving the instability issue of the F-1 was directed towards developing damping techniques for the detrimental transverse instability modes [1].

In order to successfully damp the transverse instability modes to a reasonable level, a passive injector-plate baffle system was developed. It was found that through a combination of the appropriate injector design and baffle pattern, the onset of high-frequency transverse instabilities could be successfully prevented within the engine [1].

While Project First was successful in delivering a stable combustor, it took many design iterations and full-scale tests to find a workable solution that ended up being tailored specifically to the F-1 engine. Thus, fundamental understanding behind the phenomenon of thermo-acoustic instabilities is vital to avoid costly liquid rocket engine development campaigns.

1.3 Background

1.3.1 Liquid Rocket Engines

For current space travel, liquid rocket engines have become the main propulsion system used in heavy launch vehicles. Due to their high performance (i.e., high specific impulse), these engines are implemented to provide large amounts of thrust for a substantial time duration. Aside from their high specific impulse, liquid propellant systems are much more controllable during operation than solid propellant systems. For these reasons, liquid rocket engines are predominantly implemented in the core stages of launch vehicles [2].

In order to generate this thrust, combustion within the engine's combustor must first take place. This combustion process occurs when two propellants, the fuel and oxidizer (e.g., LH_2/LO_X, RP-1/LO_X, N_2O_4/N_2H_4, etc.), are introduced into the combustor and interact in a manner that causes chemical reactions to sustain combustion. The more energetic the propellant combination, the larger amount of chemical potential energy available for conversion into thermal enthalpy of the mixture during combustion; this thermal enthalpy is then converted into kinetic energy once the product gas mixture is accelerated through the nozzle. This energy conversion process is what produces thrust to propel the rocket.

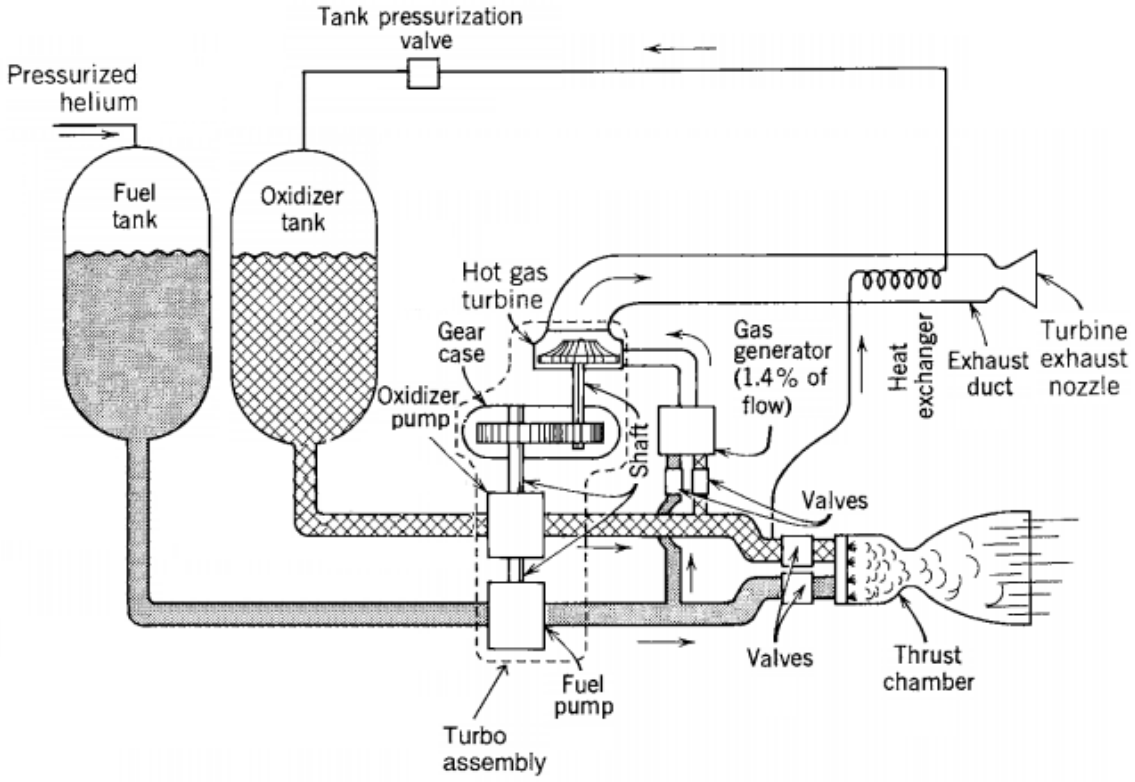

Figure 1.1: Propellant Delivery System for Typical Liquid Rocket Engines: Taken and Edited from [2].

The efficiency and stability of liquid propellant combustion is dictated by the controlled interaction of the propellants within the combustor. Typically, efficiency within the combustor is improved through high chamber temperatures and pressures ($T \approx 2500-3600$ K and $p \approx 20$ MPa) and as such, liquid rocket engine combustors tend to operate in this range [2].

To initiate sustained combustion, a delivery system is employed to supply the liquid propellants to the combustor in a metered fashion. These systems are designed in such a way to apply the necessary pressure to drive the propellants through the delivery system and into the combustor. A schematic of a typical propellant delivery system for liquid rocket engines can be seen in Figure 1.1 [2, 3].

1.3.2 Combustion Chamber Processes

Prior to understanding the onset of combustion instabilities, it is important to address the processes that occur within the combustor during the interaction between the fuel and oxidizer. The main propellant interaction processes directly depend on the type of combustion (i.e., premixed or non-premixed) and whether the incoming propellants are either subcritical or supercritical in nature. In regards to the type of combustion which occurs, liquid rocket engines almost entirely employ non-premixed combustion systems, as they are safer and more controllable than premixed systems. For the conditions seen in liquid rocket engine combustors, however, both subcritical and supercritical conditions can exist, and therefore, will be covered in greater detail.

Subcritical injection takes place when the temperature and pressure of the incoming propellants do not exceed their respective critical temperature and pressure (T_{cr} and p_{cr}). Under these conditions, the state of the propellants can exist in a distinct liquid, vapor or gaseous phase. Under supercritical conditions, however, the temperature and pressure of the incoming propellants do exceed their respective critical values, causing a supercritical fluid to exist within the combustor. Under supercritical conditions, there is not a distinguishable difference between the gaseous and liquid phases of the flow. Conceptually, propellant interaction for a non-premixed combustion system under subcritical propellant injection can be divided in the following processes: (1) Injection, (2) Atomization, (3) Vaporization, (4) Mixing and (5) Combustion.

Injection

The injection of the fuel and oxidizer is the first process that occurs within the combustion chamber. The injection system is designed to deliver the propellants into the combustor in a manner which promotes efficient combustion (i.e., high amounts of atomization, vaporization and mixing). Injection systems for liquid rocket engines can be classified under one of two main categories. The first type implements injector elements that introduce the fuel and oxidizer individually through a series of patterned holes on the injector plate, while the second type employs injector elements that deliver both propellants through each injector to create a series of conical sprays at the injection plane. Both injection systems have proven to be successful in delivering propellants effectively for combustion and thus, have been incorporated within rocket applications [2].

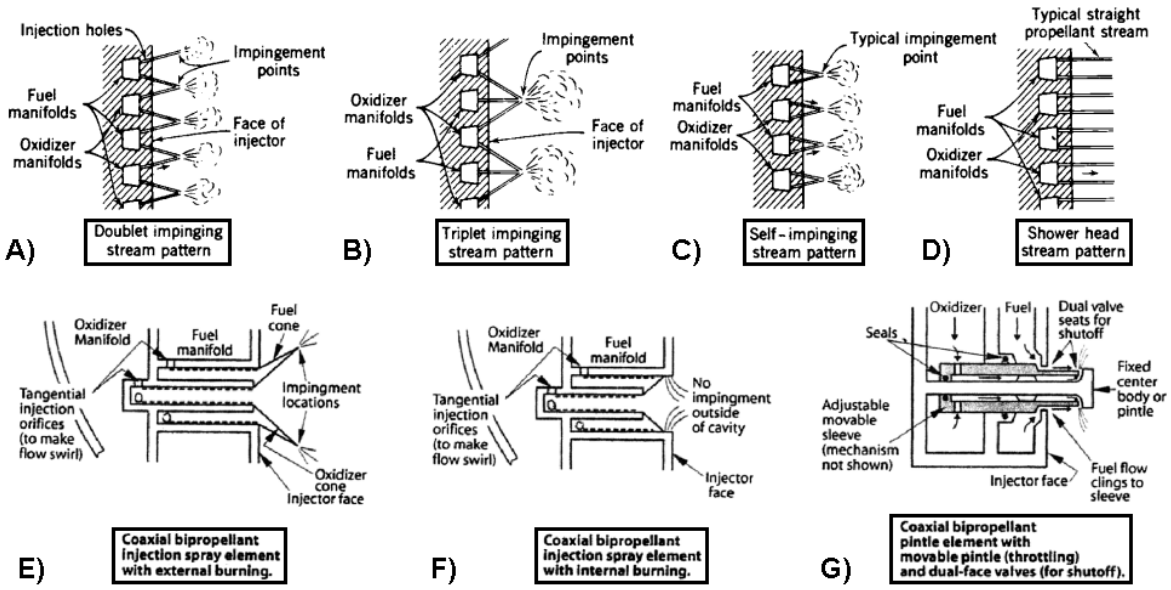

Figure 1.2: Propellant Injection Stream Patterns for Typical Liquid Rocket Engines: Taken and Edited from [2].

Within the two main categories of propellant injection systems for liquid rocket engines, there exist multiple variations of injection schemes. Common propellant injection patterns include the following: (1) Doublet Impinging Stream Pattern, (2) Triplet Impinging Stream Pattern, (3) Self-Impinging Stream Pattern, (4) Shower Head Stream Pattern and (5) Coaxial Bipropellant Injectors (Multiple Types). These can be seen in Figure 1.2 [2].

The first four injection patterns are examples of the separate fuel and oxidizer injection element type, while the three coaxial bipropellant injectors are examples of the combined fuel and oxidizer injector type [2].

Of the four separate element injection patterns (shown in Figure 1.2.A−D), the shower head stream pattern injection system is the simplest in design, as the propellants are injected separately into the combustor in the axial direction. For the

impinging stream patterns, the injectors are designed to angle the sprays from the fuel and oxidizer elements towards each other to increase mixing, while the shower head design encourages natural mixing. One injector design derived from the triplet impinging stream pattern is the pentad injector. It employs an inner flow path (typically the oxidizer) and four impinging streams (usually the fuel) which surround the inner stream at a specific angle (e.g., 30°, 45°, 60°, etc.). This design promotes fine atomization and enhanced mixing, while providing an equal momentum distribution of the streams due to their symmetric configuration [2, 4, 5].

Aside from these injection patterns, the implementation of coaxial bipropellant injectors is also common within liquid rocket engines. In this injection scheme, each injector element is equipped with an inner and outer flow path for the fuel and oxidizer, where there exists a difference in velocity between the propellant flows. As seen in Figure 1.2, coaxial injectors typically pass the oxidizer through the inner flow path and inject the fuel through the outer path. For typical liquid rocket engine applications, the oxidizer core travels on the order of 30 m/s and is surrounded by the fuel flow travelling at 300 m/s (approximately ten times quicker). This injector configuration and velocity difference between channels tends to greatly increase propellant mixing [2].

Some coaxial injectors employ propellant swirl, where the two flow paths are given a tangential velocity component within the injector through orifices. This is shown in the first two coaxial bipropellant injector configurations (Figure 1.2.E and 1.2.F). When flow swirl is imparted on the propellants, the mixing process of the propellants is effectively enhanced [2, 3].

Atomization

Upon the injection of the fuel and oxidizer, the propellants begin to quickly disburse into droplets through atomization. This disbursement and formation of droplets can be attributed to the shear layer and capillary forces of the propellant jet; the shear layer and capillary forces are generated due to the velocity difference of the jet and surrounding fluid. Capillary forces tend to agitate the jet core, causing perturbations to form on the jet core surface. From these perturbations, flow ligaments form and grow, eventually detaching to create large droplets. These large droplets then break up even further into smaller droplets; the presence of these smaller droplets is an indication that complete subcritical atomization has occurred [3, 6].

During supercritical propellant injection, there is no definitive atomization process. The lack of a distinguishable difference between the gaseous and liquid phases of the flow allows the supercritical jet shear layer to be characterized by the mixing between the turbulent gas phase of fluids of largely varying densities. Instead of droplets detaching and breaking up from the jet core shear layer, threadlike structures generate and are mostly dissolved prior to the structures detaching from the jet core. It is this generation and dissolving of threadlike structures which governs this process for supercritical propellant injection. A comparison schematic showing the propellant injection for both subcritical and supercritical conditions can be seen in Figure 1.3 [3, 6].

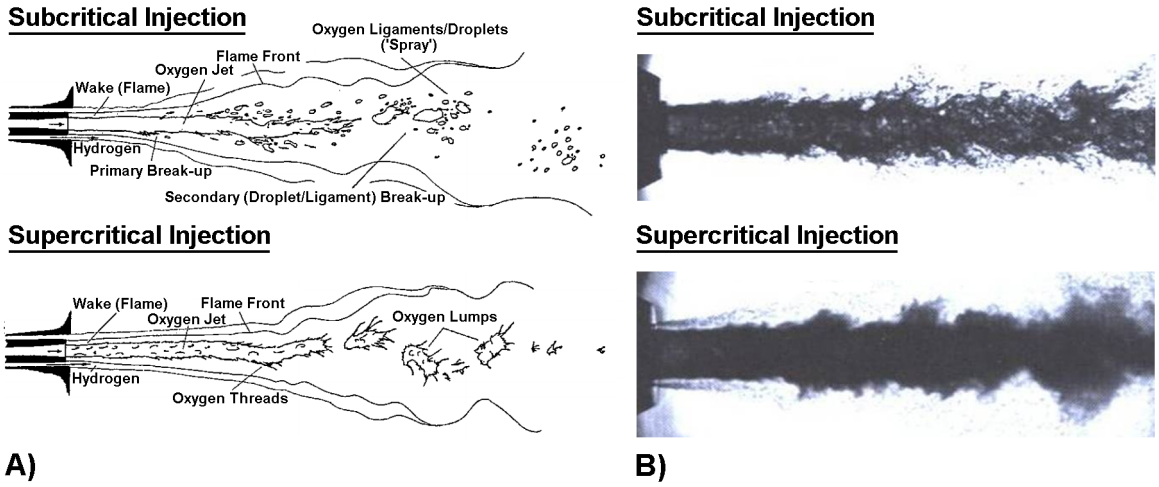

Figure 1.3: Comparison Between Subcritical and Supercritical Propellant Injection – A) Schematics and B) High-Speed Images: Taken and Edited from [6, 7].

Vaporization

Similarly to atomization, vaporization is another process that only occurs during subcritical propellant injection. Vaporization is the diffusion of liquid propellant droplets into the gaseous mixture. Small liquid droplets must vaporize at a rate rapid enough for efficient mixing to occur for combustion. This vaporization process can take place through either droplet boiling or evaporation. Droplet boiling occurs when the droplet liquid is heated to its boiling point due to the heat transferred across the temperature gradient between the surrounding gas and droplet. Evaporation of the droplet is caused when the droplet surface reaches thermodynamic equilibrium with the surrounding gas, which can be attributed to the concentration of chemical species within the combustible mixture [6, 8].

Both of these processes occur concurrently and have shown to be dependent on one another, particularly during the vaporization of large and small droplets. Large droplets tend to evaporate more quickly due to increased surface area, permitting increased heating of the liquid in the droplet for boiling. Small droplets on the other hand, are more easily heated due to smaller amounts of liquid necessary for boiling, and this heating causes a change in thermodynamic equilibrium to the point where evaporation is enhanced. As these processes are inherently dependent on each other, droplet boiling and evaporation are considered as a combined entity of vaporization [8].

Mixing

Mixing is the propellant interaction process that precedes combustion. For combustion to occur, sufficient mixing of the propellants must take place at an equivalence ratio suited for sustained chemical reaction. Chemical mixing in liquid rocket engines will be turbulent, as the Reynolds number of the propellant flow into the combustion chamber are large enough to fall within the turbulent regime. Thus, molecular mixing takes place through turbulent mass diffusion of the fuel and oxidizer towards each other from regions of high to low species concentration. This process permits regions of adequate equivalence ratio to be generated for sufficient chemical reaction to occur. Once this takes place, combustion is able to be sustained [9].

Combustion

Chemical reaction for combustion is the final process the propellants undergo, leading to large amounts of heat release within the combustor. Essentially, combustion is a self-sustained chemical oxidation of the fuel, where the heat generated in the reaction zone (i.e., flame) is partially used to preheat and vaporize (if applicable) the propellant droplets, which in turn continues to drive the flame. Through proper molecular mixing and ignition, along with localized chemical reactions occurring on a small enough time scale, a reaction zone characterized by high heat release will be generated [10].

From a chemical standpoint, the combustion process can be described using a chemical reaction mechanism through which the reactants are converted into combustion products. The formation rate of combustion products is directly dependent on this mechanism and the reaction rates of its elementary reaction steps. During combustion, intermediate chemical radicals, which are highly reactive elements (e.g., H, O, CH*, OH*, HO_2, etc.), are the most significant species which propagate the elementary reactions within the chemical mechanism [9].

For this chemical reaction mechanism, radical chain branching, radical chain termination and the rate-limiting steps are typically the most notable elementary reactions for combustion. Radical pooling (the formation of a massive amount of chemical radicals) due to radical chain branching is first necessary to progress enough

chemical reactions to initiate combustion. Conversely, the destruction of radicals (i.e., chain termination) tends to be associated with the formation of combustion products and the majority of heat release. The overall progression of the chemical mechanism is always restricted by the slowest step within the reaction mechanism, which is deemed the rate-limiting step. As there exists many chemical times across the elementary reaction steps, the non-limiting reactions have times scale so short in comparison to the rate-limiting step that these elementary reactions appear to happen infinitely fast. The rate-limiting reaction generally is dependent on the amount of energy required for the reaction to occur (i.e., activation energy) and whether energy is released (exothermic) or absorbed (endothermic) during the reaction. Often times, endothermic reactions require more activation energy and thus, are typically associated with rate-limiting steps [9, 10].

In liquid rocket engines, aside from having knowledge of the combustion chemistry of the propellants, there is a desire to have an understanding of where the reaction zone will stabilize within the combustion chamber. For non-premixed combustion systems, the reaction zone is located in a region where the fuel and oxidizer molecularly mix at stoichiometric proportions. For example, in typical injection schemes (e.g., coaxial/pentad type injection), the flame is attached to a recirculation zone located near the propellant jet core that expands downstream in the shear layer of the jet; this recirculation zone causes the flame to break up the fuel and oxidizer, while providing pre-heating to the incoming propellant. These two effects combine to stabilize the reaction zone in the combustor [3, 6].

1.4 Thermo-Acoustic Instabilities

During the burning of propellants, periodic oscillations of combustion may occur within the combustor, which are often manifested as periodic oscillations in chamber pressure. Historically, it has been said that when these pressure fluctuations are less than ±5% of the mean chamber pressure, operation of the combustor is considered "smooth" (see Figure 1.4.A), while if the pressure oscillations within the combustor are systemically ordered and exceed $p'/p_c \approx 10\%$, a combustion instability is present. This can be seen in Figure 1.4.B, where a thermo-acoustic instability on the order of 3.45 MPa amplitude became active during a test of the F-1 engine. However, since the development of the F-1, classifying combustion instability excitation has shifted to focus on the sinusoidal/steep-fronted nature of spontaneous chamber pressure oscillations, rather than strictly their amplitude [2, 11].

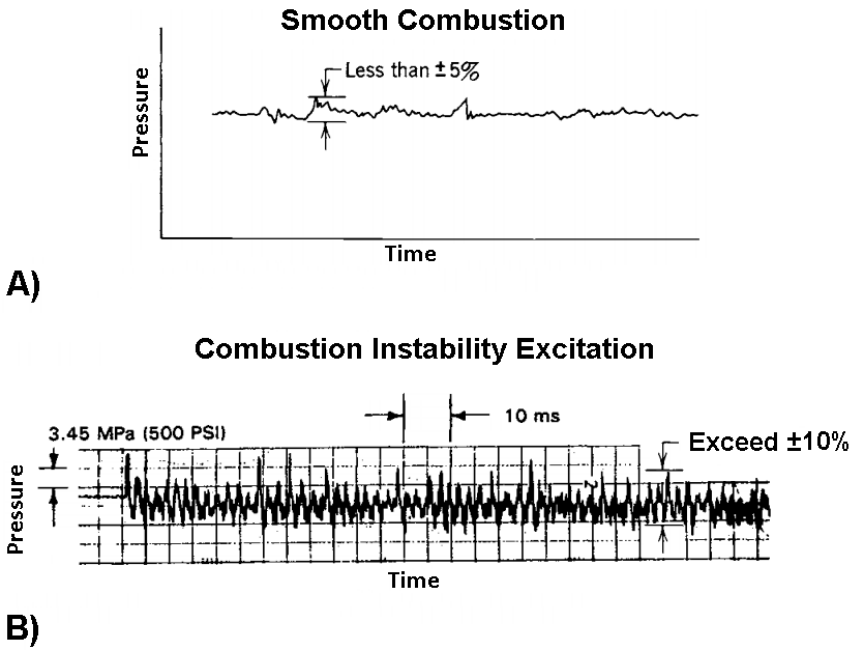

Figure 1.4: Pressure Oscillation Traces for A) Smooth Combustion and B) Combustion Instability Excitation from an F-1 Engine Test: Taken and Edited from [2, 12].

Generally, flames have naturally occurring instabilities, which produce noise in two forms; the first kind of noise is generated from the presence of instabilities within the turbulent flow of the reaction zone (deemed autonomous noise), while the second type of noise comes from the coupling between the chamber acoustics and flame front. This coupling noise is the acoustic source of significance in studying the onset of spontaneous thermo-acoustic combustion instabilities [13].

The unsteady heat release associated with combustion can be thought of as an acoustic source which propagates sound disturbances throughout the combustor (see Figure 1.5). Once the pressure waves traveling away from the source see an acoustic boundary, they reflect back towards the flame; the combination of these reflected waves creates acoustic pressure and velocity fluctuations in the vicinity of the injector plate, which alter the incoming propellant stream and cause local perturbations to the unsteady heat release rate. If the acoustic oscillations alter the burning rate with the correct phasing, the intensity of the instabilities within the reaction zone is increased and cause amplified flame oscillations. This in turn causes larger amplitude acoustic disturbances to be generated from the unsteady heat release oscillations, which then drive the instability's growth [11, 13, 14].

The presence of combustion instabilities within liquid rocket engine combustors can have detrimental effects to both the operation and lifetime of the engine. The effect of combustion instabilities can range from an increase in acoustic noise to a total failure of the chamber in less than one second through over-pressurization, increased heat transfer to the engine walls or large amplitude structural vibrations. Structural concerns due to enhanced heat transfer have been seen to primarily affect the injector

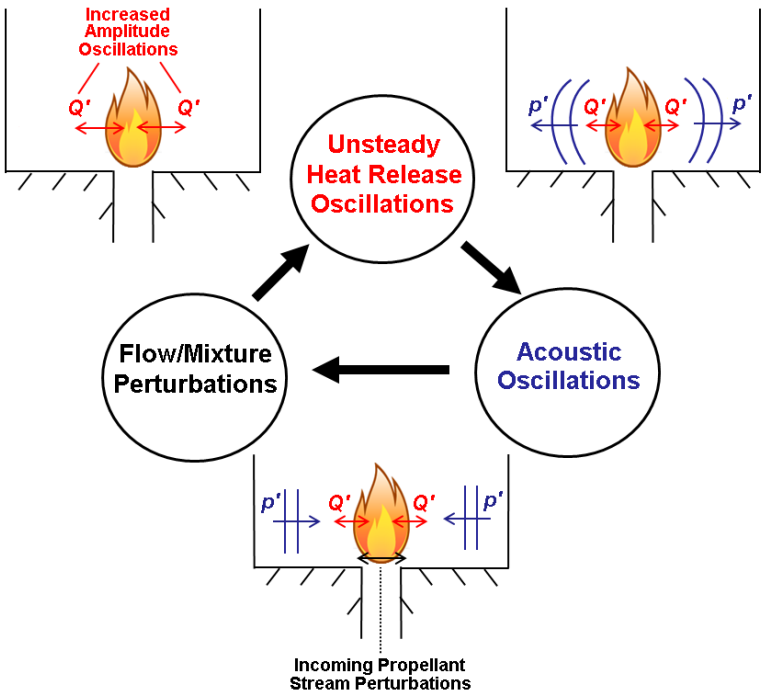

Figure 1.5: Unsteady Flame/Acoustic Interaction Schematic: Based off a Similar Diagram Presented in [15].

plate and nozzle throat of liquid rocket engines. As thermo-acoustic instabilities can lead to a total engine failure, it is important to understand the physical driving mechanisms behind this phenomenon [11, 16].

Although the onset of combustion instabilities tends to be engine specific, the fundamental physics dictating their driving and damping within the combustion chamber is applicable to all engine designs. Essentially, combustion instabilities arise when the energy increase from the unsteady heat release acoustic energy is larger than the acoustic energy losses to the system; this means there is a vital energy exchange with the acoustic energy dispersed throughout the combustor. Thus, the way this energy is disseminated is vital in whether a spontaneous instability becomes active.

Within the combustor, the chemical energy of the combustible mixture is transformed into various forms of energy, one of which is acoustic energy. There exists a trade-off that takes place between the acoustic energy generated through unsteady heat release and the acoustic losses dispersed from the unsteady heat source. If this acoustic energy generated is greater than the acoustic losses produced, combustion instabilities can propagate within the combustor. Thus, the more acoustic damping present within the chamber, the less likely combustion instabilities will be generated. For typical liquid rocket combustor operating conditions, however, the acoustic losses tend to be less than the acoustic energy present within the system, which creates an environment conducive for the chamber acoustic modes to become excited, as well as spontaneous combustion instabilities. Thus, the acoustic damping and boundary conditions of the combustion chamber play a large role in the onset of thermo-acoustic instabilities [3, 16].

Formally, this theory has been mathematically represented by Lord Rayleigh in 1878. In his study, Rayleigh came up with a model that described the exchange of acoustic energy generated by sound waves and the energy created through unsteady heat release. Rayleigh's criterion called for the fluid to be inviscid, and as with many acoustic models, only considered linear perturbations (i.e., neglecting any higher order interactions that may be present within the system). Thus, Rayleigh's criterion states that the amplitude of a sound wave traveling through an inviscid medium will increase if the following condition is met [3, 16, 17]:

$$\int_0^L \frac{(\gamma-1)}{\overline{\rho c^2}}\overline{Q'p'}dx > (p'u'A)_L - (p'u'A)_0 \tag{1.1}$$

γ - Specific Heat Ratio of the Fluid
ρ - Density of the Fluid
c - Sound Speed through the Fluid
Q - Heat Release per Unit Length
p - Pressure of the Fluid
x - Axial Location
A - Cross-sectional Area
$\mathbf{u}$ - Velocity of the Fluid
L - Length of the Combustor

Note: The prime terms are fluctuating quantities.
The subscripts 0 and L denote the combustor inlet and exit plane [16].

Two conclusions can be reached from Rayleigh's criterion: (1) Acoustic perturbations are enhanced when the total energy gained through unsteady combustion is larger than the total energy dissipated through the system boundaries and (2) Energy of the acoustic perturbations is increased when the rate of unsteady heat release is in phase with the pressure oscillations. Thus, if the unsteady heat release rate is of a large enough amplitude and its phase offset with the acoustic pressure oscillations is approximately zero (at least $|\phi^o| < 90^o$), growth of the instability is promoted [11, 16, 17].

1.4.1 Low-Frequency Combustion Instabilities

Within the combustion chamber, there are multiple combustion instability mode types that can be excited during operation. Largely, these are categorized as either low-frequency (LF) or high-frequency (HF) instabilities. Low-frequency instabilities are primarily due to coupling of the injector or propellant feed system to the unsteady heat release of combustion. This type, referred to as "chugging"

instability, is normally on the order of $f \approx 100$ Hz or lower and typically has a linear growth rate from low to high amplitudes. When the feed system couples with combustion at these frequencies, unsteady heat release is onset by fluctuations present within the propellant injection system, which then couple with the acoustic modes of the chamber, generating the feedback necessary to sustain instability growth [18].

Within the combustion chamber, very low frequency instability modes can also be excited (on the order of $f \approx 1-100$ Hz). This type, denoted as "POGO" instability, is attributed to the oscillation of the propellant flow rate, which arises from gravitational force loading on the liquid propellant storage tanks. The driving mechanism behind POGO instabilities is the coupling of chamber thrust oscillations to the structural mode of the rocket. While this type of instability is related to the rocket engine, it does not primarily interact with the combustion of propellants. This is because POGO instabilities act at such low frequencies (with extremely long time periods) they cannot alter the mechanisms for combustion; it is for this reason that POGO is generally not classified as a primary type of combustion instability. Noted in Table 1.1 is a historical example of the Titan II, 1st Stage Engine, which experienced a low-frequency POGO instability during its development [18, 19].

Table 1.1: A Historical Example of a Liquid Rocket Motor that Experienced a Low-Frequency "POGO" Instability: Taken and Edited from [19].

PROJECT	MOTOR	ORGANIZATION CONTRACTOR	PROPELLANTS	THRUST (lbf)	PERFORMANCE (%)	CHAMBER PRESSURE (psia)	INSTABILITY ENCOUNTERED	STABILIZATION DERIVES	INJECTOR TYPE
Gemini	Titan II 1st Stage	USAF/NASA Aerojet	50% N_2H_4) A50 50% UDMH) N_2O_4	236,400	97.2	783.0	POGO Mode ±2.5g	Standpipe inserted into N_2O_4 feedlines	Like doublet

1.4.2 High-Frequency Combustion Instabilities

High-frequency instabilities, which are sometimes referred to as "screech" modes, tend to be on the order of $f \approx 1000-10{,}000$ Hz and are the most damaging of instability types. These instabilities are believed to be the most dangerous because they are characterized by very large acoustic pressure and velocity fluctuations at high frequencies, which are localized throughout the combustor; these acoustic fluctuations lead to an increase in localized heat release rates due to faster mixing of the propellants. If the heat release rate becomes too large, it can ultimately cause harm to the combustor [16].

Longitudinal Instabilities

High-frequency instabilities can be classified as either longitudinal, transverse, or a combination of the two. High-frequency longitudinal modes have oscillations that fluctuate along the axial direction of the combustor. Longitudinal modes are typically not dependent on the combustor cross sectional shape, but rather are dictated by the longitudinal boundary conditions of the combustor. In liquid rocket engines, there exists some natural damping of these instabilities due to the nozzle and axial spatial distribution of combustion, causing this instability type to often be less harmful than transverse modes. However, longitudinal instabilities do occur commonly during liquid rocket engine development, creating issues similar to transverse modes. As seen in Table 1.2, a high-frequency longitudinal instability occurred during the development of the Titan II, 2^{nd} Stage Engine [18, 19].

Table 1.2: A Historical Example of a Liquid Rocket Motor that Experienced a High-Frequency Longitudinal Instability: Taken and Edited from [19].

PROJECT	MOTOR	ORGANIZATION CONTRACTOR	PROPELLANTS	THRUST (lbf)	PERFORMANCE (%)	CHAMBER PRESSURE (psia)	INSTABILITY ENCOUNTERED	STABILIZATION DERIVES	INJECTOR TYPE
Gemini	Titan II 2nd Stage	USAF/NASA Aerojet	50% N_2H_4 50% UDMH]A50 N_2O_4	100,000	97.4	827.0	Longitudinal *mode*	7 *compartment* copper baffles	Quadlet

Transverse Instabilities

Transverse instabilities have oscillations that propagate perpendicularly to the injector surface. As opposed to longitudinal instabilities, transverse modes are affected by both the cross sectional shape of the combustor and the combustor wall boundary conditions. For typical cylindrical combustors, transverse modes are manifested as one of the following: (1) Purely Tangential, (2) Purely Radial or (3) Combined Tangential-Radial Modes. Also, combinations of longitudinal and transverse modes are possible, but not very common in liquid rocket engines. Historically, purely transverse modes have shown to be the most dangerous type of high-frequency instability. Schematics denoting the acoustic pressure and velocity distributions for some common transverse modes can be seen in Figure 1.6 [18, 19].

Tangential modes have pressure node lines which split the combustor in the circumferential direction. These instabilities can take the form of two variations: (1) Spinning or (2) Standing. Spinning tangential modes occur when the instability node line(s) spin tangentially around the chamber at a rate equal to the instability frequency in a clockwise/counter-clockwise fashion (*Note: The spinning direction is arbitrary*). Standing tangential modes occur when the instability node(s) have a fixed

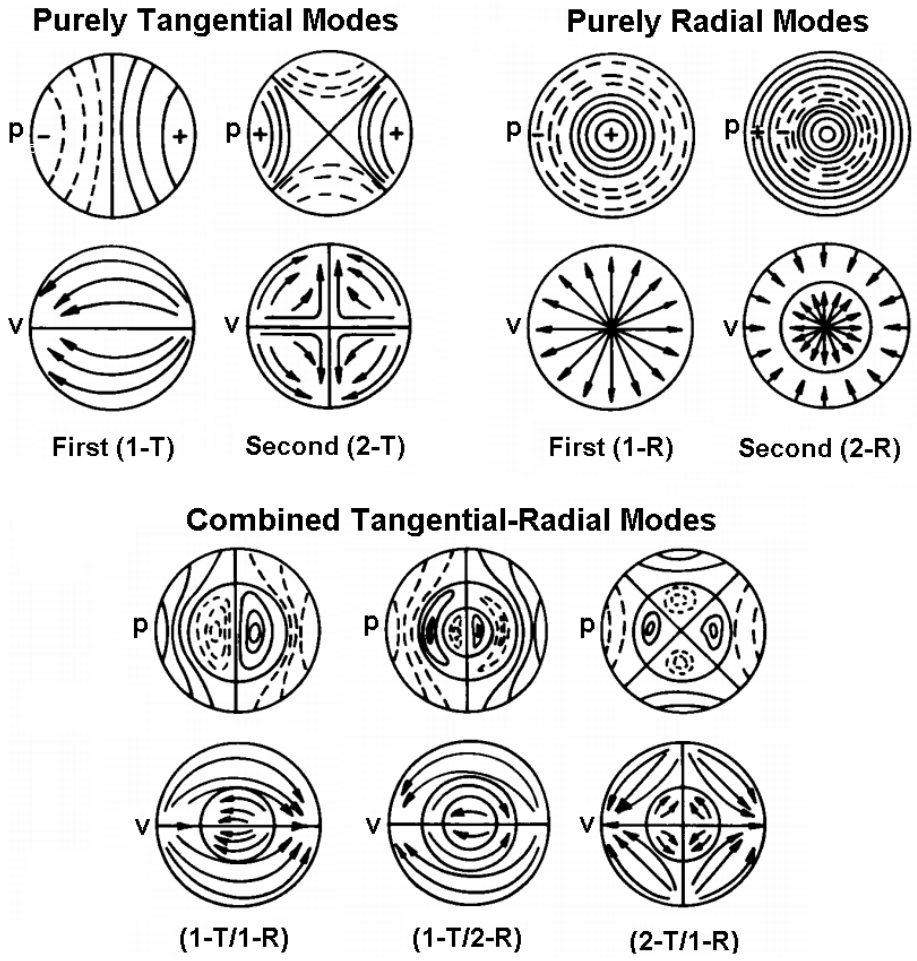

Figure 1.6: Acoustic Pressure and Velocity Distributions for Common Transverse Instability Modes [18].

orientation in the combustor. While these two mode variations are independent of one another, spinning tangential modes are able to be transformed into standing modes spontaneously and standing tangential modes can also shift node positions. Thus, a hybrid of these mode variations is possible in combustion chambers [18, 20].

Radial modes have circular pressure node lines oriented orthogonal to the radial axis of the combustor. Due to the orientation of the circular node lines for radial modes, there does not exist multiple variations of this mode type. The final type of

high-frequency transverse instabilities are combined tangential-radial modes. As the name suggests, combined modes have both a tangential and radial component, with node lines that split the chamber in both the circumferential and radial directions. As this mode type has a tangential component, both spinning and standing variations of this type are possible [18].

First Tangential Mode Instability

Specifically, the first tangential (1-T) mode has shown to be the most harmful during the development of historic liquid rocket engines. This mode often has the highest energy content associated with its pressure oscillation, causing it to be the transverse instability that is typically excited within cylindrical combustion chambers [8].

As with all tangential instabilities, the first tangential mode has both spinning and standing variations. The first spinning tangential mode is characterized by a high heat intensity pocket of combustion products moving tangentially around the inside of the combustor, close to the inner wall. Thus, when the spinning 1-T mode is active, combustion products spin unabated around the combustor. The first standing tangential mode is typified by a high heat pocket of combustion products which travels back and forth across the combustor, perpendicular to its node line. Cycle images for the two variations of the first tangential mode can be seen in Figures 1.7 and 1.8 [20].

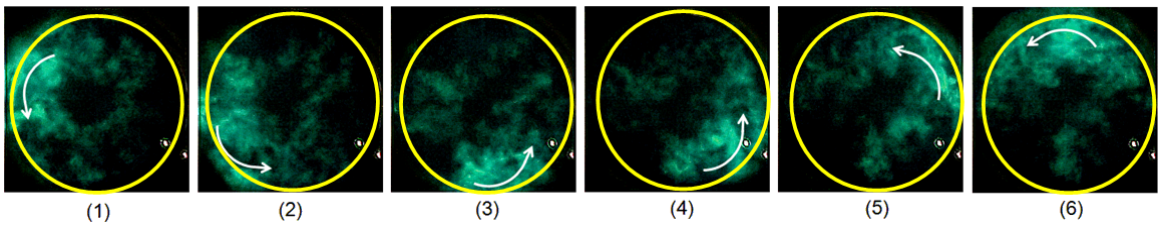

Figure 1.7: Images Documenting One Cycle of the Spinning First Tangential Mode [20]. *Note: For this model LRE combustor, the frequency of this instability was $f \approx 5000$ Hz.*

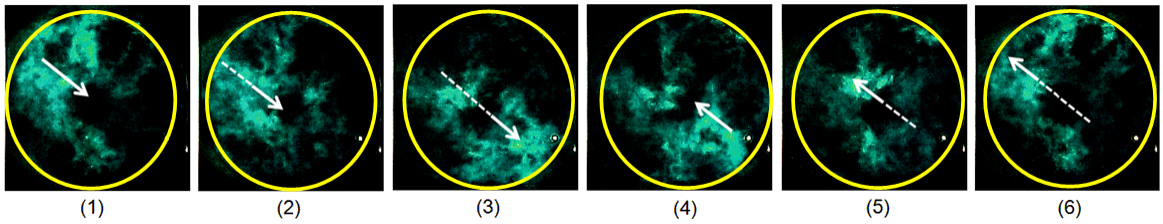

Figure 1.8: Images Documenting One Cycle of the Standing First Tangential Mode [20]. *Note: For this model LRE combustor, the frequency of this instability was $f \approx 5000$ Hz.*

While both of these mode variations are possible, the first spinning tangential mode tends to be the most fierce and harmful transverse mode. This can be primarily attributed to the increased heat transfer to the combustor walls. Spinning modes are the most efficient at perturbing hot combustion products towards the combustor walls, while also increasing combustor performance through enhanced chemical mixing. Combined, these two effects cause spinning transverse modes to be associated with the greatest increase of heat transfer upon their excitation. As seen in Table 1.3, the first tangential mode (excited at $f = 1800$ Hz and $f = 500$ Hz) was the primary combustion instability seen during the development of the F-1 and J-2 engines for the Saturn V, respectively [19].

Table 1.3: Historical Examples of Liquid Rocket Motors that Experienced a First Tangential Mode Instability: Taken and Edited from [19].

PROJECT	MOTOR	ORGANIZATION CONTRACTOR	PROPELLANTS	THRUST (lbf)	PERFORMANCE (%)	CHAMBER PRESSURE (psia)	INSTABILITY ENCOUNTERED	STABILIZATION DERIVES	INJECTOR TYPE
Apollo Saturn IB S-IVB Saturn V S-II, IVB	J-2	NASA/ Rocketdyne	LH_2 LOX	230,000	98.6	686.0	1800 Hz First Tangential Mode	3 compartment aluminum baffles	Coaxial
Apollo Saturn V S-IC	F-1	NASA/ Rocketdyne	RP-1 LOX	1,552,000	93.8	1128.0	500 Hz First Tangential Mode	13 compartment copper baffles	Like doublet

First Radial Mode Instability

While not typically as harmful as the first tangential mode, the first radial (1-R) mode instability has also been found to appear during engine development. The first radial mode perturbs the hot combustion products and incoming propellants in a manner in which combustion efficiency is enhanced, albeit typically less than that of the first tangential mode. If the chemical mixing is augmented in such a way that heat transfer to the combustor walls is raised beyond a threshold, the 1-R mode can be just as detrimental to the operation of the engine. As seen in Table 1.4, the first radial mode (excited at $f \approx 3500$ Hz) was one instability that was seen during the development of the lunar module ascent engine for the Apollo Lunar Lander [19, 21].

Table 1.4: A Historical Example of a Liquid Rocket Motor that Experienced a First Radial Mode Instability: Taken and Edited from [19].

PROJECT	MOTOR	ORGANIZATION CONTRACTOR	PROPELLANTS	THRUST (lbf)	PERFORMANCE (%)	CHAMBER PRESSURE (psia)	INSTABILITY ENCOUNTERED	STABILIZATION DERIVES	INJECTOR TYPE
Apollo/ Lunar module ascent	LMAE	NASA Bell	50% N_2H_4 50% UDMH) A50 N_2O_4	3,500	97.1	120.0	First Radial Third Tangential modes	3 compartment baffles	Unlike doublet

1.4.3 Coupling Mechanisms

To better understand the onset of combustion instabilities through Rayleigh's criterion, it is important to quantify the mechanisms behind unsteady heat release. In general, unsteady heat release is directly related to the processes that occur during propellant interaction within the chamber. A variation in one of these mechanisms can directly affect the burning rate oscillations' amplitude and phase, while altering the spatial distribution of combustion. As alterations to the unsteady heat release play a direct role in driving the instability, it is necessary to understand how these combustion mechanisms interact with the acoustic pressure and velocity oscillations within the chamber [11, 22].

Characteristic times of the processes for combustion have a direct effect on the onset of combustion instabilities. Inherently, there exists a time delay, referred to as "time lag", associated with each propellant interaction process. It has been suggested that thermo-acoustic instabilities are more likely to become excited at frequencies where the characteristic time for combustion is of the same order of magnitude as the time period for acoustic oscillations (e.g., for $f \approx 1000$ Hz, $\tau_{\text{comb}} \approx \tau_{\text{acous}} \approx 1$ ms). This characteristic time for combustion is dictated by the rate controlling mechanism (i.e., the process with the longest time scale), in which all other processes appear to occur instantaneously in relation to the longest step. If the rate controlling process modifies the unsteady heat release in such a way that its amplitude and phase are adequate to overcome the damping forces (as per Rayleigh's criterion), this mechanism will play a large role in the excitation of combustion instability modes [11].

Typically, when the characteristic time of a process is much greater than the acoustic oscillation time period, the process does not directly interact with acoustic pressure and velocity oscillations. In this case, the time it takes for the mechanism to occur is too long for it to be drastically modified by the oscillation. However, if the characteristic time of the process is shorter than the time period of oscillation, the process and oscillation typically are able to interact with one another, albeit mostly in a quasi-steady fashion. While these types of processes can interact with the oscillation, they are not rate controlling, and thus do not play as large a role as the rate controlling process [11].

Although a propellant interaction process may not have a time scale on the order of the acoustic oscillations, the mechanism can still affect instability driving. While the characteristic time dictates whether or not a mechanism is likely to directly interact with acoustic oscillations, an instability response can be achieved if the process affects the characteristic time of another combustion process that is rate controlling. Aside from this, mechanisms can have an indirect effect on the driving of combustion instability modes if there is an alteration to the spatial distribution of heat release within the combustor, rather than modifying the unsteady heat release rate. Thus, if a combustion process lies within one of these three categories, it should be considered as a potential mechanism that attributes to the driving of the instability [11].

Injection

For subcritical injection (see Section 1.3.2), the main propellant interaction processes that occur within the combustor are the following: (1) Injection, (2) Atomization, (3) Vaporization, (4) Mixing and (5) Combustion. In general, the injection of propellants takes place through feed systems where the characteristic pipe dimensions (i.e., length and volume) are sufficiently large to yield characteristic times of injection much greater than 1 ms. While propellant injection tends to not have a characteristic time permitting direct interaction with high-frequency acoustic oscillations, the manner in which the propellants are injected play a large role in affecting atomization, vaporization and mixing. For example, the way propellant is injected controls the original size of propellant droplets for atomization, which also alters the vaporization and mixing processes. Thus, propellant injection can be a large factor in indirectly altering the growth of combustion instabilities [11].

Atomization

Propellant atomization tends to not be a rate controlling process, as its characteristic time typically ranges from $\tau_{\text{atom}} = 10$ ns (10^{-8} s) to 10 μs (10^{-5} s). With atomization not being rate controlling, it is not the primary mechanism attributed to directly affecting unsteady heat release. Rather, it is similar to propellant injection, as atomization can have an indirect effect on the oscillation through the droplet size. It has been seen that during atomization, acoustic pressure and velocity oscillations can vary the initial droplet size, which modifies the vaporization and mixing processes [11, 23].

Vaporization

In subcritical injection, vaporization is typically the rate controlling process for combustion. As vaporization occurs through both droplet boiling and evaporation, it is important to understand which of these concurrent processes is rate limiting. Boiling primarily involves droplet liquid heating, while evaporation involves heating of the droplet boundary-layer; the characteristic time associated with heating of the droplet liquid is generally longer than boundary-layer heating, causing boiling to be the limiting process for vaporization. Also, the characteristic time for droplet boiling is of the same order of magnitude as droplet lifetime (e.g., in kerosene derived fuels) or larger (e.g., in LO_X), making the process of liquid heating rate controlling. Generally, the characteristic time for droplet boiling is on the order of $\tau_{vap} = 1$ ms (10^{-3} s), permitting the mechanism to directly interact with the acoustic oscillations. Thus, vaporization is most likely the primary coupling mechanism responsible for driving high-frequency combustion instabilities in subcritical propellant injection systems [11].

Mixing

Turbulent chemical mixing in liquid rocket engines has a characteristic time ranging from $\tau_{mix} = 10$ μs (10^{-5} s) to 1 ms (10^{-3} s), and is generally shorter than 1 ms. With chemical mixing tending to occur more rapidly than vaporization, chemical mixing is not the rate controlling process, and is often not considered in subcritical injection as a primary mechanism that directly affects the burning rate. However, chemical mixing can have an effect (albeit slight) on the spatial distribution of heat

release within the combustor; the degree this effect has on driving the instability is much smaller than vaporization for subcritical injection [11].

During supercritical injection, there are no appreciable atomization or vaporization processes which occur. Thus, the primary mechanism(s) causing unsteady heat release fluctuations at frequencies on the order of the acoustic oscillations become more complicated. As the dissolving and turbulent mixing of threadlike structures in the jet core are now pertinent for supercritical injection instead of droplet vaporization, the rate-controlling process for combustion is modified. It is expected that for supercritical injection, instability driving is primarily attributed to the dispersion and turbulent mixing of threadlike structures from the jet core; it is this process that is rate limiting, having a time period similar to the acoustic oscillations. Thus, a coupling between this mechanism and the acoustic oscillations is anticipated, however, the particulars of this coupling are not entirely identified. This coupling is the primary source of interest in understanding combustion instabilities in supercritical propellant injection systems [6, 11].

Combustion

Once the propellants are sufficiently mixed, chemical reactions for combustion occur. Chemical times for combustion are proportional to the chemical kinetic rates of reaction and are dictated by the longest step in the chemical mechanism. Chemical kinetic rates are highly dependent on pressure and temperature, and at conditions for liquid rocket engines (i.e., high pressure and temperature), these chemical times will be short. Typically, characteristic chemical times are on the order of

$\tau_{\text{chem}} = 100$ μs (10^{-4}) to 1 cs (10^{-2} s). For subcritical injection, chemical reactions for combustion are not rate controlling, as they generally are an order of magnitude smaller than the characteristic time for vaporization. However, during fuel rich combustion (similar to those seen during ignition), chemical times become on the order of $\tau_{\text{chem}} \approx 1$ ms (10^{-3} s), allowing the process to directly interact with acoustic oscillations. Thus, depending on the conditions within the chamber, chemical kinetics may be a contributing factor in driving combustion instabilities [11, 23].

CHAPTER 2

BACKGROUND

2.1 Historic Combustion Instability Control Techniques

To design stable and reliable combustors, mitigation techniques preventing the onset of thermo-acoustic instabilities have been developed. Depending on the type of instability, the suppression technique employed varies and is often tailored to remove a specific instability.

Over the course of history for liquid rocket engine design, numerous methods have been implemented to suppress high-frequency instabilities. Compared to low-frequency modes, high-frequency combustion instabilities are much more difficult to prevent. Thus, predicting the effectiveness of a high-frequency instability suppression technique is difficult for a given chamber design. Control techniques for high-frequency combustion instabilities aim to either provide enough damping to take away the energy for instability driving or break the coupling between the unsteady heat release and acoustic pressure oscillations within the chamber. Therefore, these suppression methods focus on damping the acoustic modes of the chamber or altering the energy release process for combustion (either temporally or spatially), or a combination of the two.

2.1.1 Longitudinal Mode Control

Historically, high-frequency longitudinal combustion instabilities were eliminated through modifying the geometry of the combustor. Commonly found in combustors having large combustor lengths compared to their diameters, longitudinal instabilities were often suppressed by altering the combustor length. Modifying the combustor length changes the acoustic longitudinal resonant frequency and thus decouple the time period of oscillation for the chamber acoustics and unsteady heat release. However, certain longitudinal instabilities have shown to not easily be removed in this fashion (as seen in many turbine engine combustors), calling for a more aggressive suppression approach (detailed in Section 2.2.3) [18, 19].

2.1.2 Transverse Mode Control

As covered in Section 1.4.2, high-frequency transverse combustion instabilities were extremely problematic for many landmark liquid rocket engines. Thus, there exists many different mitigation techniques developed for high-frequency transverse instabilities. These techniques can be classified as either passive or active systems. As the name suggests, passive systems aim to damp combustion instability modes in a non-responsive fashion, while active systems alter the instability response dynamically in real time. Both control types have advantages and disadvantages, with passive systems historically being implemented in liquid rocket engines due to their inclusion of non-movable parts. Thus, as the following passive mitigation techniques have been incorporated in flight-rated combustors, they will be covered in greater detail: (1) Symmetric Injector Plate Baffle, (2) Symmetric Fuel Injector Distribution and (3) Resonance Absorbers.

Symmetric Injector Plate Baffle

To prevent the onset of high-frequency instabilities, symmetric plate baffle systems have become the standard method employed for liquid rocket engines developed in the United States. This suppression technique has been implemented from the development of the Atlas HA-5 (Project Mercury) through to the F-1 (Apollo Program) and the more recent Space Shuttle Main Engine (Space Shuttle Program). Symmetric plate baffle systems are comprised of metal barriers attached to the injector face, which segment the injection plane in both the tangential and radial directions. Axially, these baffle systems penetrate the combustor at lengths long enough to provide adequate acoustic damping, while not permitting unwanted heat transfer or performance loss. The symmetric injector system developed for the F-1 engine can be seen in Figure 2.1 [19].

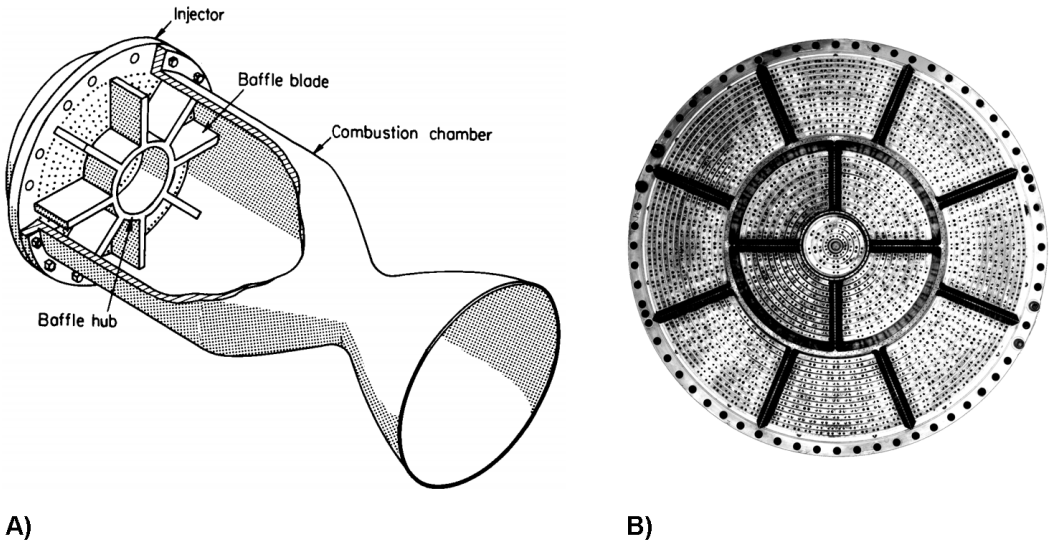

Figure 2.1: Example of a Symmetric Injector Plate Baffle System - A) Conceptual Schematic and B) Baffle Design for the F-1 Engine: Taken and Edited from [18, 24].

Complete understanding as to why symmetric baffles are effective in preventing the onset of transverse combustion instabilities is still not known. However, certain effects have been identified as possible reasons for their success. Essentially, the addition of the baffle system significantly modifies the acoustic resonance properties of the combustion chamber; this can be seen in Figure 2.2, which details the effect an injector plate baffle system has on the acoustic resonant frequencies of a liquid rocket engine combustor.

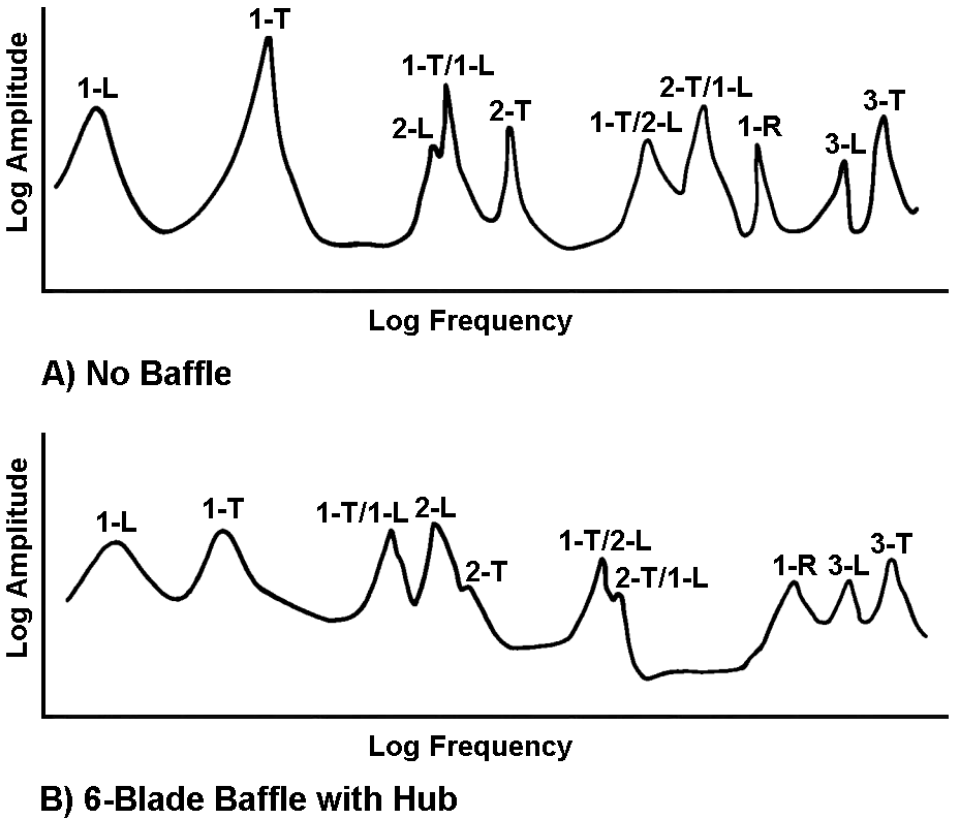

Figure 2.2: Acoustic Resonance Characteristics of a Liquid Rocket Engine Combustor A) without and B) with an Injector Plate Baffle System: Taken and Edited from [18].

As can be seen in Figure 2.2, the addition of a baffle has a dual effect on the acoustic resonances. The frequencies of the lower-order transverse modes (specifically the 1-T mode) are drastically reduced, while decreasing the amplitudes of all resonant frequencies. Through decreasing the resonant frequency amplitudes for all modes, the baffle effectively increases the damping of acoustic energy by providing more boundaries for acoustic losses. Essentially, this makes the Rayleigh criterion for sustained combustion instability growth more difficult to be achieved [18].

In addition to altering the chamber acoustic modes, the injector plate baffle system modifies the oscillatory flow over the injection plane. Due to the physical boundaries baffle blades place on the combustor, transverse acoustic velocity oscillations cannot easily propagate across the injector plate, limiting the unsteady oscillations between baffle compartments. Also, an acoustic velocity node is created at each baffle boundary, greatly reducing the amplitude of velocity oscillations that may be present. By curtailing the amount of velocity oscillations that move throughout the entirety of the combustor, the baffle system makes unsteady heat release less likely to be onset by transverse acoustic velocity oscillations [18, 19].

Injector plate baffle systems also provide energy damping of oscillations within the combustion chamber. Blades on the injector plate allow the shedding of vortices and flow separation to occur, along with enhanced viscous dissipation within the chamber; these effects contribute to the energy dissipation of oscillations. To successfully damp out an instability, this energy dissipation effect can either be large enough to directly reduce the instability amplitude to a non-sustaining level or provide

adequate energy removal to prohibit adequate instability driving between the acoustic and heat release oscillations [19].

Upon considering the axial lengths of baffle systems, typically increasing the baffle length increases the damping effect on the system. However, after a certain damping threshold has been reached, the losses will never be greater than the acoustic energy gained from unsteady heat release. Therefore, the baffle will not have any greater effect past this desired blade length. This, compounded with the potential for unwanted heat transfer and performance loss with blades penetrating too far into the combustor, dictates the desired baffle system length [18, 19].

While effective, symmetric injector plate baffles have some drawbacks. In general, their designs have been developed through trial and error processes. For instance, during the baffle development of the F-1 engine, no stringent baffle design criteria for the optimal blade number and pattern was ever determined. This is partially because adding baffle components can alter the oscillation patterns within the combustion chamber in an unpredictable manner. Also, certain baffle designs can produce new acoustic modes within the chamber at frequencies where themo-acoustic instabilities can be sustained. Aside from these design issues, traditional injector plate baffle systems all incorporated a passive design. Passive baffle systems are not as versatile as active systems, as they are not capable of making real time adjustments to help prevent combustion instabilities. Thus, traditional baffle systems and their development can be improved [3, 25].

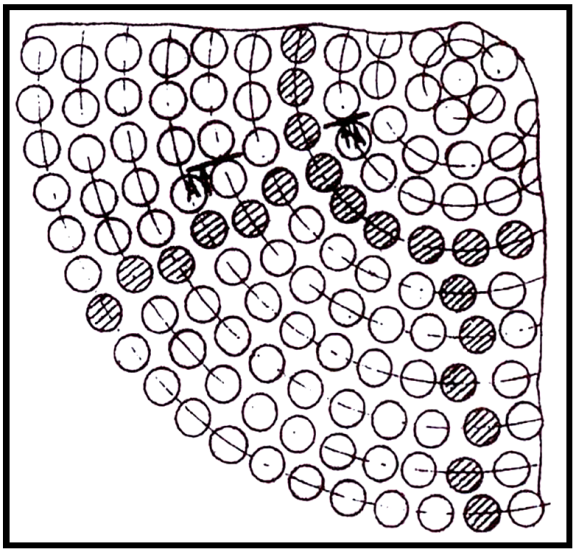

Figure 2.3: Schematic of a Symmetric Fuel Injector Distribution [25].

Symmetric Fuel Injector Distribution

Aside from employing baffle systems to prevent the onset of high-frequency instabilities, Russian built liquid rocket engines have incorporated symmetric fuel injector distributions. This mitigation approach entails strategically positioned fuel injectors to simulate baffle conditions. To segment the combustor similarly to a physical baffle, patterned fuel injectors operate under modified spray conditions (e.g., axial spray instead of radial) apart from the rest of the injectors. A schematic of a typical symmetric fuel injector distribution can be seen in Figure 2.3 [25].

The ideology for implementing this approach over traditional baffle systems concerns engine reliability. Liquid rocket engines with altered fuel sprays are ostensibly more stable than with baffle systems, as baffles can reduce reliability due the blades being directly exposed to the high heat of combustion [25].

As modified fuel injector distributions essentially reproduce baffle conditions using the injectors' sprays, the mechanisms behind its effectiveness are similar to a physical injector plate baffle. Primarily, the modified spray distribution significantly alters the oscillatory flow over the injection plate rather than damping the acoustic modes. By perturbing transverse acoustic velocity oscillations by regions of modified spray, it becomes more difficult for unsteady oscillations to travel between combustor segments and some of their energy is dissipated as they travel through regions of modified spray. These flow effects make it more difficult for the growth of combustion instability modes to be promoted within the chamber [25].

Resonance Absorbers

Acoustic resonance absorbers are another passive mitigation technique that prevent the onset of combustion instabilities through solely removing the acoustic energy available for instability growth. Acoustic resonators are side chambers attached to the combustor that are geometrically tailored to damp out the resonant frequency of the dominant instability mode. Acoustically, these chambers act as Helmholtz resonators, which take the acoustic energy out of a specific resonance; the frequencies at which these absorbers resonate depend on the volume of the side chamber and are independent of geometry. Thus, typical resonance absorbers, such as the one seen in Figure 2.4, have simple geometric shapes [25].

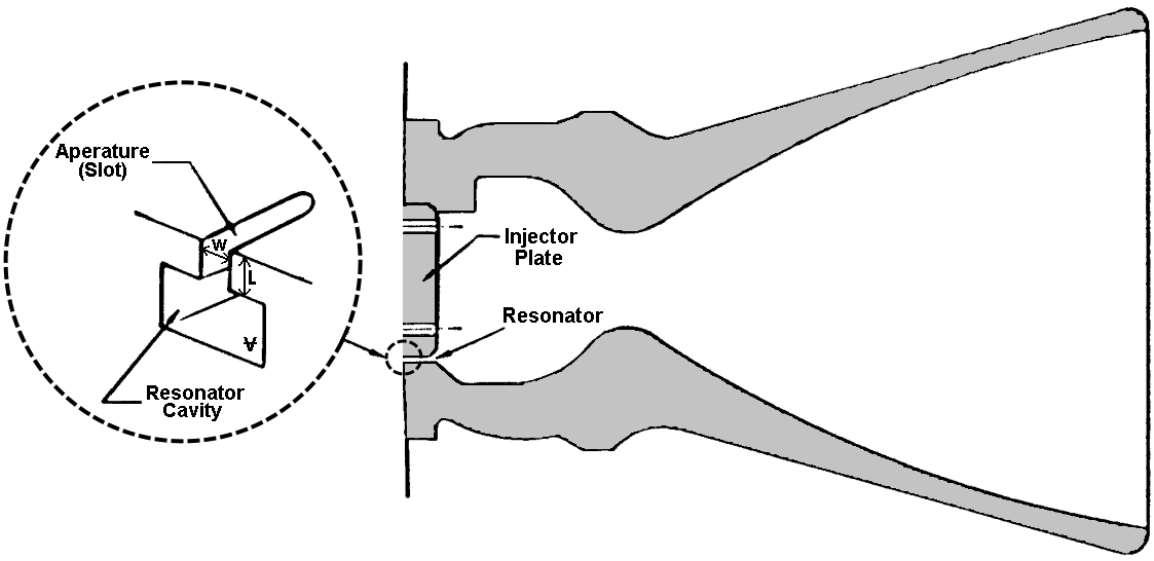

Figure 2.4: Schematic of a Liquid Rocket Engine with an Acoustic Resonance Absorber: Taken and Edited from [26].

To maximize their damping effect, these acoustic side lobes are located at an acoustic pressure anti-node of the instability. As the acoustic hard-wall boundary condition is applicable for the injector plate and walls of the combustor, there exists zero acoustic velocity at these locations; this corresponds to a pressure anti-node for all modes. Thus, resonance absorbers are typically installed at the injector plate, near the combustor walls (see Figure 2.4) [25, 27].

Although effective, resonance absorbers have certain drawbacks. While resonance absorbers often do not alter the oscillatory flow within the chamber, the acoustic characteristics are significantly affected. As with baffle systems, the instability successfully damped by the resonance absorbers can be substituted by another. Specifically, frequency bifurcation of the instability has been seen in combustors incorporating resonance absorbers. Frequency bifurcation occurs when

the main resonant frequency is damped and replaced by two other resonances (i.e., one at a frequency lower and another higher than the original resonance). As the acoustic pressure distribution can be altered in an unpredictable fashion when resonance absorbers are added, tailoring these side chambers is often a challenging process [18, 25].

2.2 Advanced Combustion Instability Control Techniques

More recently, there has been research into designing more versatile combustion instability mitigation systems. Some of these techniques aim to improve upon the historically implemented methods, while others (mainly active control techniques) are focused on dynamically controlling the dominant instability through various means. To date, many advancements have been made in both areas. The following mitigation techniques have shown to efficiently control thermo-acoustic instabilities in laboratory-scaled combustors, and as such, will be covered in greater detail: (1) Asymmetric Injector Plate Baffle, (2) Asymmetric Fuel Injector Distribution and (3) Fuel Line Flow Modulation.

2.2.1 Asymmetric Injector Plate Baffle

For this research investigation, a replica model liquid rocket combustor (seen in Figure 2.5) was equipped with six propellant injectors and a single baffle blade capable of traversing the entire length of the combustor. Using this configuration, numerous studies were performed to determine the effectiveness of an asymmetric baffle system at controlling the first spinning tangential mode instability. From these tests, the

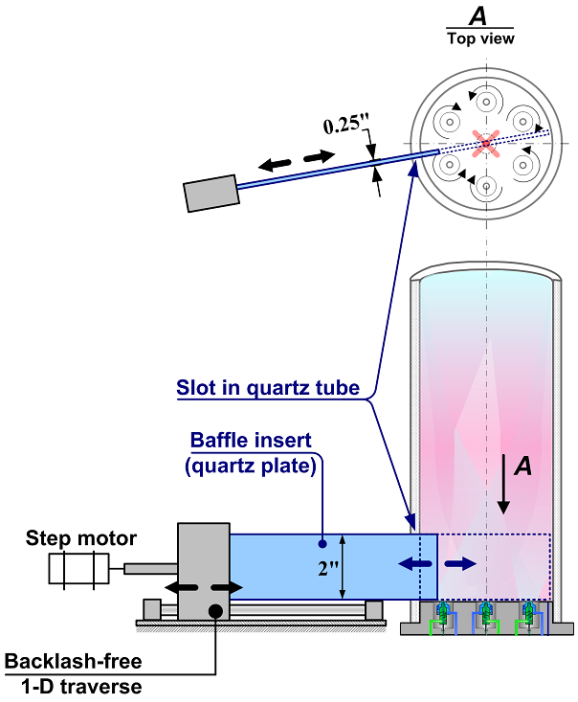

Figure 2.5: Asymmetric Baffle System for the Model Liquid Rocket Combustor [28].

combustor behavior (i.e., unstable/stable regimes of operation) corresponding to baffle insertion length were characterized [28].

During testing, the combustor was purposefully brought to unstable conditions, with the first spinning tangential instability being excited at $f \approx 5000$ Hz. Under these conditions, the baffle blade was inserted into the combustor. Beginning with 0% baffle insertion, the blade was incrementally traversed to 100% combustor diameter insertion. When the baffle was $\approx 10-30\%$ inserted into the chamber, the 1-T spinning tangential mode was fully damped, leading to stable conditions within the combustor. At this baffle insertion length, the suppression of the 1-T spinning tangential mode was considered to be due to enhanced acoustic damping of the system, similarly to a traditional baffle system. Once the baffle was inserted past 40% of the combustor's

diameter, another instability, the first standing tangential mode, became excited within the combustion chamber [28].

As the first standing mode was excited at 40% baffle insertion, the chamber pressure oscillations increased until the baffle was inserted 70% into the combustor. Past this point, the amplitude of instability began to decrease again until the baffle was inserted 100% into the combustor. Thus, this laboratory experiment showed the baffle blade configuration (i.e., the amount of baffle insertion) affects the chamber acoustics to the point where another mode was excited (similarly to certain symmetric plate baffle configurations). The pressure amplitude response of the oscillation corresponding to the baffle insertion length can be seen in Figure 2.6.A [28].

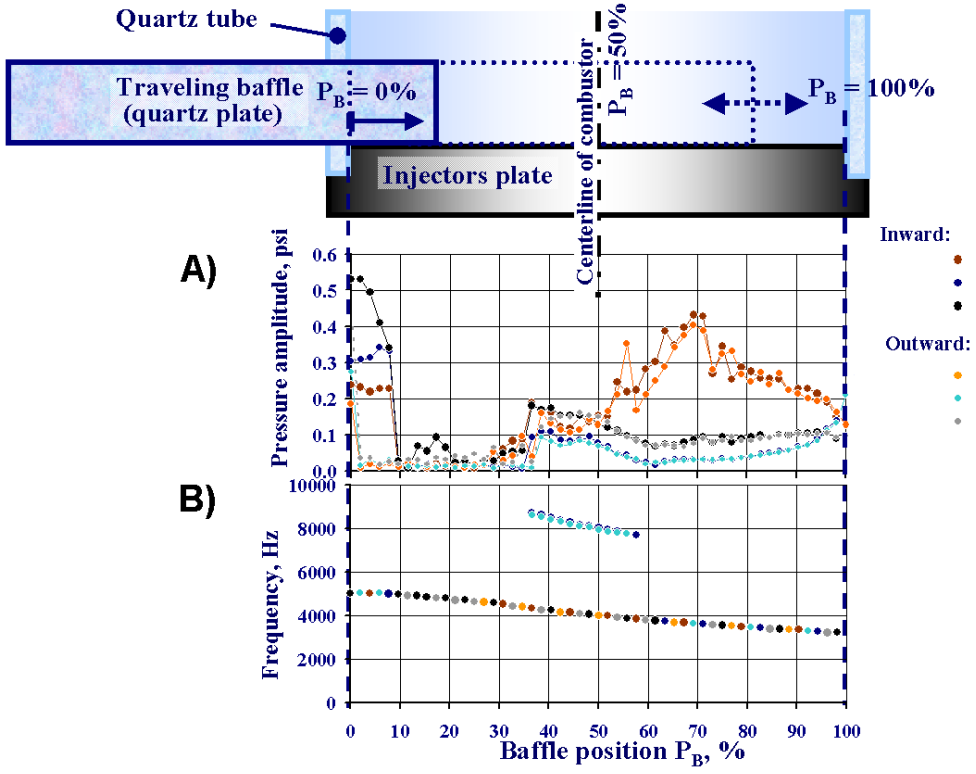

Figure 2.6: A) Instability Pressure Amplitude and B) Frequency Corresponding to Baffle Insertion Length [28].

Aside from the oscillation amplitude response, Figure 2.6.B shows the instability frequency linearly decreases from approximately 5000 Hz to 3000 Hz across the baffle insertion range; the linear frequency dependence on baffle insertion is attributed to an acoustic characteristic change, rather than an adjustment in the reaction zone location (i.e., the flame moving away from the injector plate). Therefore, this investigation proved an asymmetric baffle can successfully reduce the amplitude and frequency of the first spinning tangential instability mode in a controllable fashion. This approach could be implemented during combustor design, to finely tune baffle blade lengths to develop stable engines in a more efficient manner [28].

2.2.2 Asymmetric Fuel Injector Distribution

By applying the asymmetry aspect from the asymmetric baffle study (Section 2.2.1) to a fuel injector distribution system (Section 2.1.2), an asymmetric fuel injector distribution was developed to control high-frequency thermo-acoustic instabilities. In this study, a model liquid rocket engine combustor was equipped with six "smart" coaxial injectors that permitted the injectors' sprays to be changed from radial to axial spray through altering the injectors' air-split ratio, $K = \frac{\%\ p_{\text{inner}}}{\%\ p_{\text{outer}}}$ (the percentage ratio of the inner to outer pressure of the injectors' passages). To achieve asymmetry with the injectors' sprays, a single fuel injector was capable of altering its spray characteristics independent of the other five injectors. Using this configuration (shown in Figure 2.7), numerous studies were performed to characterize the effectiveness of an asymmetric fuel injector distribution at controlling the first

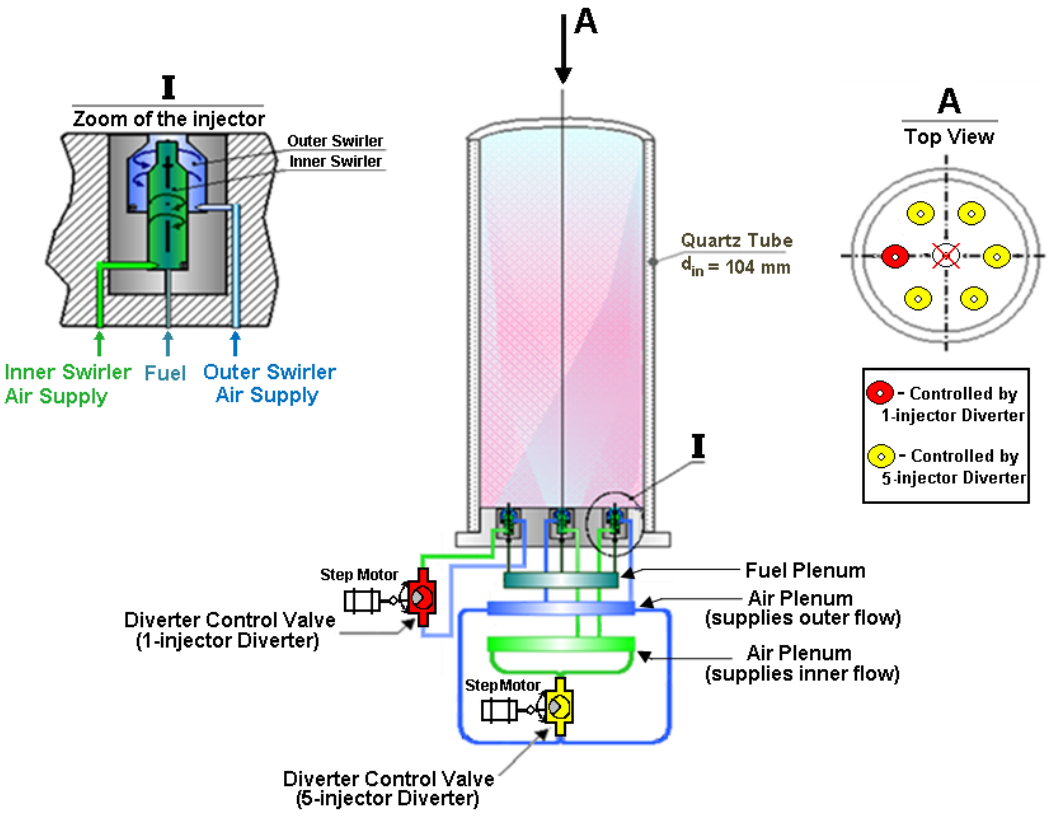

Figure 2.7: Asymmetric Fuel Injector Distribution System for the Model Liquid Rocket Combustor [20].

spinning tangential instability. From these tests, the unstable/stable regimes of the combustor corresponding to the spray shape of the single injector were resolved [20].

To demonstrate instability control, the combustor was deliberately operated under unstable conditions during testing, with the first spinning tangential instability being excited at $f \approx 5000$ Hz and $p'/p_c \approx 10\%$; this instability was consistently excited by setting all six injectors to radial spray ($K \approx 25/75$). With the 1-T spinning mode active, the spray of the single injector was changed from radial to axial independently of the rest (which continued to hold radial spray conditions). When the air-split ratio of the single injector was increased from $K_1 = 27/73 - 55/45$, there was a drastic

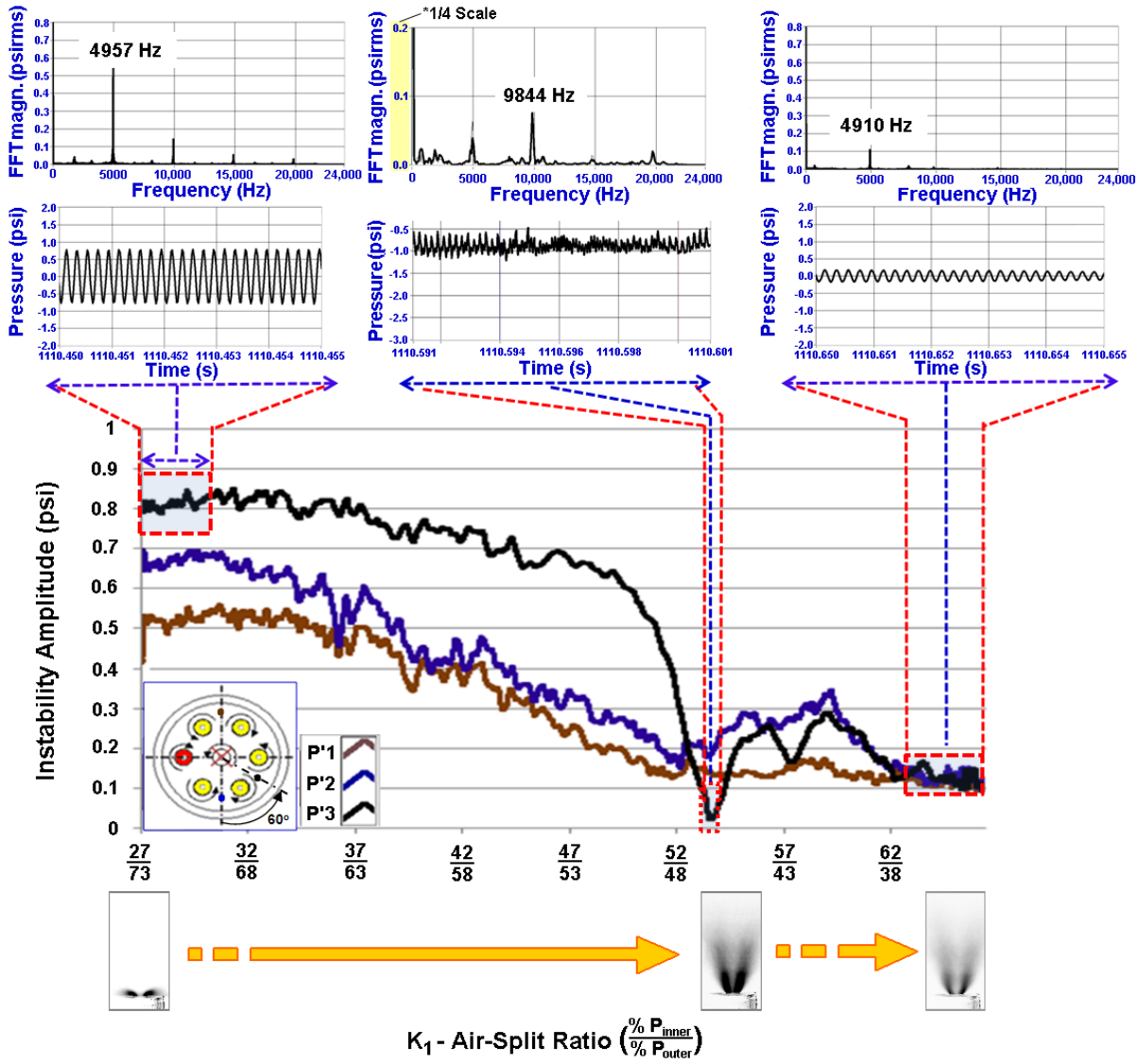

Figure 2.8: Instability Amplitude vs. Air-Split Ratio (K_1) Plot [20].

Note: Frequency Spectra and Time Histories for $P'3$ at various air-split ratios are also shown.

reduction in oscillation amplitude, with the minimum amplitude being attained at $K_1 = 54/46$. For this air-split ratio, the 1-T spinning mode was fully damped within the combustor [20].

By increasing the air-split ratio of the single injector further to $K_1 = 64/36$ (i.e., mostly axial spray), the spinning mode was transformed into a standing mode at

approximately 5000 Hz, with a significantly lower amplitude ($\approx$ 6X smaller than the undamped 1-T spinning mode). Thus, for this single injector spray condition, there exists stable conditions within the combustor. The pressure amplitude response and frequency spectra of the instability corresponding to the air-split ratio of the single injector can be seen in Figure 2.8 [20].

To characterize the frequency response of the instability, Figure 2.8 shows the frequency spectra from one of the pressure transducers at various points during the experiment. From the first and third frequency spectra, the large amplitude 1-T spinning mode and low amplitude 1-T standing mode both appear at $f \approx 5000$ Hz, respectively. During the mode transition (shown in the second frequency spectra), a doubling in oscillation frequency is present; this is due to the mode's nodal plane passing over the pressure transducer port, rather than a physical doubling of the instability frequency. As the asymmetric fuel injector distribution suppressed the 1-T spinning tangential instability without reducing the frequency of oscillation, it signifies this approach does not have a direct effect on the acoustic modes of the combustor as does a physical baffle. Instead, breaking the symmetry of the reaction zone interrupts the media path through which the acoustic wave propagates to an extent that a significant depletion of oscillation energy occurs [20].

As this asymmetric fuel injector distribution reliably controlled the first spinning tangential instability, it could be employed as an engine design approach in liquid rocket engines which seek to incorporate adjustable spray injectors. Specifically, this approach could easily tailor the injector spray pattern to develop a stable combustor in a streamlined fashion.

2.2.3 Propellant Line Flow Modulation

While passive instability control techniques have been traditionally implemented in liquid rocket engines due to solely consisting of non-movable parts, many advancements have been made in the area of active instability control. One area investigated has been instability control through the active modulation of fuel entering the combustion chamber. By pulsing the fuel flow rate at frequencies on the order of the dominant instability, it can provide a suppression effect if the incoming fuel is perturbed in a manner that significantly damps acoustic oscillations at the injector plate or causes the feedback between the unsteady heat release and acoustic pressure to be broken. This technique has been developed mainly for turbine engine applications, through the use of fast-response actuation valves. However, research demonstrating fuel flow modulation through acoustic driving has also shown to be effective [29, 30].

Fast-Response Actuation Valve Study

One active control study employed harmonic fuel modulation through the use of a fast-response actuation valve. This study demonstrated that damping a $f \approx 400$ Hz first longitudinal (1-L) instability was possible when the fuel was modulated both at the frequency of the dominant instability mode (with the proper phase offset) and at frequencies other than the primary instability (regardless of phase). To test the concept, a fast-response actuation valve was housed on the fuel line upstream of a laboratory-scaled turbine engine combustor operating at $p_c \approx 100-150$ psi [29].

Prior to the modulation frequency sweep study, a series of $0^{o}-360^{o}$ phase sweep tests were performed for the actuation valve frequency matching the 1-L instability. In these tests, a 2X instability amplitude decrease was achieved with the optimal phase for fuel flow modulation (*Note: This amplitude reduction was with respect to the largest instability amplitude during fuel modulation*) [29].

For the actuation frequency sweep tests, the modulation signal was swept from $500-50$ Hz at a rate of 0.9 Hz/sec, with arbitrary phase. To characterize the instability response to non-coherent fuel flow, both the frequency and amplitude of the 1-L instability were monitored. As can be seen in Figures 2.9 and 2.10, both the instability frequency and amplitude are drastically affected by the frequency of fuel modulation. When the actuation frequency was swept across $400-300$ Hz, a noticeable frequency shift of the first longitudinal instability is present towards the actuation frequency. However, when the actuation signal is not within this range, the instability frequency response does not directly follow the control signal. Thus, the frequency of instability is most prone to oscillation from fuel flow modulation within $300-400$ Hz [29].

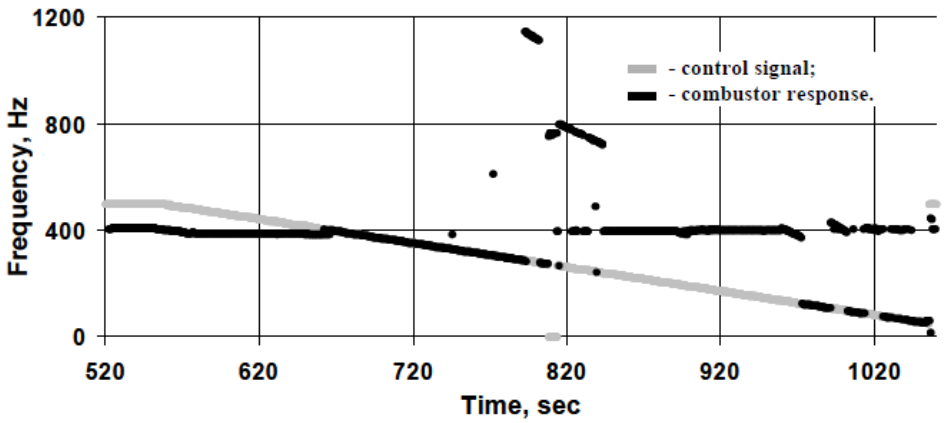

Figure 2.9: Combustion Instability Frequency Response Due to the Alteration in Fuel Flow Rate Actuation Frequency [29].

Non-coherent fuel flow modulation also has a significant effect on the amplitude of the first longitudinal combustion instability. As can be seen in Figure 2.10, the instability amplitude was reduced up to ten times for the following frequencies: (1) 50 Hz, (2) 120−130 Hz, (3) 170−180 Hz and (4) 250−330 Hz. Also, when the fuel flow is modulated at frequencies close to the dominant instability (i.e., $f \approx 400$ Hz), there exists large amplitude instability oscillations; this suggests the actuation signal phase is much more significant as the modulation frequency approaches the dominant instability [29].

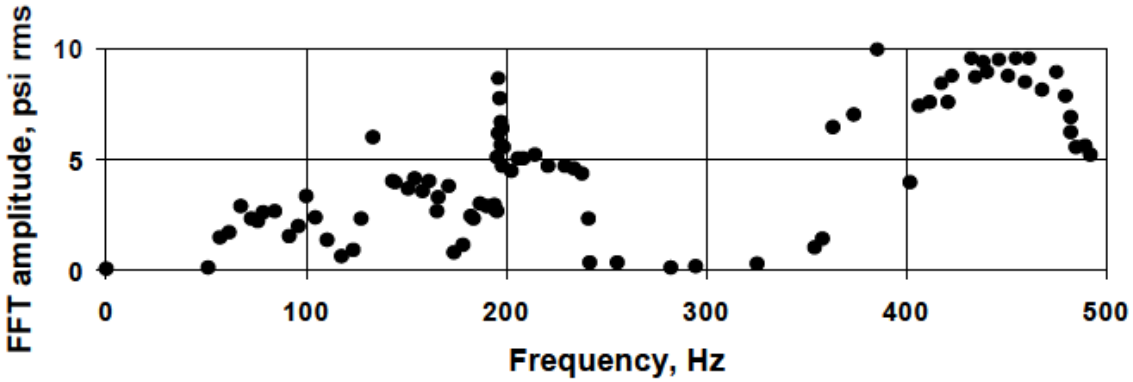

Figure 2.10: Combustion Instability Amplitude Response Due to the Alteration in Fuel Flow Rate Actuation Frequency [29].

The results from this study indicate that within these four regimes, the incoming propellant is perturbed in such a way that the feedback mechanism(s) responsible for driving the 400 Hz instability at a natural chamber resonance were eliminated, and as such, led to a significant instability suppression. Thus, non-coherent fuel flow modulation within the appropriate frequency range is an effective way to control combustion instabilities.

Application of Acoustic Driving

Aside from pulsing the incoming propellant flow through fast-response actuating valves, there has been work done with modulating the incoming fuel through acoustic driving. To test this concept, a model dump combustor was equipped with acoustic speakers in the fuel line to modulate the flow entering the mixing region of a coaxial injector at an amplitude of $u'/\overline{u} = 22\%$. A pressure transducer downstream of the injection plane was employed to measure the pressure trace of the instability, which was then filtered and phase-shifted as the acoustic driver signal. A schematic of the experiment configuration is shown in Figure 2.11.A [30].

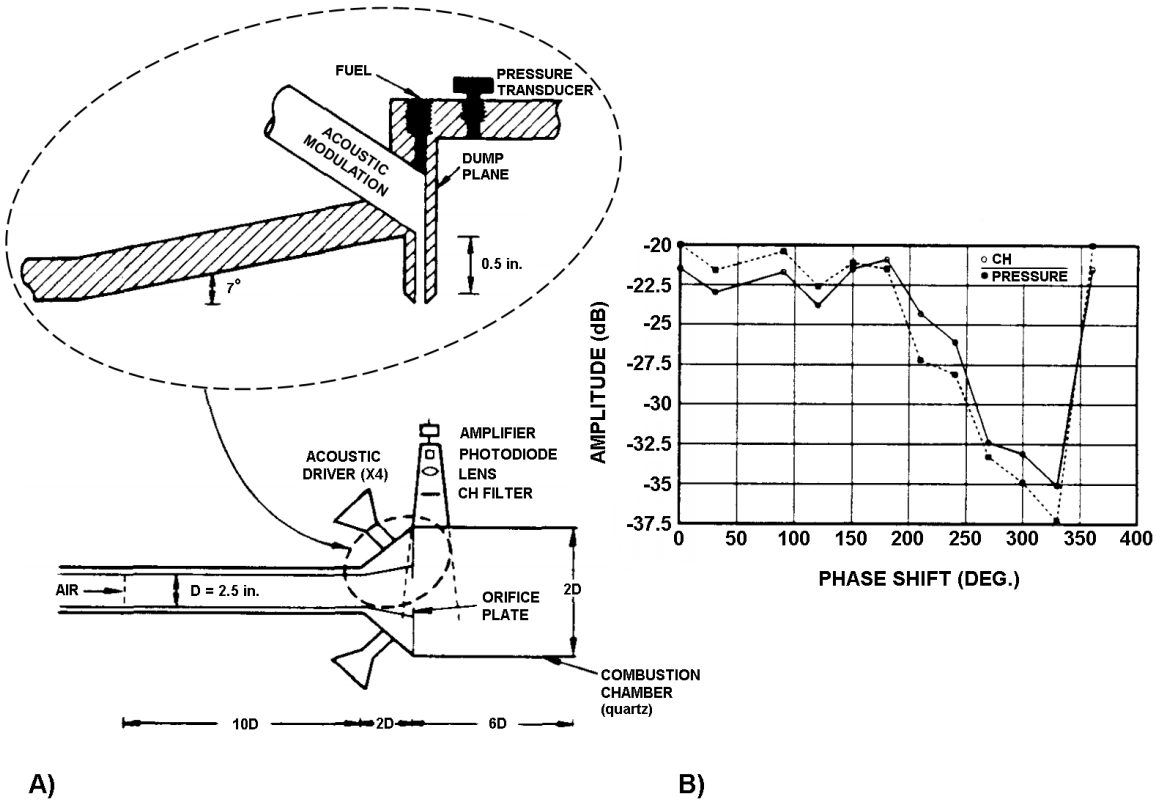

Figure 2.11: A) Experiment Configuration with Acoustic Fuel Flow Modulation and B) Instability Suppression Plot through Acoustic Forcing: Taken and Edited from [30].

With this set-up, the pressure amplitude of a $f \approx 300$ Hz instability was significantly reduced by approximately 13 dB with the appropriately phased acoustic signal (shown in Figure 2.11.B). At this phasing, there is significant acoustic damping at the inlet of the combustor, as well as a reduction of the burning rate oscillations through an obviation of the large scale vortical structure coherence within the propellant jet shear layer. This mitigation technique is capable of reducing the amplitude of acoustic and unsteady heat release oscillations to the point where combustion instability feedback can no longer be sustained, effectively suppressing the thermo-acoustic instability. Therefore, this concept has shown potential as a high-frequency combustion instability suppression method for liquid rocket engines [30, 31].

2.3 Fundamental Combustion Instability Work

2.3.1 Flame-Acoustic Interaction under Controlled Acoustic Excitation

Recently, there has been work done on the fundamental flame-acoustic interaction that takes place under controlled acoustic excitation. The experiment configuration used for this research consisted of a rectangular combustor with a single coaxial injector (burning GH_2/GO_2 or $GH_2{-}GCH_4/GO_2$) and an acoustic compression driver located at the wall of the combustor. This set-up (shown in Figure 2.12) permitted transverse acoustic waves to be applied at specified frequencies to characterize the flame-acoustic interaction within the model combustor [32, 33].

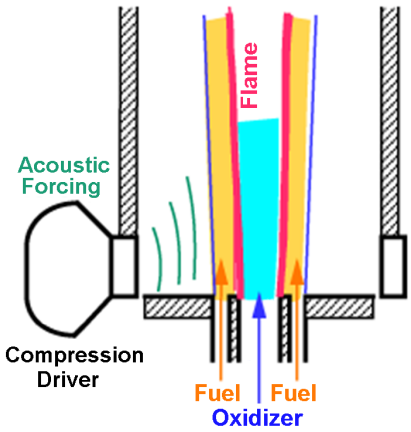

Figure 2.12: Schematic of the Single Injector Combustor with Transverse Acoustic Forcing: Taken and Edited from [32].

The applied driver signal of 1150 Hz was selected as it fell between the first two dominant resonant modes of the chamber. At this driver signal, a standing wave acoustic mode would not be excited, essentially isolating the interaction between the flame and traveling acoustic waves. Under acoustic excitation, the portion of the flame closest to the speaker experienced significant flame distortion, while the opposite side of the flame was largely unaffected. This phenomena was shown to be more prevalent when the density ratio between the oxidizer and fuel ($\rho_{\text{ox}}/\rho_{\text{fuel}}$) was large [33].

When acoustic waves interact with the propellant interface, it can result in the production of local vorticity, which can ultimately affect the flame's stability. Eq. (2.1) is the vorticity equation, which describes how vorticity of a fluid particle progresses as it travels with the flow:

$$\frac{D\overline{\boldsymbol{\omega}}}{Dt} = \frac{\bigtriangledown\rho \times \bigtriangledown p}{\rho^2} + (\overline{\boldsymbol{\omega}} \cdot \bigtriangledown)\overline{\mathbf{u}} - \overline{\boldsymbol{\omega}}(\bigtriangledown \cdot \overline{\mathbf{u}}) + \nu \bigtriangledown^2 \overline{\boldsymbol{\omega}} + (\bigtriangledown\nu) \times \bigtriangledown^2\overline{\mathbf{u}} \qquad (2.1)$$

$\overline{\boldsymbol{\omega}}$ - Vorticity of the Fluid $\overline{\mathbf{u}}$ - Velocity of the Fluid
ρ - Density of the Fluid ν - Kinematic Viscosity of the Fluid
p - Pressure of the Fluid

While vorticity is caused by various phenomena, the term describing vorticity generation through the interaction between the propellant interface and acoustic waves is the $\frac{\nabla\rho \times \nabla p}{\rho^2}$ term, which represents baroclinic torque; vorticity from baroclinic torque arises if the gradients of pressure and density are significantly large and misaligned with one another. Schematics demonstrating unstable and stable interactions between compression waves and the fuel-oxidizer interface caused by baroclinic torque are shown in Figure 2.13.

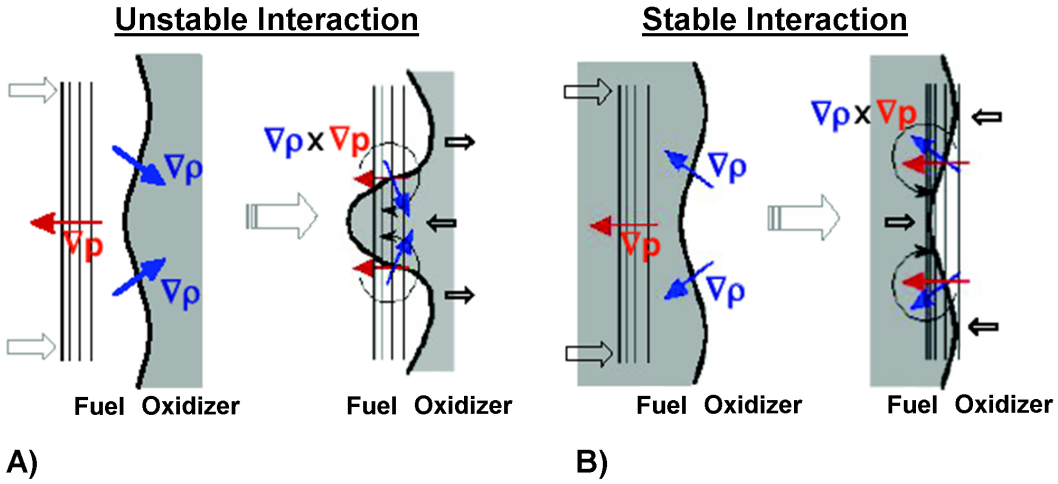

Figure 2.13: A) Perturbation Growth and B) Decay at the Fuel-Oxidizer Interface Due to the Alignment of ∇p and $\nabla \rho$ [32].

As can be seen in Figure 2.13, the alignment of the pressure and density gradients is vital in dictating whether a stable or unstable interaction occurs. When the pressure and density gradients are misaligned with one another, as is the case in Figure 2.13.A, the generated torque amplifies wrinkling of the flame. However, when the pressure and density gradients are in the same direction (Figure 2.13.B), the torque created reduces flame wrinkling. Thus, baroclinic torque is a contributing

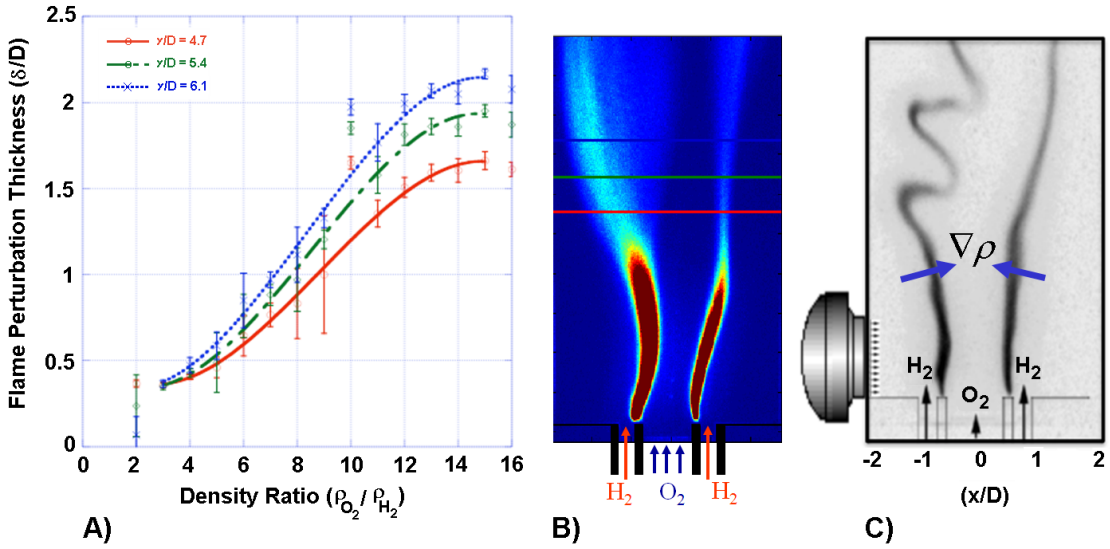

Figure 2.14: A) Flame Perturbation Thickness vs. Density Ratio Plot, B) OH* Chemiluminescence and C) Schlieren Images with Acoustic Forcing: Taken and Edited from [32].

mechanism in flame stability, especially when the density ratio between the oxidizer and fuel is particularly large [32].

The effect of baroclinic torque is presented in Figure 2.14. The normalized flame perturbation thickness at three spatial planes downstream of the injection plane for varying propellant density ratios is shown in Figure 2.14.A. At each spatial plane, the flame perturbation thickness increases fairly linearly over almost the entire range of density ratios, until $\rho_{\text{ox}}/\rho_{\text{fuel}} \approx 14$, where the flame perturbation thickness begins to asymptote. Severe flame wrinkling from baroclinic torque can also be seen in the OH* chemiluminescence and schlieren images in Figure 2.14.B and 2.14.C, respectively. Therefore, this study demonstrated that acoustic driving of a flame can give rise to vorticity phenomena, which under certain conditions, can significantly affect flame stability. Consequently, this can potentially affect the propagation of combustion instabilities.

2.4 Advancement to the State-of-the-Art

Drawing from these combustion instability suppression techniques and flame-acoustic interaction research, it is proposed that applying specifically tailored acoustic forcing within the oxidizer supply of a propellant injector can be used to control high-frequency combustion instabilities. While both mechanical and acoustic modulation of the incoming propellant were able to suppress low-frequency thermo-acoustic instabilities (see Section 2.2.3), there are advantages to modulating the propellant flow through acoustic means. Acoustic modulation permits the incoming propellant to be altered in a wide array of ways (e.g., applying band-limited white noise, single frequencies, etc.), as opposed to solely pulsing the flow at a single frequency mechanically. Thus, this study aims to demonstrate an original suppression technique for high-frequency combustion instabilities where the dominant mode is controlled by applying band-limited white noise and single-frequency acoustic modulation within the oxidizer supply of a propellant injector.

CHAPTER 3

EXPERIMENTAL APPROACH

3.1 Overview

The combustion instability control technique developed in this study involves the strategic application of acoustic forcing within the oxidizer supply of a propellant injector. To do this, an acoustic driver was located at the injector base and connected to a digital signal generator through an amplifier. This system was designed to be capable of producing pressure disturbances at amplitudes large enough to modulate the propellant flow acoustically. With this set-up, the following two studies were able to be carried out: (1) Band-Limited White Noise Study and (2) Single-Frequency Acoustic Modulation Study.

3.1.1 Band-Limited White Noise Study

One benefit of acoustically modulating the propellant is the ability to perturb the incoming flow at multiple frequencies, simultaneously. As was discussed in the fast-response actuation valve study (Section 2.2.3), modulating the incoming fuel at individual frequencies within a certain range can significantly damp an instability. Expanding upon this concept, applying the appropriate frequency width band-limited white noise (BLWN) signal can provide a more reliable method to suppress a high-frequency combustion instability. Thus, this study aims to control the dominant instability by applying band-limited white noise within the oxidizer supply of an injector. To find the optimum signal for instability suppression, a specified band width of white noise will be swept across a frequency range, both in an ascending and descending fashion; this sweep method will identify the most effective modulation signal(s), as well as characterize any hysteresis effects that may be present.

3.1.2 Single-Frequency Acoustic Modulation Study

Aside from the band-limited white noise study, another series of tests will involve applying single-frequency acoustic modulation (SFAM). This will be done in a similar fashion to the fast-response actuation valve study. Thus, a range of pure sinusoidal tones with arbitrary phase will be applied from 0 Hz to $f_{\text{instability}}$, again both in an ascending and descending fashion. By sweeping across this frequency range, the specific signals leading to a suppression will be identified. Not only will this determine the effectiveness of single-frequency acoustic modulation as a instability control method, but will also further characterize the frequency content of the optimum band-limited white noise signal.

3.2 Experiment Overview

3.2.1 Single Element Model Rocket Combustor (SEMRC)

The atmospheric liquid rocket engine combustor used in this investigation implements a single injector (located 9.53 mm from the combustor wall), which burns gaseous methane (GCH_4) and gaseous oxygen (GO_2). The injector is surrounded by a closed, cylindrical combustor with $d_{\text{inner}} = 10.16$ cm and $l_{\text{comb}} = 16.51$ cm. The combustor top consists of a non-choked converging area restriction with a 1.59 cm diameter opening, to avoid entrainment of the surrounding air within the chamber. A view of the single element model rocket combustor (SEMRC) can be seen in Figure 3.1, with its dimensions detailed in Figure 3.3.

Figure 3.1: View of the Single Element Model Rocket Combustor.

3.2.2 Injector

The impinging pentad-style injector consisted of an inner oxidizer post surrounded by four impinging fuel jets at 45° angles, as shown in Figure 3.3.C. The fuel and oxidizer begin to mix in the injector prior to entering the combustor, which is a deviation from standard triplet impinging injection stream patterns. As the combustor operates at ambient pressure, there is no appreciable pressure drop between the supply line and combustor. To provide the acoustic modulation of the oxidizer flow, a speaker (150 W JBL 2446J compression driver) is mounted at the base of the injector's oxidizer supply located 17.78 cm from the injection plane. This driver is then connected to a digital signal generator through an amplifier (AE Techron LVC 608 Constant Current Amplifier).

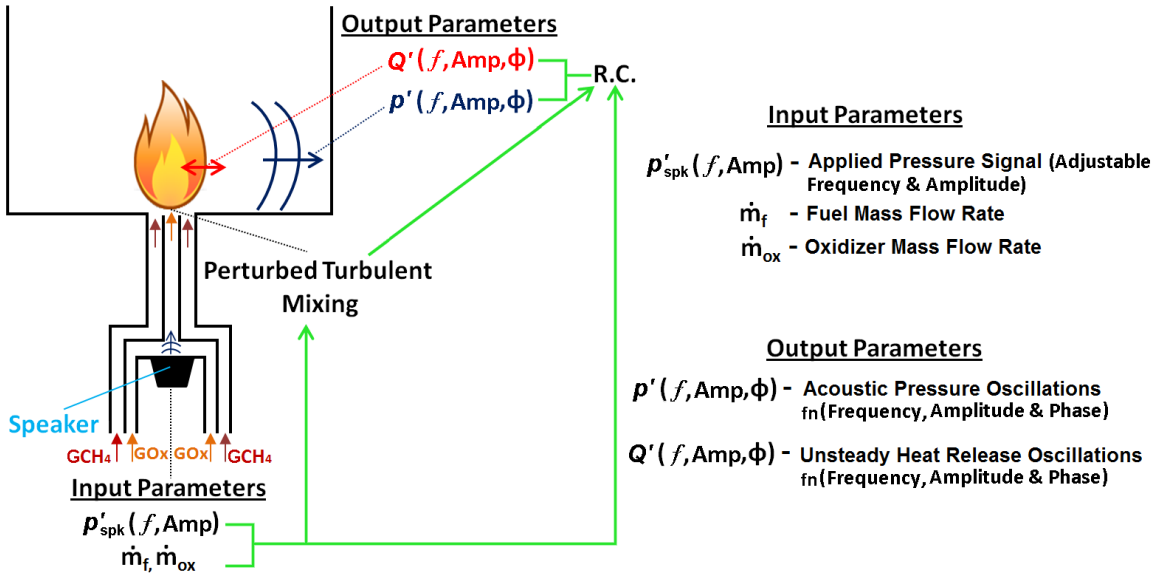

Figure 3.2: Experiment Configuration Schematic with Acoustic Modulation.

As shown in Figure 3.2, this configuration permits an acoustic signal to be applied for a given experiment set point (dictated by $\dot{m}_f$ and $\dot{m}_{ox}$). With the correct input signal characteristics (i.e., frequency and amplitude), the output parameters in the combustor, p' and Q', will be altered through the perturbed incoming propellant, which can lead to a significant decrease in instability strength (as dictated by the Rayleigh criterion, R.C.).

3.2.3 JBL 2446J Compression Driver

The acoustic speaker is a mid-range JBL Professional 2446J compression driver capable of generating pressure disturbances up to f = 20,000 Hz, at levels exceeding 110 dB when mounted on a plane wave tube. This speaker was selected as it is able to produce the desired pressure disturbances at large enough amplitudes to affect the oscillatory behavior within the SEMRC. A summary of the relevant technical specifications for the JBL 2446J provided by the manufacturer is presented in Table 3.1 [34].

Table 3.1: Technical Specifications for the JBL 2446J Compression Driver [34].

Model #	**Nominal Impedance, Ω**	**Voice Coil Diameter, cm**
JBL 2446J	16	10.16
Throat Diameter, cm		**Power Capacity**
5.08		100 W above 500 Hz 150 W above 1000 Hz

3.2.4 Measurement Devices

The SEMRC is outfitted with high-frequency pressure transducers and thermocouples to characterize the mean and oscillatory behavior in the combustion chamber during operation. Together, these measurement devices detail the excited instability and how it is affected by applied acoustic forcing from the speaker.

High-Speed Data Acquisition System

The data acquisition (DAQ) system contains two modules connected to a PXI-6070E High-Speed DAQ Card. One of the data acquisition modules is a National Instruments SCXI-1102B, where the data is sampled and low-pass filtered at 200 Hz. This data acquisition module measures both the low-frequency static pressure measurements from the system, along with the data from the thermocouples located around the combustor. For the high-frequency measurements, a National Instruments SCXI-1143 DAQ module is employed. This DAQ module allows each channel to be recorded at $f_s = 55{,}000$ Hz, with a cross channel time delay of 3 μs and quantization uncertainty of $u_q = 1.22$ mV (at a 95% confidence interval). As the cutoff frequency set is set to $f_{\text{cutoff}} = 8333$ Hz, the high-frequency data is low-pass Butterworth filtered (eliminating all frequencies above 8333 Hz on each channel). Using this set-up, all of the data of interest from the measurement devices are able to be recorded.

Static Pressure Transducers

Static pressure transducers are implemented in the experiment to monitor the operating pressure in the fuel and oxidizer lines. Thus, multiple Setra Systems Model 280E pressure transducers are located within the propellant lines (main and ignition) of the system. These capacitance-type transducers work by generating an output voltage proportional to a change in the capacitance of the transducer's sensing material (stainless steel) while under pressure. As the pressure on the sensing material is increased, its capacitance is decreased, which alters the output voltage of the device; this permits a pressure measurement to be made. These transducers have pressure ranges suitable for measuring the static pressure within the propellant feed lines, with an operating temperature range of T = -20−60 °C [35].

High-Frequency Piezoelectric Pressure Transducers

High-frequency piezoelectric pressure transducers are strategically located within the combustor and injector (shown in Figure 3.3.A and 3.3.B) to measure the acoustic pressure at these locations. This type of pressure transducer incorporates a piezoelectric material (quartz), which generates a charge under stress. As such, a voltage proportional to the pressure is output by the transducer. PCB 106B transducers were chosen as they can naturally resolve pressure oscillations smaller than 1 Pa ($p'_{\text{res.}} = 0.6895$ Pa) for the frequency range of interest ($f \approx 0-10{,}000$ Hz) [36].

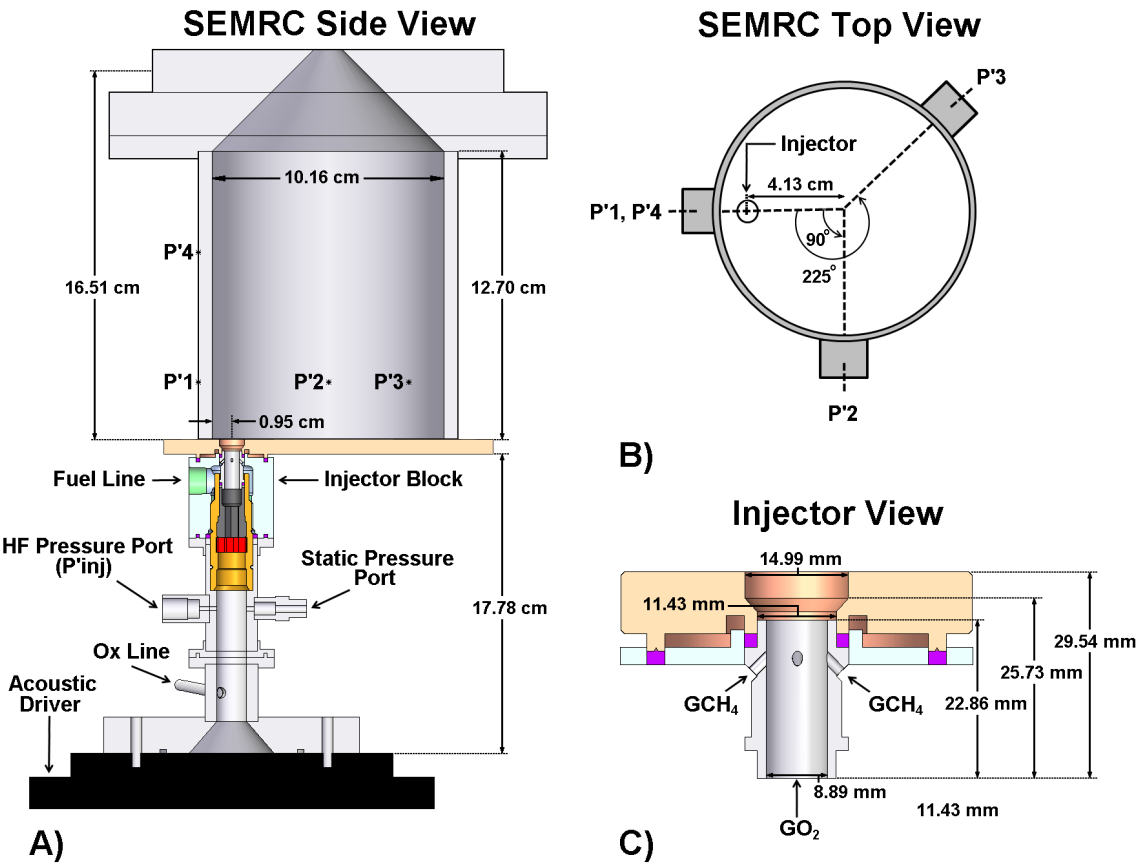

Figure 3.3: A) Side and B) Top Dimensioned Views of the SEMRC and C) Pentad Injector.

Within the combustor, there are four high-frequency pressure transducers. These transducers, denoted $P'1-P'4$, are spaced throughout the chamber to resolve both transverse and longitudinal modes. $P'1$, $P'2$ and $P'3$ are located on the same axial plane (2.54 cm from the injection plane), with $P'1$ and $P'2$ offset 90° azimuthally, as well as $P'1$ and $P'3$ being offset 225°. $P'4$ is the transducer used to discern longitudinal modes within the chamber and thus, $P'4$ is oriented along the same azimuth as $P'1$, but at a higher axial plane located 5.72 cm above the other transducers'

measurement plane. Aside from the pressure transducers positioned within the combustor, another transducer, P'_{inj}, is placed in the oxidizer supply line of the injector to monitor the acoustic response of the oxidizer supply during experimentation.

Thermocouples

Static temperature measurements are made using Omega Engineering K-Type Model KMQXL-062U-12 thermocouples, to quantify the various system temperatures. This type thermocouple incorporates nickel-chromium and nickel-aluminum alloys for the positive and negative terminals, respectively. By bringing these two metals into contact with one another at the thermocouple sensor, an electric potential proportional to the temperature is produced; this permits the thermocouple to output a measured voltage. This model thermocouple was selected as it can operate at temperatures up to $T \approx 1335$ °C, which is above the conditions experienced during combustor operation [37].

Similarly to the pressure transducers, three thermocouples, denoted $T'1$, $T'2$ and $T'3$, are located at the azimuths of the first three pressure transducers within the SEMRC, at an axial plane located 2.92 cm above the transverse pressure transducer plane. The fourth thermocouple, $T'4$, is positioned at the same azimuth as $T'1$ at an axial location 5.72 cm above the transverse thermocouple plane. Aside from these thermocouples within the chamber, there is also a single thermocouple, T'_{inj}, located within the oxidizer supply line.

3.3 Test Campaign

Presented in Table 3.2 is a summary of the test campaign. Encompassed in this plan are six major tests, three phases comprised of both band-limited white noise and single-frequency acoustic modulation studies. This test campaign is designed to fully characterize the effectiveness of acoustically modulating the incoming oxidizer flow as a means to control a high-frequency instability.

Table 3.2: Test Campaign Summary.

Testing Phase	Description	Modulation Signals	Modulation Signal Amplitude
1	Principle Baseline Testing	BLWN SFAM	Single Level
2	Signal Amplitude Study	BLWN SFAM	Variable
3	Pure Acoustic Testing	BLWN SFAM	Variable

Phase one is the foundation for this work. During the principle baseline tests, both modulation signal types will be swept across a frequency range up to the instability frequency at a single amplitude level. This amplitude will match the spontaneous instability amplitude generated within the chamber, to ensure the acoustic forcing is at an appropriate level to affect the oscillatory behavior of the combustor. Multiple instability control tests will be performed at this signal amplitude to determine which modulation signal(s) consistently provide a suppression of the instability.

Phase two is a more detailed signal amplitude sensitivity study for the band-limited white noise and single-frequency acoustic modulation approaches. This is an extension of the phase one work, which investigated only one modulation signal amplitude. Five signal amplitude levels, spanning the hardware capabilities of the acoustic driver will be tested, to quantify the instability suppression threshold and evolution of the suppression regime(s). Combined, this will further detail the instability control technique and identify certain mechanism(s) attributed to the suppression effect.

After the signal amplitude study is carried out, a series of pure acoustic tests will be performed for both modulation signal types. These tests will isolate and identify the acoustic response of the oxidizer supply line and combustor due to the applied driver signals. As with phase two, varying amplitude levels will be investigated to fully describe the isolated acoustic response; this will assist in further identifying the suppression mechanism(s).

CHAPTER 4

DATA ANALYSIS METHODOLOGY

4.1 Acoustic Analysis Tools

To analyze the high-frequency pressure data and characterize the combustion instability mode(s) excited within the model combustor, the two following data analysis methods were developed: (1) Analytical Acoustic Model for a Closed-Top Cylindrical Chamber and (2) Numerical Acoustic Model.

The first data analysis tool is the basis for identifying the combustion instability excited within the cylindrical model rocket combustor. In this section, an analytical solution of the acoustic pressure distribution for all mode types (transverse, longitudinal and combined modes) is generated using linear acoustic theory. This analytical solution is then used to reconstruct the ideal acoustic responses measured by the high-frequency pressure transducers within the chamber when a specific mode is active.

The second data analysis tool is the numerical acoustic model, which describes the effects of non-homogeneous sound speed on instability modes. As the experiments incorporate a single-element combustor, temperature gradients exist within the chamber during operation. This gives rise to non-homogeneous sound speed conditions, which can affect the frequency and pressure distribution of instability modes. Thus, a numerical model is developed by transforming the linear wave equation into an eigenmode expression, which provides a solvable form for a grided geometry with spatially varying sound speed. By performing a non-homogeneous sound speed sensitivity study on a geometry similar to the experiment combustor, the model will illustrate how the ideal instability mode (predicted using the analytical model) can appear during combustor operation. Consequently, this will lead to a better understanding of the acoustic pressure measured during testing.

4.1.1 Analytical Acoustic Model for a Closed-Top Cylindrical Chamber

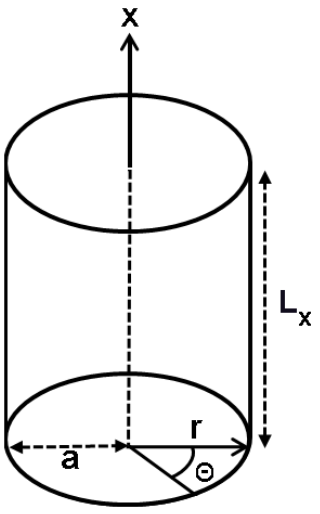

Closed-Top Cylindrical Combustion Chamber

Boundary Conditions:

$$x \text{ Direction} - \left(\frac{\partial p'}{\partial x}\right)\Big|_{x=0} = 0, \quad \left(\frac{\partial p'}{\partial x}\right)\Big|_{x=L_x} = 0$$

$$r \text{ Direction} - \left(\frac{\partial p'}{\partial r}\right)\Big|_{r=a} = 0$$

To determine the acoustic mode pressure distribution for a closed-top cylindrical chamber, the method of separation of variables is employed to solve the linear wave equation in cylindrical coordinates. Refer to Sections A.1 and A.2 for detailed derivations of the linear wave equation in cylindrical coordinates, which is given by

$$\frac{1}{\bar{c}^2}\frac{\partial^2 p'}{\partial t^2} = \frac{\partial^2 p'}{\partial x^2} + \frac{\partial^2 p'}{\partial r^2} + \frac{1}{r}\frac{\partial p'}{\partial r} + \frac{1}{r^2}\frac{\partial^2 p'}{\partial \theta^2} \tag{4.1}$$

The pressure distribution solution can be expressed as

$$p'(r,\theta,x,t) = X(x)\Phi(\theta)R(r)\exp(i\omega t) \tag{4.2}$$

where

$$\frac{\partial^2 p'}{\partial t^2} = -\omega^2 X(x)\Phi(\theta)R(r)\exp(i\omega t) \tag{4.3.A}$$

$$\frac{\partial^2 p'}{\partial x^2} = X''(x)\Phi(\theta)R(r)\exp(i\omega t) \tag{4.3.B}$$

$$\frac{\partial p'}{\partial r} = X(x)\Phi(\theta)R'(r)\exp(i\omega t) \tag{4.3.C}$$

$$\frac{\partial^2 p'}{\partial r^2} = X(x)\Phi(\theta)R''(r)\exp(i\omega t) \tag{4.3.D}$$

and

$$\frac{\partial^2 p'}{\partial \theta^2} = X(x)\Phi''(\theta)R(r)\exp(i\omega t) \tag{4.3.E}$$

Substituting all components of Eq. (4.3) into the linear wave equation in cylindrical coordinates yields

$$\frac{-\omega^2}{\overline{c}^2}X(x)\Phi(\theta)R(r)\exp(i\omega t) = \Big(X''(x)\Phi(\theta)R(r) + X(x)\Phi(\theta)R''(r) + \frac{1}{r}X(x)\Phi(\theta)R'(r) + \frac{1}{r^2}X(x)\Phi''(\theta)R(r)\Big)\exp(i\omega t) \tag{4.4}$$

which can be rewritten as

$$\frac{X''(x)}{X(x)} + \frac{R''(r)}{R(r)} + \frac{1}{r}\frac{R'(r)}{R(r)} + \frac{1}{r^2}\frac{\Phi''(\theta)}{\Phi(\theta)} = \frac{-\omega^2}{\overline{c}^2} \tag{4.5}$$

To determine a solution for $X(x)$, the solely x-dependent terms are isolated. Thus, Eq. (4.5) becomes

$$\frac{-X''(x)}{X(x)} = \frac{\omega^2}{\overline{c}^2} + \frac{R''(r)}{R(r)} + \frac{1}{r}\frac{R'(r)}{R(r)} + \frac{1}{r^2}\frac{\Phi''(\theta)}{\Phi(\theta)} \tag{4.6}$$

where

$$k_x^2 = \frac{\omega^2}{\overline{c}^2} + \frac{R''(r)}{R(r)} + \frac{1}{r}\frac{R'(r)}{R(r)} + \frac{1}{r^2}\frac{\Phi''(\theta)}{\Phi(\theta)} \tag{4.7}$$

Combining these two expressions yields an ordinary differential equation including only x-dependent terms:

$$X''(x) + k_x^2 X(x) = 0 \tag{4.8}$$

The general solution for Eq.(4.8) can be expressed as

$$X(x) = C_1\sin(k_x x) + C_2\cos(k_x x) \tag{4.9}$$

To reach the final solution for $X(x)$, two boundary conditions at $x = 0$ and $x = L_x$ are applied to the general solution. For this analysis, all chamber boundaries are assumed to be acoustically closed (i.e., implement the hard-wall boundary condition). This condition causes the velocity normal to the wall to be zero. Thus, the boundary conditions are

$$\left(\frac{\partial p'}{\partial x}\right)\bigg|_{x=0} = X'(0) = 0 \tag{4.10}$$

and

$$\left(\frac{\partial p'}{\partial x}\right)\bigg|_{x=L_x} = X'(L_x) = 0 \tag{4.11}$$

Applying the boundary condition at x = 0 yields

$$k_x C_1 \cos(k_x 0) - k_x C_2 \sin(k_x 0) = 0 \tag{4.12}$$

which reduces to

$$C_1 = 0 \tag{4.13}$$

Applying the boundary condition at $x = L_x$ and implementing $C_1 = 0$ produces

$$-k_x C_2 \sin(k_x L_x) = 0 \tag{4.14}$$

which causes k_x to be written as

$$k_x = \frac{l\pi}{L_x} \tag{4.15}$$

The final solution for $X(x)$ is reached by substituting Eqs. (4.13) and (4.15) into Eq. (4.9):

$$X(x) = C_2 \cos\left(\frac{l\pi x}{L_x}\right) \tag{4.16}$$

With $X(x)$ quantified, a solution for $\Phi(\theta)$ can be found by isolating the θ-dependent terms in Eq. (4.7) as follows

$$\frac{-\Phi''(\theta)}{\Phi(\theta)} = r^2\left(\frac{R''(r)}{R(r)} + \frac{1}{r}\frac{R'(r)}{R(r)} + \frac{\omega^2}{\overline{c}^2} - k_x^2\right) \tag{4.17}$$

where

$$m^2 = r^2\left(\frac{R''(r)}{R(r)} + \frac{1}{r}\frac{R'(r)}{R(r)} + \frac{\omega^2}{\overline{c}^2} - k_x^2\right) \tag{4.18}$$

By combining Eqs. (4.17) and (4.18), an ordinary differential equation with solely θ-dependent terms can be written as

$$\Phi''(\theta) + m^2\Phi(\theta) = 0 \tag{4.19}$$

which has a general solution

$$\Phi(\theta) = C_3 \sin(m\theta) + C_4 \cos(m\theta) \tag{4.20}$$

Due to $\Phi(\theta)$ acting in the azimuthal direction, there are no physical boundary conditions imposed. Thus, the final $\Phi(\theta)$ solution takes the same form as the general solution:

$$\Phi(\theta) = C_3 \sin(m\theta) + C_4 \cos(m\theta) \tag{4.21}$$

To attain a solution for $R(r)$, the terms in Eq. (4.18) that are entirely r-dependent are isolated. This is done by first multiplying Eq. (4.18) through by $R(r)$:

$$\left(m^2 - r^2 \left(\frac{\omega^2}{\overline{c}^2} - k_x^2 \right) \right) R(r) = r^2 R''(r) + r R'(r) \tag{4.22}$$

where

$$k^2 = \frac{\omega^2}{\overline{c}^2} = k_r^2 + k_x^2 \tag{4.23}$$

Substituting Eq. (4.23) into Eq. (4.22) yields

$$r^2 R''(r) + r R'(r) + (r^2 k_r^2 - m^2) R(r) = 0 \tag{4.24}$$

which is an ordinary differential equation with entirely r-dependent terms that takes a form similar to the following:

$$\alpha^2 \frac{d^2 R(r)}{d\alpha^2} + \alpha \frac{dR(r)}{d\alpha} + (\alpha^2 - m^2) R(r) = 0 \tag{4.25}$$

Eq. (4.25) is Bessel's Equation, which has a set of known solutions. Therefore, Eq. (4.24) is modified into its form by implementing the following variable transformation:

$$\alpha = k_r r \tag{4.26}$$

Incorporating this variable transformation and the chain rule of calculus, the components of Eq. (4.24) can be written as

$$R'(r) = \frac{dR(r)}{dr} = \left(\frac{dR(r)}{d\alpha}\right)\left(\frac{d\alpha}{dr}\right) = \left(\frac{dR(r)}{d\alpha}\right)k_r \tag{4.27}$$

$$\begin{aligned} R''(r) = \frac{dR'(r)}{dr} &= \left(\frac{d^2R(r)}{d\alpha^2}\right)\left(\frac{d\alpha}{dr}\right)\left(\frac{d\alpha}{dr}\right) + \left(\frac{dR(r)}{d\alpha}\right)\left(\frac{d^2\alpha}{dr^2}\right) \\ &= \left(\frac{d^2R(r)}{d\alpha^2}\right)\left(k_r\right)\left(k_r\right) + \left(\frac{dR(r)}{d\alpha}\right)\left(0\right) \\ &= \left(\frac{d^2R(r)}{d\alpha^2}\right)k_r^2 \end{aligned} \tag{4.28}$$

By substituting the modified forms of $R'(r)$ and $R''(r)$ into Eq. (4.24), the differential equation is transformed into Bessel's Equation taking the form

$$\alpha^2\frac{d^2R(r)}{d\alpha^2} + \alpha\frac{dR(r)}{d\alpha} + (\alpha^2 - m^2)R(r) = 0 \tag{4.29}$$

where $\alpha = k_r r$.

With Eq. (4.29) in the proper form, its general solution is given by

$$R(r) = C_5 J_m(k_r r) + C_6 Y_m(k_r r) \tag{4.30}$$

where J_m = Bessel Function of the First Kind and Y_m = Bessel Function of the Second Kind.

The general solution for $R(r)$ is a superposition of the Bessel Functions of the first and second kind. Prior to applying the boundary condition to this solution form, it is necessary to graphically observe these two functions. These are shown in Figures 4.1 and 4.2.

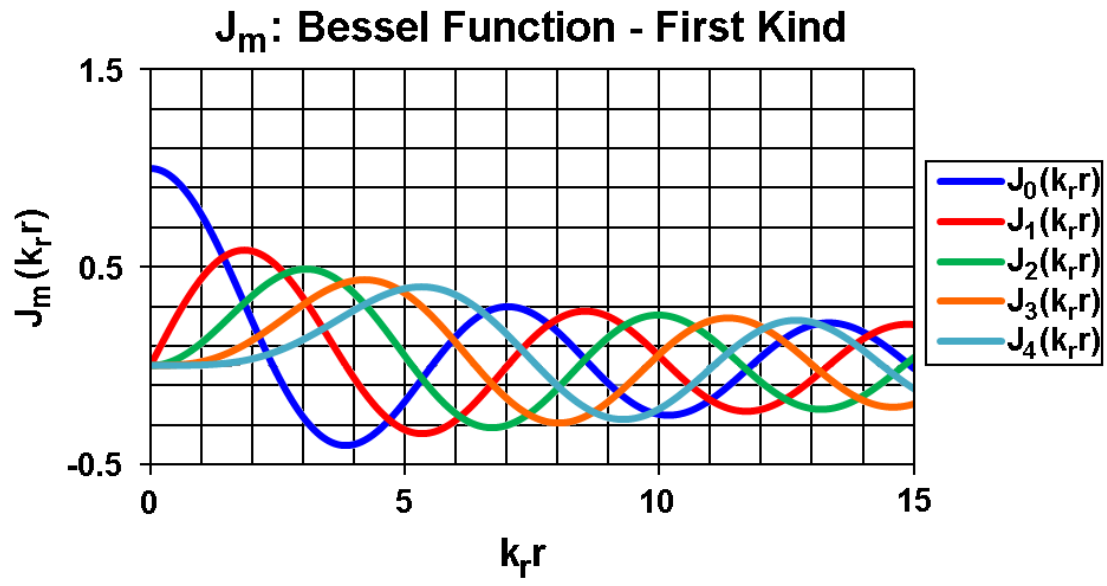

Figure 4.1: Plot of the Bessel Function of the First Kind.

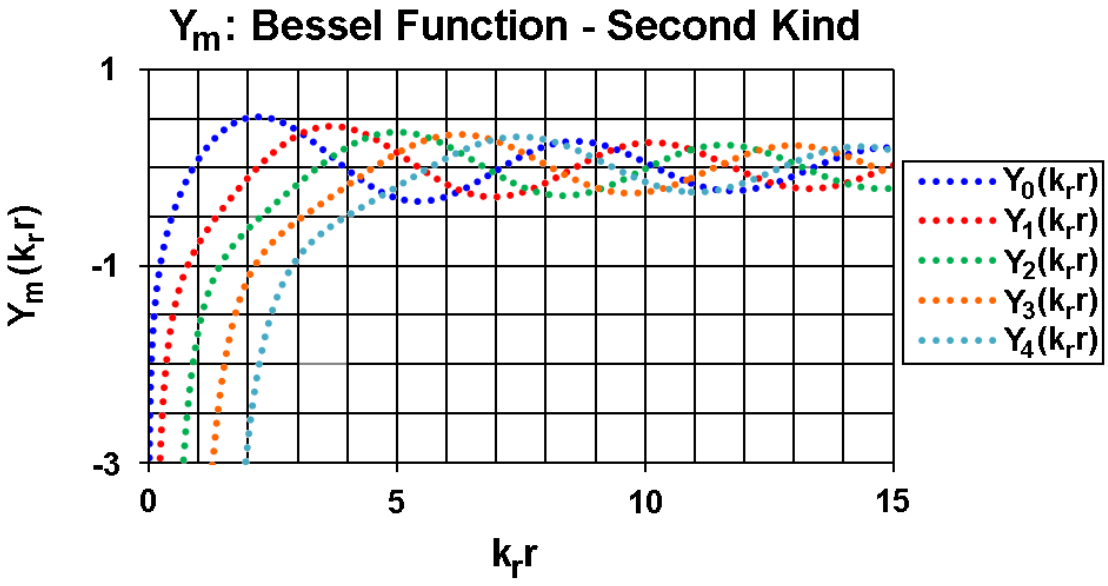

Figure 4.2: Plot of the Bessel Function of the Second Kind.

As can be seen from these two plots, the Bessel Function of the first kind (all orders) is finite at each value for α. However, for the Bessel Function of the second kind (all orders), the solutions approach $-\infty$ as $\alpha \to 0$. Hence, $R(r)$ is not defined at $r = 0$, forcing $C_6 = 0$ for all solutions (as the instantaneous pressure has to be defined at each spatial location within the chamber). Thus, the general solution for $R(r)$ simplifies to

$$R(r) = C_5 J_m(k_r r) \tag{4.31}$$

To reach the final solution for $R(r)$, the following hard-wall boundary condition at $r = a$ is applied to the Eq. (4.31):

$$\left(\frac{\partial p}{\partial r}\right)\Bigg|_{r=a} = R'(a) = 0 \tag{4.32}$$

This yields

$$C_5 J'_m(k_r a) = 0 \tag{4.33}$$

which reduces to

$$J'_m(k_r a) = 0 \tag{4.34}$$

To fulfill this condition, the $k_r a$ values for the various transverse modes correspond to the critical points of $J_m(k_r r)$. Visually, these critical points are shown in Figure 4.3.

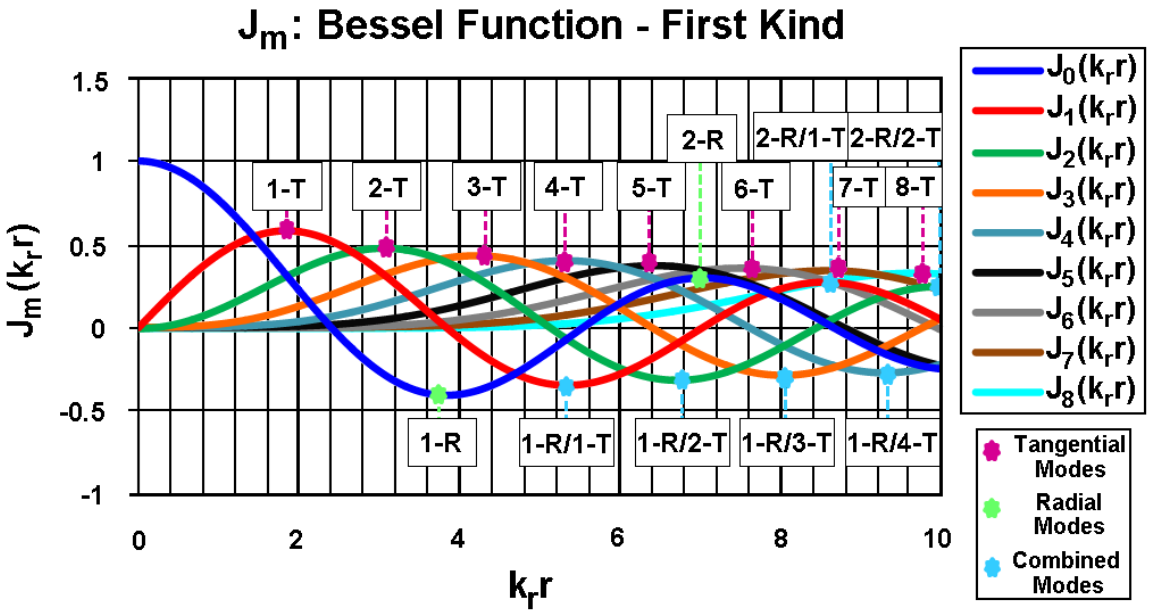

Figure 4.3: Plot of the Bessel Function of the First Kind with Mode Critical Points.

The critical point locations for the first sixteen transverse modes are summarized in Table 4.1.

Table 4.1: Critical Point Locations for the First Sixteen Transverse Acoustic Modes.

Acoustic Transverse Mode	m	n	$k_r a$ value for $J'(k_r a) = 0$
1-T	1	0	1.8412
2-T	2	0	3.0542
1-R	0	1	3.8317
3-T	3	0	4.2012
4-T	4	0	5.3176
1-R/1-T	1	1	5.3314
5-T	5	0	6.4156
1-R/2-T	2	1	6.7061
2-R	0	2	7.0156
6-T	6	0	7.5013
1-R/3-T	3	1	8.0152
2-R/1-T	1	2	8.5363
7-T	7	0	8.5779
1-R/4-T	4	1	9.2824
8-T	8	0	9.6474
2-R/2-T	2	2	9.9695

With the critical points quantified, the boundary condition for the first sixteen transverse modes of the cylindrical chamber is known. Thus, the final solution for $R(r)$ is

$$R(r) = C_5 J_m(k_r r) \tag{4.35}$$

where $J'_m(k_r a) = 0$ for the $k_r a$ values shown in Table 4.1.

Combining the solutions for $X(x)$, $\Phi(\theta)$ and $R(r)$ produces the acoustic mode pressure distribution for a cylindrical chamber closed on both ends:

$$\begin{aligned} p'(r,\theta,x,t) &= X(x)\Phi(\theta)R(r)\exp(i\omega t) \\ &= C_2 \cos\left(\frac{l\pi x}{L_x}\right)\Big(C_3 \sin(m\theta) + C_4 \cos(m\theta)\Big) C_5 J_m(k_r r)\exp(i\omega t) \end{aligned} \tag{4.36}$$

Eq. (4.36) can be transformed into another useful form similar to that of Zucrow [38] through trigonometric identity manipulation. This process is shown in Section A.3, which produces the final form of the acoustic mode pressure distribution for a closed-top cylindrical chamber:

$$p'(r,\theta,x,t) = J_m(k_r r)\cos\left(\frac{l\pi x}{L_x}\right)\Big[F\cos(m\theta + \omega t - \phi_1) + G\cos(m\theta - \omega t - \phi_2)\Big] \tag{4.37}$$

This expression is able to describe the pressure distribution for all the possible acoustic modes (longitudinal, transverse and combined modes) that can exist within the chamber. Spinning and standing tangential modes can also be readily modeled through the amplitude constants (F and G) and phase angles (ϕ_1 and ϕ_2). If the

transverse amplitude constants are equal and the phase angles the same, a standing tangential mode exists, while if either amplitude constant is set to zero, a spinning transverse mode is modeled (either in the clockwise or counter-clockwise direction, depending on which constant is set to zero).

To derive a relation which predicts the acoustic mode frequencies, the solutions for k_r and k_x are substituted into Eq. (4.23):

$$k^2 = k_r^2 + k_x^2 = \left(\frac{k_r a}{a}\right)^2 + \left(\frac{l\pi}{L_x}\right)^2 \tag{4.38}$$

Implementing the wave number definition $k^2 = \omega^2/\bar{c}^2$, Eq. (4.38) can be solved for the frequency mode relation. This yields

$$f_{lmn} = \frac{\bar{c}}{2\pi}\sqrt{\left(\frac{k_r a}{a}\right)^2 + \left(\frac{l\pi}{L_x}\right)^2} \tag{4.39}$$

where the values of $k_r a$ are found in Table 4.1 for the first sixteen transverse acoustic modes.

4.1.2 Numerical Acoustic Model

During experimentation, measured temperatures within the combustor can range from $T = 800{-}1500$ K (up to 1600 K). Thus, there are thermal gradients that exist within the chamber, causing non-homogeneous sound speed effects to be present. To illustrate how this can affect the acoustic pressure distribution and modal frequencies, a numerical acoustic model similar to that implemented by Sliphorst was created [8]. To develop this model, the linear wave equation is converted into an eigenmode equation.

Thus, the linear wave equation in cylindrical coordinates and its solution form are given by

$$\frac{1}{\bar{c}^2}\frac{\partial^2 p'}{\partial t^2} = \frac{\partial^2 p'}{\partial x^2} + \frac{\partial^2 p'}{\partial r^2} + \frac{1}{r}\frac{\partial p'}{\partial r} + \frac{1}{r^2}\frac{\partial^2 p'}{\partial \theta^2} \tag{4.40}$$

and

$$p'(r,\theta,x,t) = p_o(r,\theta,x)\exp(i\omega t) \tag{4.41}$$

where

$$\frac{\partial^2 p'}{\partial t^2} = -\omega^2 p_o(r,\theta,x)\exp(i\omega t) \tag{4.42.A}$$

$$\frac{\partial^2 p'}{\partial x^2} = \frac{\partial^2 p_o(r,\theta,x)}{\partial x^2}\exp(i\omega t) \tag{4.42.B}$$

$$\frac{\partial p'}{\partial r} = \frac{\partial p_o(r,\theta,x)}{\partial r}\exp(i\omega t) \tag{4.42.C}$$

$$\frac{\partial^2 p'}{\partial r^2} = \frac{\partial^2 p_o(r,\theta,x)}{\partial r^2}\exp(i\omega t) \tag{4.42.D}$$

and

$$\frac{\partial^2 p'}{\partial \theta^2} = \frac{\partial^2 p_o(r,\theta,x)}{\partial \theta^2}\exp(i\omega t) \tag{4.42.E}$$

Substituting all components of Eq. (4.42) into Eq. (4.40) and simplifying using the Laplace operator yields

$$\bigtriangledown^2 p_o(r,\theta,x) + \frac{\lambda}{\bar{c}^2}p_o(r,\theta,x) = 0 \tag{4.43}$$

where $\bar{c}$ is the average sound speed for a given spatial node and $\lambda = \omega^2$ (leading to $f = \sqrt{\lambda}/2\pi$).

Eq. (4.43) permits the eigenvalues corresponding to each acoustic mode to be determined in the presence of varying sound speed regions. To solve for the acoustic eigenmodes, each geometric boundary requires a specified condition. In this model, all boundaries are assumed to be acoustically closed (i.e., implement the hard-wall assumption). Hence, this can be written as a Neumann Form Boundary Condition, given by

$$\bigtriangledown p_o(r, \theta, x) = 0 \tag{4.44}$$

Model Validation

To validate the numerical acoustic code, the first four longitudinal eigenfrequencies and corresponding pressure distributions were determined for a closed chamber with dimensions similar to the SEMRC ($d_{\text{num,model}} = 10.16$ cm and $l_{\text{num,model}} = 15.24$ cm). For this model validation, homogeneous sound speed conditions were assumed, with $\overline{c} = 754$ m/s. The Partial Differential Equation Toolbox within MATLAB was implemented to carry out this numerical analysis. The model eigenfrequencies were then compared to the analytical solution of a closed chamber given by Eq. (4.39), which for purely longitudinal modes reduces to

$$f_l = \frac{l\overline{c}}{2L_x} \tag{4.45}$$

where $\overline{c}$ and L_x are the same as those used for the numerical model geometry.

The results from this eigenfrequency validation are presented in Table 4.2. Upon comparison, there is excellent agreement between the numerical model and

analytical frequency solutions. The frequencies found using both methods were identical for the first three longitudinal modes, with the frequency of the fourth longitudinal mode only deviating by 2 Hz (0.02% Error).

Table 4.2: Longitudinal Eigenfrequency Comparison between the Numerical Acoustic Model and Analytical Solution.

Mode	$f\,(Hz)$	$f_l\ (Hz)$	Percent Error (%)
1-L	2475	2475	0.00
2-L	4949	4949	$''$
3-L	7424	7424	$''$
4-L	9900	9898	0.02

The corresponding pressure distributions found using the numerical acoustic model (shown in Figure 4.4) are in agreement with the expected longitudinal mode shapes from classic acoustic theory. Thus, with both the acoustic mode frequencies and pressure distributions matching the analytical solutions, the numerical acoustic model has been successfully validated.

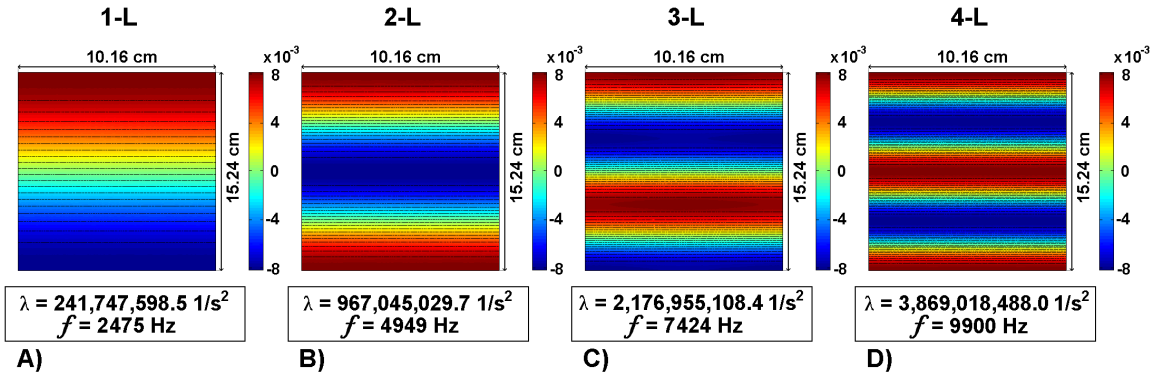

Figure 4.4: Pressure Distributions of the First Four Longitudinal Acoustic Eigenmodes for Homogenous Sound Speed Conditions: A) 1-L, B) 2-L, C) 3-L and D) 4-L.

4.2 Signal Analysis Tools

Aside from the acoustic analysis methods, various signal tools were developed to post-process the high-frequency instability data. The first tool is a two-way Butterworth bandpass filter that was necessary to filter the raw high-frequency signal around the instability frequency within the time domain. The second tool is the fast Fourier analysis technique adopted to extract the instability frequency and amplitude content. As both of these tools are integral in characterizing the measured instability response, sensitivity studies were performed to illustrate their ability to correctly analyze the data.

4.2.1 Time-Domain Characterization: Two-Way Butterworth Bandpass Filter

To detail the dominant instability mode(s), post-process filtering of the high-frequency data is often required. By filtering around the instability frequency, unwanted noise will be eliminated from the signals, permitting their phase offsets to be easily determined. However, the implementation of a digital filter can add a phase shift to the data, depending on the manner it is applied. For this research (i.e, the phase offset between signals is of interest), it is desirable to incorporate a digital filter that does not impose any phase shift to the data.

The phase shift generated from a digital filter can be negated through the use of a two-way filter. A two-way filter is applied to the data in both the forward and reverse directions, unlike a traditional one-way (forward direction) filter; this causes the phase shift to be negated. Thus, a two-way Butterworth bandpass filter similar

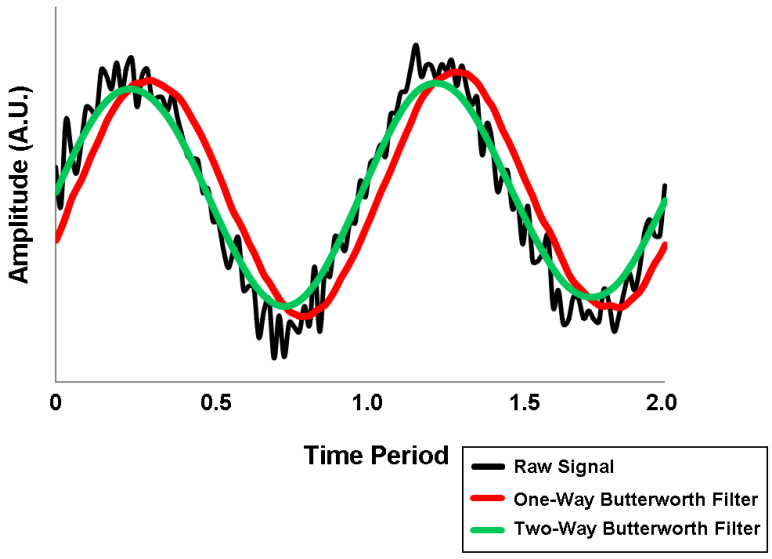

Figure 4.5: Imposed Phase Shift Comparison between One-Way and Two-Way Filters: Based off a Similar Plot Presented in [8].

to that used by Sliphorst was created [8]. A plot demonstrating the applied phase shift between a typical one-way filter and the two-way filter for this study can be seen in Figure 4.5.

4.2.2 Frequency-Domain Characterization: Fast Fourier Transform

The fast Fourier transform (FFT) is a means to analyze the frequency content of a sampled signal. By decomposing the signal into its various frequency components (i.e., bins) through an FFT, certain signal characteristics can be deduced. These include the signal's amplitude and phase associated with the dominant frequency.

Performing a fast Fourier transform to determine the dominant mode amplitude is preferred to extracting it from the raw time-domain signal, as this signal would need to be filtered to accurately resolve a modal amplitude. Applying a filter in this manner can artificially decrease the measured signal amplitude. Thus, the FFT function in MATLAB was selected as the primary tool for quantifying modal amplitudes.

To ensure the MATLAB FFT function is capable of accurately determining the signal amplitude, a sensitivity study was performed. For this analysis, sinusoidal signals of a known constant amplitude ($\text{Sign}_{\text{Amp}} = 1.00$) with varying amounts of noise were analyzed using the FFT function. These signals were given the same parameters of an instability typically measured by the high-frequency pressure transducers ($f = 2400$ Hz at $f_s = 55{,}000$ Hz). To create quantified levels of noise, the parameter signal-to-noise ratio (SNR) was implemented. Mathematically, SNR is defined as

$$SNR = \frac{\text{Power}_{\text{signal}}}{\text{Power}_{\text{noise}}} \tag{4.46}$$

where a higher value of SNR corresponds to a "cleaner" (more pure) signal.

Presented in Table 4.3 are the cases for this sensitivity study. These span eleven orders of magnitude, from a virtually pure sinusoidal signal ($\text{SNR} = 1 * 10^{10}$) to a signal where the noise is on the same order of magnitude as the signal amplitude ($\text{SNR} = 1 * 10^{0}$).

Table 4.3: Analyzed Cases for the Signal-to-Noise Ratio FFT Amplitude Sensitivity Study.

Case	SNR	Case	SNR
1	$\mathbf{1 * 10^{10}}$	7	$1 * 10^{4}$
2	$1 * 10^{9}$	8	$1 * 10^{3}$
3	$1 * 10^{8}$	**9**	$\mathbf{1 * 10^{2}}$
4	$1 * 10^{7}$	10	$1 * 10^{1}$
5	$1 * 10^{6}$	**11**	$\mathbf{1 * 10^{0}}$
6	$1 * 10^{5}$		

Note: The bolded cases will be discussed in greater detail.

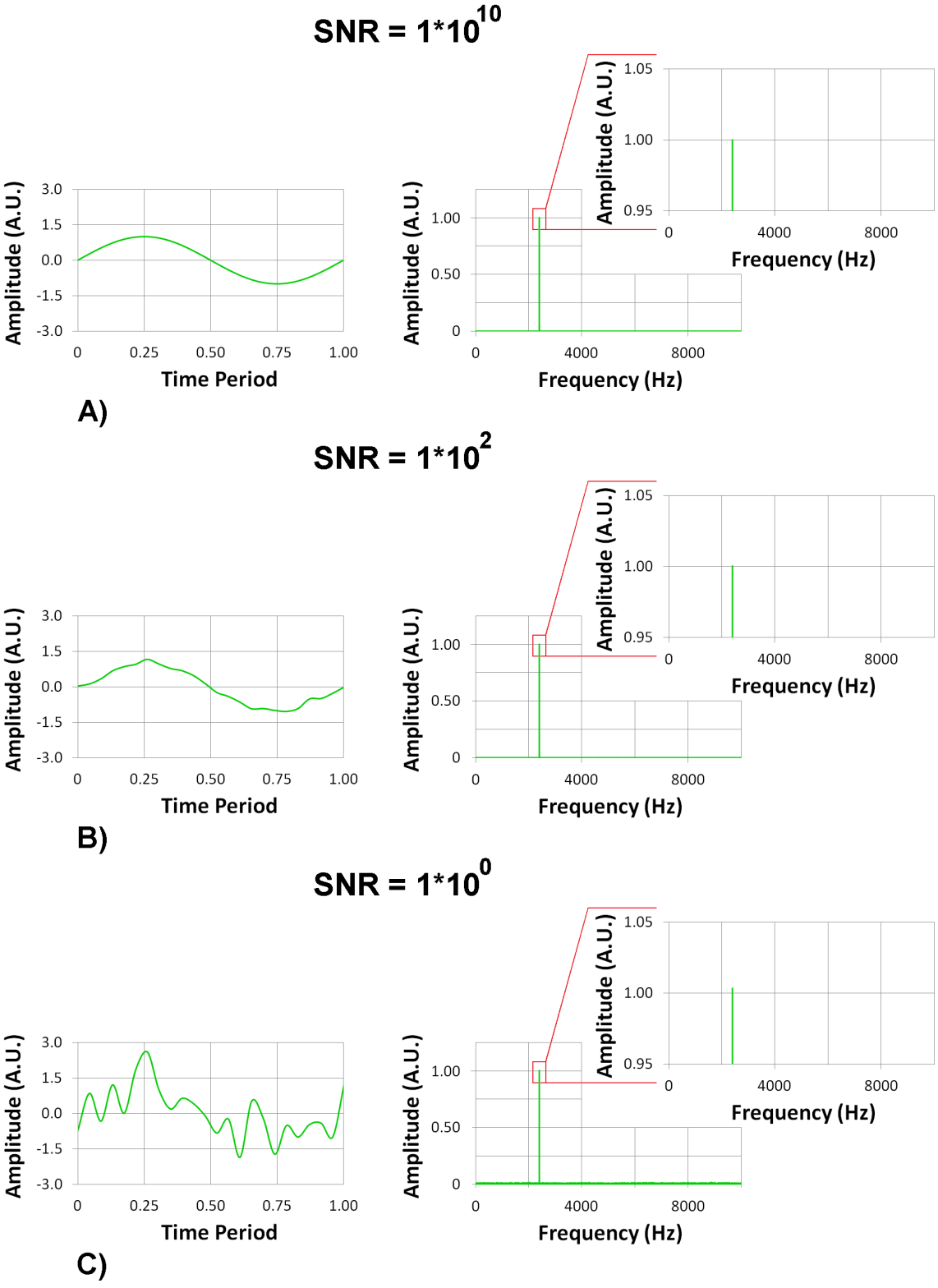

Figure 4.6: Time Histories and Frequency Spectra for the Following Signal-to-Noise Ratio Cases: A) $1 * 10^{10}$, B) $1 * 10^{2}$ and C) $1 * 10^{0}$.

For each case, the generated signal was processed using the MATLAB FFT function and the amplitude of the 2400 Hz signal was extracted. The time histories and frequency spectra for three of the SNR cases are shown in Figure 4.6. For SNR $= 1 * 10^{10}$ (pure sinusoidal signal), the amplitude from the time history and frequency spectra seen in Figure 4.6.A both are identical, $\text{Sign}_{\text{Amp}} = 1.00$. For SNR $= 1 * 10^{2}$ (signal with moderate noise), Figure 4.6.B shows the amplitude taken from the frequency spectra is almost the same as the pure sinusoidal signal ($< 0.05\%$ Error). For the final case SNR $= 1 * 10^{0}$ (signal with maximum noise), the amplitude from the frequency spectra shown in Figure 4.6.C has an approximate 0.35% Error discrepancy with the pure sinusoidal signal amplitude.

A plot of the frequency spectra amplitude percent error for the fourteen SNR cases is shown in Figure 4.7. Across these cases, there is no appreciable error of the signal amplitude taken from the MATLAB FFT function until SNR $= 1 * 10^{3}$, where the error begins to exponentially increase with each magnitude drop in signal-to-noise ratio until SNR $= 1 * 10^{0}$, where the maximum percent error is $\approx 0.35\%$.

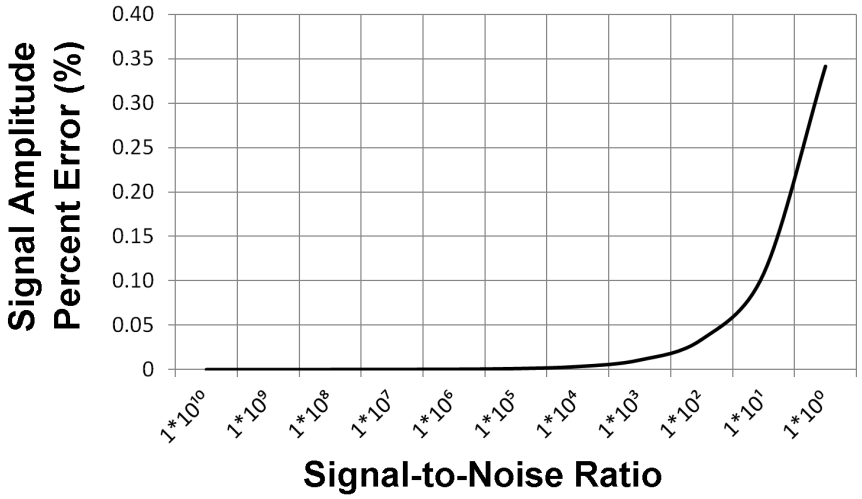

Figure 4.7: Signal Amplitude Percent Error Sensitivity Due to Signal-to-Noise Ratio.

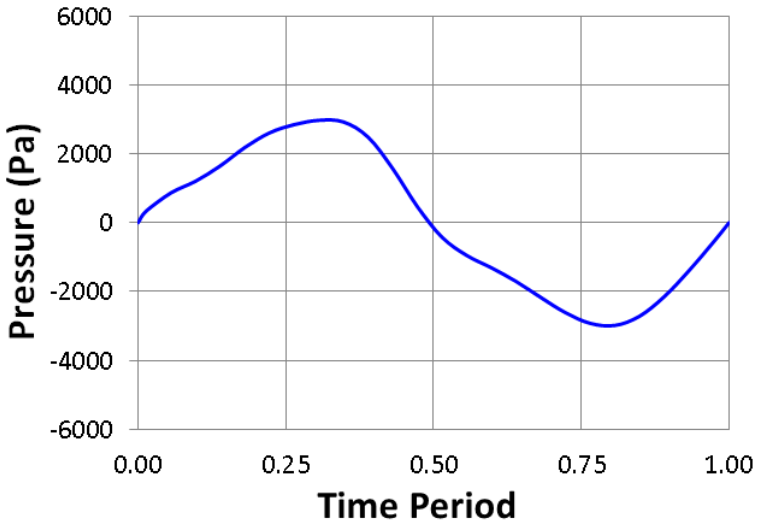

Figure 4.8: Example High-Frequency Pressure Data Taken from $P'3$ during an Instability Baseline Test Performed on 06-28-2013.

An example of the raw high-frequency pressure data taken from an instability baseline test can be seen in Figure 4.8. From this plot, the signal-to-noise ratio of a typical pressure trace seen during the experiments appears to be on the order of SNR $= 1 * 10^2 - 1 * 10^3$; this corresponds to a signal amplitude percent error of less than 0.1%. As this error is significantly low, the MATLAB FFT function is sufficient to determine the instability amplitude for the experimental data.

CHAPTER 5

EXPERIMENTAL RESULTS

This study aims to demonstrate control of a spontaneously excited high-frequency combustion instability through the strategic application of acoustic forcing within the oxidizer supply of a propellant injector. To do this, three main test phases were carried out, with each phase designed to characterize a certain aspect of the instability control approach (see Section 3.3).

For each new test phase to build upon the previous, a high-frequency instability needed to be consistently excited within the model combustor. This instability would be the primary target for suppression throughout the study. Thus, a series of baseline instability tests without acoustic modulation was performed prior to phase one testing.

5.1 Instability Mode Determination

In these instability baseline tests, the mass flow rate of the incoming propellants (GCH_4/GO_2) were varied to alter the oscillatory behavior of the combustor. Upon testing various flow conditions, it was found that providing the propellants at $\dot{m}_f = 0.168$ g/s and $\dot{m}_{ox} = 0.671$ g/s led to the spontaneous excitation of a $f \approx 2430$ Hz pressure oscillation within the combustor. These flow conditions were selected as they correspond to an equivalence ratio $\phi_{\text{avg}} \approx 1$, essentially eliminating chemical reaction for combustion as a dominant instability driving mechanism (as $\tau_{\text{chem}} << \tau_{\text{acous}}$ when $\phi_{\text{avg}} = 1$).

Across these baseline tests, the 2430 Hz instability was found to repeatedly be excited for these flow rates. Thus, this instability was chosen as the primary target of investigation. A plot of the raw pressure data and its frequency spectra from an instability baseline test are shown in Figure 5.1.

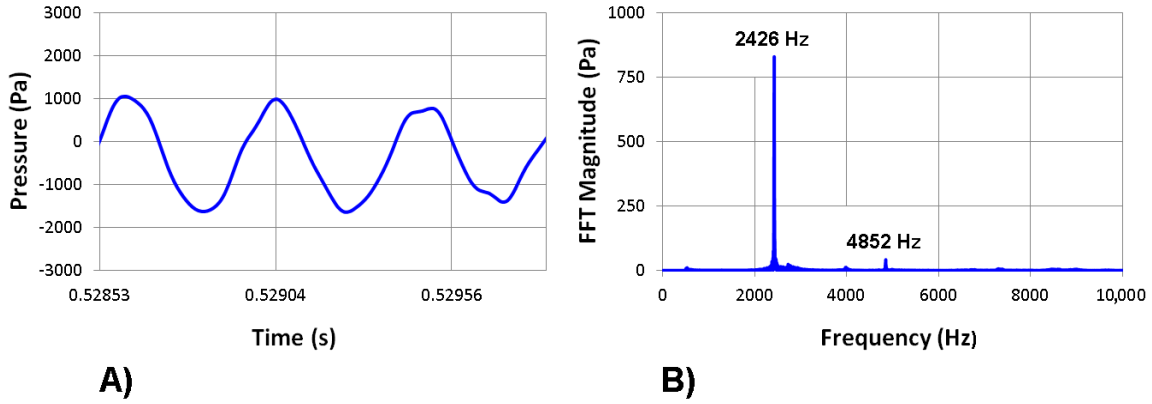

Figure 5.1: A) Raw Time History and B) Frequency Spectra Measured by $P'3$ from an Instability Baseline Test Performed on 06-25-2013.

In Figure 5.1.A, the waveform of the raw pressure trace is seen to be sinusoidal in nature with a predominant frequency of $f \approx 2430$ Hz. This supports the frequency spectra from Figure 5.1.B, where the peak signal frequency is 2426 Hz with a cascading harmonic at 4852 Hz. As the measured acoustic pressure signal is consistent with empirical thermo-acoustic instability behavior, a high-frequency combustion instability at 2430 Hz is confirmed to be excited within the model combustor for $\dot{m}_f = 0.168$ g/s and $\dot{m}_{ox} = 0.671$ g/s.

The frequency of this 2430 Hz instability matches the first longitudinal (1-L) mode determined for a closed-closed cylindrical chamber with homogeneous thermal conditions at an average combustor temperature experienced during operation ($T_{\text{comb}} \approx 1000$ K). While the instability frequency matches the first longitudinal mode for the temperature conditions mentioned previously, the amplitudes detected by the three pressure transducers at the same axial location ($P'1-P'3$) do not always measure the same amplitude as expected with a traditional longitudinal mode. Phase analysis of the dynamic pressure data for the three axial plane transducers also only demonstrates intermittent agreement with that of a 1-L mode throughout the testing phases. To determine if non-homogeneous sound speed within the combustor can cause this phenomena, the numerical acoustic model developed in Section 4.1.2 was implemented.

5.1.1 Numerical Acoustic Model: Non-Homogeneous Sound Speed Study

The effects of non-homogeneous chamber sound speed on the first longitudinal acoustic mode were investigated using five model geometries. For this study, the

chamber was assumed to be closed, with geometric dimensions similar to the model combustor ($d_{\text{num,model}} = 10.16$ cm and $l_{\text{num,model}} = 15.24$ cm). The model consisted of two regions, a high temperature "flame" region located at the wall and the surrounding gas encompassing the rest of the chamber. For each geometry, the flame region was modeled as an asymmetric inverted triangular region of varying width and height. Schematics of the five model geometries are shown in Figure 5.2.

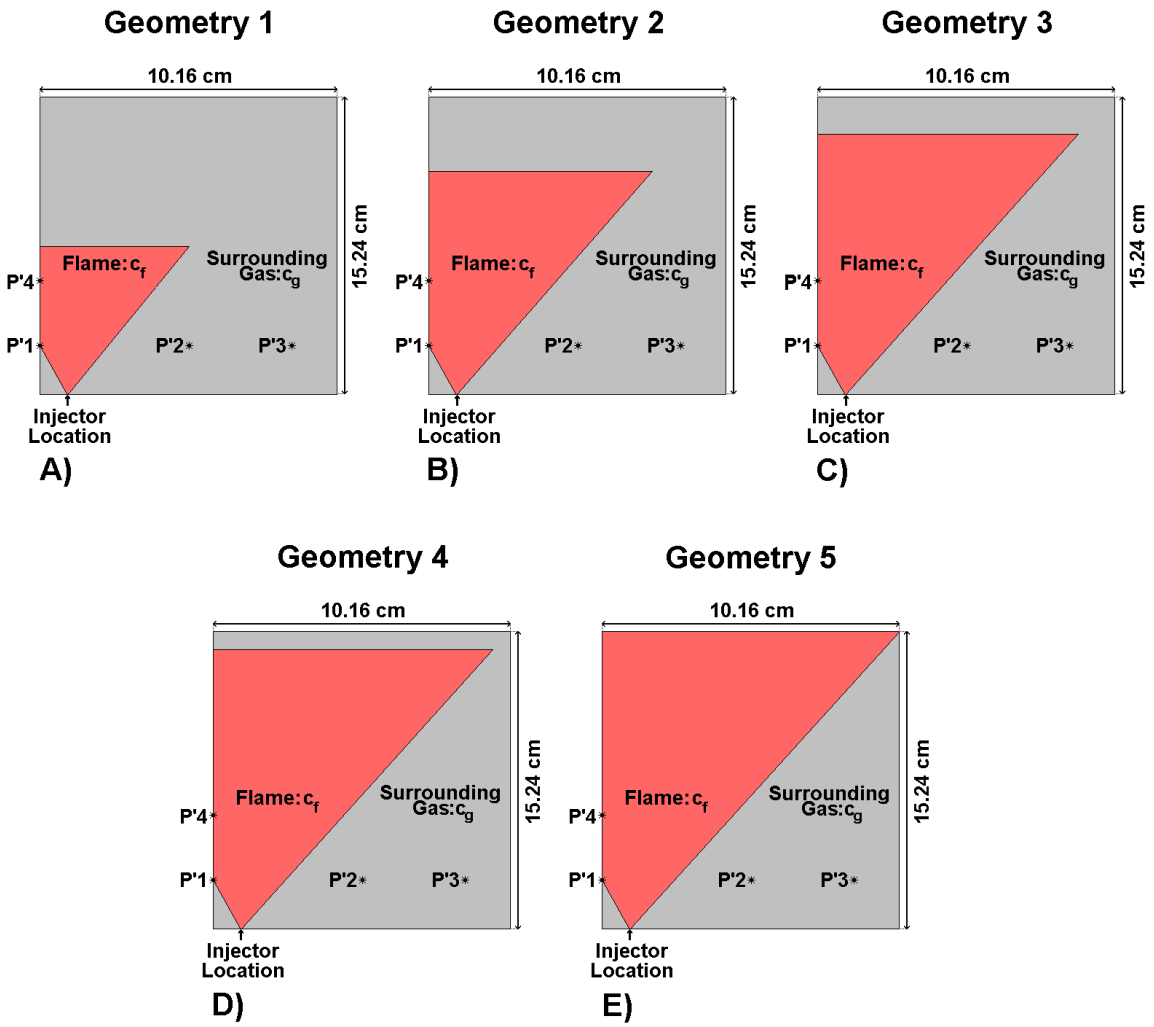

Figure 5.2: Model Schematics for the Non-Homogeneous Sound Speed Study: A) Geometry 1, B) Geometry 2, C) Geometry 3, D) Geometry 4 and E) Geometry 5.

In this analysis, the sound speed of the flame region was held constant at $c_f = 967$ m/s (that of a GO_x/GCH_4 mixture at $T = 2400$ K), where the sound speed of the surrounding gas ranged from $c_g = 967-338$ m/s across fourteen different cases. These cases (presented in Table 5.1) were chosen to span a large range, from high temperature sound speeds experienced during combustion to ambient conditions.

Table 5.1: Analyzed Cases for the Non-Homogeneous Sound Speed Study.

Case	c_g (m/s)	T_g (K)	c_f (m/s)	T_f (K)	c_g/c_f
1	967	2400	967	2400	1.00
2	919	2165	″	″	0.95
3	870	1943	″	″	0.90
4	822	1733	″	″	0.85
5	774	1536	″	″	0.80
6	725	1350	″	″	0.75
7	677	1176	″	″	0.70
8	629	1014	″	″	0.65
9	580	864	″	″	0.60
10	532	726	″	″	0.55
11	484	600	″	″	0.50
12	435	486	″	″	0.45
13	387	384	″	″	0.40
14	338	294	″	″	0.35

Across these fourteen cases, the frequency and pressure distribution of the first longitudinal mode were determined to see how these modal characteristics are affected by non-homogeneous sound speed conditions. A plot of the modal frequency response due to sound speed variation for each model geometry can be seen in Figure 5.3.

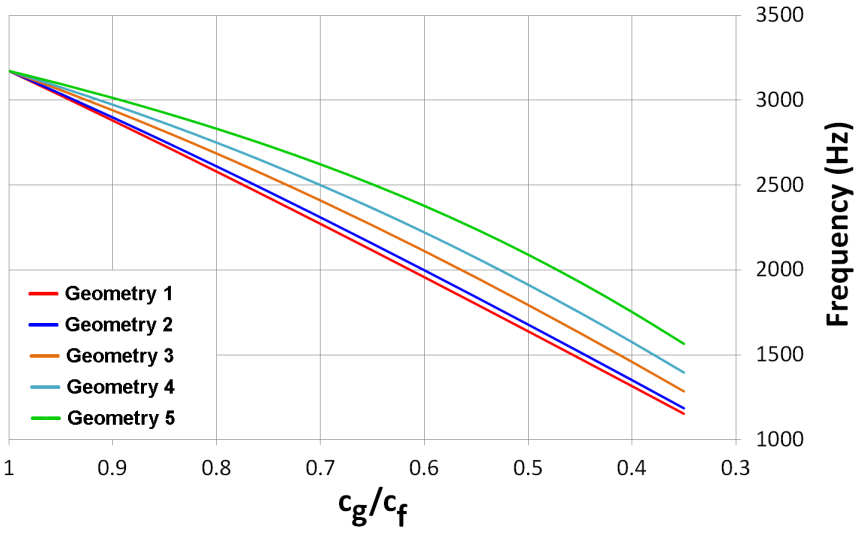

Figure 5.3: Alteration of the First Longitudinal Mode Frequency Due to Non-Homogeneous Sound Speed Conditions.

Consistent with acoustic theory, the modal frequency for each geometry decreases as the surrounding gas sound speed is reduced, albeit at different rates. This frequency ranged from $\approx 3200-1300$ Hz across the fourteen cases, with a significant variation existing between the five model geometries. Geometries 1 and 2 follow an extremely similar trend, where the frequency of the 1-L mode for the lowest sound speed case $c_g/c_f = 0.35$ was 1153 Hz and 1185 Hz, respectively. However, Geometries $3-5$ have significant deviations in their frequency reduction rate. In the lowest sound speed case, the frequency of the 1-L mode ranged from $1285-1565$ Hz for these three model geometries. Therefore, as expected, the larger the flame region within the combustor, the less sensitive the 1-L mode frequency is to non-homogeneous sound speed variations.

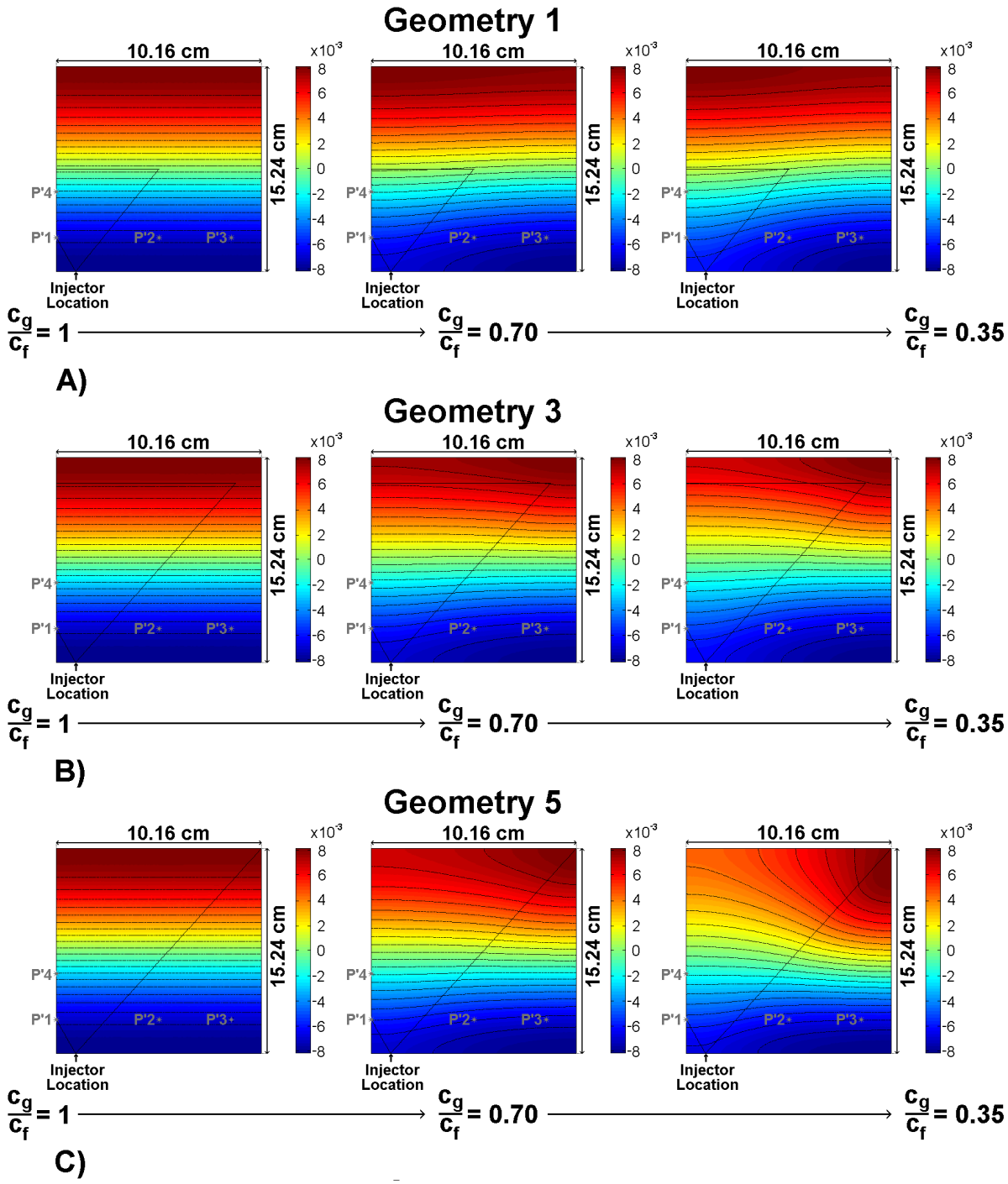

Figure 5.4: Alteration of the First Longitudinal Acoustic Mode Pressure Distribution Due to Non-Homogenous Sound Speed Conditions for A) Geometry 1, B) Geometry 3 and C) Geometry 5.

The alteration of the first longitudinal mode pressure distribution across the fourteen cases is shown in Figure 5.4. When a thermal gradient is present within the chamber, the acoustic pressure lines bend to varying degrees for all flame size geometries. Specifically, warping of the acoustic pressure lines is present within the axial transducer plane for the sound speed ratio $c_g/c_f \approx 0.60-0.75$, which corresponds to conditions matching the measured 2430 Hz first longitudinal instability. Therefore, pressure line bending effectively alters the amplitude, as well as potentially the phase of the acoustic pressure measured at locations on the same axial plane. This provides some explanation for the observed behavior from $P'1-P'3$ during testing.

5.2 Experiment Testing: Phase One

5.2.1 Band-Limited White Noise: Principle Baseline Testing

The tests within this study aim to apply various bands of white noise to suppress the 2430 Hz instability. For each test (seen in Table 5.2), the given propellant flow rates resulted in a constant equivalence ratio $\phi_{\text{avg}} = 0.99 \pm 0.03$ (at a 95% confidence interval).

Table 5.2: Flow Conditions and Average Instability Characteristics for the Band-Limited White Noise Principle Baseline Tests.

Test #	ϕ_{avg}	$P'1_{\text{Bsl.}}/P_c, \%$	$P'2_{\text{Bsl.}}/P_c, \%$	$P'3_{\text{Bsl.}}/P_c, \%$	$P'4_{\text{Bsl.}}/P_c, \%$	Average f, Hz
06-28-01	**0.97**	**1.04**	**1.07**	**1.41**	**0.20**	**2432**
06-28-02	**0.97**	**1.18**	**0.86**	**0.93**	**0.31**	**2425**
07-30-01	0.99	0.15	1.26	4.66	0.43	2391
07-30-02	1.01	0.20	0.98	3.54	0.44	2402
07-30-03	1.00	0.17	2.51	1.67	0.26	2417
07-30-04	1.00	0.73	1.65	4.50	0.25	2436
07-30-05	0.99	0.56	1.11	5.62	0.23	2421

Note: The bolded tests will be discussed in greater detail.

Before each test, the acoustic driver was turned on at a constant amplitude to appropriately set the volume. During each purely acoustic pre-test, the speaker was set to output 0−2500 Hz band-limited white noise, without any combustion occurring. The volume level was then fixed to approximately 2.0 kPa-rms, which was measured from P'_{inj}.

Each test began with the speaker turned off and the 2430 Hz instability spontaneously excited within the combustor. With the propellant flow conditions held constant, the acoustic driver was turned on and first set to output band-limited white noise from 0−500 Hz. The applied white noise signal was then slowly shifted in increments of 100 Hz, keeping a constant band of 500 Hz (i.e., the second increment was 100−600 Hz, the third was 200−700 Hz, etc.), until a band of 2000−2500 Hz was reached. To examine hysteresis effects, the applied white noise signal was then decreased in the same amounts all the way back down to 0−500 Hz. The applied modulation signal characteristics are summarized in Table 5.3.

Table 5.3: Signal Specifications for the Band-Limited White Noise Principle Baseline Tests.

Frequency Range (Hz)	**Lowest Band**	**Highest Band**	**Increment/ Decrement (Hz)**	**Signal Amplitude (kPa-rms)**
0−2500 Hz	0−500 Hz	2000−2500 Hz	100 Hz	2.0

The amplitude response of the instability for the application of various bands of white noise in Test 06-28-01 can be seen in Figure 5.5. In this figure, the amplitude

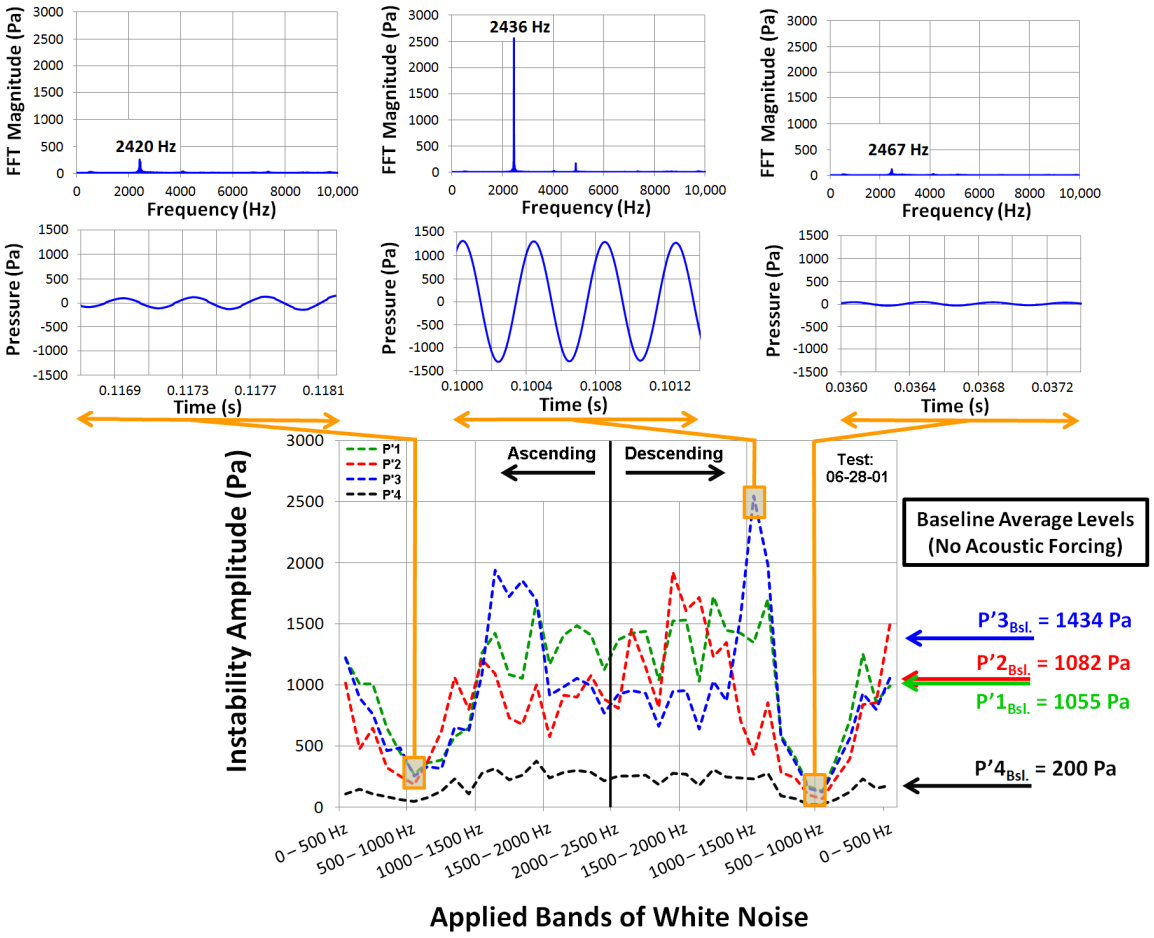

Figure 5.5: Instability Amplitude vs. Applied Bands of White Noise for Test 06-28-01.
Note: Frequency Spectra and Time Histories for $P'3$ at three different bands of white noise are also shown.

corresponding to the dominant 2430 Hz instability for each high-frequency pressure transducer can be seen, as well as the frequency spectra and filtered time histories for $P'3$. $P'3$ was selected to be shown in greater detail as it is the pressure transducer having the largest change in instability amplitude across all pressure transducers.

With the speaker applying 0−500 Hz band-limited white noise during the beginning of the test, the three pressure transducers, $P'1$, $P'2$ and $P'3$, were at

instability amplitudes very similar to their baseline average levels, with an instability frequency of 2386 Hz. Once the white noise band was increased from 0−500 Hz to 500−1000 Hz, there was a significant decrease in pressure amplitude seen across all pressure transducers. At this point, there was a maximum suppression of the 2420 Hz instability in the ascending application direction. This increase in instability frequency can be attributed to chamber heating and is present throughout all tests.

Once the white noise band was increased further from 500−1000 Hz to 1200−2000 Hz, there was a sharp increase in instability amplitude seen by the three pressure transducers; the application of certain frequency bands of white noise within this range actually corresponds to instability amplitudes exceeding baseline averages. From 1500−2000 Hz to 2000−2500 Hz, the instability amplitudes measured by $P'1$ and $P'2$ stayed mostly constant, while $P'3$ showed a decrease from 1380 Pa to 1035 Pa, where it then leveled out.

For the application of white noise bands in the descending direction (signal sweep from high frequency to low frequency), the trend measured by the pressure transducers was fairly consistent, with $P'3$ again showing a sharp increase in amplitude from 1200−1700 Hz to 900−1400 Hz. It is at this point the maximum amplitude of 2550 Pa was detected by $P'3$, where the instability frequency was 2436 Hz. After this sharp spike in amplitude, all transducers saw a significant reduction in pressure amplitude once 500−1000 Hz band-limited white noise was again applied, denoting a maximum suppression of the 2467 Hz instability in the reverse application direction.

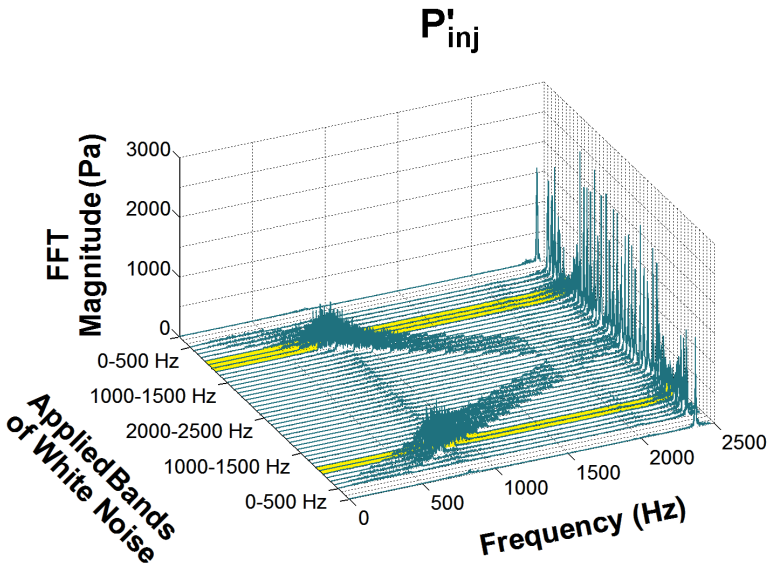

Figure 5.6: P'_{inj} Waterfall Plot for Test 06-28-01.

Note: Enlarged Waterfall Plot of P'_{inj} can be seen in Section B.1.1.

During the test, the acoustic pressure measured by P'_{inj} within the oxidizer supply (see Figure 5.6) generally shows there is the specified white noise frequency band being applied at uniform amplitudes of excitation, at a level significantly less than the 2430 Hz instability (measured from within the oxidizer supply). However, for the maximum suppression frequency bands (500−1000 Hz) in both signal sweep directions, band-limited white noise is naturally amplified within the oxidizer supply with a 844 Hz peak at levels comparable to the 2430 Hz instability measured at that location. While 500−1000 Hz white noise is amplified within the oxidizer supply upstream of the combustor, this frequency band is not detected by any of the transducers within the chamber at appreciable amplitudes, as evidenced in the frequency spectra of $P'3$ shown in Figure 5.5.

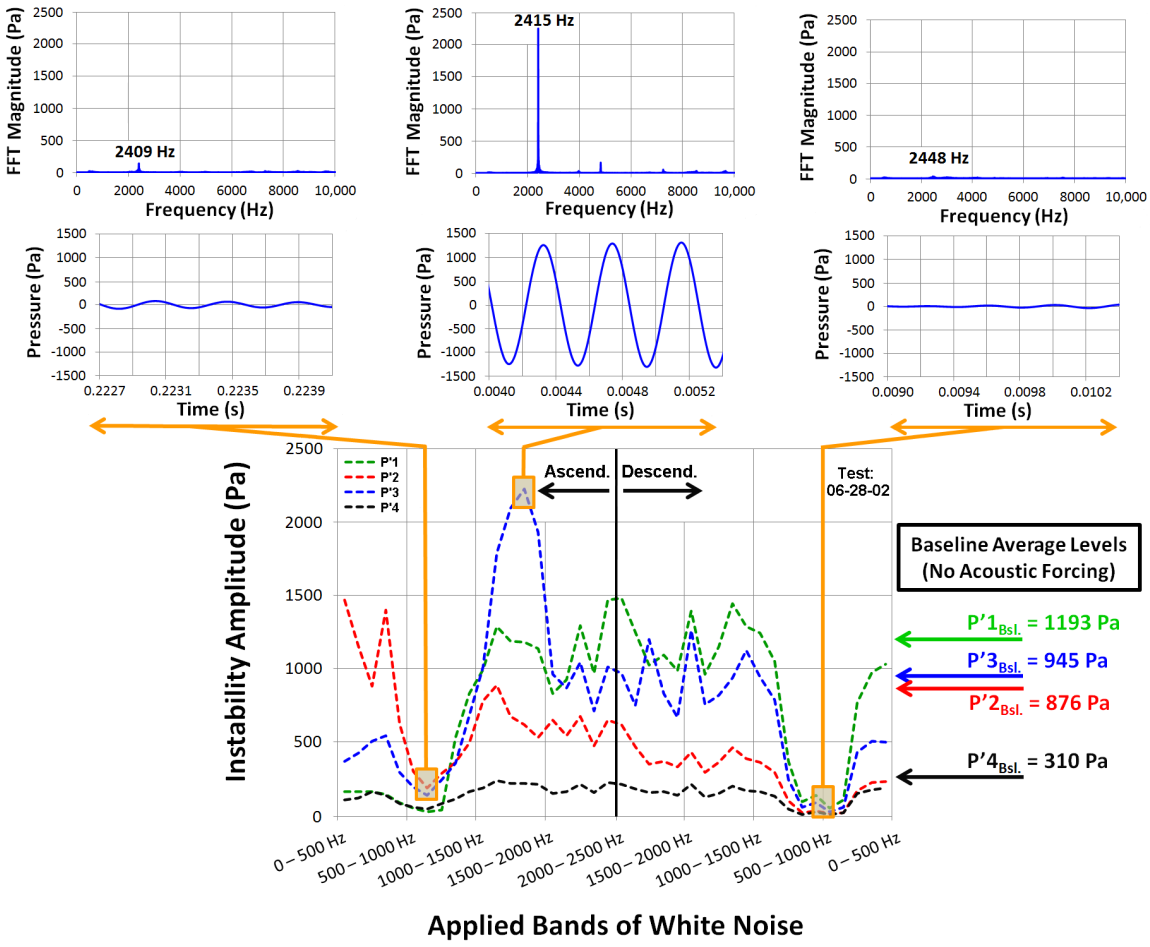

Figure 5.7: Instability Amplitude vs. Applied Bands of White Noise for Test 06-28-02. *Note: Frequency Spectra and Time Histories for $P'3$ at three different bands of white noise are also shown.*

Similar to the prior test, Figure 5.7 shows the amplitude response of the instability under varying bands of white noise for Test 06-28-02. Again, the dominant instability amplitude for all pressure transducers, as well as the time histories and frequency spectra for $P'3$ can be seen in this figure.

Interestingly, at the start of this test, the amplitudes of $P'1$, $P'2$ and $P'3$ were all different from their baseline average levels once the acoustic driver was set to output 0−500 Hz band-limited white noise. Unlike the previous test, at this point

both $P'1$ and $P'3$ appeared damped, while $P'2$ was increased. Despite this change, however, the trend for the three pressure transducers was the same, with a significant decrease in instability amplitude during 600−1100 Hz band-limited white noise. At this point, there was a maximum suppression of the 2409 Hz instability achieved in the ascending signal direction.

With the white noise band increased further from 600−1100 Hz to 1200−1700 Hz, all transducers again measured a significant rise in instability amplitude, with $P'1$ and $P'3$ being increased past their baseline average levels. At this point, $P'3$ saw its maximum value of 2275 Pa with an instability frequency of 2415 Hz. After this maximum was reached, $P'3$ decreased to approximately 965 Pa at 1500−2500 Hz band-limited white noise application, where all of the transducer amplitudes stayed relatively constant until 2000−2500 Hz.

For the application of white noise bands in the descending direction, this test was not as consistent as the previous. From 2000−2500 Hz to 1000−1500 Hz, the instability amplitudes detected by all of the transducers remained relatively constant, with $P'3$ not drastically rising at approximately 1000−1500 Hz. However, once the modulation signal was decreased past 1000−1500 Hz to 500−1000 Hz, there was a very pronounced instability suppression across all of the transducers. Again, 500−1000 Hz band-limited white noise led to a maximum suppression of the 2448 Hz instability.

Figure 5.8 shows the P'_{inj} waterfall plot from Test 06-28-02. As with Test 06-28-01, the suppression regimes for P'_{inj} coincide with the rest of the transducers within the SEMRC for both signal sweep directions. The applied modulation signal detected by P'_{inj} also exhibits a natural amplification of the bands containing

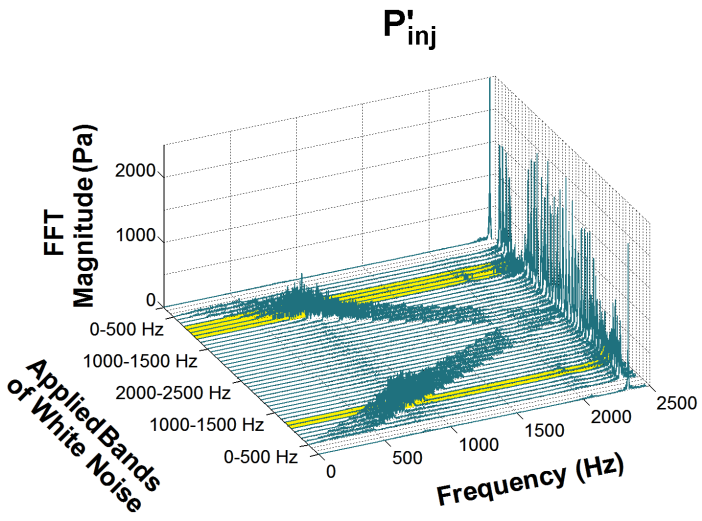

Figure 5.8: P'_{inj} Waterfall Plot for Test 06-28-02.

Note: Enlarged Waterfall Plot of P'_{inj} can be seen in Section B.1.2.

$f \approx 850$ Hz, where the maximum suppression bands of $500-1000$ Hz/$600-1100$ Hz are centered. As this acoustic phenomenon is present across these tests, it is a potential factor contributing to the instability suppression.

Table 5.4 summarizes the instability suppression characteristics (i.e., the maximum percent amplitude reductions based on baseline averages) of the four pressure transducers, for all tests, in both signal sweep directions. Across the tests, the maximum instability suppression was reached by applying either $500-1000$ Hz or $600-1100$ Hz band-limited white noise, regardless of the application direction. Aside from this (excluding Test 07-30-01), the average instability minimum reached during the descending sweep of each test showed a larger instability suppression, when compared to the instability suppression characteristics in the ascending signal application direction. Thus, these tests demonstrated that applying band-limited white noise within the correct range can consistently suppress a high-frequency combustion instability.

Table 5.4: Maximum Instability Suppression Characteristics for the Band-Limited White Noise Principle Baseline Tests.

Ascending Signal Application Direction							
			% Reduction (Based on Baseline Averages)				
Test #	Frequency Band for Max. Suppression	Instability Freq., Hz	$P'1$, %	$P'2$, %	$P'3$, %	$P'4$, %	Avg., %
06-28-01	**500−1000 Hz**	**2420**	**74.4**	**82.6**	**82.1**	**74.9**	**78.5**
06-28-02	**600−1100 Hz**	**2409**	**97.5**	**78.5**	**85.1**	**84.6**	**86.4**
07-30-01	600−1100 Hz	2373	75.7	83.1	79.3	49.2	71.8
07-30-02	500−1000 Hz	2392	70.0	42.3	69.7	73.4	63.8
07-30-03	500−1000 Hz	2394	49.0	75.6	70.3	62.3	64.3
07-30-04	500−1000 Hz	2430	90.2	56.3	46.8	71.8	66.3
07-30-05	700−1200 Hz	2401	93.9	47.7	70.3	62.9	68.7
Descending Signal Application Direction							
			% Reduction (Based on Baseline Averages)				
Test #	Frequency Band for Max. Suppression	Instability Freq., Hz	$P'1$, %	$P'2$, %	$P'3$, %	$P'4$, %	Avg., %
06-28-01	**500−1000 Hz**	**2467**	**87.5**	**93.1**	**91.5**	**88.6**	**90.2**
06-28-02	**500−1000 Hz**	**2448**	**95.5**	**98.3**	**96.9**	**96.0**	**96.7**
07-30-01	600−1100 Hz	2417	49.2	81.3	53.7	69.8	63.5
07-30-02	500−1000 Hz	2428	58.6	72.9	52.4	80.9	66.2
07-30-03	600−1100 Hz	2441	78.6	74.9	88.1	84.0	81.4
07-30-04	600−1100 Hz	2441	90.2	62.8	63.9	59.6	69.1
07-30-05	600−1100 Hz	2440	68.8	75.0	89.0	88.4	80.3

5.2.2 Single-Frequency Acoustic Modulation: Principle Baseline Testing

To further explore the concept of acoustically modulating the incoming oxidizer flow as a means of instability control, a set of single-frequency sweep tests at a constant signal amplitude was performed. In this study, pure sinusoidal tones (with arbitrary phase) ranging from 50−2500 Hz were applied by the acoustic driver at a level of approximately 2.0 kPa-rms (measured from P'_{inj}). Beginning at 50 Hz, single-frequency acoustic modulation was applied in increments of 50 Hz until 2500 Hz,

at which point the signal frequency was slowly decreased in 50 Hz amounts until 50 Hz was reached again. The characteristics of the modulation signal for this study are summarized in Table 5.5.

Table 5.5: Signal Specifications for the Single-Frequency Acoustic Modulation Principle Baseline Tests.

Frequency Range (Hz)	**Increment/ Decrement (Hz)**	**Speaker Amplitude RMS (kPa-rms)**
50−2500 Hz	50 Hz	2.0

To provide the correct signal amplitude, prior to each test, the acoustic speaker was set to output a 2450 Hz pure sinusoidal tone at approximately 2.0 kPa-rms, measured from within the oxidizer supply. This was done to provide a level of acoustic modulation similar to the band-limited white noise principle baseline tests (see Section 5.2.1). The signal provided by the driver was then held at a constant amplitude across the entire frequency sweep range.

Table 5.6: Flow Conditions and Average Instability Characteristics for the Single-Frequency Acoustic Modulation Principle Baseline Tests.

Test #	ϕ	$P'1_{\text{Bsl.}}/P_c, \%$	$P'2_{\text{Bsl.}}/P_c, \%$	$P'3_{\text{Bsl.}}/P_c, \%$	$P'4_{\text{Bsl.}}/P_c, \%$	Average f, Hz
08-01-01	1.00	0.10	0.76	0.97	0.01	2431
08-01-02	0.98	0.16	0.43	0.78	0.01	2434
08-01-03	0.99	0.15	0.60	1.85	0.01	2449
08-01-04	**0.99**	**0.15**	**1.26**	**1.18**	**0.01**	**2461**
08-01-05	**0.99**	**0.15**	**5.67**	**1.38**	**0.01**	**2456**

Note: The bolded cases will be discussed in greater detail.

Five tests were performed for this study, where the provided propellant flow rates yielded a constant equivalence ratio $\phi_{\text{avg}} = 0.99 \pm 0.006$ (at a 95% confidence interval). The experiment flow conditions and average baseline amplitudes of the 2430 Hz instability for these tests are presented in Table 5.6. As the baseline instability amplitudes measured across the transducers were the largest for Tests 08-01-04 and 08-01-05 (up to $p'/p_c \approx 5.5\%$), these were chosen to be discussed in greater detail.

Figure 5.9 shows the baseline normalized instability amplitude response from Test 08-01-04 for the four transducers within the SEMRC. For these plots, the instability amplitudes measured from $P'1-P'4$ were normalized based on the average baseline instability amplitude measured at the respective transducer location for each test, where the "dashed" and "solid" lines represent the ascending and descending signal sweeps, respectively. During both signal frequency sweeps, there generally exists a suppression of the 2430 Hz oscillation from the first applied signal $f = 50$ Hz to approximately 1300 Hz, with two frequency ranges yielding a 70+% average instability reduction across the four transducers. In the ascending direction, this first suppression region is from 150−300 Hz, with a maximum average reduction of 99% occurring at 200 Hz. The second suppression range occurs at 550−1100 Hz, where the maximum average reduction of 96% is located at 650 Hz. During the descending signal application, the suppression region characteristics match very similarly to those found during the ascending sweep. The first suppression region for the descending signal sweep is slightly expanded to 150−350 Hz, with a 99% maximum reduction again

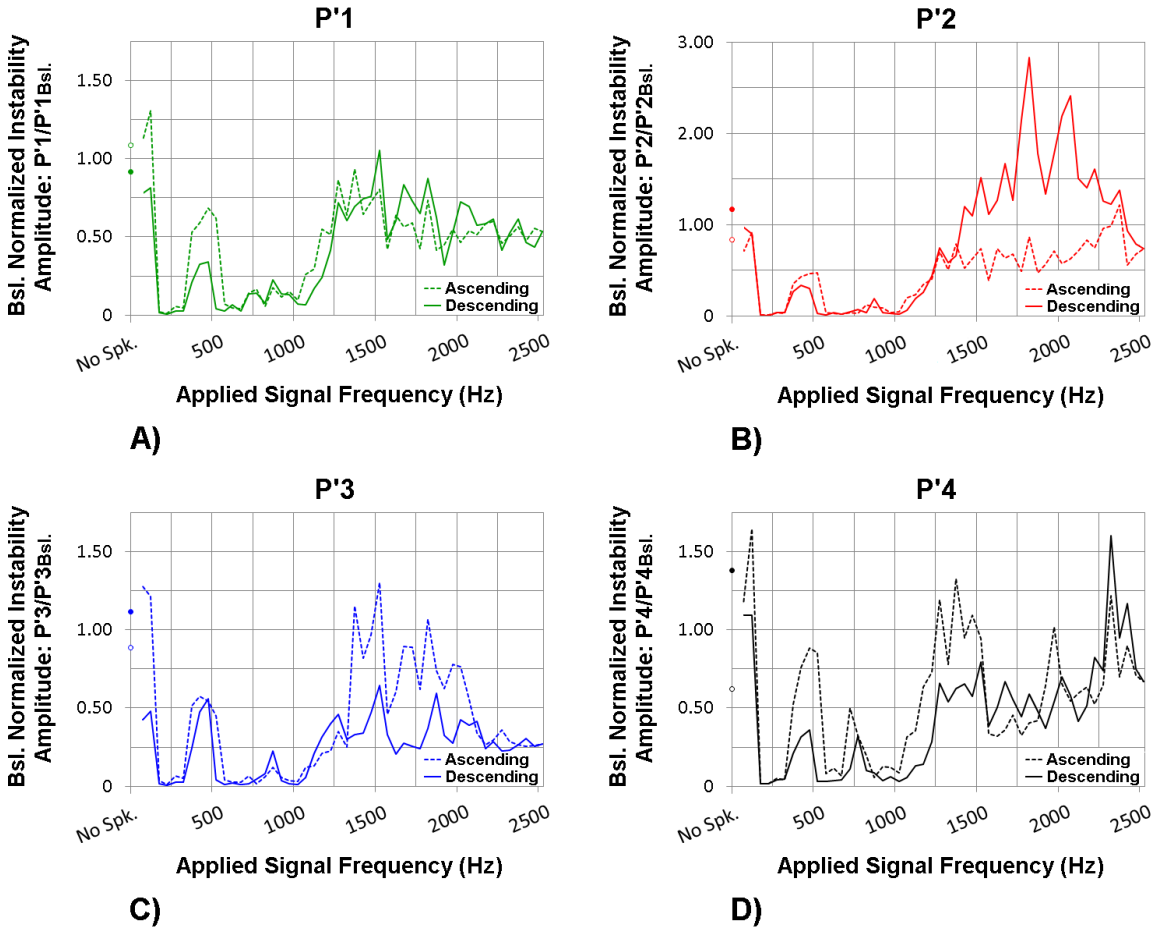

Figure 5.9: Baseline Normalized Instability Amplitude Response from Test 08-01-04 for A) $P'1$, B) $P'2$, C) $P'3$ and D) $P'4$.

Note: Maximum Normalized Instability Amplitude Response can be seen in Section B.2.2.

at 200 Hz. The frequency range of the second suppression region is also expanded to 500−1150 Hz, having a maximum reduction of 98% at 550 Hz.

Figure 5.10 shows the baseline normalized instability amplitude response from Test 08-01-05. As with Test 08-01-04, there exists a suppression of the 2430 Hz instability from approximately 50−1300 Hz, again with two frequency ranges providing a 70+% average instability reduction. The first frequency range causing a suppression is from 200−400 Hz in the ascending signal application direction and

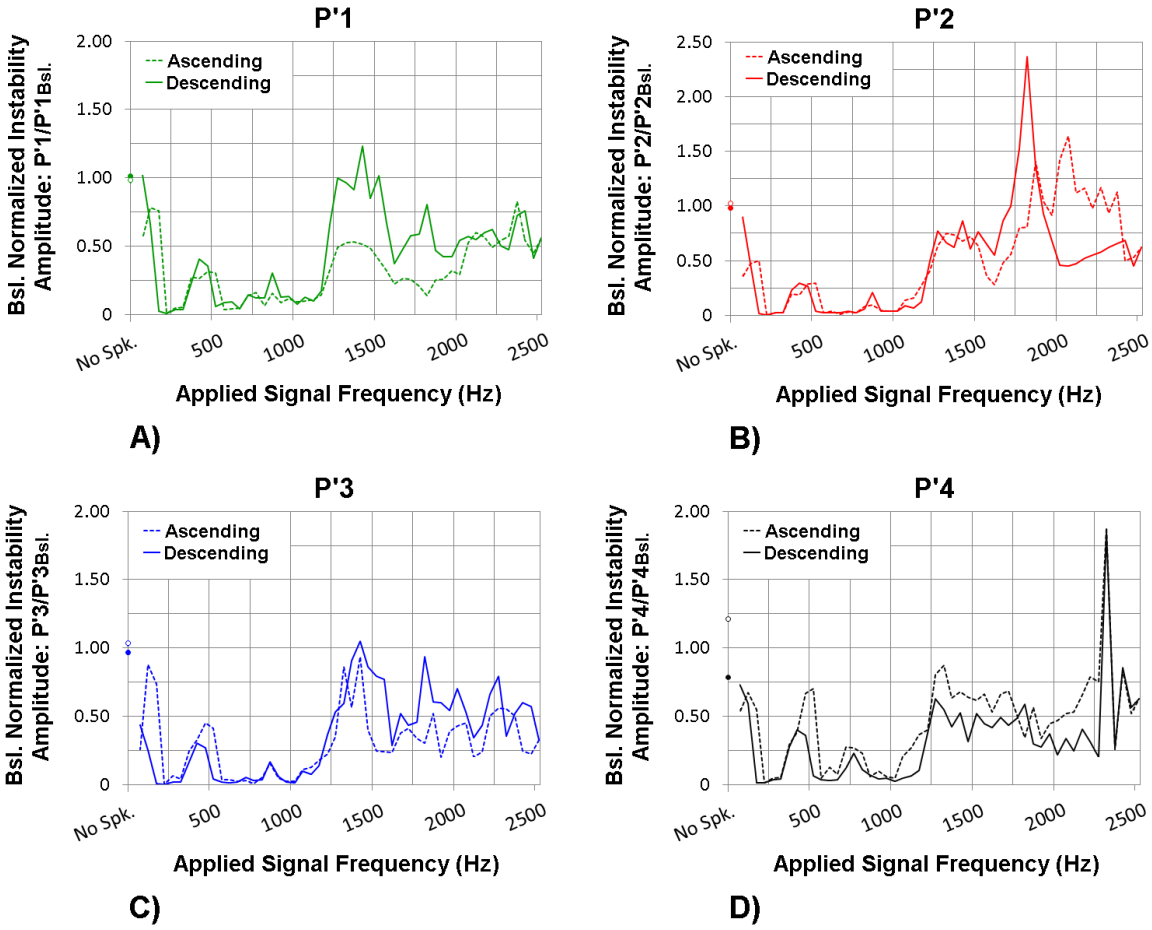

Figure 5.10: Baseline Normalized Instability Amplitude Response from Test 08-01-05 for A) $P'1$, B) $P'2$, C) $P'3$ and D) $P'4$.

Note: Maximum Normalized Instability Amplitude Response can be seen in Section B.2.4.

from 150−350 Hz in the descending direction. The maximum suppression modulation signal in this frequency range was 200 Hz, causing a 99% average instability reduction for both sweep directions. The second suppression range was 550−1150 Hz in the ascending direction, which slightly expanded to 500−1150 Hz during the descending signal sweep. Maximum suppressions of 96% and 97% were achieved at 550 Hz and 650 Hz for the ascending and descending sweeps, respectively. The maximum suppression characteristics from these tests are summarized in Table 5.7.

Table 5.7: Maximum Instability Suppression Characteristics for the Selected Single-Frequency Acoustic Modulation Principle Baseline Tests.

First Suppression Regime - Ascending Signal Direction ($f \approx 150-400$ Hz)						
		% Reduction (Based on Baseline Averages)				
Test #	Frequency Applied for Maximum Suppression	P'1, %	P'2, %	P'3, %	P'4, %	Avg., %
08-01-04	200 Hz	99.0	99.3	98.8	98.6	98.9
08-01-05	〃	99.4	99.6	99.6	98.9	99.4
First Suppression Regime - Descending Signal Direction ($f = 150-350$ Hz)						
		% Reduction (Based on Baseline Averages)				
Test #	Frequency Applied for Maximum Suppression	P'1, %	P'2, %	P'3, %	P'4, %	Avg., %
08-01-04	200 Hz	99.4	99.4	99.4	98.4	99.2
08-01-05	〃	99.4	99.5	99.7	98.7	99.3
Second Suppression Regime - Ascending Signal Direction ($f \approx 550-1150$ Hz)						
		% Reduction (Based on Baseline Averages)				
Test #	Frequency Applied for Maximum Suppression	P'1, %	P'2, %	P'3, %	P'4, %	Avg., %
08-01-04	650 Hz	96.0	97.7	97.6	93.7	96.3
08-01-05	550 Hz	96.4	97.5	96.4	95.4	96.4
Second Suppression Regime - Descending Signal Direction ($f = 500-1150$ Hz)						
		% Reduction (Based on Baseline Averages)				
Test #	Frequency Applied for Maximum Suppression	P'1, %	P'2, %	P'3, %	P'4, %	Avg., %
08-01-04	550 Hz	97.3	98.5	99.1	96.7	97.9
08-01-05	650 Hz	95.9	97.7	98.0	96.6	97.0

Waterfall plots summarizing the instability response from the pressure transducers measuring the highest amplitudes in the SEMRC (i.e., $P'2$ and $P'3$) are shown in Figure 5.11. In these waterfall plots, the various suppression regions described previously can be seen in greater detail. Within the first suppression range

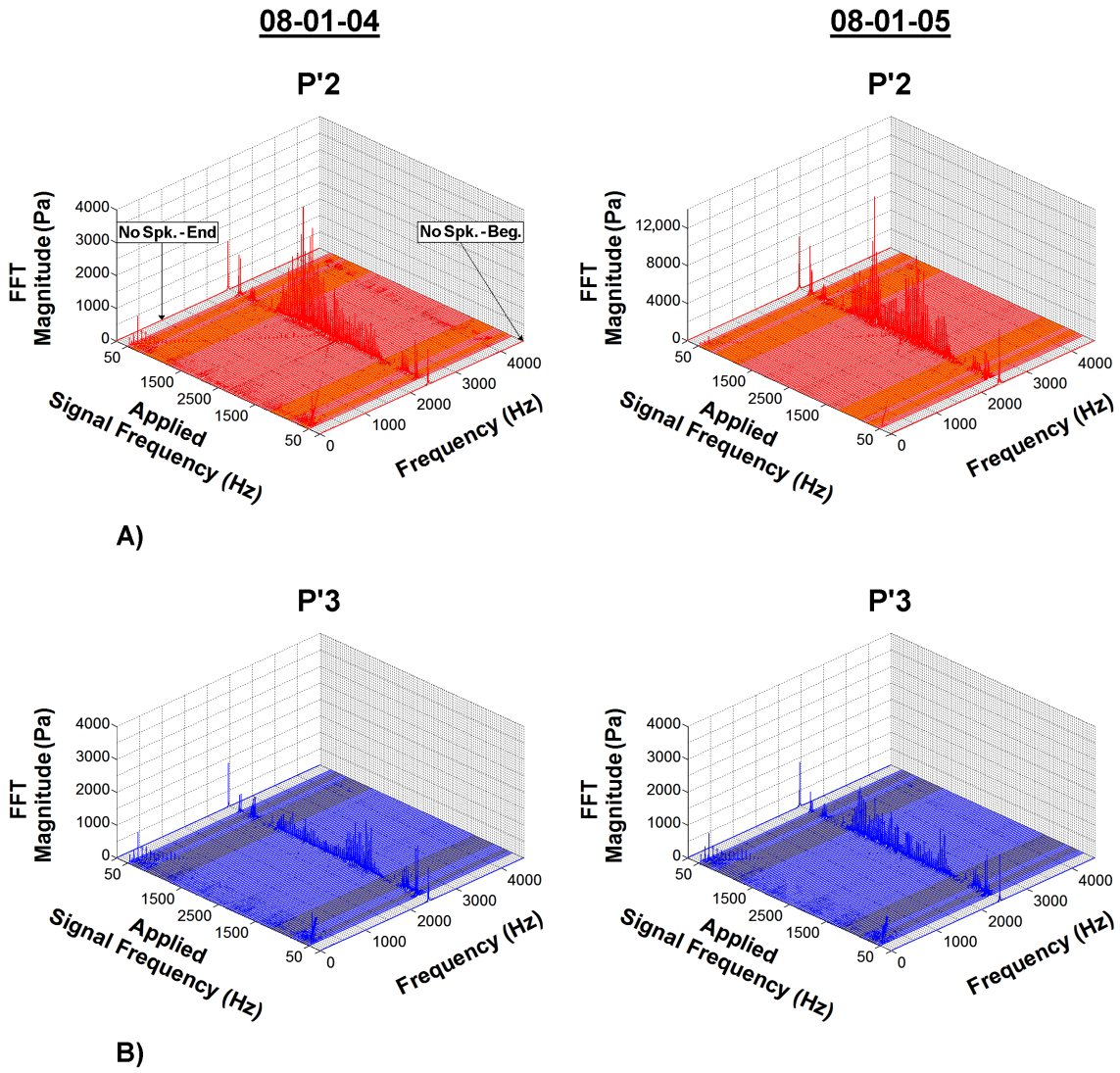

Figure 5.11: A) $P'2$ and B) $P'3$ Waterfall Plots for Tests 08-01-04 and 08-01-05.

Note: Enlarged Waterfall Plots can be seen in Section B.2.1 for Test 08-01-04 and Section B.2.3 for Test 08-01-05.

for these tests, some of the acoustic tones applied by the speaker, particularly those $\leq$ 550 Hz, are actually detected by both transducers. The largest of these signals is 150 Hz, which is at a level lower than the baseline instability averages for $P'2$ and $P'3$; this phenomena differs from the band-limited white noise principle baseline tests, as the varying bands of white noise were not detected by the transducers in any

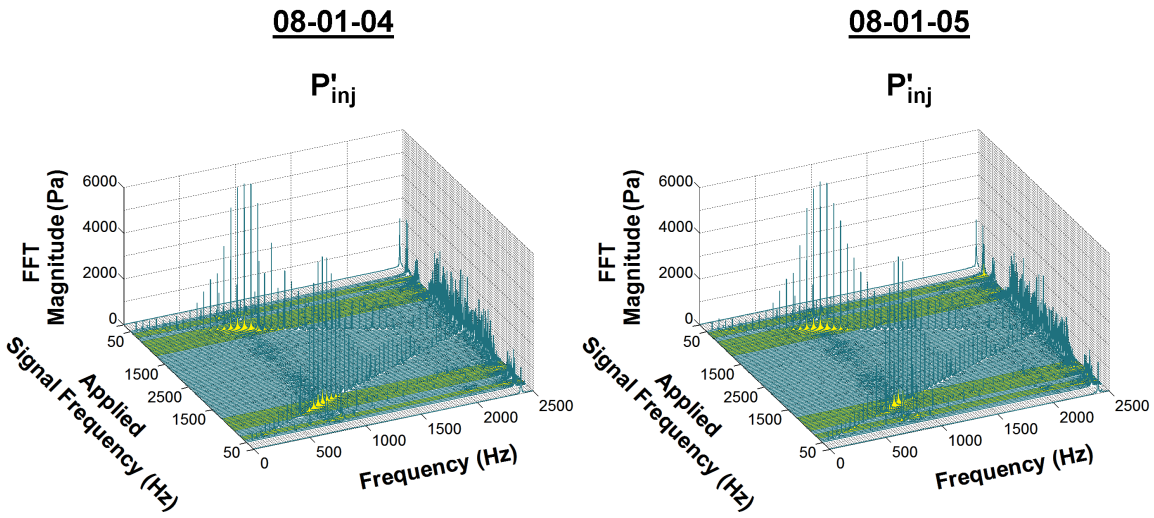

Figure 5.12: P'_{inj} Waterfall Plots for Tests 08-01-04 and 08-01-05.

Note: Enlarged Waterfall Plots can be seen in Section B.2.1 for Test 08-01-04 and Section B.2.3 for Test 08-01-05.

appreciable amount. This could be a contributing factor to the suppression of the instability within this lower frequency range.

The instability response from within the oxidizer supply line is summarized by P'_{inj} waterfall plots for Tests 08-01-04 and 08-01-05 in Figure 5.12. In these plots, both the applied modulation signal and spontaneous instability are again detected in the oxidizer supply, just as with the band-limited white noise tests. The instability amplitude follows the same suppression trend as the transducers inside the combustor, with two distinct suppression regions present for each the ascending and descending sweeps. This is to be expected, as coupling between the combustor and inlet during the excitation of spontaneous instabilities is a well documented phenomenon [18]. For the signal applied by the speaker, the amplitudes of the single frequency tones from approximately $500-1100$ Hz (with the maximum achieved at 850 Hz) match and exceed the baseline instability amplitude measured from P'_{inj}. This range of amplified

signals matches very similarly to both the second suppression band for these tests, as well as the band-limited white noise principle baseline tests, where a maximum suppression was consistently reached at 500−1000 Hz/600−1100 Hz.

From these tests, it is evident that applying single-frequency acoustic modulation within the oxidizer supply is another effective way to suppress a high-frequency instability, yielding similar results to the application of band-limited white noise.

5.3 Experiment Testing: Phase Two

5.3.1 Band-Limited White Noise: Signal Amplitude Study

As applying band-limited white noise has shown to be effective at suppressing a high-frequency instability (see Section 5.2.1), a signal amplitude sensitivity study was performed to determine the speaker amplitude suppression threshold. For this set of tests, the acoustic driver provided white noise in frequency bands of 500 Hz from 0−500 Hz to 2000−2500 Hz, in increments of 100 Hz. Once the 2000−2500 Hz band was reached, the 500 Hz signal band was slowly brought down in movements of 100 Hz until 0−500 Hz. In this study, the amplitude was held constant during each test and slowly increased between tests. Characteristics of this applied band-limited white noise signal are summarized in Table 5.8.

Table 5.8: Signal Specifications for the Band-Limited White Noise Signal Amplitude Study.

Frequency Range (Hz)	**Lowest Band**	**Highest Band**	**Increment/ Decrement (Hz)**	**Signal Amplitude Range (RMS %)**
0−2500 Hz	0−500 Hz	2000−2500 Hz	100 Hz	13−62

Similar to the principle baseline testing, the acoustic driver was turned on at a constant amplitude prior to each test. During each purely acoustic pre-test, the speaker was set to output 0−2500 Hz band-limited white noise, without combustion occurring within the SEMRC. The amplitude was then fixed to one of the seven investigated levels. The speaker amplitude is expressed as an RMS %, which is the ratio of the RMS pressure from the pure acoustic signal to the RMS pressure of the spontaneously excited combustion instability (with no acoustic excitation), both measured by P'_{inj}.

Three tests were performed at each of the seven signal amplitude levels, which resulted in a combined twenty one tests. The propellant flow rates supplied in the study led to a constant equivalence ratio $\phi_{\text{avg}} = 0.99 \pm 0.006$ (at a 95% confidence interval). The flow conditions from the complete test set are presented in Table 5.9, of which the five bolded will be discussed further.

Table 5.9: Flow Conditions for the Band-Limited White Noise Signal Amplitude Study.

Test #	ϕ_{avg}	Signal Amplitude (RMS %)	Test #	ϕ_{avg}	Signal Amplitude (RMS %)
10-02-13%-01	1.01		10-02-48%-01	0.98	
10-02-13%-02	**0.97**	13	10-02-48%-02	0.99	48
10-02-13%-03	0.98		10-02-48%-03	0.98	
10-02-20%-01	0.98		10-02-57%-01	0.99	
10-02-20%-02	0.98	20	10-02-57%-02	1.00	57
10-02-20%-03	0.99		**10-02-57%-03**	**1.00**	
10-02-30%-01	0.99		**10-02-62%-01**	**0.98**	
10-02-30%-02	1.02	30	10-02-62%-02	0.98	62
10-02-30%-03	**0.98**		10-02-62%-03	1.01	
10-02-40%-01	**0.99**				
10-02-40%-02	0.99	40			
10-02-40%-03	0.99				

Note: The bolded tests will be discussed in greater detail.

As can be seen in Table 5.10, $P'3$ was the pressure transducer that measured the largest instability amplitude for these tests. For this reason, it was selected to be shown in greater detail as it is representative of the instability response within the combustor.

Table 5.10: Average Instability Characteristics for the Selected Band-Limited White Noise Signal Amplitude Tests.

Test #	$P'1_{\text{Bsl.}}/P_c, \%$	$P'2_{\text{Bsl.}}/P_c, \%$	$P'3_{\text{Bsl.}}/P_c, \%$	$P'4_{\text{Bsl.}}/P_c, \%$	Avg. f , Hz
10-02-13%-02	0.77	0.15	2.22	0.38	2405
10-02-30%-03	0.13	0.13	3.61	0.21	2443
10-02-40%-01	0.10	0.12	1.97	0.15	2443
10-02-57%-03	0.29	0.10	0.52	0.10	2427
10-02-62%-01	0.61	0.60	1.58	0.49	2430

Waterfall plots from $P'3$ are shown in Figure 5.13. As with previous suppression tests, each test began with the 2430 Hz oscillation spontaneously excited without any acoustic signal applied from the speaker. Once this was achieved, the speaker was set to output the lowest frequency band signal, then gradually swept to the highest frequency band and then back down. It was at this point the acoustic driver was shut off, with the instability amplitude again measured, marking the end of the test. When comparing the spontaneous instability baseline at the beginning of a test to the end for the entire band-limited white noise investigation, generally there exists an increase in spontaneous instability amplitude. This phenomenon can be attributed to gradual heating of the SEMRC during testing.

From these waterfall plots, it is apparent that no appreciable suppression of the 2430 Hz first longitudinal oscillation was present for either the 13% or 30% RMS

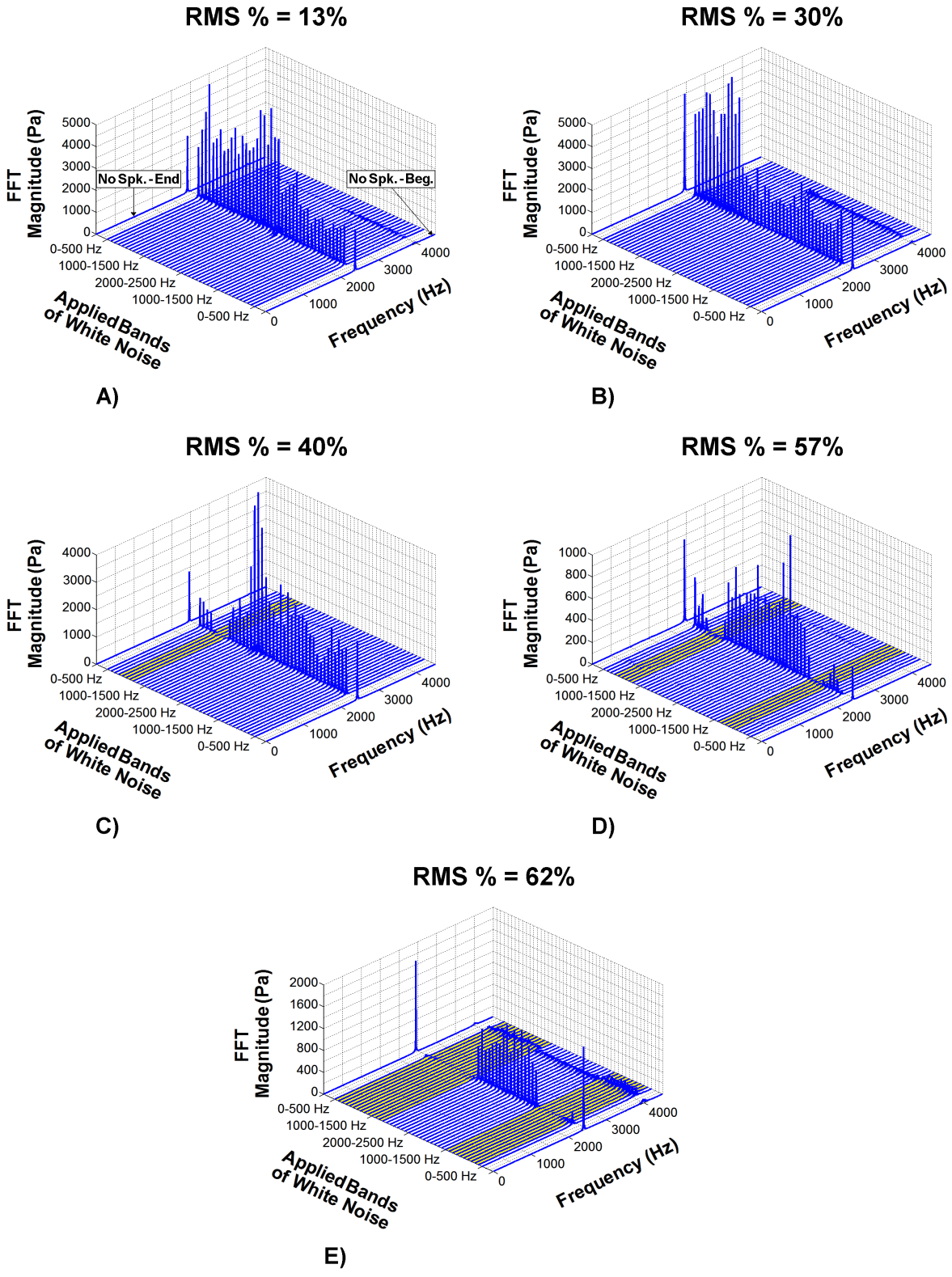

Figure 5.13: $P'3$ Waterfall Plots for the Band-Limited White Noise Signal Amplitude Study: A) 13%, B) 30%, C) 40%, D) 57% and E) 62%.

Note: Enlarged Waterfall Plots can be seen in Section B.3.1.

white noise tests (Figure 5.13.A and 5.13.B). For the 40% RMS test (Figure 5.13.C), however, there was a partial suppression of the instability for the ascending signal sweep and a full suppression during the descending signal application, both centered around 500−1000 Hz/600−1100 Hz. As the suppression effectiveness is varied for the two signal sweep directions, it is apparent that 40% RMS signal amplitude is at a threshold for suppression when applying band-limited white noise in this manner.

The 57% RMS test (Figure 5.13.D) contains results matching the band-limited white noise principle baseline tests, where significant suppression regions exist in both signal sweep directions. As such, the suppression bands for the two signal application directions were centered around the 500−1000 Hz/600−1100 Hz frequency bands.

The final test, 62% RMS signal amplitude (Figure 5.13.E), was at the maximum level for this study. During this test, there exists significantly expanded suppression frequency ranges for both the ascending and descending signal sweeps. Once the first band of white noise was applied, the instability appeared to be immediately damped, until the 1100−1600 Hz band was reached, at which point the instability spontaneously reached levels similar to the baseline, until the stability transition region of 1300−1800 Hz was again reached during the descending band-limited white noise sweep.

To provide insight into the acoustic behavior within the oxidizer supply, corresponding waterfall plots from P'_{inj} are shown in Figure 5.14. In these plots, both the supplied band-limited white noise signal and spontaneous instability measured from P'_{inj} can be seen. As expected, the applied signal portion of the waterfall plots

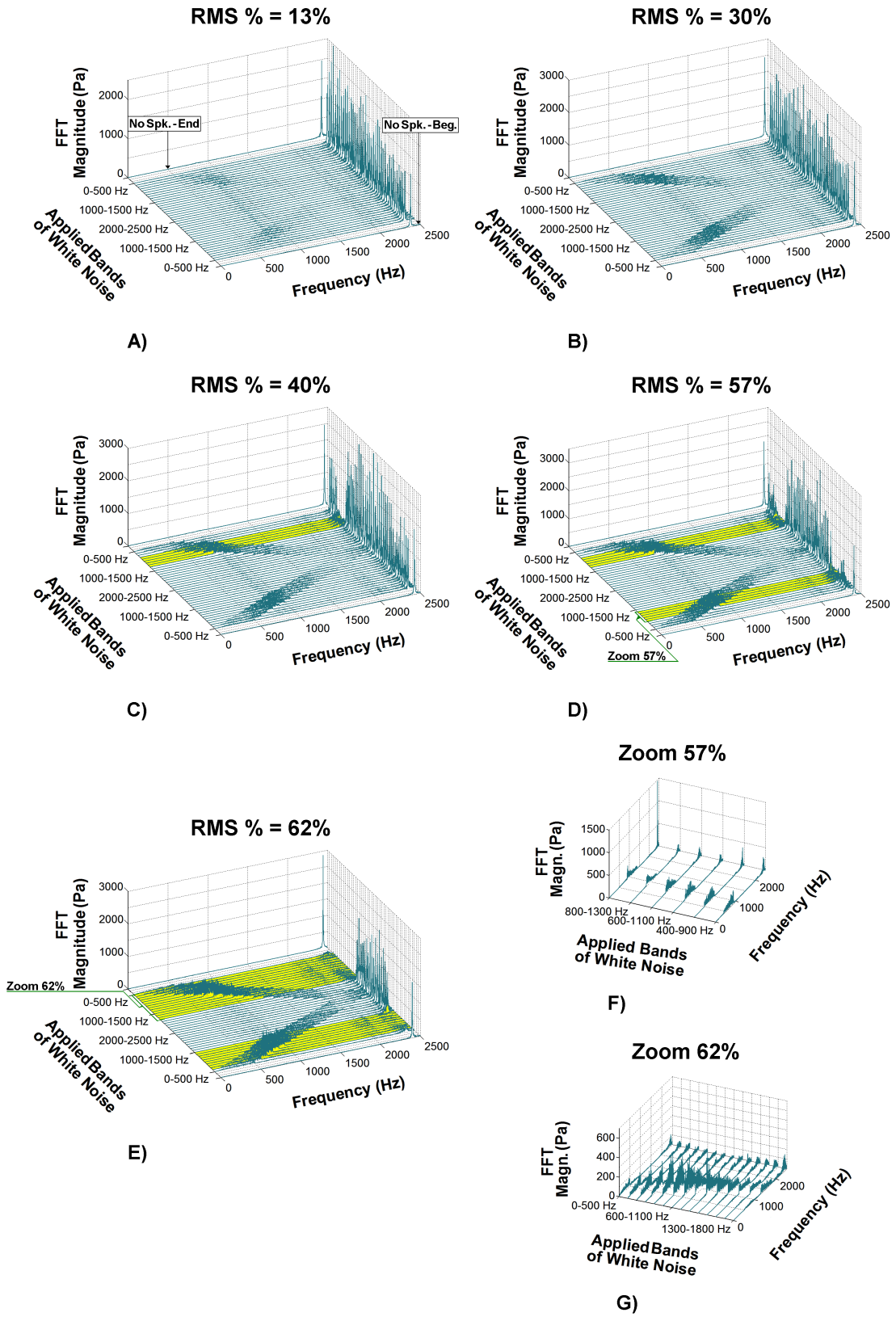

Figure 5.14: P'_{inj} Waterfall Plots for the Band-Limited White Noise Signal Amplitude Study: A) 13%, B) 30%, C) 40%, D) 57%, E) 62%, F) Zoom 57% and G) Zoom 62%.

Note: Enlarged Waterfall Plots can be seen in Section B.3.2.

shows there are the specified frequency bands being applied at constant amplitudes within the oxidizer supply line, which uniformly increase between tests. Although the modulation signal is amplified across the tests, the applied bands of white noise always appear at levels significantly less than the baseline 2430 Hz first longitudinal oscillation measured from P'_{inj}. Also, the response of the instability measured from P'_{inj} followed the same behavior as that within the combustor, with the suppression regions aligning with those from $P'1-P'4$.

Two zoomed views of the suppression regions from the 57% and 62% RMS tests can be seen in Figure 5.14.F and 5.14.G, respectively. From $400-900$ Hz to $800-1300$ Hz during the 57% RMS test, the band-limited white noise signal appears to be naturally amplified with an approximate $850-950$ Hz peak band at levels comparable to the instability measured at P'_{inj}. For the 62% RMS test, similar behavior can be seen from $0-500$ Hz to $1200-1700$ Hz , where a natural amplification of the frequency bands containing 900 Hz occurs. Also, for this suppression region, the band-limited white noise signal is on the order or higher than the instability measured from P'_{inj}. Thus, it is possible that for lower speaker amplitude tests (i.e., $40\%-57\%$) where a suppression centered around $500-1000$ Hz/$600-1100$ Hz occurs, the acoustic modulation signal is increased past a certain threshold naturally by the oxidizer supply line geometry, leading to a suppression of the instability within this frequency range. For higher speaker amplitude tests, such as the 62% RMS test, lower bands of white noise generated by the speaker are inherently above the suppression threshold, leading to an expansion of the suppression regime.

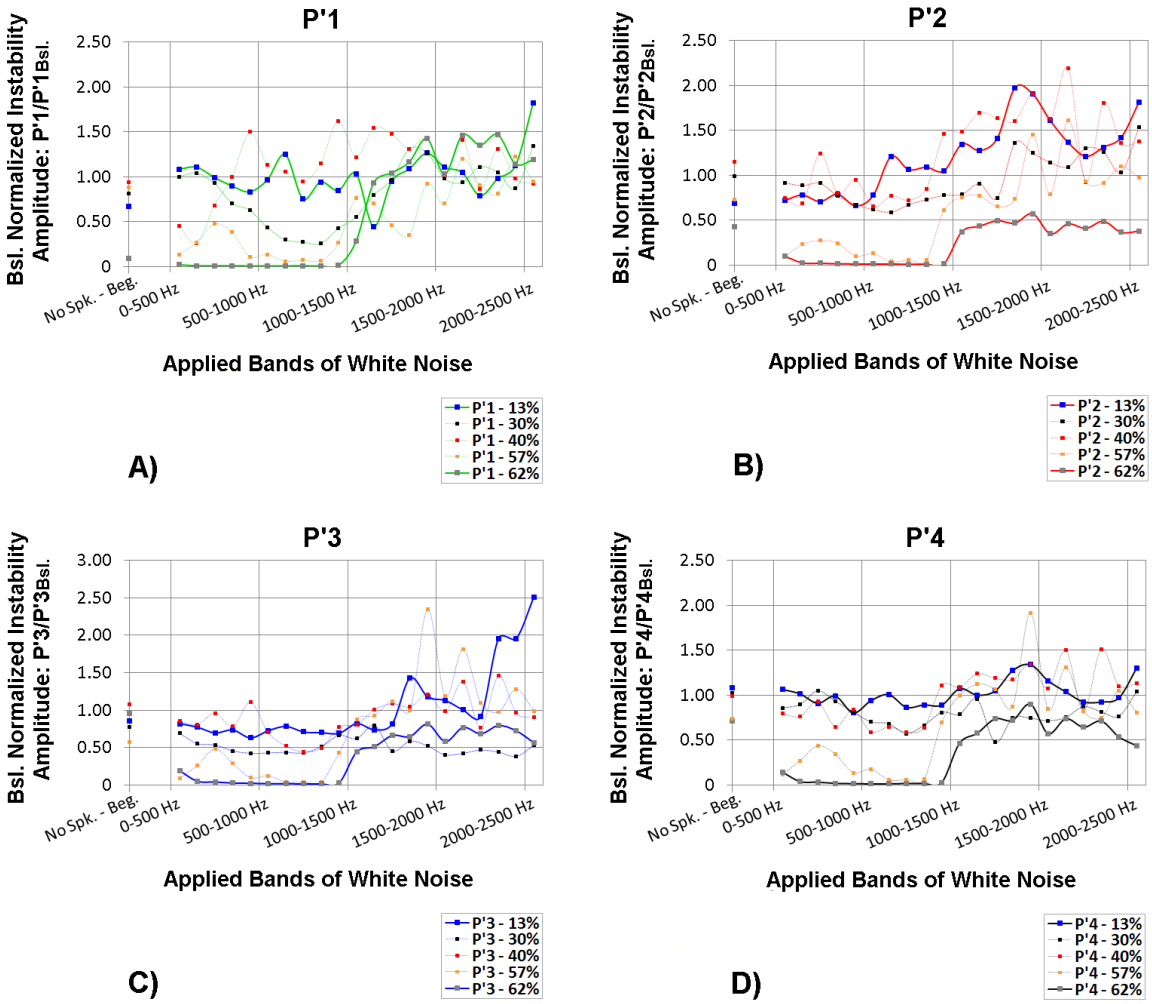

Figure 5.15: Baseline Normalized Instability Amplitude Response in the Ascending Band-Limited White Noise Direction for A) $P'1$, B) $P'2$, C) $P'3$ and D) $P'4$.

Note: Maximum Normalized Instability Amplitude Response can be seen in Section B.3.3.

To summarize the amplitude response of the four pressure transducers located within the model combustor, baseline normalized instability amplitude plots for the ascending and descending signal sweeps are presented in Figures B.15 and B.16, respectively. For each plot, the instability amplitudes were normalized in the same manner as the single-frequency acoustic modulation tests (see Section 5.2.2), as the baseline instability averages can vary from one test to another.

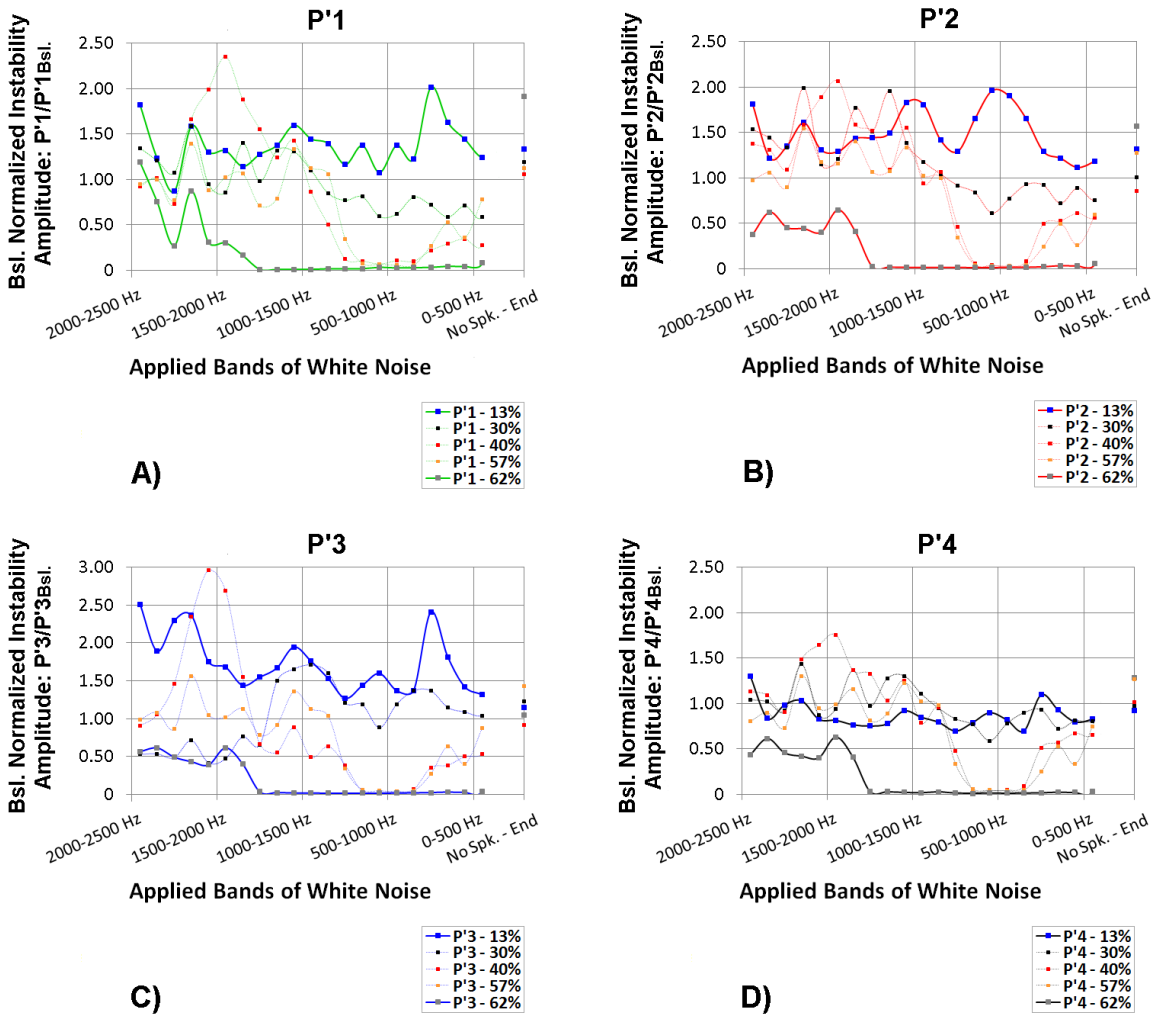

Figure 5.16: Baseline Normalized Instability Amplitude Response in the Descending Band-Limited White Noise Direction for A) $P'1$, B) $P'2$, C) $P'3$ and D) $P'4$.

Note: Maximum Normalized Instability Amplitude Response can be seen in Section B.3.3.

When considering the ascending sweep direction, there was no appreciable suppression of the instability detected by any of the four transducers for the lowest amplitude signal (13% RMS), as all of the transducers' levels fluctuate around their baselines for the duration of the signal sweep. As such, this is the first bounding case for the study. It is not until the 57% RMS test where a 70+% average instability reduction of the first longitudinal instability was achieved from 400−900 Hz to

800−1300 Hz, with a maximum suppression at 600−1100 Hz. This maximum suppression yielded a 95% average instability amplitude reduction across the four pressure transducers, based on their baseline averages. For the 62% RMS test, a suppression of the oscillation was evident across a larger applied signal range from 100−600 Hz to 900−1400 Hz, with a 99% average instability amplitude reduction achieved at 700−1200 Hz. As the suppression range and reduction level was at a maximum for the 62% RMS test, this is the second bounding case of the study.

The instability response captured in the descending signal direction was very similar to the ascending sweep, with the addition of a suppression region in the 40% RMS test. During this test, there was a 70+% average reduction of the instability amplitude from 300−800 Hz to 800−1300 Hz, with 96% average dampening achieved at the maximum suppression band of 600−1100 Hz. For the 57% RMS test, the suppression range was from 400−900 Hz to 700−1200 Hz, where the maximum suppression of 96% occurred at 500−1000 Hz. As the frequency bands for instability mitigation in these two tests are nearly identical in the descending direction, applying these bands of white noise within this signal amplitude range should consistently produce this suppression phenomena, as also evidenced during the principle baseline testing. In the 62% RMS test, the suppression band was expanded further from that in the ascending direction to 0−500 Hz to 1300−1800 Hz, with a 99% average instability reduction occurring at the maximum suppression band of 700−1200 Hz.

Table 5.11 is a summary of the maximum instability suppression characteristics for this study. This table presents a complete account of the reduction percentages for all transducers based on their per-test baseline averages. Generally, the maximum

Table 5.11: Maximum Instability Suppression Characteristics for the Band-Limited White Noise Signal Amplitude Study.

Ascending Signal Direction						
		% Reduction (Based on Baseline Averages)				
Test #	Frequency Band Applied for Maximum Suppression	$P'1$, %	$P'2$, %	$P'3$, %	$P'4$, %	Avg., %
10-02-13%-02	None	N/A	N/A	N/A	N/A	N/A
10-02-30%-03	〃	〃	〃	〃	〃	〃
10-02-40%-01	〃	〃	〃	〃	〃	〃
10-02-57%-03	600−1100 Hz	94.2	96.5	96.2	94.5	95.4
10-02-62%-01	700−1200 Hz	99.2	99.3	98.8	98.6	99.0
Descending Signal Direction						
		% Reduction (Based on Baseline Averages)				
Test #	Frequency Band Applied for Maximum Suppression	$P'1$, %	$P'2$, %	$P'3$, %	$P'4$, %	Avg., %
10-02-13%-02	None	N/A	N/A	N/A	N/A	N/A
10-02-30%-03	〃	〃	〃	〃	〃	〃
10-02-40%-01	600−1100 Hz	93.3	96.3	97.6	95.8	95.8
10-02-57%-03	500−1000 Hz	94.7	97.3	96.7	96.5	96.3
10-02-62%-01	700−1200 Hz	98.5	99.0	98.8	99.1	98.8

average percent reduction increases slightly with higher signal amplitudes in both sweep directions, denoting there indeed is a signal amplitude threshold for instability suppression. Therefore, this study further expanded the instability control technique and identified certain acoustic mechanism(s) attributed to the suppression effect.

5.3.2 Single-Frequency Acoustic Modulation: Signal Amplitude Study

To further characterize strategic acoustic forcing of the incoming oxidizer flow as a means of instability control, a second signal amplitude investigation was performed by implementing single-frequency acoustic modulation. For this study, pure sinusoidal tones (with arbitrary phase) from 500−2500 Hz were applied at five RMS % amplitudes ranging from 16−82%. The RMS % for this study is defined in a similar fashion to the previous signal amplitude study, as it is the RMS ratio of the

pure acoustic signal at 2450 Hz to the spontaneous instability measured from within the oxidizer supply line (without any acoustic forcing present). In these tests, the speaker was first set to output 2500 Hz and gradually decreased in amounts of 50 Hz to 500 Hz, at which point it was slowly increased back to 2500 Hz. The signal frequency range was reduced and sweep direction reversed to prevent damage to the speaker diaphragm at high signal amplitudes. Characteristics of this acoustic modulation signal are summarized in Table 5.12.

Table 5.12: Signal Specifications for the Single-Frequency Acoustic Modulation Signal Amplitude Study.

Frequency Range (Hz)	**Increment/ Decrement (Hz)**	**Signal Amplitude Range (RMS %)**
500−2500 Hz	50 Hz	16−82

Five tests were performed in this study, which implemented the standard propellant flow rates; this led to a constant equivalence ratio $\phi_{\text{avg}} = 0.98 \pm 0.006$ (at a 95% confidence interval) for these tests. Along with these flow conditions, Table 5.13 presents the average oscillation characteristics for the tests within this signal amplitude study.

Table 5.13: Flow Conditions and Average Instability Characteristics for the Single-Frequency Acoustic Modulation Signal Amplitude Study.

Test #	ϕ_{avg}	Sign. Amp. (RMS %)	$P'1_{\text{Bsl.}}/P_c, \%$	$P'2_{\text{Bsl.}}/P_c, \%$	$P'3_{\text{Bsl.}}/P_c, \%$	$P'4_{\text{Bsl.}}/P_c, \%$	f, Hz
06-10-16%	0.98	16	0.80	0.18	0.37	0.07	2447
06-10-32%	″	32	0.78	0.16	0.38	0.06	2444
06-10-45%	″	45	0.77	0.16	0.41	0.06	2436
06-10-58%	″	58	0.72	0.23	0.35	0.06	2395
06-10-82%	0.99	82	0.26	0.39	1.24	0.05	2389

As can be seen in Table 5.13, $P'1$ measured the largest oscillation amplitude for a majority of the tests. Thus, waterfall plots illustrating its response were generated and are shown in Figure 5.17. During the 16% RMS test (Figure 5.17.A), no suppression regions were present in either frequency sweep direction. It is not until the 32% RMS test (Figure 5.17.B) that a thin suppression region appeared at 500−550 Hz for both signal application directions. Within this suppression range, the applied signal was detected by $P'1$, although at a level much smaller than the nominal instability amplitude. In the 45% RMS test (Figure 5.17.C), there were two thin suppression regions present, with one again at 500−550 Hz and another at 900 Hz, in both signal sweep directions. These two suppression regimes widened across the 58% and 82% RMS tests (Figure 5.17.D and 5.17.E), to approximately 500−650 Hz and 500−750 Hz for the first suppression region and to approximately 750−950 Hz and 850−1050 Hz for the second regime. Also, between these tests, the transition frequency where instability baseline levels were again reached (i.e., no appreciable suppression present) was expanded from approximately 1000 Hz for the 58% RMS test to 1300 Hz for the 82% RMS test. This is consistent with the trends seen in the band-limited white noise signal amplitude study, where the suppression regions were observed to broaden at higher modulation signal amplitudes.

Figure 5.18 shows the P'_{inj} waterfall plots for this test set. Generally, these plots display similar trends to the previous signal amplitude study, in that the instability response measured from within the oxidizer supply line followed the same behavior as that from within the SEMRC. As expected, the applied signals slowly grew in amplitude across the tests, with the 500−1100 Hz signals being at the largest

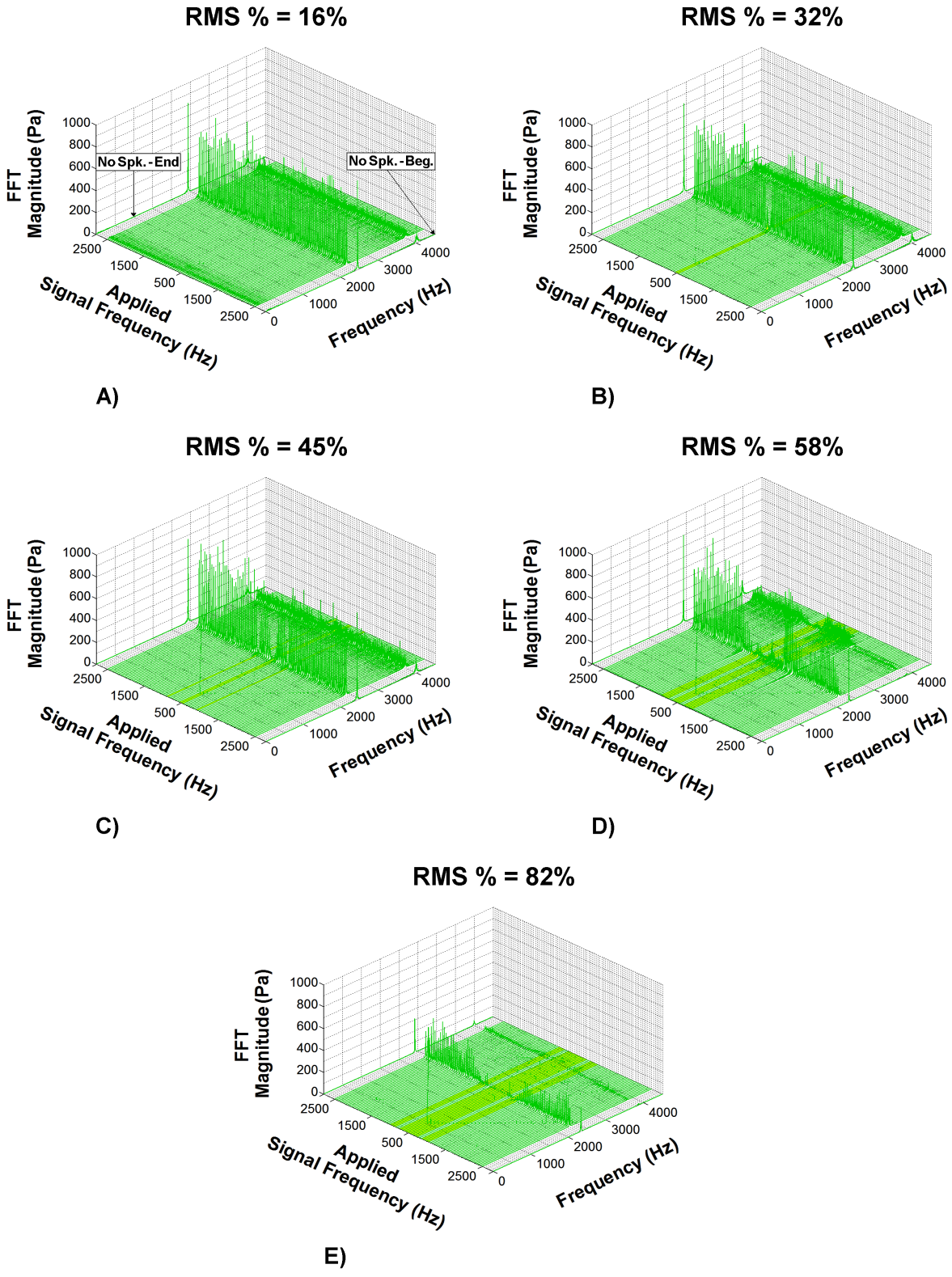

Figure 5.17: $P'1$ Waterfall Plots for the Single-Frequency Acoustic Modulation Signal Amplitude Study: A) 16%, B) 32%, C) 45%, D) 58% and E) 82%.

Note: Enlarged Waterfall Plots can be seen in Section B.4.1.

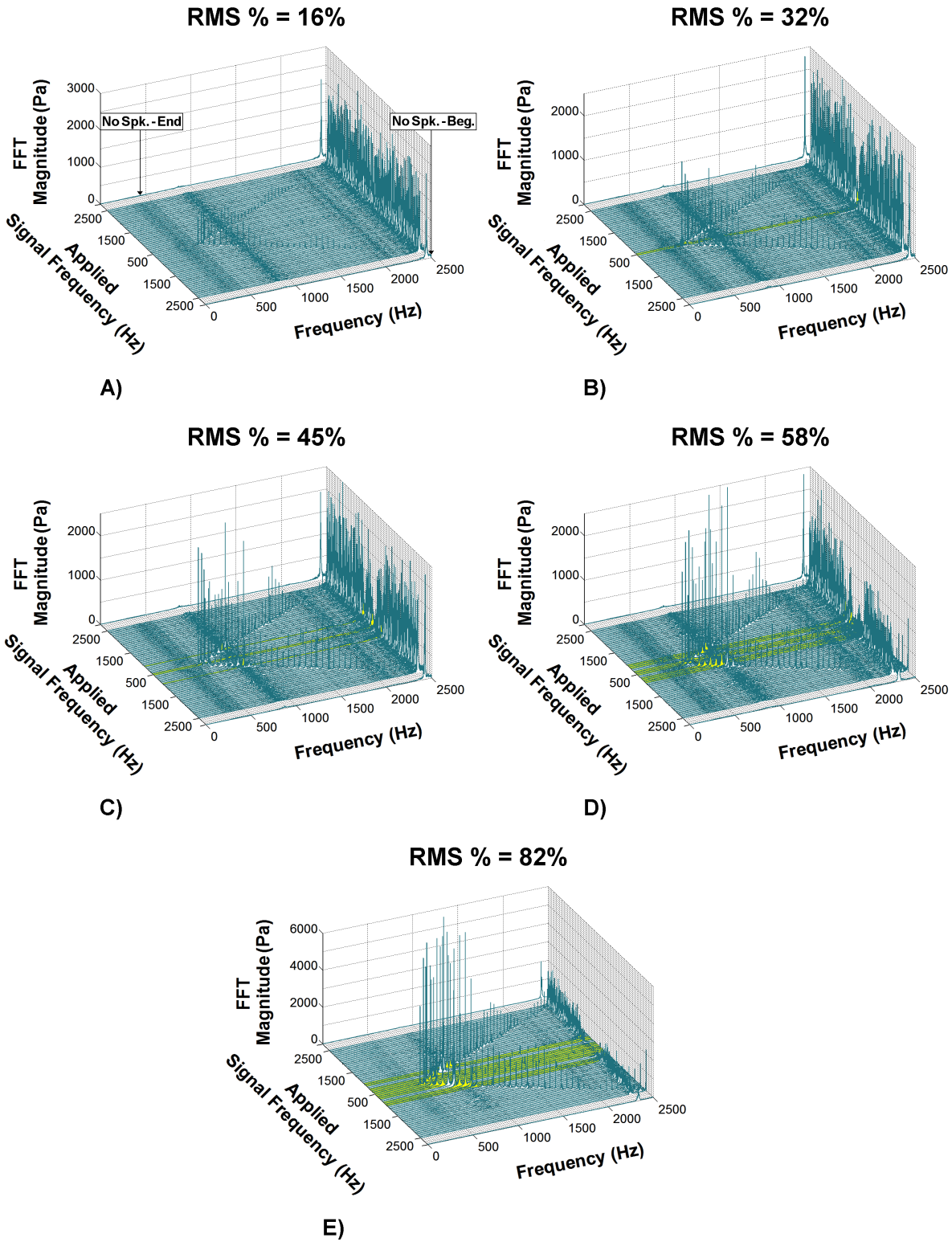

Figure 5.18: P'_{inj} Waterfall Plots for the Single-Frequency Acoustic Modulation Signal Amplitude Study: A) 16%, B) 32%, C) 45%, D) 58% and E) 82%.

Note: Enlarged Waterfall Plots can be seen in Section B.4.2.

levels. For the 58% and 82% RMS tests, the applied signal amplitudes within this frequency range exceed those of the nominal instability measured from P'_{inj}. Thus, there is a correlation between the expansion of the instability suppression regimes and the amplification of the signals within this frequency range.

To illustrate the suppression regimes in greater detail, the instability amplitude response data for the range of 500−1500 Hz were normalized based upon the transducers' maximum test value for both signal sweep directions (see Figures 5.19 and 5.20). In this study, the bounding cases are the 16% RMS test (i.e., no appreciable instability suppression present) and the 82% RMS test, where the most expansive suppression regimes occur. The other three RMS % tests show the transition of the suppression regimes between these bounding cases. In the 32% RMS test, the suppression band from 500−550 Hz is the only regime exceeding a 70% average reduction in instability amplitude, with a maximum average suppression of 94% at 500 Hz for both sweep directions. During the 45% RMS test, there were two regions exceeding this 70% threshold, with one again at 500−550 Hz, where an 89% maximum reduction at 500 Hz is present for the descending sweep and a 97% reduction at 550 Hz achieved for the ascending sweep. The second region was at 900 Hz, with 89% and 95% max reductions for the descending and ascending sweeps, respectively. In the 58% RMS test, the entire suppression range was from approximately 500−1000 Hz, with two slightly expanded regimes exceeding the 70% average instability reduction threshold. In the descending direction, the first suppression region is again from 500−550 Hz, with the largest suppression of 90% being achieved at 500 Hz. In the ascending sweep direction, however, this region is

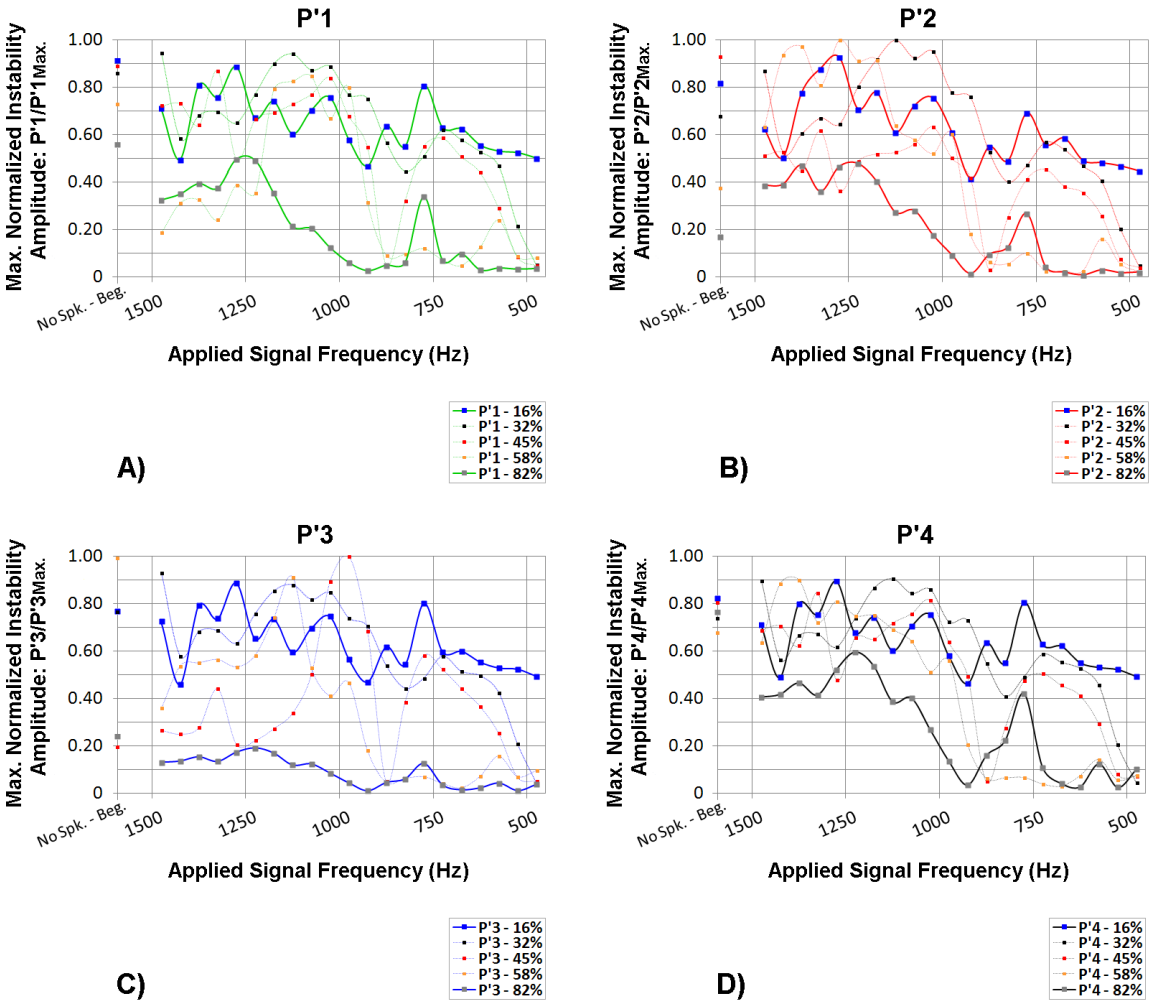

Figure 5.19: Maximum Normalized Instability Amplitude Response in the Descending Direction for A) $P'1$, B) $P'2$, C) $P'3$ and D) $P'4$.

expanded to 500−650 Hz, with a maximum instability amplitude reduction of 97% being achieved at 550 Hz. The second suppression region is from 650−900 Hz in the descending signal direction, with a 95% maximum achieved at 700 Hz, whereas in the ascending direction, this suppression regime is from 750−950 Hz, with a 95% maximum at 900 Hz. For the 82% RMS test, the entire suppression range became approximately 500−1300 Hz, with the two 70+% average suppression regions

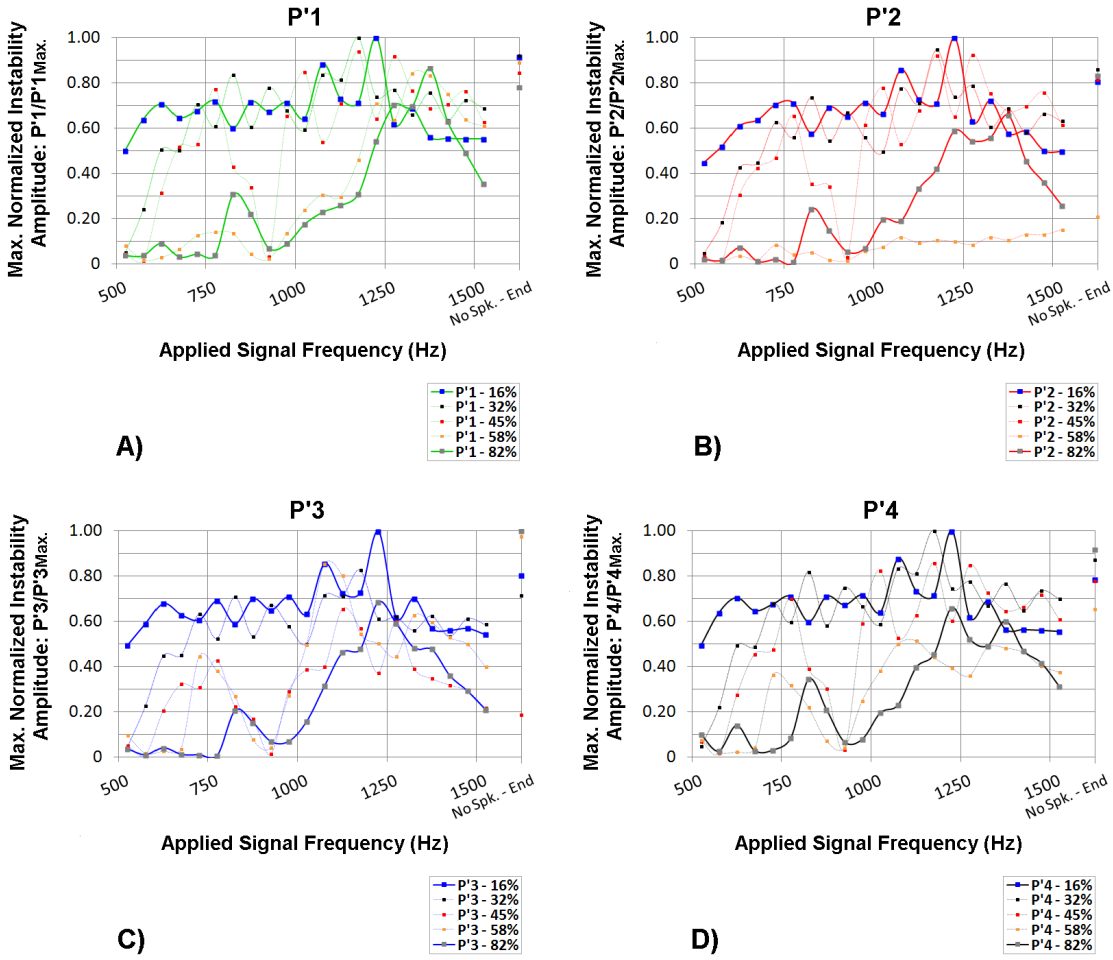

Figure 5.20: Maximum Normalized Instability Amplitude Response in the Ascending Direction for A) $P'1$, B) $P'2$, C) $P'3$ and D) $P'4$.

expanding to include all frequencies below approximately 1050 Hz, except for a 100 Hz region from 750−850 Hz. Thus, in both sweep directions, the first suppression regime is located at 500−750 Hz, with 97% maximum reductions occurring at 650 Hz. The second suppression regimes are also very similar, with one at 850−1050 Hz in the descending direction, where a 97% maximum is present at 950 Hz and another at 850−1000 Hz for the ascending signal sweep, with a 90% maximum at 900 Hz. These maximum instability reduction characteristics are summarized in Table 5.14.

Table 5.14: Maximum Instability Suppression Characteristics for the Single-Frequency Acoustic Modulation Signal Amplitude Study.

First Suppression Regime - Ascending Signal Direction						
		% Reduction (Based on Baseline Averages)				
Test #	Frequency Applied for Maximum Suppression	$P'1$, %	$P'2$, %	$P'3$, %	$P'4$, %	Avg., %
06-10-16%	None	N/A	N/A	N/A	N/A	N/A
06-10-32%	500 Hz	94.1	93.8	93.8	94.1	94.0
06-10-45%	550 Hz	97.8	98.4	93.4	97.5	96.8
06-10-58%	〃	97.6	96.0	98.3	96.6	97.1
06-10-82%	650 Hz	95.3	97.6	98.0	96.3	96.8
First Suppression Regime - Descending Signal Direction						
		% Reduction (Based on Baseline Averages)				
Test #	Frequency Applied for Maximum Suppression	$P'1$, %	$P'2$, %	$P'3$, %	$P'4$, %	Avg., %
06-10-16%	None	N/A	N/A	N/A	N/A	N/A
06-10-32%	500 Hz	94.1	93.8	93.8	94.1	94.0
06-10-45%	〃	94.5	95.5	73.0	91.0	88.5
06-10-58%	〃	89.9	92.3	90.2	88.3	90.2
06-10-82%	650 Hz	95.4	98.2	96.3	96.6	96.6
Second Suppression Regime - Ascending Signal Direction						
		% Reduction (Based on Baseline Averages)				
Test #	Frequency Applied for Maximum Suppression	$P'1$, %	$P'2$, %	$P'3$, %	$P'4$, %	Avg., %
06-10-16%	None	N/A	N/A	N/A	N/A	N/A
06-10-32%	〃	〃	〃	〃	〃	〃
06-10-45%	900 Hz	96.0	96.4	92.2	95.7	95.1
06-10-58%	〃	97.1	94.9	95.6	93.5	95.3
06-10-82%	〃	89.6	89.1	88.8	91.9	89.8
Second Suppression Regime - Descending Signal Direction						
		% Reduction (Based on Baseline Averages)				
Test #	Frequency Applied for Maximum Suppression	$P'1$, %	$P'2$, %	$P'3$, %	$P'4$, %	Avg., %
06-10-16%	None	N/A	N/A	N/A	N/A	N/A
06-10-32%	〃	〃	〃	〃	〃	〃
06-10-45%	900 Hz	94.2	96.5	73.1	93.7	89.4
06-10-58%	700 Hz	93.9	91.7	97.5	95.3	94.6
06-10-82%	950 Hz	95.8	97.1	98.3	95.7	96.7

From these tests, it is evident that applying single-frequency acoustic modulation at varying signal amplitudes produces results paralleling some of the observations from the band-limited white noise signal amplitude study. Mainly, the suppression band frequencies expanded at larger modulation signal amplitudes in both studies. However, upon comparing the suppression bands for both maximum amplitude tests, applying band-limited white noise showed to more reliably suppress the instability across the entire frequency range than single-frequency acoustic modulation. Particularly when single frequency signals between 750−850 Hz were applied at the maximum level (82% RMS), the 70% average suppression threshold was not exceeded, whereas for the band-limited white noise study, no such intermittent instability suppression was present. Although this is evident, it is recognized that implementing single-frequency acoustic modulation could be an effective means to properly tailor the band-limited white noise signal to yield the most consistent instability suppression.

5.4 Experiment Testing: Phase Three

5.4.1 Band-Limited White Noise: Pure Acoustic Testing

To isolate the acoustic response of the oxidizer supply and SEMRC to applied acoustic forcing, a series of pure acoustic tests were carried out. The first set of tests entailed sweeping varying white noise bands over the same range from the suppression tests (see Section 5.3.1). This was performed at four signal amplitude levels, ranging from 0.387−2.042 kPa-rms (for the full 0−2500 Hz pre-test signal measured from P'_{inj});

these signal amplitudes encompassed those similar to the previous signal amplitude study. Characteristics of the applied band-limited white noise signal are summarized in Table 5.15.

Table 5.15: Signal Specifications for the Band-Limited White Noise Pure Acoustic Tests.

Test #	**Lowest Band**	**Highest Band**	**Increment/ Decrement (Hz)**	**Sign. Amp. (kPa-rms)**	$T'_{\text{inj.}}$ **(K)**
11-04-01	0−500 Hz	2000−2500 Hz	100 Hz	0.387	293
11-04-02	″	″	″	0.996	″
11-04-03	″	″	″	1.280	″
11-04-04	″	″	″	2.042	292

Figure 5.21 shows P'_{inj} waterfall plots for the four signal amplitude levels. Appearing in these plots are the specified frequency bands of white noise being applied within the oxidizer supply line, at levels that uniformly increase with the modulation signal amplitude. For each signal amplitude test, there is a natural amplification evident for the bands of white noise from 400−900 Hz to 800−1300 Hz. This is most apparent in the 2.042 kPa-rms case, in which two distinct peak bands exist from approximately 500−650 Hz and 750−950 Hz. This result is consistent with the band-limited white noise signal amplitude study, where the maximum instability suppression regions centered around 500−1000 Hz/600−1100 Hz encompass these naturally amplified bands.

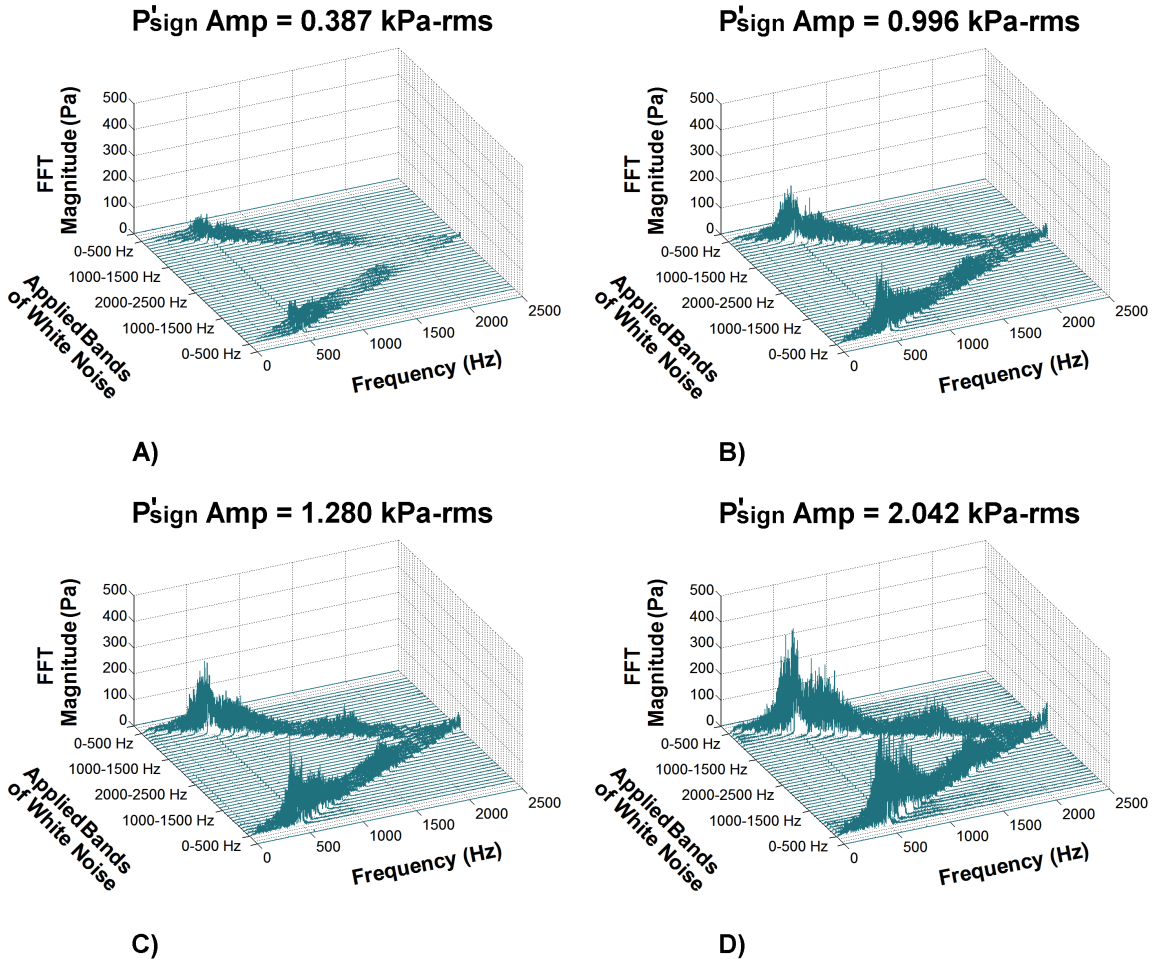

Figure 5.21: P'_{inj} Waterfall Plots for the Band-Limited White Noise Pure Acoustic Tests: A) 0.387 kPa-rms, B) 0.996 kPa-rms, C) 1.280 kPa-rms and D) 2.042 kPa-rms.

Note: Enlarged Waterfall Plots can be seen in Section B.5.4.

Shown in Figure 5.22 are the waterfall plots of $P'1$ for the four signal amplitude levels. In these plots, the acoustic response of the combustor due to the applied bands of white noise can be seen. For each of the four signal amplitude levels, it is apparent that there is no appreciable amount of band-limited white noise detected by $P'1$. This is consistent with the results from the previous band-limited white noise suppression experiments, and signifies that the oxidizer supply line is the primary area affected by the provided acoustic forcing.

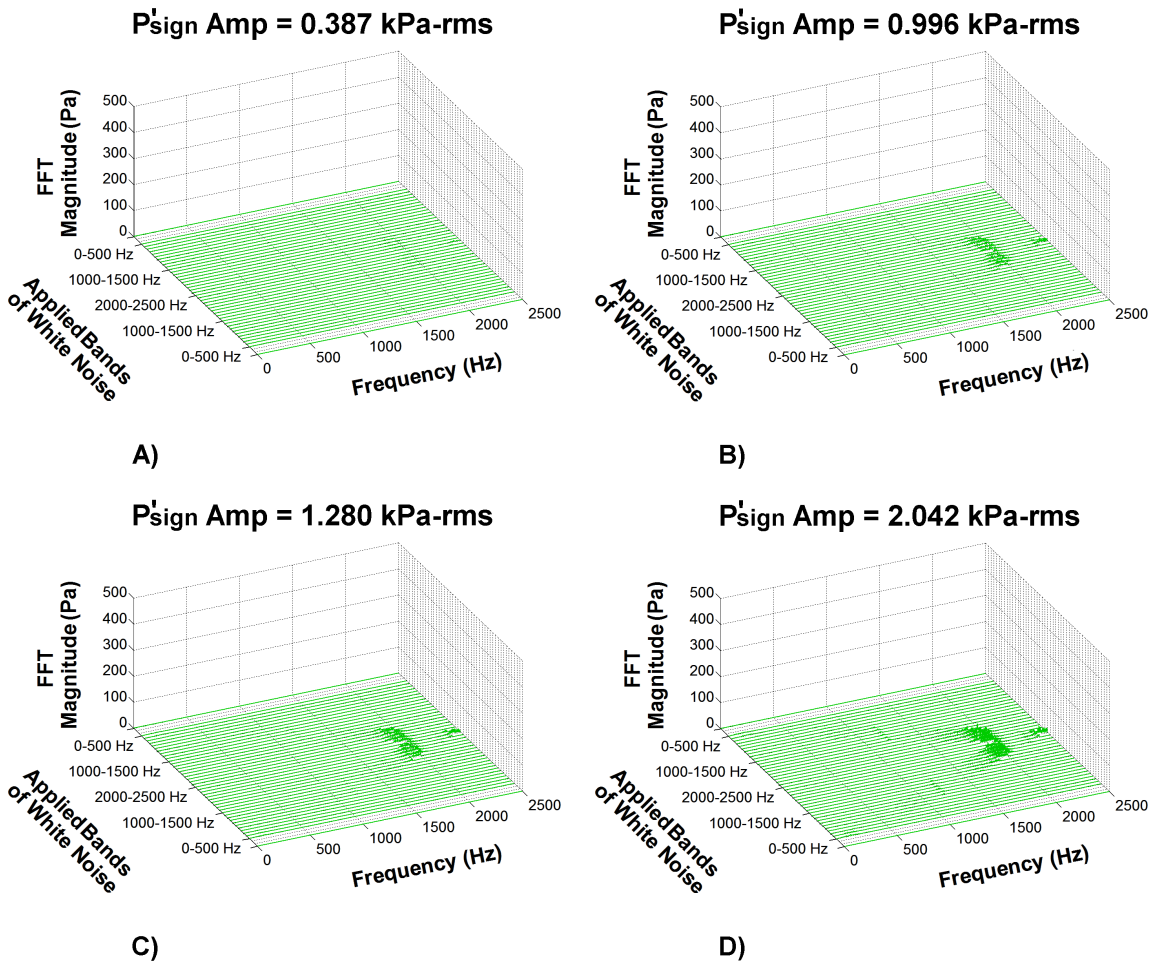

Figure 5.22: $P'1$ Waterfall Plots for the Band-Limited White Noise Pure Acoustic Tests: A) 0.387 kPa-rms, B) 0.996 kPa-rms, C) 1.280 kPa-rms and D) 2.042 kPa-rms.

Note: Enlarged Waterfall Plots of $P'1-P'3$ can be seen in Sections B.5.1–B.5.3.

5.4.2 Single-Frequency Acoustic Modulation: Pure Acoustic Testing

The second pure acoustic test entailed sweeping pure sinusoidal tones across the same range from the previous instability suppression tests (see Section 5.3.2). Similarly to these tests, the pure sinusoidal tones were again applied with arbitrary

phase. This was performed at four signal amplitude levels, ranging from 0.485−2.014 kPa-rms (for the 2450 Hz pre-test signal measured from P'_{inj}). These amplitudes levels were selected as they cover those similar to the single-frequency acoustic modulation signal amplitude study. Characteristics of this acoustic modulation signal are summarized in Table 5.16.

Table 5.16: Signal Specifications for the Single-Frequency Acoustic Modulation Pure Acoustic Tests.

Test #	**Frequency Range (Hz)**	**Increment/ Decrement (Hz)**	**Signal Amplitude (kPa-rms)**	$\boldsymbol{T'_{\text{inj.}}}$ **(K)**
11-04-06	500−2500 Hz	50 Hz	0.485	292
11-04-07	″	″	0.972	293
11-04-08	″	″	1.366	″
11-04-09	″	″	2.014	″

Waterfall plots from P'_{inj} for the four signal amplitude levels are shown in Figure 5.23. In these plots, there exists similar phenomena to the band-limited white noise pure acoustic tests, as there is a natural amplification of the signals from $f \approx 500-1000$ Hz. For the highest signal amplitude, 2.014 kPa-rms, there are two distinct peak signals from approximately 500−700 Hz and 800−900 Hz. This coincides with the results from the signal amplitude study, where two suppression regions for the maximum 82% RMS test exist from 500−750 Hz and 850−1050 Hz.

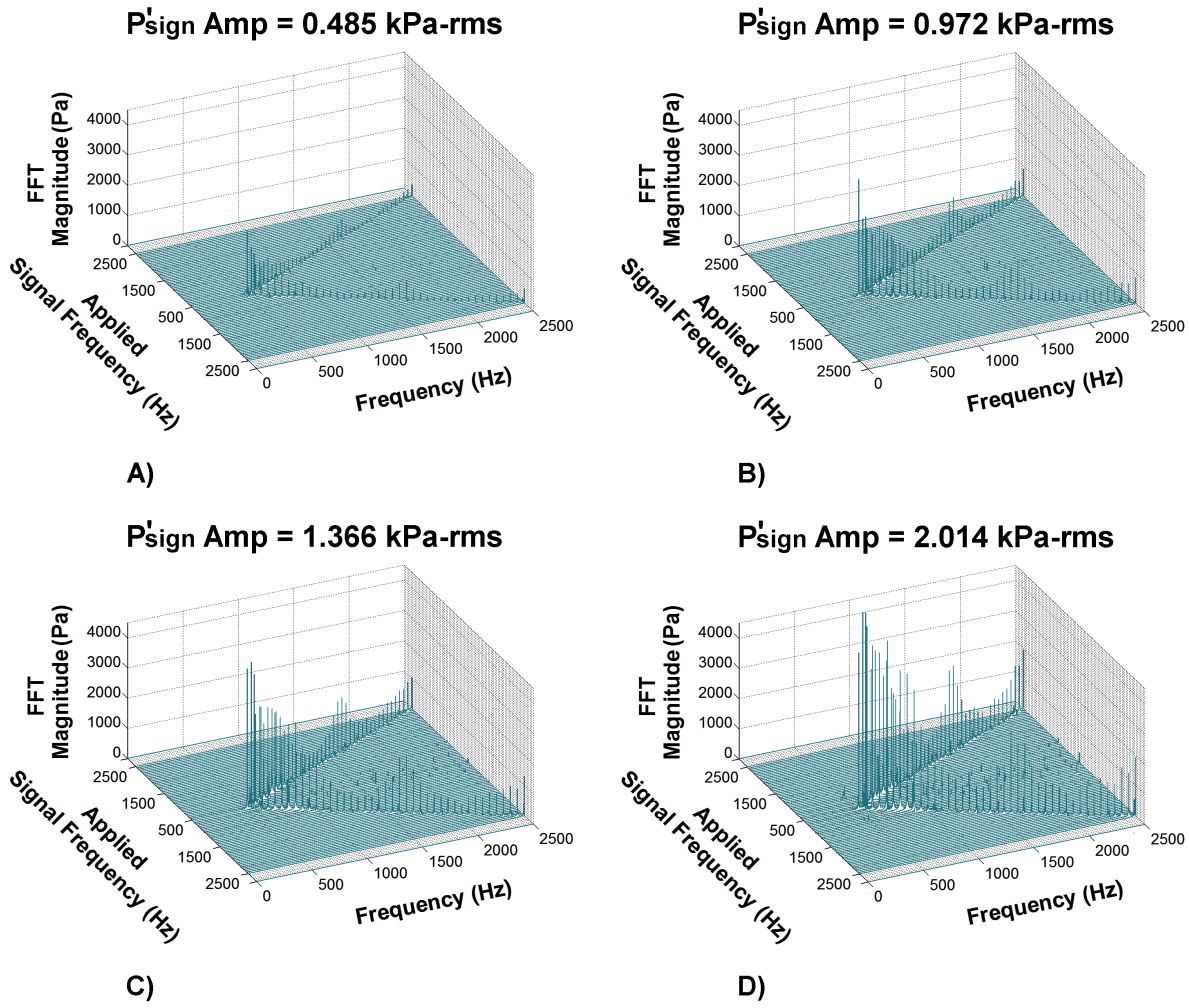

Figure 5.23: P'_{inj} Waterfall Plots for the Single-Frequency Acoustic Modulation Pure Acoustic Tests: A) 0.485 kPa-rms, B) 0.972 kPa-rms, C) 1.366 kPa-rms and D) 2.014 kPa-rms.

Note: Enlarged Waterfall Plots can be seen in Section B.6.4.

A summary of the waterfall plots from $P'1$ from this pure acoustic study can be seen in Figure 5.24. As with the band-limited white noise pure acoustic tests, there is not a significant response from the transducers within the SEMRC in comparison to the oxidizer supply line. Again, denoting the oxidizer supply is the main area where the applied acoustic forcing is concentrated.

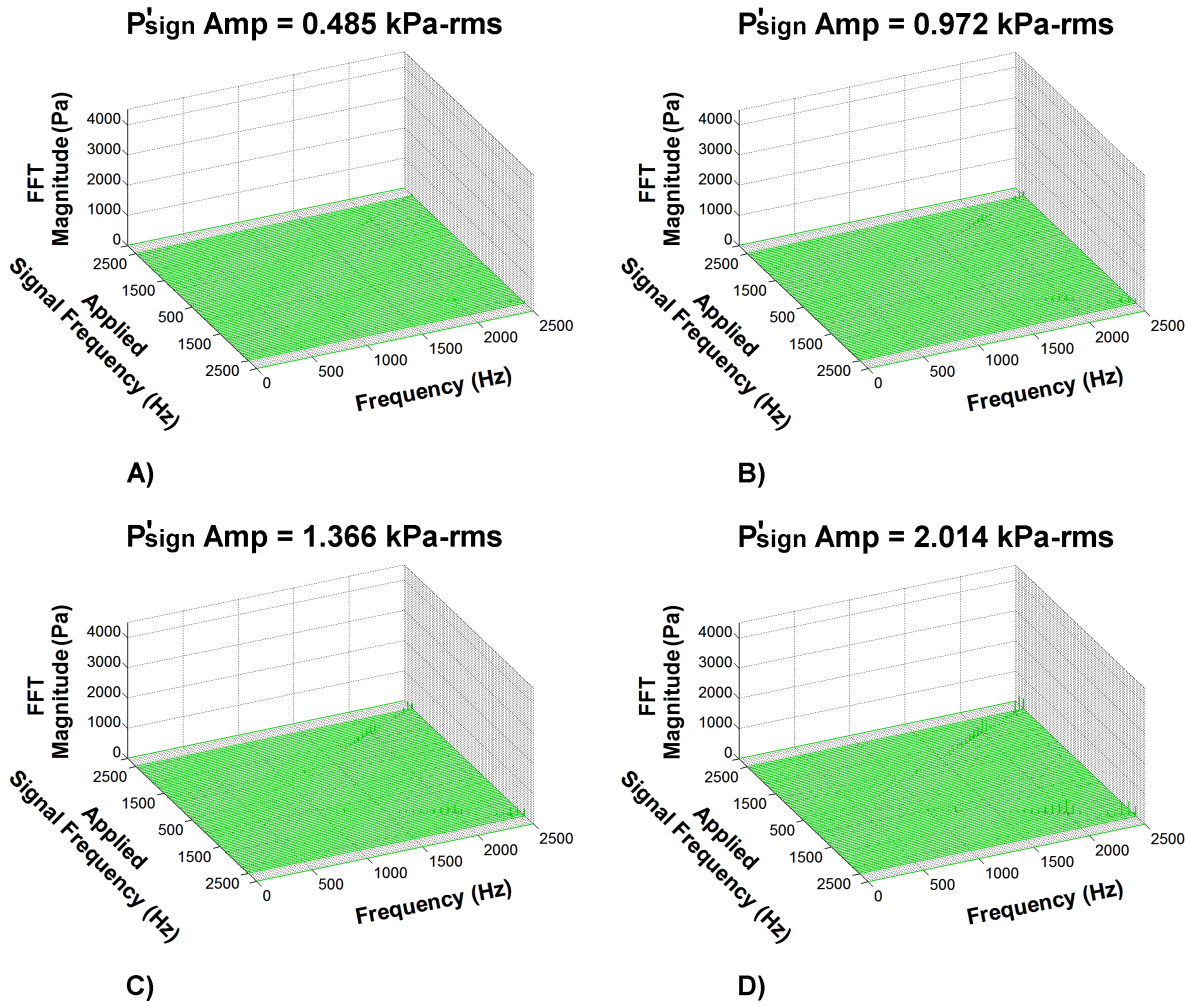

Figure 5.24: $P'1$ Waterfall Plots for the Single-Frequency Acoustic Modulation Pure Acoustic Tests: A) 0.485 kPa-rms, B) 0.972 kPa-rms, C) 1.366 kPa-rms and D) 2.014 kPa-rms.

Note: Enlarged Waterfall Plots of $P'1-P'3$ can be seen in Sections B.6.1–B.6.3.

As the naturally amplified frequency bands exhibited in these pure acoustic tests correlate to the suppression regimes from the previous instability tests, this signifies the acoustic response of the oxidizer supply is a major contributor to this instability control technique. Thus, altering the acoustic response of the oxidizer supply line through its geometry could lead to a change in the modulation signals for instability suppression.

CHAPTER 6

LINEAR MODAL ANALYSIS RESULTS

As the experiments successfully demonstrated strategic acoustic modulation as a viable high-frequency instability control approach, a linear modal analysis was undertaken to investigate the effects of acoustic modulation at the inlet boundary on the longitudinal instability modes of a dump combustor. It is the goal of this analysis to identify the physical mechanisms that contribute to the effectiveness of this combustion instability suppression technique.

Rani and Rani recently developed an acoustically consistent modal analysis approach that successfully predicted the longitudinal and transverse mode frequencies, as well as the stability of a dump combustor [39]. In that study, matching conditions were developed that enabled the dispersion relations to be consistently recovered for the purely axial modes in ducts with multiple discontinuities, while also ensuring that the system of equations was not overdetermined [39]. The model predictions were in agreement with the modal frequencies and stability observed in the experiments of Yu et al. [40]. Consequently, the current study adopts the approach derived by Rani and Rani to perform a 1-D modal analysis of the acoustically modulated SEMRC.

6.1 Theory

The governing equation for this analysis is the linear homogeneous acoustic wave equation with mean flow (see Section A.4 for detailed derivation), given by

$$\frac{1}{\overline{c}^2}\frac{\overline{\mathrm{D}}^2 p'}{\overline{\mathrm{D}}t^2} - \bigtriangledown^2 p' \;=\; 0 \tag{6.1}$$

where

$$\frac{\overline{\mathrm{D}}}{\overline{\mathrm{D}}t} \;=\; \frac{\partial}{\partial t} + (\overline{\mathbf{u}} \cdot \bigtriangledown) \tag{6.2}$$

Acoustic pressure fluctuations in 1-D cartesian coordinates can be expressed as

$$p'(x,t) \;=\; \exp(i\Omega t)\Big(A^+ \exp(ik^+ x) + A^- \exp(ik^- x)\Big) \tag{6.3}$$

where

$$k^{\pm} \;=\; \frac{(\Omega/\overline{c})(\overline{M} \mp 1)}{1 - \overline{M}^2} \tag{6.4}$$

Implementing the definition of sound speed $\overline{c}^2 = \frac{\partial p}{\partial \rho}\Big|_s$, acoustic density fluctuations $\rho'(x,t)$ can be written as

$$\rho'(x,t) \;=\; \frac{p'(x,t)}{\overline{c}^2} \;=\; \frac{1}{\overline{c}^2}\exp(i\Omega t)\Big(A^+ \exp(ik^+ x) + A^- \exp(ik^- x)\Big) \tag{6.5}$$

The acoustic velocity fluctuations $u'(x,t)$ may be derived from the linearized inviscid axial momentum equation:

$$\frac{\partial u'}{\partial t} + \overline{u}\frac{\partial u'}{\partial x} = -\frac{1}{\overline{\rho}}\frac{\partial p'}{\partial x} \tag{6.6}$$

Substituting the acoustic pressure solution into Eq. (6.6), $u'(x,t)$ can then be solved for as

$$u'(x,t) = -\frac{1}{\overline{\rho}}\exp(i\Omega t)\left(\frac{k^+}{\Omega + \overline{u}k^+}A^+\exp(ik^+x) + \frac{k^-}{\Omega + \overline{u}k^-}A^-\exp(ik^-x)\right) \tag{6.7}$$

6.2 Application to Combustor Geometry

A model geometry representative of the laboratory burner used in the experiments was considered, and is shown in Figure 6.1. The geometry consisted of two ducts of differing cross-sectional areas, with an area discontinuity at their interface. Region 1 of the combustor was a simplified geometry of the oxidizer supply line, while Region 2 represented the combustion chamber of the SEMRC.

The acoustic fluctuating properties for Regions 1 and 2 may be written as

$$p'_\beta(x,t) = \exp(i\Omega t)\left(A^+_\beta\exp(ik^+_\beta x) + A^-_\beta\exp(ik^-_\beta x)\right) \tag{6.8.A}$$

$$\rho'_\beta(x,t) = \frac{1}{\overline{c}^2_\beta}\exp(i\Omega t)\left(A^+_\beta\exp(ik^+_\beta x) + A^-_\beta\exp(ik^-_\beta x)\right) \tag{6.8.B}$$

$$u'_\beta(x,t) = -\frac{1}{\overline{\rho}_\beta}\exp(i\Omega t)\left(\frac{k^+_\beta}{\Omega + \overline{u}_\beta k^+_\beta}A^+_\beta\exp(ik^+_\beta x) + \frac{k^-_\beta}{\Omega + \overline{u}_\beta k^-_\beta}A^-_\beta\exp(ik^-_\beta x)\right) \tag{6.8.C}$$

where $\beta = 1,2$ is the region index.

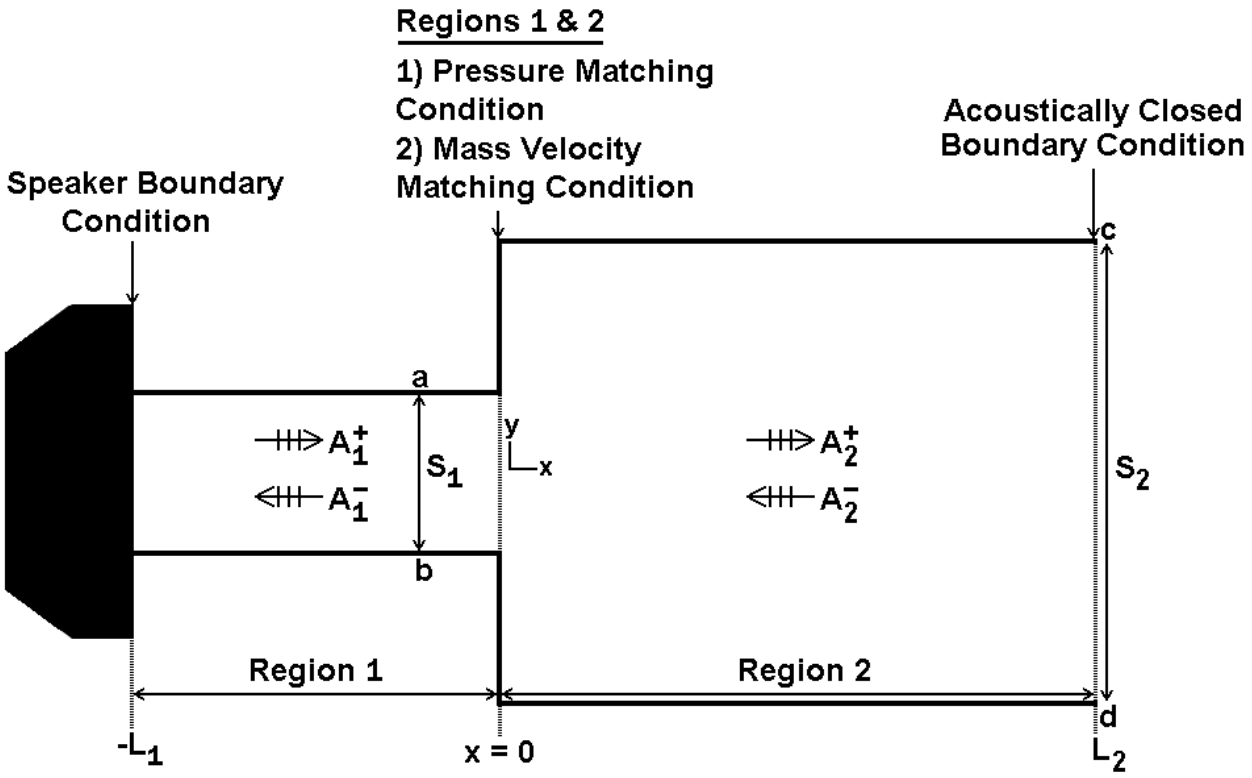

Figure 6.1: Schematic of the Combustor Model Geometry.

For these acoustic properties, the unknown coefficients are the complex wave amplitudes, $A_\beta^\pm$. Therefore, a system of four equations is needed to determine the dispersion relation. These equations are obtained from the two boundary conditions located at $x = -L_1$ and $x = L_2$, and from a pair of matching conditions at the area discontinuity $x = 0$. A speaker impedance boundary condition is applied at the inlet of Region 1, while the boundary at the exit of Region 2 is assumed to be acoustically closed. The matching conditions applied at the interface are the matching conditions for the purely axial modes presented in Rani and Rani [39]; these conditions involve matching total pressure and acoustic mass velocity at the interface.

6.2.1 Pressure Matching Condition

The pressure matching condition is achieved through the continuity of total pressure at the aperture $x = 0$. The form of this matching condition for axial modes is given by [39]

$$\int_{S_1} \left(p_1 + \frac{1}{2}\rho_1 u_1^2 \right) \mathrm{d}y \;=\; \int_{S_1} \left(p_2 + \frac{1}{2}\rho_2 u_2^2 \right) \mathrm{d}y \tag{6.9}$$

Performing Reynolds decomposition of variables (e.g., $\rho = \overline{\rho} + \rho'$), followed by their substitution into Eq. (6.9) and linearizing yields

$$\int_{-S_1/2}^{S_1/2} \left(p_1' + \frac{1}{2}\rho_1' \overline{u}_1^2 + \overline{\rho}_1 \overline{u}_1 u_1' \right) \mathrm{d}y \;=\; \int_{-S_1/2}^{S_1/2} \left(p_2' + \frac{1}{2}\rho_2' \overline{u}_2^2 + \overline{\rho}_2 \overline{u}_2 u_2' \right) \mathrm{d}y \tag{6.10}$$

Acoustic properties from Regions 1 and 2 (at $x = 0$) were substituted into Eq. (6.10) and integrated across the aperture cross section, yielding

$$\begin{aligned} & A_1^+ \left(1 + \frac{\overline{M}_1^2}{2} - \overline{u}_1 \frac{k_1^+}{\Omega + \overline{u}_1 k_1^+} \right) + A_1^- \left(1 + \frac{\overline{M}_1^2}{2} - \overline{u}_1 \frac{k_1^-}{\Omega + \overline{u}_1 k_1^-} \right) \\ = \; & A_2^+ \left(1 + \frac{\overline{M}_2^2}{2} - \overline{u}_2 \frac{k_2^+}{\Omega + \overline{u}_2 k_2^+} \right) + A_2^- \left(1 + \frac{\overline{M}_2^2}{2} - \overline{u}_2 \frac{k_2^-}{\Omega + \overline{u}_2 k_2^-} \right) \end{aligned} \tag{6.11}$$

6.2.2 Velocity Matching Condition

The velocity matching condition was obtained by imposing continuity of axial acoustic mass velocity at $x = 0$, which may be written as [39]

$$\int_{S_1} \rho_1 u_1 \, \mathrm{d}S \;=\; \int_{S_2} \rho_2 u_2 \, \mathrm{d}S \tag{6.12}$$

Similar to the pressure matching condition, the linearized form of the acoustic mass velocity matching condition is

$$\int_{-S_1/2}^{S_1/2} (\rho_1' \overline{u}_1 + \overline{\rho}_1 u_1') \, \mathrm{d}y \;=\; \int_{-S_2/2}^{S_2/2} (\rho_2' \overline{u}_2 + \overline{\rho}_2 u_2') \, \mathrm{d}y \tag{6.13}$$

which becomes

$$S_1(\rho_1' \overline{u}_1 + \overline{\rho}_1 u_1') \;=\; S_2(\rho_2' \overline{u}_2 + \overline{\rho}_2 u_2') \tag{6.14}$$

Substituting the acoustic density and velocity fluctuations at $x = 0$ for Regions 1 and 2 into Eq. (6.14) provides the final form of the acoustic mass velocity matching condition:

$$\begin{aligned} & S_1 \left[A_1^+ \left(\frac{\overline{M}_1}{\overline{c}_1} - \frac{k_1^+}{\Omega + \overline{u}_1 k_1^+} \right) + A_1^- \left(\frac{\overline{M}_1}{\overline{c}_1} - \frac{k_1^-}{\Omega + \overline{u}_1 k_1^-} \right) \right] \\ = \; & S_2 \left[A_2^+ \left(\frac{\overline{M}_2}{\overline{c}_2} - \frac{k_2^+}{\Omega + \overline{u}_2 k_2^+} \right) + A_2^- \left(\frac{\overline{M}_2}{\overline{c}_2} - \frac{k_2^-}{\Omega + \overline{u}_2 k_2^-} \right) \right] \end{aligned} \tag{6.15}$$

6.2.3 Acoustically Closed Boundary Condition

The acoustically closed (i.e., hard-wall) boundary condition was applied at $x = L_2$, which may be expressed as

$$\frac{\partial p'}{\partial x} \;=\; 0 \tag{6.16}$$

Substituting the pressure fluctuation form of Region 2 into Eq. (6.16) yields

$$A_2^+ k_2^+ \exp\left(k_2^+ L_2\right) + A_2^- k_2^- \exp\left(i k_2^- L_2\right) \;=\; 0 \tag{6.17}$$

6.2.4 Acoustic Speaker Boundary Condition

The final boundary condition applied at the inlet of the oxidizer supply line, $x = -L_1$, was representative of acoustic forcing at the inlet, where acoustic impedance $Z_{\text{spk}} = p'_{\text{spk}}/u'_{\text{spk}}$. The speaker impedance, Z_{spk}, is found by modeling the speaker as a mass-spring-damper system, similar to that in the study by Black [41]. The current approach involved approximating the speaker diaphragm as a single degree-of-freedom oscillator, as shown in Figure 6.2.

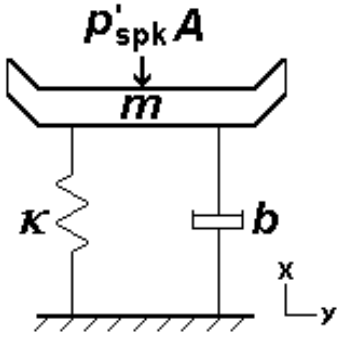

Figure 6.2: Schematic of the Speaker Mass-Spring-Damper System.

The governing equation of motion for the speaker diaphragm may be written as

$$m\ddot{x} + b\dot{x} + \kappa x \;=\; -\,p'_{\text{spk}} A \tag{6.18}$$

A - Diaphragm Area
b - Diaphragm Damping Coefficient
κ - Diaphragm Spring Constant
m - Diaphragm Mass
p'_{spk} - Acoustic Pressure at the Diaphragm
$x \;=\; \int u'_{\text{spk}} dt$ - Diaphragm Displacement
$\dot{x} \;=\; u'_{\text{spk}}$ - Diaphragm Velocity
$\ddot{x} \;=\; \dot{u}'_{\text{spk}}$ - Diaphragm Acceleration

Assuming harmonic motion, where $\ddot{x} = \dot{u}'_{\text{spk}} = i\Omega_{\text{spk}} u'_{\text{spk}}$, $\dot{x} = u'_{\text{spk}}$ and $x = \int u'_{\text{spk}} dt = -iu'_{\text{spk}}/\Omega_{\text{spk}}$, Eq. (6.18) becomes

$$Z_{\text{spk}} = \frac{p'_{\text{spk}}}{u'_{\text{spk}}} = -\frac{1}{A}\left[b + i\left(\Omega_{\text{spk}} m - \frac{\kappa}{\Omega_{\text{spk}}}\right)\right] \tag{6.19}$$

where speaker constants b and κ are determined experimentally.

Substituting the acoustic properties from Region 1 (at $x = -L_1$) into $Z_{\text{spk}} = p'_1/u'_1$, and integrating across the inlet yielded the following acoustic speaker boundary condition:

$$\begin{aligned} &A_1^+ \exp\left(-ik_1^+ L_1\right)\left(1 - \frac{b + i(\Omega_{\text{spk}} m - \kappa/\Omega_{spk})}{\overline{\rho}_1 A}\frac{k_1^+}{\Omega + \overline{u}_1 k_1^+}\right) + \\ &A_1^- \exp\left(-ik_1^- L_1\right)\left(1 - \frac{b + i(\Omega_{\text{spk}} m - \kappa/\Omega_{spk})}{\overline{\rho}_1 A}\frac{k_1^-}{\Omega + \overline{u}_1 k_1^-}\right) = 0 \end{aligned} \tag{6.20}$$

6.3 Speaker Constant Determination

The procedure to determine the speaker constants was similar to that of Quinlan and Zinn [42], which consisted of the following steps: (1) Deriving the Speaker Model Frequency Response Function (SMFRF) of a short hard-wall-terminated duct with an attached speaker, (2) Determining experimentally the mechanical resonance of the speaker and the acoustic resonant frequency of the duct geometry and (3) Obtaining the speaker constants by matching the SMFRF to experimentally determined resonant frequencies (both mechanical and acoustic).

6.3.1 Development of the Speaker Model Frequency Response Function (SMFRF)

The Speaker Model Frequency Response Function was found using the mass-spring-damper oscillator model employed by Quinlan and Zinn [42]. In this model, the speaker diaphragm experiences both a pressure force and an applied coil force, as shown in Figure 6.3. The coil force, F_{coil}, includes the Lorentz force applied from the voice-coil, F_{Lorentz}, as well as the backward electromotive force (BEMF), F_{BEMF}.

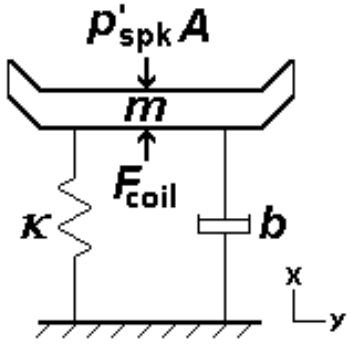

Figure 6.3: Schematic of the Speaker Mass-Spring-Damper System Used to Determine the SMFRF.

The governing equation of motion for this single degree-of-freedom speaker diaphragm may be written as

$$m\ddot{x} + b\dot{x} + \kappa x \;=\; F_{\text{coil}} - p'_{\text{spk}}A \tag{6.21}$$

where

$$F_{\text{coil}} \;=\; F_{\text{Lorentz}} + F_{\text{BEMF}} \tag{6.22}$$

The Lorentz force is a magnetic force that arises due to the flow of current I through the voice-coil that is suspended in a uniform magnetic field B created by the speaker's magnet [43]. This force can be expressed as

$$F_{\text{Lorentz}} \;=\; I \int_{\text{coil}} BI \times dA \tag{6.23}$$

Accounting for the gain across the amplifier (G_{amp}), the Lorentz force on the diaphragm becomes

$$F_{\text{Lorentz}} \;=\; G_{\text{amp}} N \pi d_{\text{dphgm}} BI \tag{6.24}$$

where $\ell_{\text{wire}} = N\pi d_{\text{dphgm}}$ is the length of the coil and d_{dphgm} is the diameter of the diaphragm.

The force due to BEMF, F_{BEMF}, is caused by the current countering the coil's movement, which can be written as

$$F_{\text{BEMF}} \;=\; BN\pi d_{\text{dphgm}} I_{\text{BEMF}} \tag{6.25}$$

The BEMF current I_{BEMF}, BEMF voltage V_{BEMF} and the speaker's electrical impedance Z_{el} are related as $Z_{\text{el}} = V_{\text{BEMF}}/I_{\text{BEMF}}$, where Z_{el} was supplied by the speaker manufacturer as a function of signal frequency. The voltage induced by the BEMF within the speaker voice-coil is given by [43]

$$V_{\text{BEMF}} \;=\; -\int_{\text{coil}} \dot{x} \times B \; d\ell \;=\; -N\pi d_{\text{dphgm}} B\dot{x} \tag{6.26}$$

Using Eqs. (6.25) and (6.26) yields

$$F_{\text{BEMF}} = \frac{-(N\pi d_{\text{dphgm}}B)^2\dot{x}}{Z_{\text{el}}} \tag{6.27}$$

The total F_{coil} can now be written as

$$F_{\text{coil}} = G_{\text{amp}}N\pi d_{\text{dphgm}}BI - \frac{(N\pi d_{\text{dphgm}}B)^2\dot{x}}{Z_{\text{el}}} \tag{6.28}$$

The speaker pressure p'_{spk} in Eq. (6.21) is related to the speaker diaphragm velocity u'_{spk} through the inlet mechanical impedance of the duct geometry as $Z_{\text{mech,sys}} = p'_{\text{spk}}A/u'_{\text{spk}}$. For a duct of length L with a piston at $x = 0$ and a hard-wall boundary at $x = L$, $Z_{\text{mech,sys}} = -i[\rho_0 cA\cot(kL)]$ [44]. Replacing p'_{spk} in Eq. (6.21) and implementing the harmonic motion assumption yields the SMFRF $H(f)$ as follows:

$$H(f) = \frac{u'_{\text{spk}}}{I} = \frac{G_{\text{amp}}N\pi d_{\text{dphgm}}B}{b + \frac{(N\pi d_{\text{dphgm}}B)^2}{Z_{\text{el}}} + i\left(\Omega_{\text{spk}}m - \frac{\kappa}{\Omega_{\text{spk}}} - \rho_0 cA\cot(kL)\right)} \tag{6.29}$$

To simplify Eq. (6.29), the imaginary portion of the denominator needs to be eliminated. Thus, the real and imaginary parts of the denominator are defined as

$$X = b + \frac{(N\pi d_{dphgm}B)^2}{Z_{el}}, \quad Y = \Omega_{spk}m - \frac{\kappa}{\Omega_{spk}} - \rho_0 cA\cot(kL) \tag{6.30}$$

Implementing these definitions and multiplying the numerator and denominator in Eq. (6.29) by the denominator's complex conjugate, $H(f)$ becomes

$$H(f) = G_{amp} N \pi d_{dphgm} B \left(\frac{X - iY}{X^2 + Y^2} \right) \tag{6.31}$$

From Eq. (6.31), the magnitude of the SMFRF can be expressed as:

$$|H(f)| = G_{amp} N \pi d_{dphgm} B \sqrt{\left(\frac{X}{X^2 + Y^2} \right)^2 + \left(\frac{Y}{X^2 + Y^2} \right)^2} \tag{6.32}$$

Substituting back in the definitions from Eq. (6.30) yields the final form for the magnitude of the SMFRF:

$$|H(f)| = G_{amp} N \pi d_{dphgm} B * \sqrt{\left(\frac{b + \frac{(N\pi d_{dphgm} B)^2}{Z_{el}}}{\left(b + \frac{(N\pi d_{dphgm} B)^2}{Z_{el}}\right)^2 + \left(\Omega_{spk} m - \frac{\kappa}{\Omega_{spk}} - \rho_0 c A \cot(kL)\right)^2} \right)^2 + \left(\frac{\Omega_{spk} m - \frac{\kappa}{\Omega_{spk}} - \rho_0 c A \cot(kL)}{\left(b + \frac{(N\pi d_{dphgm} B)^2}{Z_{el}}\right)^2 + \left(\Omega_{spk} m - \frac{\kappa}{\Omega_{spk}} - \rho_0 c A \cot(kL)\right)^2} \right)^2} \tag{6.33}$$

6.3.2 Experimental Determination of the Speaker System Resonances

To determine constants b and κ, the mechanical resonance of the speaker, as well as the system acoustic resonant frequency were found experimentally using the apparatus shown in Figure 6.4. The facility consists of a JBL 2446J speaker mounted to a short tube ($l_{\text{const,sys}} \approx 6.4$ cm) with a flush mounted pressure transducer at the hard-wall-terminated end. The short tube length was chosen to reduce the number of acoustic resonances that could be excited within the system, and thus accentuate

the mechanical resonance of the speaker [42]. Using this apparatus, the speaker was sent individual harmonic signals ranging from 100−3000 Hz in increments of 50 Hz at a constant current, with the pressure at the closed end being measured for each input signal. The signal was generated by a BK Precision 4040A Function Generator and passed through an AE Techron LVC 608 Constant Current Amplifier.

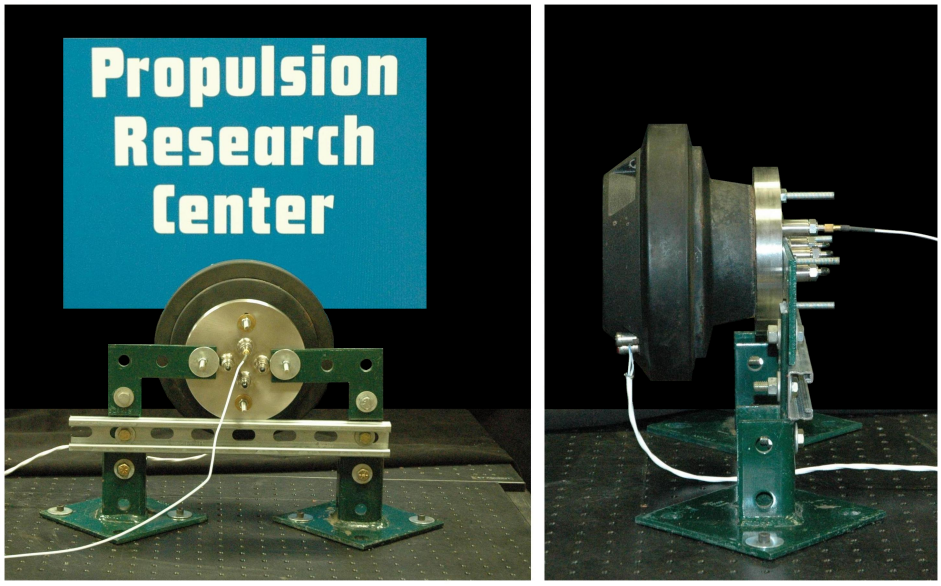

Figure 6.4: Speaker Constant Determination Test Facility.

From this experiment, it was determined that the mechanical resonant frequency of the speaker was $f_{\text{mech,spk}} = 700$ Hz, while the system acoustic resonance was $f_{\text{acous,sys}} = 2700$ Hz. The speaker damping coefficient and spring constant were obtained using an iterative process in which b and κ in Eq. (6.33) were varied until the SMFRF resonances (i.e., the two peak frequencies in Figure 6.5) matched the experimentally determined resonances.

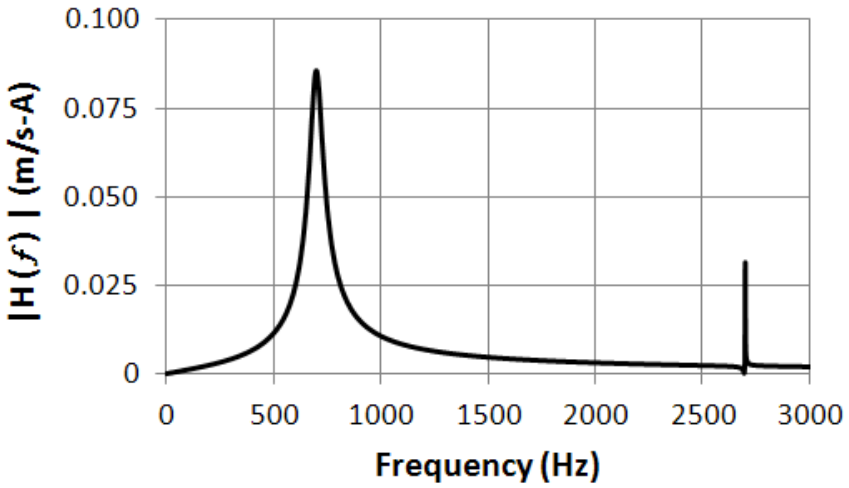

Figure 6.5: Speaker Model Transfer Function for the JBL 2446J Speaker.

The resulting speaker model parameters are presented in Table 6.1. The diaphragm mass m and the number of coil turns N were estimated using the information provided by Quinlan et al. [42, 43]. Aside from these parameters, the diaphragm diameter d_{dphgm}, speaker magnetic field B and electrical impedance Z_{el} were obtained from the JBL 2446J specification sheet [34].

Table 6.1: Speaker Model Parameters and Technical Specifications for the JBL 2446J Speaker.

Model #	d_{dphgm}**, cm**	B**, T**	**Electrical Impedance Range, Ω**
JBL 2446J	10.92	1.9	$\approx$ 9.5–25.5 for f = 0–3000 Hz
N	m**, kg**	κ**, N/m**	b**, N-s/m**
28.5	0.04	762,000	$2 * 10^{-12}$

6.4 Assembly of the Boundary and Matching Conditions

The boundary and matching conditions were assembled to get a homogeneous matrix system of equations of the form $\mathbf{CA} = 0$, where $\mathbf{C}$ is the coefficient matrix and $\mathbf{A}$ is the vector of unknown modal amplitudes. The matrix $\mathbf{C}$ is given by

$$\mathbf{C} = \begin{bmatrix} a_{11} & a_{12} & 0 & 0 \\ a_{21} & a_{22} & a_{23} & a_{24} \\ a_{31} & a_{32} & a_{33} & a_{34} \\ 0 & 0 & a_{43} & a_{44} \end{bmatrix} \tag{6.34}$$

where

$$a_{11} = \exp\left(-ik_1^+ L_1\right)\left[1 + \frac{Z_{\text{spk}}}{\overline{\rho}_1}\left(\frac{k_1^+}{\Omega + \overline{u}_1 k_1^+}\right)\right], \quad a_{12} = \exp\left(-ik_1^- L_1\right)\left[1 + \frac{Z_{\text{spk}}}{\overline{\rho}_1}\left(\frac{k_1^-}{\Omega + \overline{u}_1 k_1^-}\right)\right]$$

$$a_{21} = \left(1 + \frac{\overline{M}_1^2}{2} - \frac{\overline{u_1} k_1^+}{\Omega + \overline{u}_1 k_1^+}\right), \quad a_{22} = \left(1 + \frac{\overline{M}_1^2}{2} - \frac{\overline{u_1} k_1^-}{\Omega + \overline{u}_1 k_1^-}\right)$$

$$a_{23} = -\left(1 + \frac{\overline{M}_2^2}{2} - \frac{\overline{u_2} k_2^+}{\Omega + \overline{u}_2 k_2^+}\right), \quad a_{24} = -\left(1 + \frac{\overline{M}_2^2}{2} - \frac{\overline{u_2} k_2^-}{\Omega + \overline{u}_2 k_2^-}\right)$$

$$a_{31} = S_1\left(\frac{\overline{M}_1}{\overline{c}_1} - \frac{k_1^+}{\Omega + \overline{u}_1 k_1^+}\right), \quad a_{32} = S_1\left(\frac{\overline{M}_1}{\overline{c}_1} - \frac{k_1^-}{\Omega + \overline{u}_1 k_1^-}\right)$$

$$a_{33} = -S_2\left(\frac{\overline{M}_2}{\overline{c}_2} - \frac{k_2^+}{\Omega + \overline{u}_2 k_2^+}\right), \quad a_{34} = -S_2\left(\frac{\overline{M}_2}{\overline{c}_2} - \frac{k_2^-}{\Omega + \overline{u}_2 k_2^-}\right)$$

$$a_{43} = k_2^+ \exp\left(k_2^+ L_2\right), \quad a_{44} = k_2^- \exp\left(ik_2^- L_2\right)$$

A unique and nontrivial solution to $\mathbf{CA} = 0$ exists only when $\det(\mathbf{C}) = 0$, which yields a dispersion relation that can be solved for the complex modal frequencies using Muller's iteration technique [45]. In this analysis, the temporal dependency of fluctuations is given by $\exp(i\Omega t)$, which designates that a mode becomes unstable when the imaginary part of the frequency $\Omega_{\text{imag}} < 0$.

6.5 Linear Modal Analysis Results and Discussion

The objective of this analysis was to demonstrate an unstable to stable transition of the $f \approx 2430$ Hz first longitudinal instability when single-frequency acoustic modulation was applied at the inlet. As the frequency of the spontaneous combustion instability was seen to naturally vary from 2300−2500 Hz in the experiments, five analytical cases were considered that spanned this frequency range. Across these cases, the instability frequency was varied from 2300−2500 Hz in increments of 50 Hz by changing the mean chamber temperature T_2 from 1248−1685 K within the model. The experimentally observed instability of 2300−2500 Hz corresponded to the first longitudinal mode of the combustion chamber (i.e., Region 2 in Figure 6.1). In order for modal analysis to capture this frequency, an inlet length $L_1 = 2.54$ cm was considered. The other geometric dimensions in the model representative of the SEMRC are $L_2 = 16.51$ cm, $S_1 = 1.78$ cm and $S_2 = 10.16$ cm.

Table 6.2: Combustor Temperatures and Instability Characteristics for the Cases without Acoustic Modulation.

Case	T_1, K	T_2, K	f, Hz	Instability Growth Rate, rad/s (when $f_{\text{spk}} = 0$ Hz)
A	300	1248	2300	-0.7135
B	$''$	1343	2350	-0.7738
C	$''$	1446	2400	-0.8346
D	$''$	1559	2450	-0.8955
E	$''$	1685	2500	-0.9567

Table 6.2 summarizes the flow parameters and instability characteristics for the five analytical cases. This table also presents the instability growth rates in the absence of acoustic forcing ($f_{\text{spk}} = 0$ Hz), all of which are negative, implying that the model captures the 1-L instability mode corresponding to the combustion chamber.

After determining the baseline 1-L mode (i.e., without acoustic forcing), the effects of applied acoustic modulation ranging from $f_{\text{spk}} = 0-2500$ Hz on the 1-L mode stability were investigated. The results of this analysis are presented in Figure 6.6, which plot the 1-L mode growth rate as a function of the applied signal for each case. Also shown in Figure 6.6 (right) is the magnified view of the transition region from positive to negative growth rate (i.e., stable to unstable transition). It was observed (Figure 6.6 (left)) that the mode initially becomes more stable with an increase in applied signal frequency, attaining a peak stability and then becomes less stable with a further increase in applied signal frequency until the mode transitions to the unstable region. Once the transition point ranging from $1261-1330$ Hz was reached, the mode stayed unstable throughout the rest of the acoustic modulation range.

The predicted analytical results were found to be consistent with experimental observations as seen in Figure 6.7. For the single-frequency acoustic modulation principle baseline tests presented in Section 5.2.2, there exists a suppression of the spontaneously excited instability from the lowest applied signal $f = 50$ Hz to the stability transition frequency of $f_{\text{stbly,trans}} \approx 1300$ Hz, at which baseline instability amplitudes were again reached (i.e., no appreciable suppression present). This can be seen in Figure 6.7.A. This matched the analytic results shown in Figure 6.7.B as the instability was indeed predicted to be naturally unstable, which was then suppressed

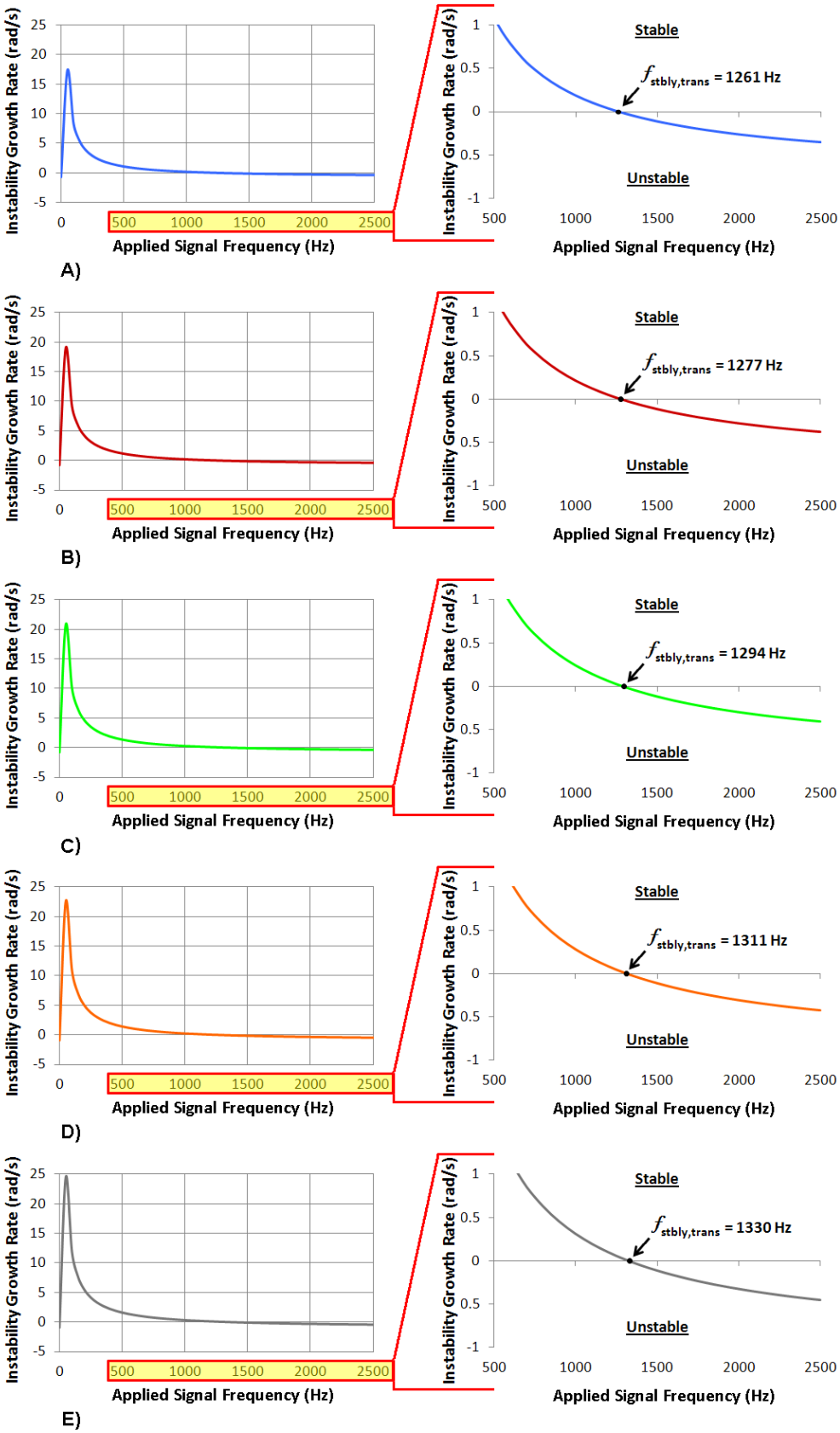

Figure 6.6: Effect of Single-Frequency Application on the First Longitudinal Instability Mode Growth Rate for A) $f = 2300$ Hz, B) $f = 2350$ Hz, C) $f = 2400$ Hz, D) $f = 2450$ Hz and E) $f = 2500$ Hz.

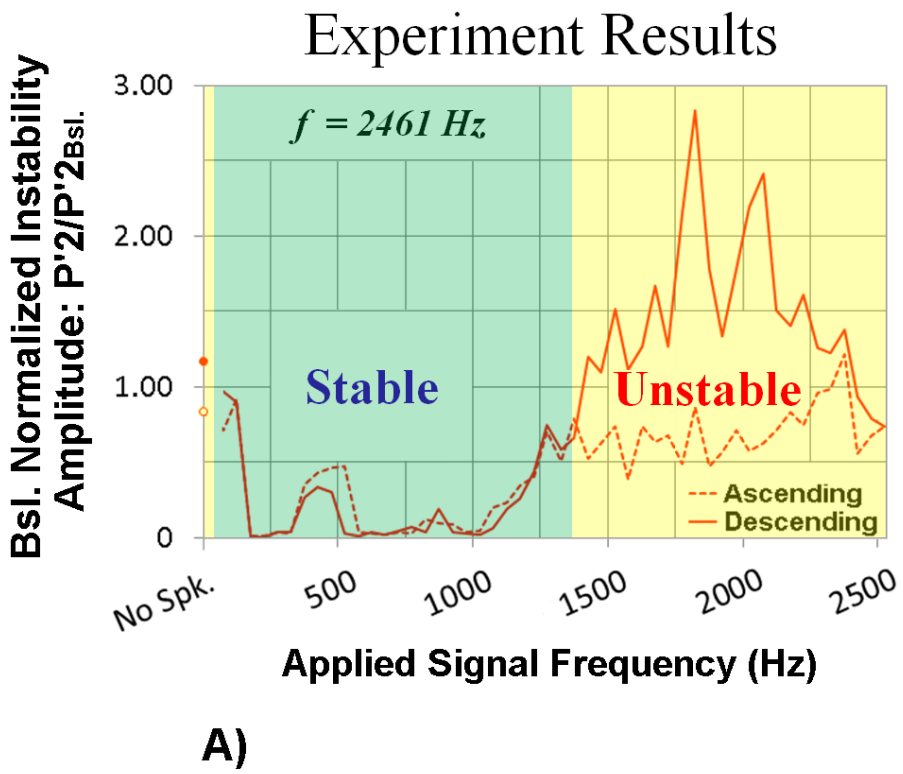

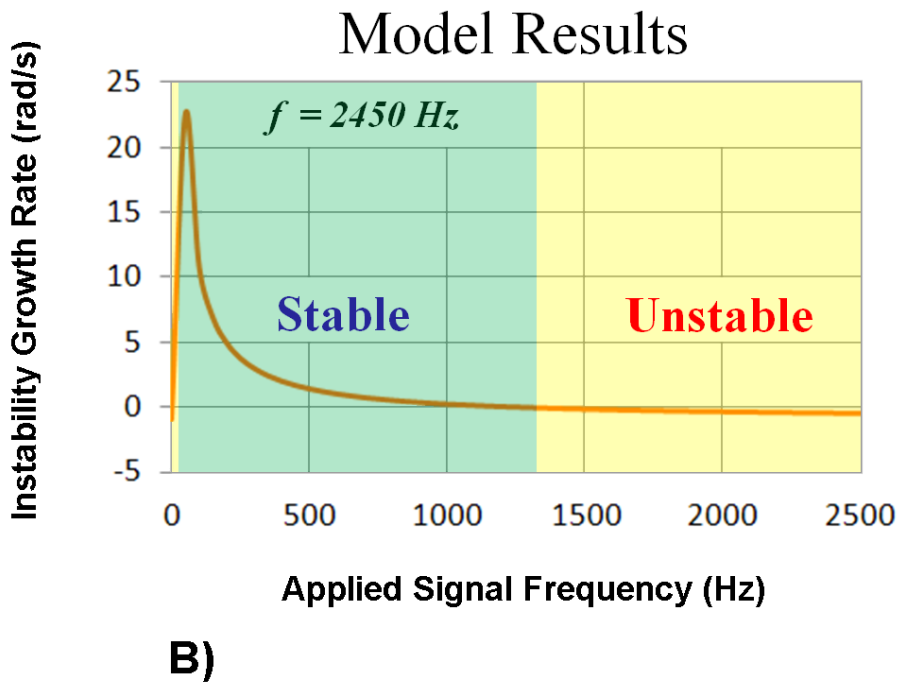

Figure 6.7: Comparison Between A) Single-Frequency Acoustic Modulation Experiment Results from Test 08-01-04 and the B) Analytical Model Prediction for the First Longitudinal Mode with $f = 2450$ Hz.

when single-frequency acoustic modulation was applied at signal frequencies until the stability transition point, where the instability mode again became unstable. Comparing the instability responses from Figure 6.7.A and 6.7.B, it is seen that the experimental transition point (1300 Hz) is in reasonable agreement with the analytical result (1261−1330 Hz).

When considering the single-frequency acoustic modulation signal amplitude study from Section 5.3.2, similar results were found. However, it is to be noted that in the experiments, the suppression behavior was most prominent for the test with the highest amplitude (82% RMS), which is where the best agreement between the experiments and theory is observed. Thus, results from this modal analysis further support the premise that the speaker inlet impedance provides a mechanism for instability suppression.

CHAPTER 7

CONCLUSIONS

7.1 Summary

Strategically applying acoustic forcing within the oxidizer supply of a propellant injector was developed in this work as a viable method to suppress a high-frequency combustion instability. Previous active instability control research demonstrated low-frequency instability suppression through both mechanical and acoustic modulation of the incoming propellant; the fast-response actuation valve study mechanically pulsed the fuel at a single frequency over a range of frequencies to produce an instability damping effect, whereas the acoustic modulation study applied a phased-delayed signal within the fuel line. Drawing from these studies, an original instability control method successfully demonstrated acoustic modulation of the incoming oxidizer with both band-limited white noise and pure sinusoidal tones as a means to suppress a high-frequency instability in a laboratory-scaled rocket combustor. Specifically, suppression of a $f \approx 2430$ Hz first longitudinal instability was achieved using both of these acoustic modulation signal types within the Single Element Model Rocket Combustor (SEMRC).

During principle baseline testing, applying bands of white noise within a certain frequency range showed to be effective at controlling the spontaneously excited high-frequency instability. Specifically, applying 500−1000 Hz/600−1100 Hz band-limited white noise at a constant amplitude of approximately 2.0 kPa-rms caused the amplitude of the 2430 Hz instability to be reduced up to 90% across multiple tests. Application of white noise bands in both the ascending and descending directions yielded similar results for the frequency bands pertaining to maximum instability suppression. However, a larger damping effect was apparent during the descending signal application across the multiple tests performed. For each of these tests, when the speaker output 400−900 Hz to 800−1300 Hz band-limited white noise, a natural amplification of these applied signals occurred within the oxidizer supply, which can be attributed to the instability suppression within this range.

A set of single-frequency sweep tests at a constant signal amplitude of 2.0 kPa-rms was also performed. For this study, single-frequency acoustic modulation with arbitrary phase was applied from 50−2500 Hz in an ascending and descending fashion. Across these tests, a general suppression of the 2430 Hz oscillation existed from 150−1300 Hz, with two distinct frequency ranges yielding a 70+% average instability reduction across the four transducers. The first suppression regime was from approximately 150−300 Hz, with a maximum average reduction of 99% occurring at 200 Hz in the tests detailed. The second suppression regime was from approximately 550−1100 Hz, with a maximum average reduction of 96−98% occurring at 550−650 Hz for these tests. Again, a natural amplification of the applied signals across the frequency range for suppression was present within the oxidizer supply.

A signal amplitude study for these two acoustic modulation approaches was performed to further characterize the effectiveness of the instability suppression technique. During the band-limited white noise study, varying 500 Hz bands of white noise from 0−500 Hz to 2000−2500 Hz were applied at speaker amplitudes from 13−62% RMS, while the single-frequency acoustic modulation study saw pure sinusoidal tones with arbitrary phase swept from 500−2500 Hz at signal amplitudes ranging from 16−82% RMS. For these two studies, it was found that an average instability reduction up to 95+% was achieved above 57% RMS for the application of band-limited white noise and 58% RMS for single-frequency acoustic modulation. Above this RMS % threshold, the frequency widths of the suppression regimes were shown to widen with increasing signal amplitude for both modulation types. At a maximum amplitude (62% RMS), the suppression region for the band-limited white noise study was shown to expand to 100−600 Hz to 900−1400 Hz in the ascending signal direction, and to 0−500 Hz to 1300−1800 Hz in the descending signal direction. Within the oxidizer supply line, the applied signal at 62% RMS showed that aside from the 400−900 Hz to 800−1300 Hz naturally amplified range, lower bands of white noise were also above the threshold for instability suppression (inherently due to the speaker amplitude), which can be attributed to the expansion of this suppression regime.

During the single-frequency acoustic modulation study, the two suppression regimes were shown to expand during the maximum amplitude level (82% RMS) test to approximately 550−750 Hz and 850−1050 Hz, with similar acoustic phenomena present for the signals applied within the oxidizer supply that led to a suppression of

the instability. Upon comparing both the band-limited white noise and single-frequency sweep studies, it was found that the band-limited white noise approach more reliably suppressed the instability across the applied range than single-frequency acoustic modulation, as there were certain frequencies in which a 70+% instability reduction was not met for the highest RMS % frequency sweep test. However, as both methods proved to be capable at suppressing a high-frequency instability, this study bolstered the strategic application of acoustic modulation within an injector as an effective method to control high-frequency combustion instabilities.

An analytical model based on linear stability analysis was developed with the purpose of predicting the behavior of a first longitudinal mode when acoustic modulation was introduced at the inlet boundary. This work supplemented the experimental investigation, which demonstrated control of the 2430 Hz first longitudinal instability through various forms of acoustic modulation. The modal analysis applied acoustically consistent matching conditions to a model dump combustor representative of the SEMRC, with an impedance boundary condition for the acoustic forcing at the inlet. This boundary condition was derived by approximating the speaker diaphragm as a mass-spring-damper oscillator, with the speaker model constants found using a bench-top experiment consisting of the speaker being attached to a short hard-wall-terminated duct. The modal analysis successfully predicted the unstable to stable transition of the first longitudinal mode within the $2300-2500$ Hz range when single-frequency acoustic modulation was applied. The transition point frequency predicted by the theory was in reasonable agreement with the experiments. Thus, the analysis supported the premise that inlet acoustic

modulation is a means to control instability, and that inlet speaker impedance provides a mechanism for instability suppression. With a primary suppression mechanism identified, this further supports this approach as a potential method to control high-frequency combustion instabilities for liquid rocket engine applications.

7.2 Recommendations and Future Work

The current instability suppression work can be further expanded by incorporating optical diagnostic tools (OH* photomultiplier tube(s) and chemiluminescence) to monitor both the unsteady heat release oscillations and flame structure during the application of single-frequency acoustic modulation and band-limited white noise. To include these measurements, an optically accessible model rocket combustor with quartz viewports will have to be implemented. By including measurements of the unsteady heat release oscillations and characterizing the flame structure, this will further characterize the mechanism(s) responsible for suppressing the instability. This will assist in advancing this instability suppression technique for future applications.

The analytical model developed within this work can also be extended. More intricate modelling of the oxidizer supply geometry could be performed. Specifically, the inclusion of a restricted area step for the injector could be implemented to determine its effect on longitudinal mode stability. Also, experimentally testing and analyzing various acoustic drivers with differing speaker constants could lead to a robust parametric characterization of the analytical model. Finally, the generation

of a more detailed model with the inclusion of non-linear effects could allow finite amplitude effects to be taken in account.

As acoustically modulating the incoming oxidizer flow has shown to be capable of controlling a high-frequency combustion instability, this approach can be extended to design a passive instability control system. Passive instability control techniques have historically been implemented on flight-rated engines due to their inclusion of non-movable parts. Thus, there is an impetus to continue their use for future spacecraft. The approach outlined within this research investigation can be used to design a passive system where the acoustic modulation suppression signals are naturally generated upstream of the combustor. For instance, directed gas flow or a secondary combustor located upstream of the main chamber can be implemented as a source for band-limited white noise, which could be mechanically filtered and naturally amplified through alterations of the propellant supply line geometry to provide the correct band of white noise leading to instability damping. To demonstrate this capability, it is recommended this concept be tested on a model combustor, such as the SEMRC.

The combustion instability test facility implemented within this study provides a platform to investigate various acoustic modulation approaches for combustion instability control. Therefore, other modulation signals can be applied to determine their effectiveness at suppressing the oscillatory behavior of the combustor. Specifically, applying a variable phase offset signal at the same frequency of the instability is one such method. As this strategy proved effective at suppressing a low-frequency instability in the model dump combustor study with acoustic

modulation, it could potentially be extended for high-frequency instability control. This concept could be tested with the current hardware existing for the SEMRC.

APPENDICES

APPENDIX A

SUPPLEMENTAL ACOUSTIC DERIVATIONS

A.1 Linear Homogeneous Acoustic Wave Equation

The linear homogeneous acoustic wave equation describes the motion of acoustic waves through a medium. In this analysis, small amplitude disturbances are assumed to propagate in a homogeneous medium with no mean flow. To derive this equation, two conservation laws (mass and momentum) are combined with an equation of state that relates acoustic pressure and density. Prior to combining these relations, a linearization process is performed on these equations to account for the small disturbance assumption. To begin this analysis, the conservation of mass (continuity) relation is given by

$$\frac{\partial \rho}{\partial t} + \bigtriangledown \cdot (\rho \mathbf{u}) = 0 \tag{A.1}$$

while conservation of momentum can be written as

$$\rho \frac{\overline{\mathrm{D}}\mathbf{u}}{\overline{\mathrm{D}}t} = - \bigtriangledown p \tag{A.2}$$

where

$$\frac{\overline{\mathrm{D}}\mathbf{u}}{\overline{\mathrm{D}}t} = \frac{\partial \mathbf{u}}{\partial t} + (\mathbf{u} \cdot \bigtriangledown)\mathbf{u} \tag{A.3}$$

This form of momentum conservation assumes the fluid is inviscid, in which no body forces (e.g., gravity) act upon the fluid. Thus, the only force acting on the fluid control volume is the net pressure force acting upon the control volume surface.

An equation of state relating the fluid pressure and density is also necessary, which takes the form

$$p \equiv \mathrm{fn}(\rho) \tag{A.4}$$

For small perturbations traveling isentropically through a medium, a Taylor Series Expansion can be used to describe this equation of state, as it represents the fluid pressure solely as a function of density:

$$p = \overline{p} + A_1\left(\frac{\rho - \overline{\rho}}{\overline{\rho}}\right) + \frac{A_2}{2!}\left(\frac{\rho - \overline{\rho}}{\overline{\rho}}\right)^2 + \frac{A_3}{3!}\left(\frac{\rho - \overline{\rho}}{\overline{\rho}}\right)^3 + \ \ldots \tag{A.5}$$

where

$$p = \overline{p} + dp \tag{A.6}$$

$$\rho = \overline{\rho} + d\rho \tag{A.7}$$

Substituting Eqs. (A.6) and (A.7) into the equation of state yields

$$dp = A_1\left(\frac{d\rho}{\overline{\rho}}\right) + \frac{A_2}{2!}\left(\frac{d\rho}{\overline{\rho}}\right)^2 + \frac{A_3}{3!}\left(\frac{d\rho}{\overline{\rho}}\right)^3 + \ \ldots \tag{A.8}$$

Assuming linear disturbances (dρ << 1), Eq. (A.8) reduces to

$$dp = A_1\left(\frac{d\rho}{\overline{\rho}}\right) \tag{A.9}$$

By solving for A_1, Eq. (A.9) becomes

$$A_1 = \overline{\rho}\left(\frac{dp}{d\rho}\right) \tag{A.10}$$

which takes a form similar to the sound speed definition for a compressible fluid, given by

$$\overline{c}^2 = \left(\frac{dp}{d\rho}\right)\Bigg|_s \tag{A.11}$$

As the original Taylor Series Expansion presented in Eq. (A.5) assumes isentropic flow ($ds = 0$), A_1 can be written as

$$A_1 = \overline{\rho}\,\overline{c}^2 \tag{A.12}$$

By implementing this A_1 expression, the linearized equation of state relation can be written as

$$p = \overline{p} + \overline{\rho}\,\overline{c}^2\left(\frac{\rho - \overline{\rho}}{\overline{\rho}}\right) \tag{A.13}$$

where for acoustic perturbations

$$p = \overline{p} + p' \tag{A.14}$$

$$\rho = \overline{\rho} + \rho' \tag{A.15}$$

In Eqs. (A.14) and (A.15), the total pressure and density are broken down into the mean and fluctuating quantities, where the fluctuating portion pertains to the acoustic property. Substituting these parameters into Eq. (A.13) yields to the final form of the acoustic equation of state:

$$p' = \rho' \overline{c}^2 \tag{A.16}$$

As the acoustic equation of state has been found, the conservation equations can be linearized. To do this, the fluid velocity is separated exactly as were the fluid pressure and density in Eqs. (A.14) and (A.15), respectively. Thus, Reynolds decomposed fluid velocity is given by

$$\mathbf{u} = \overline{\mathbf{u}} + \mathbf{u}' \tag{A.17}$$

where for no mean flow $\overline{\mathbf{u}} = 0$.

Substituting these decomposed fluid parameters into the conservation of mass relation yields

$$\frac{\partial}{\partial t}(\overline{\rho} + \rho') + (\overline{\rho} + \rho') \bigtriangledown \cdot \mathbf{u}' + \mathbf{u}' \cdot \bigtriangledown(\overline{\rho} + \rho') = 0 \tag{A.18}$$

Expanding terms, Eq. (A.18) becomes

$$\frac{\partial \overline{\rho}}{\partial t} + \frac{\partial \rho'}{\partial t} + \overline{\rho} \bigtriangledown \cdot \mathbf{u}' + \rho' \bigtriangledown \cdot \mathbf{u}' + \mathbf{u}' \cdot \bigtriangledown \overline{\rho} + \mathbf{u}' \cdot \bigtriangledown \rho' = 0 \tag{A.19}$$

This expanded form of the mass conservation relation can be simplified through neglecting the higher order terms (i.e., those terms involving squared acoustic

fluctuation properties or higher) and applying the homogeneous medium assumption. Doing this, the linearized continuity equation is

$$\frac{\partial \rho'}{\partial t} + \overline{\rho} \bigtriangledown \cdot \mathbf{u}' = 0 \tag{A.20}$$

To arrive at the final form of the linearized mass conservation equation, the acoustic equation of state Eq. (A.16) is applied to Eq. (A.20):

$$\frac{1}{\overline{c}^2}\frac{\partial p'}{\partial t} + \overline{\rho} \bigtriangledown \cdot \mathbf{u}' = 0 \tag{A.21}$$

A similar process is carried out for the momentum conservation relation. Thus, the decomposed fluid parameters from Eqs. (A.14), (A.15) and (A.17) are substituted into the momentum conservation expression Eq. (A.2):

$$(\overline{\rho} + \rho')\frac{\partial \mathbf{u}'}{\partial t} + (\overline{\rho} + \rho')\Big((\mathbf{u}' \cdot \bigtriangledown)\mathbf{u}'\Big) + \bigtriangledown(\overline{p} + p') = 0 \tag{A.22}$$

Expanding terms, Eq. (A.22) becomes

$$\overline{\rho}\frac{\partial \mathbf{u}'}{\partial t} + \rho'\frac{\partial \mathbf{u}'}{\partial t} + \overline{\rho}\Big((\mathbf{u}' \cdot \bigtriangledown)\mathbf{u}'\Big) + \rho'\Big((\mathbf{u}' \cdot \bigtriangledown)\mathbf{u}'\Big) + \bigtriangledown\overline{p} + \bigtriangledown p' = 0 \tag{A.23}$$

As with the linearized continuity relation, Eq. (A.23) is simplified by neglecting the higher order terms and applying the homogeneous medium assumption. Doing this yields the final form of the linearized momentum conservation equation:

$$\overline{\rho}\frac{\partial \mathbf{u}'}{\partial t} + \bigtriangledown p' = 0 \tag{A.24}$$

To develop the acoustic wave equation, the time derivative of the linearized mass conservation equation and the divergence of the linearized momentum conservation equation are taken. This produces

$$\frac{\partial}{\partial t}\left(\frac{1}{\overline{c}^2}\frac{\partial p'}{\partial t} + \overline{\rho}\bigtriangledown\cdot\mathbf{u}'\right) = \frac{1}{\overline{c}^2}\frac{\partial^2 p'}{\partial t^2} + \overline{\rho}\frac{\partial}{\partial t}(\bigtriangledown\cdot\mathbf{u}') \tag{A.25}$$

and

$$\bigtriangledown\cdot\left(\overline{\rho}\frac{\partial\mathbf{u}'}{\partial t} + \bigtriangledown p'\right) = \overline{\rho}\left(\bigtriangledown\cdot\frac{\partial\mathbf{u}'}{\partial t}\right) + \bigtriangledown\cdot\bigtriangledown p' \tag{A.26}$$

where $\bigtriangledown\cdot\bigtriangledown p' = \bigtriangledown^2 p'$.

Subtracting Eq. (A.26) from Eq. (A.25) yields

$$\frac{1}{\overline{c}^2}\frac{\partial^2 p'}{\partial t^2} + \overline{\rho}\frac{\partial}{\partial t}(\bigtriangledown\cdot\mathbf{u}') - \overline{\rho}\left(\bigtriangledown\cdot\frac{\partial\mathbf{u}'}{\partial t}\right) - \bigtriangledown^2 p' = 0 \tag{A.27}$$

Due to the symmetry of second derivatives, it is recognized that

$$\overline{\rho}\frac{\partial}{\partial t}(\bigtriangledown\cdot\mathbf{u}') = \overline{\rho}\left(\bigtriangledown\cdot\frac{\partial\mathbf{u}'}{\partial t}\right) \tag{A.28}$$

Thus, implementing this relation into Eq. (A.27) produces the final form of the linear homogeneous acoustic wave equation:

$$\frac{1}{\overline{c}^2}\frac{\partial^2 p'}{\partial t^2} - \bigtriangledown^2 p' = 0 \tag{A.29}$$

A.2 Linear Homogeneous Acoustic Wave Equation: Cylindrical Coordinate System Transformation

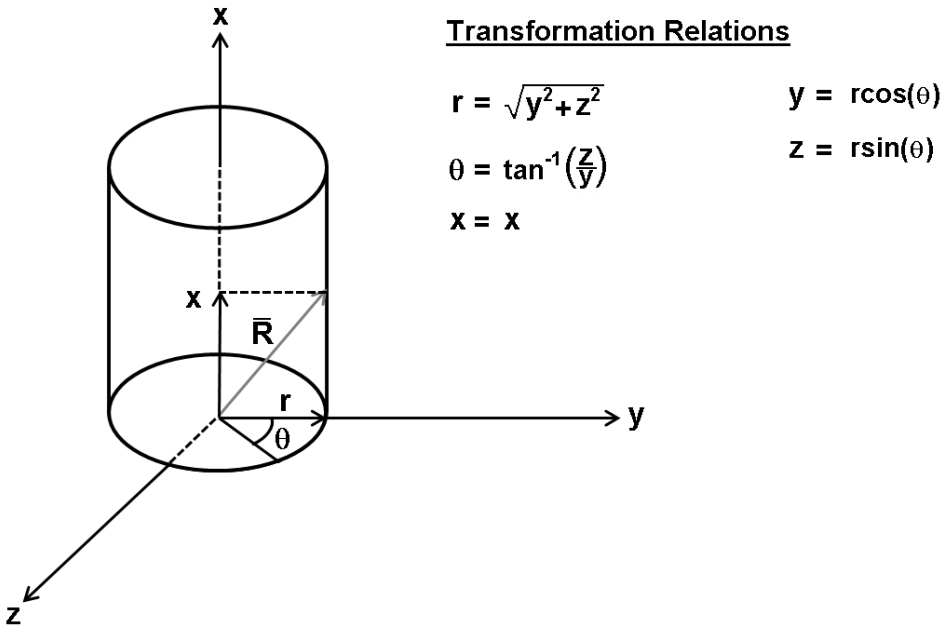

Transforming the linear homogeneous acoustic wave equation derived in Section A.1 into a cylindrical coordinate system provides a convenient equation form for the acoustic analysis of the model combustor (see Sections 4.1.1 and 4.1.2). To do this, the linear homogeneous acoustic wave equation in cartesian coordinates Eq. (A.29) is first expanded, which yields

$$\frac{1}{\overline{c}^2}\frac{\partial^2 p'}{\partial t^2} = \frac{\partial^2 p'}{\partial x^2} + \frac{\partial^2 p'}{\partial y^2} + \frac{\partial^2 p'}{\partial z^2} \tag{A.30}$$

This coordinate transformation entails the position vector $\overline{R}$ from the cartesian x-y-z coordinate system be represented in the cylindrical r-θ-x system. Thus, $\overline{R}$ can be expressed as

$$\overline{R} = \mathrm{fn}\big(r(x,y,z), \theta(x,y,z), x(x,y,z)\big) \tag{A.31}$$

Through the chain rule of calculus, the partial derivatives from Eq. (A.30) are transformed into the cylindrical coordinate system. Beginning with the x-dependent partial derivative, $\frac{\partial^2 p'}{\partial x^2}$ can be written as

$$\frac{\partial^2 p'}{\partial x^2} = \frac{\partial}{\partial x}\left(\frac{\partial p'}{\partial x}\right) \tag{A.32}$$

where

$$\frac{\partial p'}{\partial x} = \frac{\partial p'}{\partial r}\frac{\partial r}{\partial x} + \frac{\partial p'}{\partial \theta}\frac{\partial \theta}{\partial x} + \frac{\partial p'}{\partial x}\cancelto{1}{\frac{\partial x}{\partial x}} \tag{A.33}$$

Implementing the chain rule, Eq. (A.32) becomes

$$\begin{aligned}\frac{\partial^2 p'}{\partial x^2} = &\left[\frac{\partial}{\partial r}\left(\frac{\partial p'}{\partial r}\right)\frac{\partial r}{\partial x} + \frac{\partial}{\partial \theta}\left(\frac{\partial p'}{\partial r}\right)\frac{\partial \theta}{\partial x} + \frac{\partial}{\partial x}\left(\frac{\partial p'}{\partial r}\right)\cancelto{1}{\frac{\partial x}{\partial x}}\right]\frac{\partial r}{\partial x} + \frac{\partial p'}{\partial r}\left(\frac{\partial^2 r}{\partial x^2}\right) \\ &+ \left[\frac{\partial}{\partial r}\left(\frac{\partial p'}{\partial \theta}\right)\frac{\partial r}{\partial x} + \frac{\partial}{\partial \theta}\left(\frac{\partial p'}{\partial \theta}\right)\frac{\partial \theta}{\partial x} + \frac{\partial}{\partial x}\left(\frac{\partial p'}{\partial \theta}\right)\cancelto{1}{\frac{\partial x}{\partial x}}\right]\frac{\partial \theta}{\partial x} + \frac{\partial p'}{\partial \theta}\left(\frac{\partial^2 \theta}{\partial x^2}\right) \\ &+ \frac{\partial^2 p'}{\partial x^2}\end{aligned} \tag{A.34}$$

Expanding terms, Eq. (A.34) can be written as

$$\begin{aligned}\frac{\partial^2 p'}{\partial x^2} = &\frac{\partial^2 p'}{\partial r^2}\left(\frac{\partial r}{\partial x}\right)^2 + \frac{\partial^2 p'}{\partial \theta \partial r}\left(\frac{\partial \theta}{\partial x}\right)\left(\frac{\partial r}{\partial x}\right) + \frac{\partial^2 p'}{\partial x \partial r}\left(\frac{\partial r}{\partial x}\right) + \frac{\partial p'}{\partial r}\left(\frac{\partial^2 r}{\partial x^2}\right) \\ &+ \frac{\partial^2 p'}{\partial r \partial \theta}\left(\frac{\partial r}{\partial x}\right)\left(\frac{\partial \theta}{\partial x}\right) + \frac{\partial^2 p'}{\partial \theta^2}\left(\frac{\partial \theta}{\partial x}\right)^2 + \frac{\partial^2 p'}{\partial x \partial \theta}\left(\frac{\partial \theta}{\partial x}\right) + \frac{\partial p'}{\partial \theta}\left(\frac{\partial^2 \theta}{\partial x^2}\right) \\ &+ \frac{\partial^2 p'}{\partial x^2}\end{aligned} \tag{A.35}$$

To simplify this expression, the solely x-dependent partial derivatives are quantified using the transformation expressions relating the two coordinate systems.

Thus, the r-terms become

$$\frac{\partial r}{\partial x} = \frac{\partial}{\partial x}\left(\sqrt{y^2 + z^2}\right) = 0 \tag{A.36}$$

$$\frac{\partial^2 r}{\partial x^2} = \frac{\partial}{\partial x}\left(\frac{\partial r}{\partial x}\right) = \frac{\partial}{\partial x}\big(0\big) = 0 \tag{A.37}$$

while the θ-terms can be written as

$$\frac{\partial \theta}{\partial x} = \frac{\partial}{\partial x}\left(\tan^{-1}\left(\frac{z}{y}\right)\right) = \frac{1}{1 + (z/y)^2}\frac{\partial}{\partial x}\left(\frac{z}{y}\right) = \frac{1}{1 + (z/y)^2}\big(0\big) = 0 \tag{A.38}$$

$$\frac{\partial^2 \theta}{\partial x^2} = \frac{\partial}{\partial x}\left(\frac{\partial \theta}{\partial x}\right) = \frac{\partial}{\partial x}\big(0\big) = 0 \tag{A.39}$$

Substituting Eqs. (A.36)−(A.39) into Eq. (A.35) yields the final form of $\frac{\partial^2 p'}{\partial x^2}$:

$$\frac{\partial^2 p'}{\partial x^2} = \frac{\partial^2 p'}{\partial x^2} \tag{A.40}$$

As expected, the x-dependent partial derivative from Eq. (A.30) was not affected by the coordinate transformation.

Next, the y-dependent partial derivative from Eq. (A.30) is transformed using the same process as $\frac{\partial^2 p'}{\partial x^2}$. Therefore, $\frac{\partial^2 p'}{\partial y^2}$ can be expressed as

$$\frac{\partial^2 p'}{\partial y^2} = \frac{\partial}{\partial y}\left(\frac{\partial p'}{\partial y}\right) \tag{A.41}$$

where

$$\frac{\partial p'}{\partial y} = \frac{\partial p'}{\partial r}\frac{\partial r}{\partial y} + \frac{\partial p'}{\partial \theta}\frac{\partial \theta}{\partial y} + \frac{\partial p'}{\partial x}\frac{\partial x}{\partial y} \tag{A.42}$$

Using the chain rule, Eq. (A.41) can be written as

$$\begin{aligned}\frac{\partial^2 p'}{\partial y^2} = &\left[\frac{\partial}{\partial r}\left(\frac{\partial p'}{\partial r}\right)\frac{\partial r}{\partial y} + \frac{\partial}{\partial \theta}\left(\frac{\partial p'}{\partial r}\right)\frac{\partial \theta}{\partial y} + \frac{\partial}{\partial x}\left(\frac{\partial p'}{\partial r}\right)\frac{\partial x}{\partial y}\right]\frac{\partial r}{\partial y} + \frac{\partial p'}{\partial r}\left(\frac{\partial^2 r}{\partial y^2}\right) \\ &+ \left[\frac{\partial}{\partial r}\left(\frac{\partial p'}{\partial \theta}\right)\frac{\partial r}{\partial y} + \frac{\partial}{\partial \theta}\left(\frac{\partial p'}{\partial \theta}\right)\frac{\partial \theta}{\partial y} + \frac{\partial}{\partial x}\left(\frac{\partial p'}{\partial \theta}\right)\frac{\partial x}{\partial y}\right]\frac{\partial \theta}{\partial y} + \frac{\partial p'}{\partial \theta}\left(\frac{\partial^2 \theta}{\partial y^2}\right) \\ &+ \left[\frac{\partial}{\partial r}\left(\frac{\partial p'}{\partial x}\right)\frac{\partial r}{\partial y} + \frac{\partial}{\partial \theta}\left(\frac{\partial p'}{\partial x}\right)\frac{\partial \theta}{\partial y} + \frac{\partial}{\partial x}\left(\frac{\partial p'}{\partial x}\right)\frac{\partial x}{\partial y}\right]\frac{\partial x}{\partial y} + \frac{\partial p'}{\partial x}\left(\frac{\partial^2 x}{\partial y^2}\right)\end{aligned} \tag{A.43}$$

Expanding Eq. (A.43) yields

$$\begin{aligned}\frac{\partial^2 p'}{\partial y^2} = &\frac{\partial^2 p'}{\partial r^2}\left(\frac{\partial r}{\partial y}\right)^2 + \frac{\partial^2 p'}{\partial \theta \partial r}\left(\frac{\partial \theta}{\partial y}\right)\left(\frac{\partial r}{\partial y}\right) + \frac{\partial^2 p'}{\partial x \partial r}\left(\frac{\partial x}{\partial y}\right)\left(\frac{\partial r}{\partial y}\right) + \frac{\partial p'}{\partial r}\left(\frac{\partial^2 r}{\partial y^2}\right) \\ &+ \frac{\partial^2 p'}{\partial r \partial \theta}\left(\frac{\partial r}{\partial y}\right)\left(\frac{\partial \theta}{\partial y}\right) + \frac{\partial^2 p'}{\partial \theta^2}\left(\frac{\partial \theta}{\partial y}\right)^2 + \frac{\partial^2 p'}{\partial x \partial \theta}\left(\frac{\partial x}{\partial y}\right)\left(\frac{\partial \theta}{\partial y}\right) + \frac{\partial p'}{\partial \theta}\left(\frac{\partial^2 \theta}{\partial y^2}\right) \\ &+ \frac{\partial^2 p'}{\partial r \partial x}\left(\frac{\partial r}{\partial y}\right)\left(\frac{\partial x}{\partial y}\right) + \frac{\partial^2 p'}{\partial \theta \partial x}\left(\frac{\partial \theta}{\partial y}\right)\left(\frac{\partial x}{\partial y}\right) + \frac{\partial^2 p'}{\partial x^2}\left(\frac{\partial x}{\partial y}\right)^2 + \frac{\partial p'}{\partial x}\left(\frac{\partial^2 x}{\partial y^2}\right)\end{aligned} \tag{A.44}$$

To simplify Eq. (A.44), the entirely y-dependent partial derivatives are found from the transformation expressions relating the x-y-z and r-θ-x coordinate systems. For the r-terms, $\frac{\partial r}{\partial y}$ can be written as

$$\frac{\partial r}{\partial y} = \frac{\partial}{\partial y}\left(\sqrt{y^2 + z^2}\right) = 2y\left(\frac{1}{2\sqrt{y^2 + z^2}}\right) = \frac{y}{\sqrt{y^2 + z^2}} \tag{A.45}$$

where $y = r\cos(\theta)$ and $r = \sqrt{y^2 + z^2}$.

Thus, $\frac{\partial r}{\partial y}$ becomes

$$\frac{\partial r}{\partial y} = \frac{r\cos(\theta)}{r} = \cos(\theta) \tag{A.46}$$

Similarly, $\frac{\partial^2 r}{\partial y^2}$ can be expressed as

$$\frac{\partial^2 r}{\partial y^2} = \frac{\partial}{\partial y}\left(\frac{\partial r}{\partial y}\right) = \frac{\partial}{\partial y}\left(\frac{y}{\sqrt{y^2+z^2}}\right) = \frac{1}{\sqrt{y^2+z^2}} - \frac{y^2}{(y^2+z^2)^{3/2}} \tag{A.47}$$

where $y = r\cos(\theta)$ and $r = \sqrt{y^2+z^2}$.

Substituting these variable expressions and the Pythagorean identity $\sin^2(\theta) + \cos^2(\theta) = 1$ into Eq. (A.47) produces

$$\frac{\partial^2 r}{\partial y^2} = \frac{\sin^2(\theta)}{r} \tag{A.48}$$

Now considering the θ-terms, $\frac{\partial \theta}{\partial y}$ can be written as

$$\frac{\partial \theta}{\partial y} = \frac{\partial}{\partial y}\left(\tan^{-1}\left(\frac{z}{y}\right)\right) = \frac{1}{1+(z/y)^2}\frac{\partial}{\partial y}\left(\frac{z}{y}\right) = \frac{-z}{y^2+z^2} \tag{A.49}$$

where $z = r\sin(\theta)$ and $r = \sqrt{y^2+z^2}$.

From this, Eq. (A.49) becomes

$$\frac{\partial \theta}{\partial y} = \frac{-r\sin(\theta)}{r^2} = \frac{-\sin(\theta)}{r} \tag{A.50}$$

The same process is followed for $\frac{\partial^2 \theta}{\partial y^2}$:

$$\frac{\partial^2 \theta}{\partial y^2} = \frac{\partial}{\partial y}\left(\frac{\partial \theta}{\partial y}\right) = \frac{\partial}{\partial y}\left(\frac{-z}{y^2+z^2}\right) = \frac{2yz}{(y^2+z^2)^2} \tag{A.51}$$

where $y = r\cos(\theta)$, $z = r\sin(\theta)$ and $r = \sqrt{y^2+z^2}$.

Thus, Eq. (A.51) can be written as

$$\frac{\partial^2 \theta}{\partial y^2} = \frac{2\big(r\cos(\theta)\big)\big(r\sin(\theta)\big)}{r^4} = \frac{2\cos(\theta)\sin(\theta)}{r^2} \tag{A.52}$$

Similarly, the x-terms reduce to

$$\frac{\partial x}{\partial y} = \frac{\partial}{\partial y}(x) = 0 \tag{A.53}$$

$$\frac{\partial^2 x}{\partial y^2} = \frac{\partial}{\partial y}\left(\frac{\partial x}{\partial y}\right) = \frac{\partial}{\partial y}(0) = 0 \tag{A.54}$$

Substituting the expressions for $\frac{\partial r}{\partial y}$, $\frac{\partial^2 r}{\partial y^2}$, $\frac{\partial \theta}{\partial y}$, $\frac{\partial^2 \theta}{\partial y^2}$, $\frac{\partial x}{\partial y}$ and $\frac{\partial^2 x}{\partial y^2}$ into Eq. (A.44) yields the final form for $\frac{\partial^2 p'}{\partial y^2}$:

$$\begin{aligned}\frac{\partial^2 p'}{\partial y^2} = {} & \cos^2(\theta)\frac{\partial^2 p'}{\partial r^2} - \frac{\sin(\theta)\cos(\theta)}{r}\frac{\partial^2 p'}{\partial \theta \partial r} + \frac{\sin^2(\theta)}{r}\frac{\partial p'}{\partial r} \\ & - \frac{\cos(\theta)\sin(\theta)}{r}\frac{\partial^2 p'}{\partial r \partial \theta} + \frac{\sin^2(\theta)}{r^2}\frac{\partial^2 p'}{\partial \theta^2} + \frac{2\cos(\theta)\sin(\theta)}{r^2}\frac{\partial p'}{\partial \theta}\end{aligned} \tag{A.55}$$

Finally, the z-dependent partial derivative $\frac{\partial^2 p'}{\partial z^2}$ is determined using the same method as $\frac{\partial^2 p'}{\partial x^2}$ and $\frac{\partial^2 p'}{\partial y^2}$. Therefore, $\frac{\partial^2 p'}{\partial z^2}$ can be written as

$$\frac{\partial^2 p'}{\partial z^2} = \frac{\partial}{\partial z}\left(\frac{\partial p'}{\partial z}\right) \tag{A.56}$$

where

$$\frac{\partial p'}{\partial z} = \frac{\partial p'}{\partial r}\frac{\partial r}{\partial z} + \frac{\partial p'}{\partial \theta}\frac{\partial \theta}{\partial z} + \frac{\partial p'}{\partial x}\frac{\partial x}{\partial z} \tag{A.57}$$

Implementing the chain rule for Eq. (A.56) yields

$$\begin{aligned}\frac{\partial^2 p'}{\partial z^2} = {} & \left[\frac{\partial}{\partial r}\left(\frac{\partial p'}{\partial r}\right)\frac{\partial r}{\partial z} + \frac{\partial}{\partial \theta}\left(\frac{\partial p'}{\partial r}\right)\frac{\partial \theta}{\partial z} + \frac{\partial}{\partial x}\left(\frac{\partial p'}{\partial r}\right)\frac{\partial x}{\partial z}\right]\frac{\partial r}{\partial z} + \frac{\partial p'}{\partial r}\left(\frac{\partial^2 r}{\partial z^2}\right) \\ & + \left[\frac{\partial}{\partial r}\left(\frac{\partial p'}{\partial \theta}\right)\frac{\partial r}{\partial z} + \frac{\partial}{\partial \theta}\left(\frac{\partial p'}{\partial \theta}\right)\frac{\partial \theta}{\partial z} + \frac{\partial}{\partial x}\left(\frac{\partial p'}{\partial \theta}\right)\frac{\partial x}{\partial z}\right]\frac{\partial \theta}{\partial z} + \frac{\partial p'}{\partial \theta}\left(\frac{\partial^2 \theta}{\partial z^2}\right) \\ & + \left[\frac{\partial}{\partial r}\left(\frac{\partial p'}{\partial x}\right)\frac{\partial r}{\partial z} + \frac{\partial}{\partial \theta}\left(\frac{\partial p'}{\partial x}\right)\frac{\partial \theta}{\partial z} + \frac{\partial}{\partial x}\left(\frac{\partial p'}{\partial x}\right)\frac{\partial x}{\partial z}\right]\frac{\partial x}{\partial z} + \frac{\partial p'}{\partial x}\left(\frac{\partial^2 x}{\partial z^2}\right)\end{aligned} \tag{A.58}$$

Expanding Eq. (A.58) produces

$$\begin{aligned}\frac{\partial^2 p'}{\partial z^2} = &\frac{\partial^2 p'}{\partial r^2}\left(\frac{\partial r}{\partial z}\right)^2 + \frac{\partial^2 p'}{\partial \theta \partial r}\left(\frac{\partial \theta}{\partial z}\right)\left(\frac{\partial r}{\partial z}\right) + \frac{\partial^2 p'}{\partial x \partial r}\left(\frac{\partial x}{\partial z}\right)\left(\frac{\partial r}{\partial z}\right) + \frac{\partial p'}{\partial r}\left(\frac{\partial^2 r}{\partial z^2}\right) \\ &+ \frac{\partial^2 p'}{\partial r \partial \theta}\left(\frac{\partial r}{\partial z}\right)\left(\frac{\partial \theta}{\partial z}\right) + \frac{\partial^2 p'}{\partial \theta^2}\left(\frac{\partial \theta}{\partial z}\right)^2 + \frac{\partial^2 p'}{\partial x \partial \theta}\left(\frac{\partial x}{\partial z}\right)\left(\frac{\partial \theta}{\partial z}\right) + \frac{\partial p'}{\partial \theta}\left(\frac{\partial^2 \theta}{\partial z^2}\right) \\ &+ \frac{\partial^2 p'}{\partial r \partial x}\left(\frac{\partial r}{\partial z}\right)\left(\frac{\partial x}{\partial z}\right) + \frac{\partial^2 p'}{\partial \theta \partial x}\left(\frac{\partial \theta}{\partial z}\right)\left(\frac{\partial x}{\partial z}\right) + \frac{\partial^2 p'}{\partial x^2}\left(\frac{\partial x}{\partial z}\right)^2 + \frac{\partial p'}{\partial x}\left(\frac{\partial^2 x}{\partial z^2}\right)\end{aligned} \tag{A.59}$$

To simplify this expression, the z-dependent partial derivatives in terms of the original coordinate system are transformed into the r-θ-x system using the respective coordinate relations. Thus, $\frac{\partial r}{\partial z}$ can be written as

$$\frac{\partial r}{\partial z} = \frac{\partial}{\partial z}\left(\sqrt{y^2 + z^2}\right) = 2z\left(\frac{1}{2\sqrt{y^2 + z^2}}\right) = \frac{z}{\sqrt{y^2 + z^2}} \tag{A.60}$$

where $z = r\sin(\theta)$ and $r = \sqrt{y^2 + z^2}$.

Implementing these variable expressions, Eq. (A.60) becomes

$$\frac{\partial r}{\partial z} = \frac{r\sin(\theta)}{r} = \sin(\theta) \tag{A.61}$$

Similarly, $\frac{\partial^2 r}{\partial z^2}$ can be written as

$$\frac{\partial^2 r}{\partial z^2} = \frac{\partial}{\partial z}\left(\frac{\partial r}{\partial z}\right) = \frac{\partial}{\partial z}\left(\frac{z}{\sqrt{y^2 + z^2}}\right) = \frac{1}{\sqrt{y^2 + z^2}} - \frac{z^2}{(y^2 + z^2)^{3/2}} \tag{A.62}$$

where $z = r\sin(\theta)$ and $r = \sqrt{y^2 + z^2}$.

Incorporating these coordinate relations and the Pythagorean identity produces

$$\frac{\partial^2 r}{\partial z^2} = \frac{\cos^2(\theta)}{r} \tag{A.63}$$

For the θ-terms, $\frac{\partial \theta}{\partial z}$ can be expressed as

$$\frac{\partial \theta}{\partial z} = \frac{\partial}{\partial z}\left(\tan^{-1}\left(\frac{z}{y}\right)\right) = \frac{1}{1+(z/y)^2}\frac{\partial}{\partial z}\left(\frac{z}{y}\right) = \frac{y}{y^2+z^2} \tag{A.64}$$

where $y = r\cos(\theta)$ and $r = \sqrt{y^2+z^2}$.

Thus, Eq. (A.64) becomes

$$\frac{\partial \theta}{\partial z} = \frac{r\cos(\theta)}{r^2} = \frac{\cos(\theta)}{r} \tag{A.65}$$

$\frac{\partial^2 \theta}{\partial z^2}$ can similarly be transformed:

$$\frac{\partial^2 \theta}{\partial z^2} = \frac{\partial}{\partial z}\left(\frac{\partial \theta}{\partial z}\right) = \frac{\partial}{\partial z}\left(\frac{y}{y^2+z^2}\right) = \frac{-2zy}{(y^2+z^2)^2} \tag{A.66}$$

where $y = r\cos(\theta)$, $z = r\sin(\theta)$ and $r = \sqrt{y^2+z^2}$.

Substituting these variable expressions into Eq. (A.66) yields

$$\frac{\partial^2 \theta}{\partial z^2} = \frac{-2\big(r\sin(\theta)\big)\big(r\cos(\theta)\big)}{r^4} = \frac{-2\sin(\theta)\cos(\theta)}{r^2} \tag{A.67}$$

Finally, the x-terms can be expressed as

$$\frac{\partial x}{\partial z} = \frac{\partial}{\partial z}(x) = 0 \tag{A.68}$$

$$\frac{\partial^2 x}{\partial z^2} = \frac{\partial}{\partial z}\left(\frac{\partial x}{\partial z}\right) = \frac{\partial}{\partial x}(0) = 0 \tag{A.69}$$

Substituting the expressions for $\frac{\partial r}{\partial z}$, $\frac{\partial^2 r}{\partial z^2}$, $\frac{\partial \theta}{\partial z}$, $\frac{\partial^2 \theta}{\partial z^2}$, $\frac{\partial x}{\partial z}$ and $\frac{\partial^2 x}{\partial z^2}$ into Eq. (A.59) produces the final form for $\frac{\partial^2 p'}{\partial z^2}$:

$$\frac{\partial^2 p'}{\partial z^2} = \sin^2(\theta)\frac{\partial^2 p'}{\partial r^2} + \frac{\cos(\theta)\sin(\theta)}{r}\frac{\partial^2 p'}{\partial \theta \partial r} + \frac{\cos^2(\theta)}{r}\frac{\partial p'}{\partial r} + \frac{\sin(\theta)\cos(\theta)}{r}\frac{\partial^2 p'}{\partial r \partial \theta} + \frac{\cos^2(\theta)}{r^2}\frac{\partial^2 p'}{\partial \theta^2} - \frac{2\sin(\theta)\cos(\theta)}{r^2}\frac{\partial p'}{\partial \theta} \tag{A.70}$$

With the three x-y-z partial derivatives successfully transformed from the cartesian coordinate system into the cylindrical system, they are substituted into the cartesian form of the linear homogeneous acoustic wave equation. This yields the following:

$$\begin{aligned}\frac{1}{\bar{c}^2}\frac{\partial^2 p'}{\partial t^2} = \frac{\partial^2 p'}{\partial x^2} &+ \cos^2(\theta)\frac{\partial^2 p'}{\partial r^2} - \frac{\sin(\theta)\cos(\theta)}{r}\frac{\partial^2 p'}{\partial \theta \partial r} + \frac{\sin^2(\theta)}{r}\frac{\partial p'}{\partial r} - \frac{\cos(\theta)\sin(\theta)}{r}\frac{\partial^2 p'}{\partial r \partial \theta} \\ &+ \frac{\sin^2(\theta)}{r^2}\frac{\partial^2 p'}{\partial \theta^2} + \frac{2\cos(\theta)\sin(\theta)}{r^2}\frac{\partial p'}{\partial \theta} + \sin^2(\theta)\frac{\partial^2 p'}{\partial r^2} + \frac{\cos(\theta)\sin(\theta)}{r}\frac{\partial^2 p'}{\partial \theta \partial r} \\ &+ \frac{\cos^2(\theta)}{r}\frac{\partial p'}{\partial r} + \frac{\sin(\theta)\cos(\theta)}{r}\frac{\partial^2 p'}{\partial r \partial \theta} + \frac{\cos^2(\theta)}{r^2}\frac{\partial^2 p'}{\partial \theta^2} - \frac{2\sin(\theta)\cos(\theta)}{r^2}\frac{\partial p'}{\partial \theta}\end{aligned} \tag{A.71}$$

Grouping similar terms, Eq. (A.71) becomes

$$\begin{aligned}\frac{1}{\bar{c}^2}\frac{\partial^2 p'}{\partial t^2} = \frac{\partial^2 p'}{\partial x^2} &+ \left(\cos^2(\theta) + \sin^2(\theta)\right)\frac{\partial^2 p'}{\partial r^2} + \left(\frac{\cos(\theta)\sin(\theta) - \sin(\theta)\cos(\theta)}{r}\right)\frac{\partial^2 p'}{\partial \theta \partial r} \\ &+ \left(\frac{\cos^2(\theta) + \sin^2(\theta)}{r^2}\right)\frac{\partial^2 p'}{\partial \theta^2} + \left(\frac{2\cos(\theta)\sin(\theta) - 2\sin(\theta)\cos(\theta)}{r^2}\right)\frac{\partial p'}{\partial \theta} \\ &+ \left(\frac{\cos^2(\theta) + \sin^2(\theta)}{r}\right)\frac{\partial p'}{\partial r} + \left(\frac{\sin(\theta)\cos(\theta) - \cos(\theta)\sin(\theta)}{r}\right)\frac{\partial^2 p'}{\partial r \partial \theta}\end{aligned} \tag{A.72}$$

Employing the Pythagorean identity and simplifying this expression produces the final form of the linear homogeneous acoustic wave equation in cylindrical coordinates:

$$\frac{1}{\bar{c}^2}\frac{\partial^2 p'}{\partial t^2} = \frac{\partial^2 p'}{\partial x^2} + \frac{\partial^2 p'}{\partial r^2} + \frac{1}{r}\frac{\partial p'}{\partial r} + \frac{1}{r^2}\frac{\partial^2 p'}{\partial \theta^2} \tag{A.73}$$

A.3 Cylindrical Chamber Acoustic Mode Pressure Distribution Solution Transformation

Within Section 4.1.1, the acoustic mode pressure distribution for a cylindrical chamber closed on both ends was developed. This is given by

$$\begin{aligned} p'(r,\theta,x,t) &= X(x)\Phi(\theta)R(r)\exp(i\omega t) \\ &= C_2\cos\left(\frac{l\pi x}{L_x}\right)\Big(C_3\sin(m\theta)+C_4\cos(m\theta)\Big)C_5J_m(k_r r)\exp(i\omega t) \end{aligned} \quad \text{(A.74)}$$

which can be simplified and transformed into a useful form similar to that of Zucrow [38]. To do this, the amplitude constants are first combined. This yields

$$p'(r,\theta,x,t) = J_m(k_r r)\cos\left(\frac{l\pi x}{L_x}\right)\Big(C_3^*\sin(m\theta)+C_4^*\cos(m\theta)\Big)\exp(i\omega t) \quad \text{(A.75)}$$

where $C_3^* = C_2C_3$ and $C_4^* = C_2C_4$.

Applying Euler's Formula $\exp(i\omega t) = \cos(\omega t) + i\sin(\omega t)$, Eq. (A.75) becomes

$$p'(r,\theta,x,t) = J_m(k_r r)\cos\left(\frac{l\pi x}{L_x}\right)\Big(C_3^*\sin(m\theta)+C_4^*\cos(m\theta)\Big)\Big(\cos(\omega t)+i\sin(\omega t)\Big) \quad \text{(A.76)}$$

Expanding terms and grouping constants, Eq. (A.76) can be written as

$$\begin{aligned} p'(r,\theta,x,t) = J_m(k_r r)\cos\left(\frac{l\pi x}{L_x}\right)\Big(&A_1\sin(m\theta)\cos(\omega t)+A_2\cos(m\theta)\cos(\omega t) \\ &+A_3\sin(m\theta)\sin(\omega t)+A_4\cos(m\theta)\sin(\omega t)\Big) \end{aligned} \quad \text{(A.77)}$$

where $A_1 = C_3^*$, $A_2 = C_4^*$, $A_3 = iC_3^*$ and $A_4 = iC_4^*$.

To further simplify this expression, the following sine and cosine product trigonometric identities are imposed:

$$\sin(\alpha)\cos(\gamma) = \frac{\sin(\alpha+\gamma)+\sin(\alpha-\gamma)}{2} \tag{A.78.A}$$

$$\cos(\alpha)\cos(\gamma) = \frac{\cos(\alpha-\gamma)+\cos(\alpha+\gamma)}{2} \tag{A.78.B}$$

$$\sin(\alpha)\sin(\gamma) = \frac{\cos(\alpha-\gamma)-\cos(\alpha+\gamma)}{2} \tag{A.78.C}$$

$$\cos(\alpha)\sin(\gamma) = \frac{\sin(\alpha+\gamma)-\sin(\alpha-\gamma)}{2} \tag{A.78.D}$$

Implementing these identities into Eq. (A.77) and grouping similar trigonometric functions produces

$$\begin{aligned} p'(r,\theta,x,t) = J_m(k_r r)\cos\left(\frac{l\pi x}{L_x}\right)* \\ \left[\cos(m\theta-\omega t)\left(\frac{A_2+A_3}{2}\right)+\cos(m\theta+\omega t)\left(\frac{A_2-A_3}{2}\right)\right. \\ \left.+\sin(m\theta-\omega t)\left(\frac{A_1-A_4}{2}\right)+\sin(m\theta+\omega t)\left(\frac{A_1+A_4}{2}\right)\right] \end{aligned} \tag{A.79}$$

To reduce the number of amplitude constants and introduce the desired phase offset terms (ϕ_1 and ϕ_2), the following four relations are defined:

$$G\cos(\phi_2) = \frac{A_2+A_3}{2} \tag{A.80.A}$$

$$F\cos(\phi_1) = \frac{A_2-A_3}{2} \tag{A.80.B}$$

$$G\sin(\phi_2) = \frac{A_1-A_4}{2} \tag{A.80.C}$$

$$F\sin(\phi_1) = \frac{A_1+A_4}{2} \tag{A.80.D}$$

By substituting in the four relations from Eq. (A.80) and grouping similar terms, the pressure distribution relation becomes

$$p'(r,\theta,x,t) = J_m(k_r r)\cos\left(\frac{l\pi x}{L_x}\right)* \left[F\left(\cos(m\theta+\omega t)\cos(\phi_1)+\sin(m\theta+\omega t)\sin(\phi_1)\right) + G\left(\cos(m\theta-\omega t)\cos(\phi_2)+\sin(m\theta-\omega t)\sin(\phi_2)\right)\right] \quad \text{(A.81)}$$

To arrive at the final pressure distribution expression similar to the form presented by Zucrow, the Eq. (A.78) trigonometric identities again are applied to Eq. (A.81):

$$p'(r,\theta,x,t) = J_m(k_r r)\cos\left(\frac{l\pi x}{L_x}\right)\left[F\cos(m\theta+\omega t-\phi_1)+G\cos(m\theta-\omega t-\phi_2)\right] \quad \text{(A.82)}$$

A.4 Linear Homogeneous Acoustic Wave Equation with Uniform Mean Flow

The linear homogeneous acoustic wave equation with mean flow describes the motion of acoustic waves through a medium with a uniform flow. In this analysis, small amplitude disturbances are assumed to propagate in a homogeneous medium with a uniform bulk flow velocity. To derive this expression, the same process from Section A.1 is employed, where the mass and momentum conservation equations are combined with the equation of state relation Eq. (A.16). Prior to combining these relations, a linearization process is again performed on the conservation equations to successfully account for the small disturbance assumption. As the development of this acoustic wave equation is similar to the standard acoustic wave equation, the derivation will begin with the mass conservation equation, given by

$$\frac{\partial \rho}{\partial t} + \bigtriangledown \cdot (\rho \mathbf{u}) = 0 \tag{A.83}$$

Decomposing the fluid properties into their mean and fluctuating properties yields

$$p = \overline{p} + p' \tag{A.84.A}$$

$$\rho = \overline{\rho} + \rho' \tag{A.84.B}$$

$$\mathbf{u} = \overline{\mathbf{u}} + \mathbf{u}' \tag{A.84.C}$$

where $\overline{\mathbf{u}} \neq 0$.

Substituting in the Reynolds decomposed density and velocity parameters, Eq. (A.83) becomes

$$\frac{\partial}{\partial t}\left(\overline{\rho} + \rho'\right) + (\overline{\rho} + \rho') \bigtriangledown \cdot (\overline{\mathbf{u}} + \mathbf{u}') + (\overline{\mathbf{u}} + \mathbf{u}') \cdot \bigtriangledown (\overline{\rho} + \rho') = 0 \tag{A.85}$$

Expanding terms, Eq. (A.85) can be expressed as

$$\frac{\partial \overline{\rho}}{\partial t} + \frac{\partial \rho'}{\partial t} + \overline{\rho} \bigtriangledown \cdot \overline{\mathbf{u}} + \overline{\rho} \bigtriangledown \cdot \mathbf{u}' + \rho' \bigtriangledown \cdot \overline{\mathbf{u}} + \rho' \bigtriangledown \cdot \mathbf{u}'$$
$$+ (\overline{\mathbf{u}} \cdot \bigtriangledown)\overline{\rho} + (\overline{\mathbf{u}} \cdot \bigtriangledown)\rho' + (\mathbf{u}' \cdot \bigtriangledown)\overline{\rho} + (\mathbf{u}' \cdot \bigtriangledown)\rho' = 0 \tag{A.86}$$

This relation can be simplified through neglecting the higher order terms and applying the homogeneous medium assumption. Doing this, the linearized mass conservation equation can be written as

$$\frac{\partial \rho'}{\partial t} + \overline{\rho} \bigtriangledown \cdot \mathbf{u}' + (\overline{\mathbf{u}} \cdot \bigtriangledown)\rho' = 0 \tag{A.87}$$

To arrive at the final form of the linearized mass conservation equation, the acoustic equation of state Eq. (A.16) is substituted into Eq. (A.87):

$$\frac{1}{\overline{c}^2}\left(\frac{\partial}{\partial t} + (\overline{\mathbf{u}} \cdot \bigtriangledown)\right)p' + \overline{\rho} \bigtriangledown \cdot \mathbf{u}' = 0 \tag{A.88}$$

The same process is carried out for the momentum conservation relation, given by

$$\rho \frac{\overline{\mathrm{D}}\mathbf{u}}{\overline{\mathrm{D}}t} = - \bigtriangledown p \tag{A.89}$$

where

$$\frac{\overline{\mathrm{D}}\mathbf{u}}{\overline{\mathrm{D}}t} = \frac{\partial \mathbf{u}}{\partial t} + (\mathbf{u} \cdot \bigtriangledown)\mathbf{u} \tag{A.90}$$

Again, the decomposed fluid properties from Eq. (A.84) are substituted into Eq. (A.89), yielding

$$\left(\overline{\rho} + \rho'\right)\frac{\partial}{\partial t}\left(\overline{\mathbf{u}} + \mathbf{u}'\right) + (\overline{\rho} + \rho')\left[\left((\overline{\mathbf{u}} + \mathbf{u}') \cdot \bigtriangledown\right)(\overline{\mathbf{u}} + \mathbf{u}')\right] + \bigtriangledown(\overline{p} + p') = 0 \tag{A.91}$$

Expanding terms, Eq. (A.91) becomes

$$\overline{\rho}\frac{\partial\overline{\mathbf{u}}}{\partial t}+\overline{\rho}\frac{\partial\mathbf{u}'}{\partial t}+\rho'\frac{\partial\overline{\mathbf{u}}}{\partial t}+\rho'\frac{\partial\mathbf{u}'}{\partial t}+\overline{\rho}\Big((\overline{\mathbf{u}}\cdot\bigtriangledown)\overline{\mathbf{u}}+(\overline{\mathbf{u}}\cdot\bigtriangledown)\mathbf{u}'+(\mathbf{u}'\cdot\bigtriangledown)\overline{\mathbf{u}}+(\mathbf{u}'\cdot\bigtriangledown)\mathbf{u}'\Big)$$
$$+\rho'\Big((\overline{\mathbf{u}}\cdot\bigtriangledown)\overline{\mathbf{u}}+(\overline{\mathbf{u}}\cdot\bigtriangledown)\mathbf{u}'+(\mathbf{u}'\cdot\bigtriangledown)\overline{\mathbf{u}}+(\mathbf{u}'\cdot\bigtriangledown)\mathbf{u}'\Big)+\bigtriangledown\overline{p}+\bigtriangledown p'=0 \quad \text{(A.92)}$$

As with the linearized mass conservation equation, Eq. (A.92) is simplified by neglecting the higher order terms and applying the homogeneous medium assumption. Doing this produces the final form of the linearized momentum conservation equation:

$$\overline{\rho}\Big(\frac{\partial}{\partial t}+(\overline{\mathbf{u}}\cdot\bigtriangledown)\Big)\mathbf{u}'+\bigtriangledown p'=0 \quad \text{(A.93)}$$

Now that the conservation equations are linearized, $\Big(\frac{\partial}{\partial \mathrm{t}}+(\overline{\mathbf{u}}\cdot\bigtriangledown)\Big)$ is applied to Eq. (A.88) and the divergence of Eq. (A.93) is taken. This yields

$$\Big(\frac{\partial}{\partial t}+(\overline{\mathbf{u}}\cdot\bigtriangledown)\Big)\Big(\frac{1}{\overline{c}^2}\Big(\frac{\partial}{\partial t}+(\overline{\mathbf{u}}\cdot\bigtriangledown)\Big)p'+\overline{\rho}\bigtriangledown\cdot\mathbf{u}'\Big)=$$
$$\frac{1}{\overline{c}^2}\Big(\frac{\partial}{\partial t}+(\overline{\mathbf{u}}\cdot\bigtriangledown)\Big)\Big(\frac{\partial}{\partial t}+(\overline{\mathbf{u}}\cdot\bigtriangledown)\Big)p'+\overline{\rho}\Big(\frac{\partial}{\partial t}+(\overline{\mathbf{u}}\cdot\bigtriangledown)\Big)(\bigtriangledown\cdot\mathbf{u}') \quad \text{(A.94)}$$

and

$$\bigtriangledown\cdot\Big(\overline{\rho}\Big(\frac{\partial}{\partial t}+(\overline{\mathbf{u}}\cdot\bigtriangledown)\Big)\mathbf{u}'+\bigtriangledown p'\Big)=\overline{\rho}\bigtriangledown\cdot\Big(\frac{\partial}{\partial t}+(\overline{\mathbf{u}}\cdot\bigtriangledown)\Big)\mathbf{u}'+\bigtriangledown\cdot\bigtriangledown p' \quad \text{(A.95)}$$

where $\bigtriangledown\cdot\bigtriangledown p'=\bigtriangledown^2 p'$.

Subtracting Eq. (A.95) from Eq. (A.96) produces

$$\frac{1}{\overline{c}^2}\Big(\frac{\partial}{\partial t}+(\overline{\mathbf{u}}\cdot\bigtriangledown)\Big)\Big(\frac{\partial}{\partial t}+(\overline{\mathbf{u}}\cdot\bigtriangledown)\Big)p'+\overline{\rho}\Big(\frac{\partial}{\partial t}+(\overline{\mathbf{u}}\cdot\bigtriangledown)\Big)(\bigtriangledown\cdot\mathbf{u}')$$
$$-\overline{\rho}\bigtriangledown\cdot\Big(\frac{\partial}{\partial t}+(\overline{\mathbf{u}}\cdot\bigtriangledown)\Big)\mathbf{u}'-\bigtriangledown^2 p'=0 \quad \text{(A.96)}$$

Due to the symmetry of second derivatives,

$$\overline{\rho}\left(\frac{\partial}{\partial t}+(\overline{\mathbf{u}}\cdot\bigtriangledown)\right)(\bigtriangledown\cdot\mathbf{u}')=\overline{\rho}\bigtriangledown\cdot\left(\frac{\partial}{\partial t}+(\overline{\mathbf{u}}\cdot\bigtriangledown)\right)\mathbf{u}' \tag{A.97}$$

Therefore, incorporating this symmetry law into Eq. (A.96) provides the final form of the linear homogeneous acoustic wave equation with a uniform mean flow:

$$\frac{1}{\overline{c}^2}\left(\frac{\partial}{\partial t}+(\overline{\mathbf{u}}\cdot\bigtriangledown)\right)\left(\frac{\partial}{\partial t}+(\overline{\mathbf{u}}\cdot\bigtriangledown)\right)p'-\bigtriangledown^2p'=0 \tag{A.98}$$

Eq. (A.98) is also commonly written as

$$\frac{1}{\overline{c}^2}\frac{\overline{\mathrm{D}}^2p'}{\overline{\mathrm{D}}t^2}-\bigtriangledown^2p'=0 \tag{A.99}$$

where

$$\frac{\overline{\mathrm{D}}}{\overline{\mathrm{D}}t}=\frac{\partial}{\partial t}+(\overline{\mathbf{u}}\cdot\bigtriangledown) \tag{A.100}$$

APPENDIX B

SUPPLEMENTAL EXPERIMENTAL RESULTS

Presented in this appendix are supplemental results from selected experiments.

B.1 Band-Limited White Noise: Principle Baseline Testing

B.1.1 Test 06-28-01: Waterfall Plot Supplement

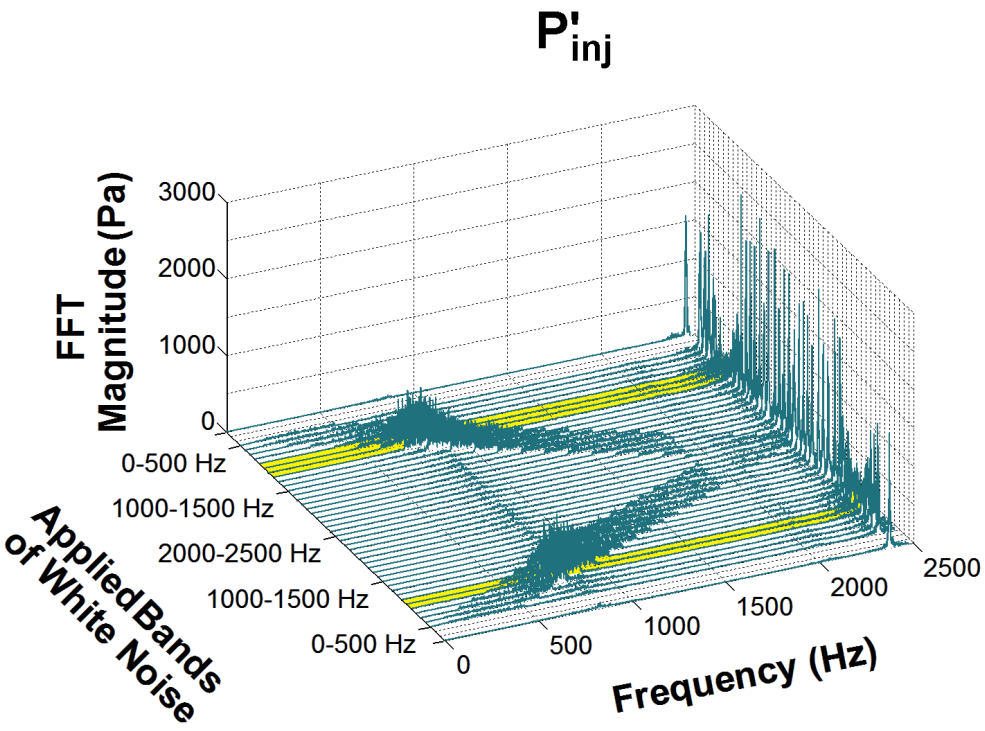

Figure B.1: Enlarged Waterfall Plot for Test 06-28-01: P'_{inj}.

B.1.2 Test 06-28-02: Waterfall Plot Supplement

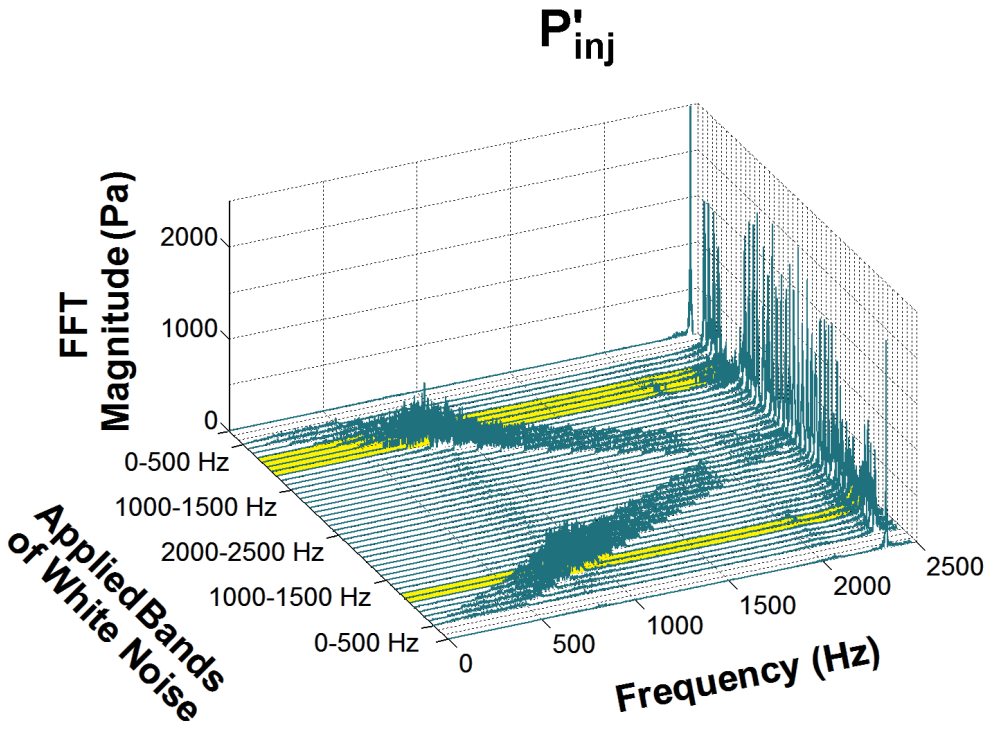

Figure B.2: Enlarged Waterfall Plot for Test 06-28-02: P'_{inj}.

B.2 Single-Frequency Acoustic Modulation: Principle Baseline Testing

B.2.1 Test 08-01-04: Waterfall Plot Supplement

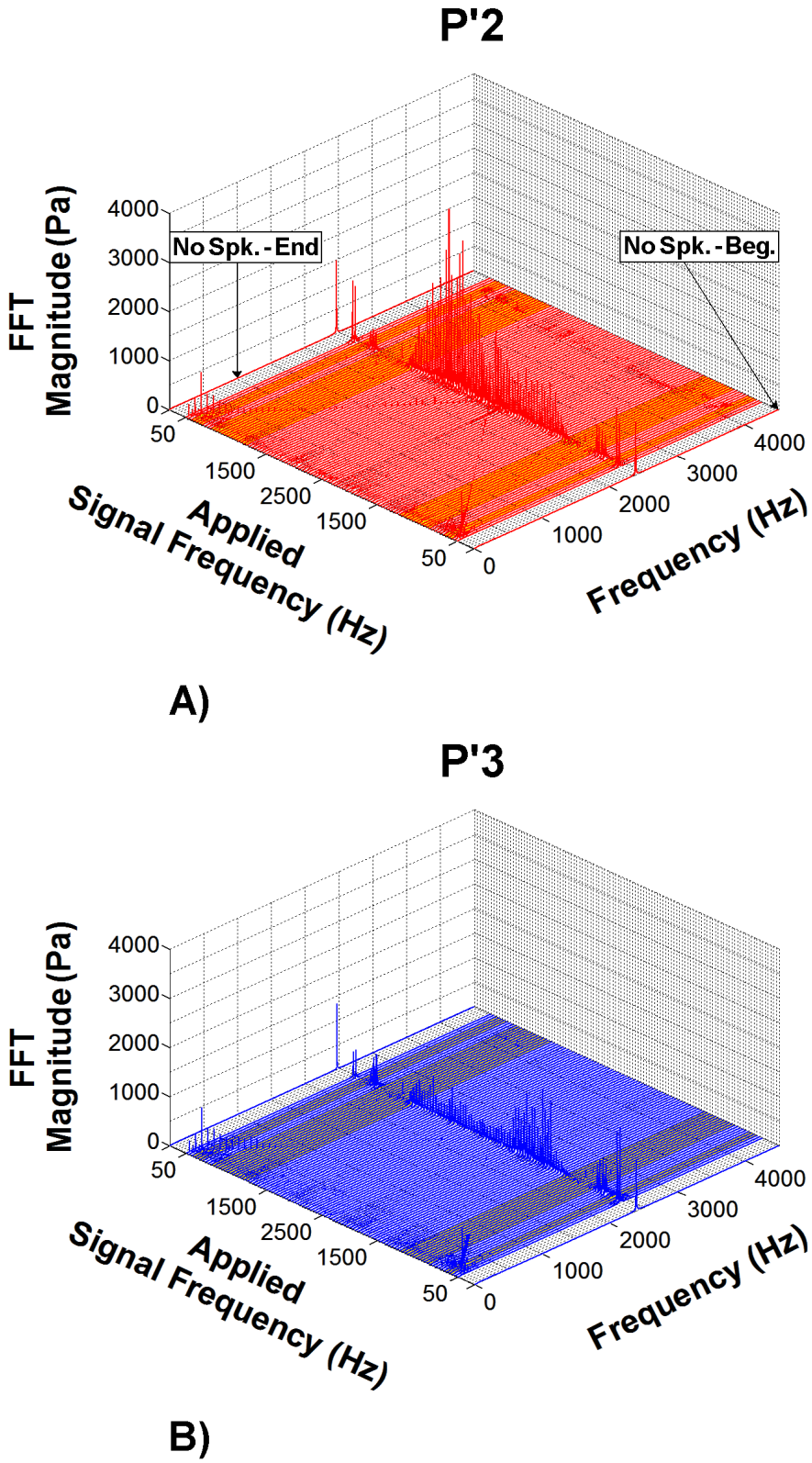

Figure B.3: Enlarged Waterfall Plots for Test 08-01-04: A) $P'2$ and B) $P'3$.

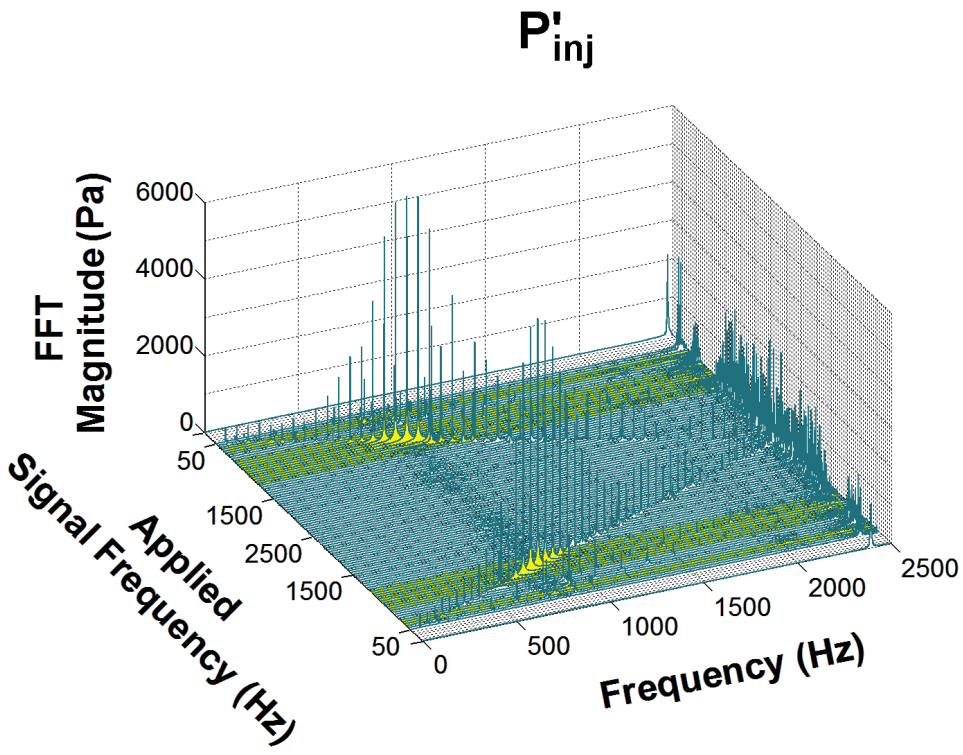

Figure B.4: Enlarged Waterfall Plot for Test 08-01-04: P'_{inj}.

B.2.2 Test 08-01-04: Maximum Normalized Instability Amplitude Response

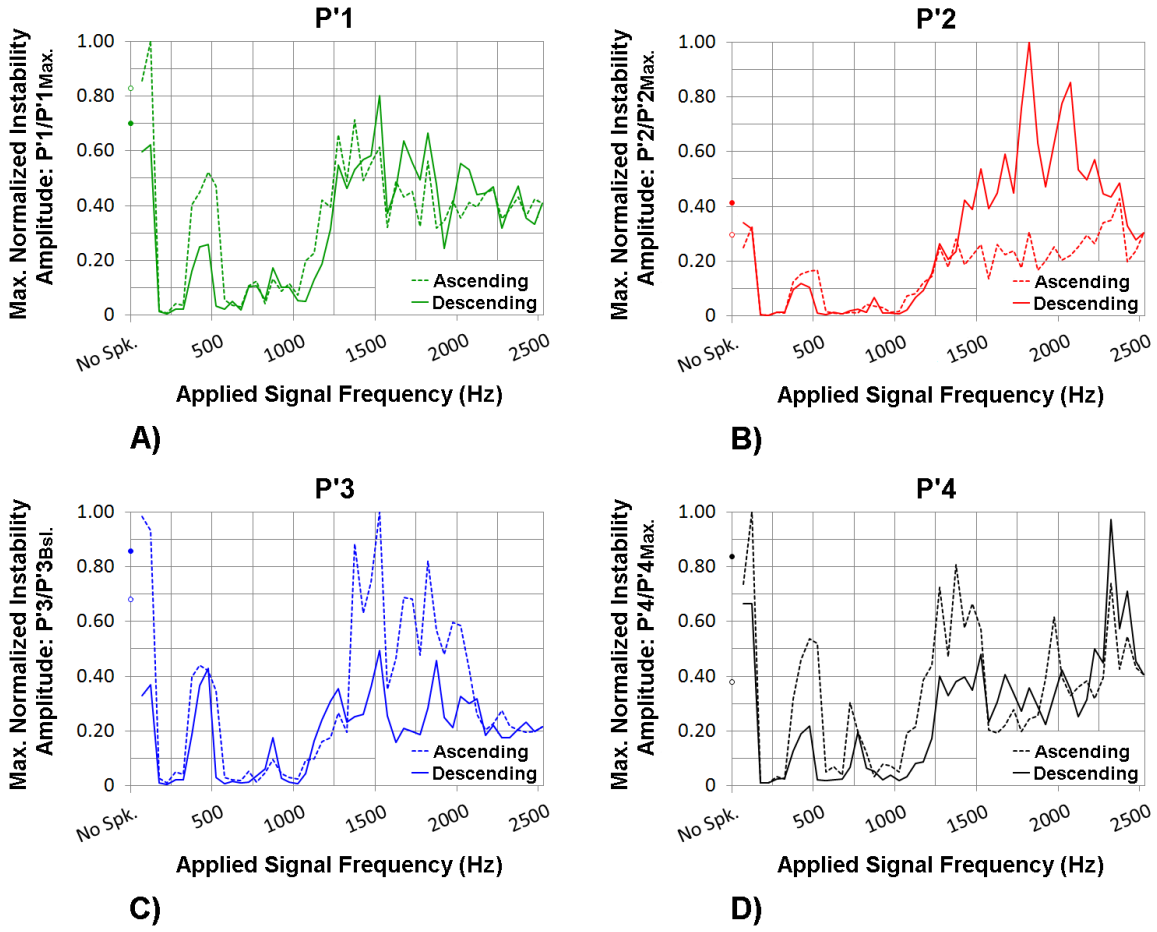

Figure B.5: Maximum Normalized Instability Amplitude Response from Test 08-01-04 for A) $P'1$, B) $P'2$, C) $P'3$ and D) $P'4$.

B.2.3 Test 08-01-05: Waterfall Plot Supplement

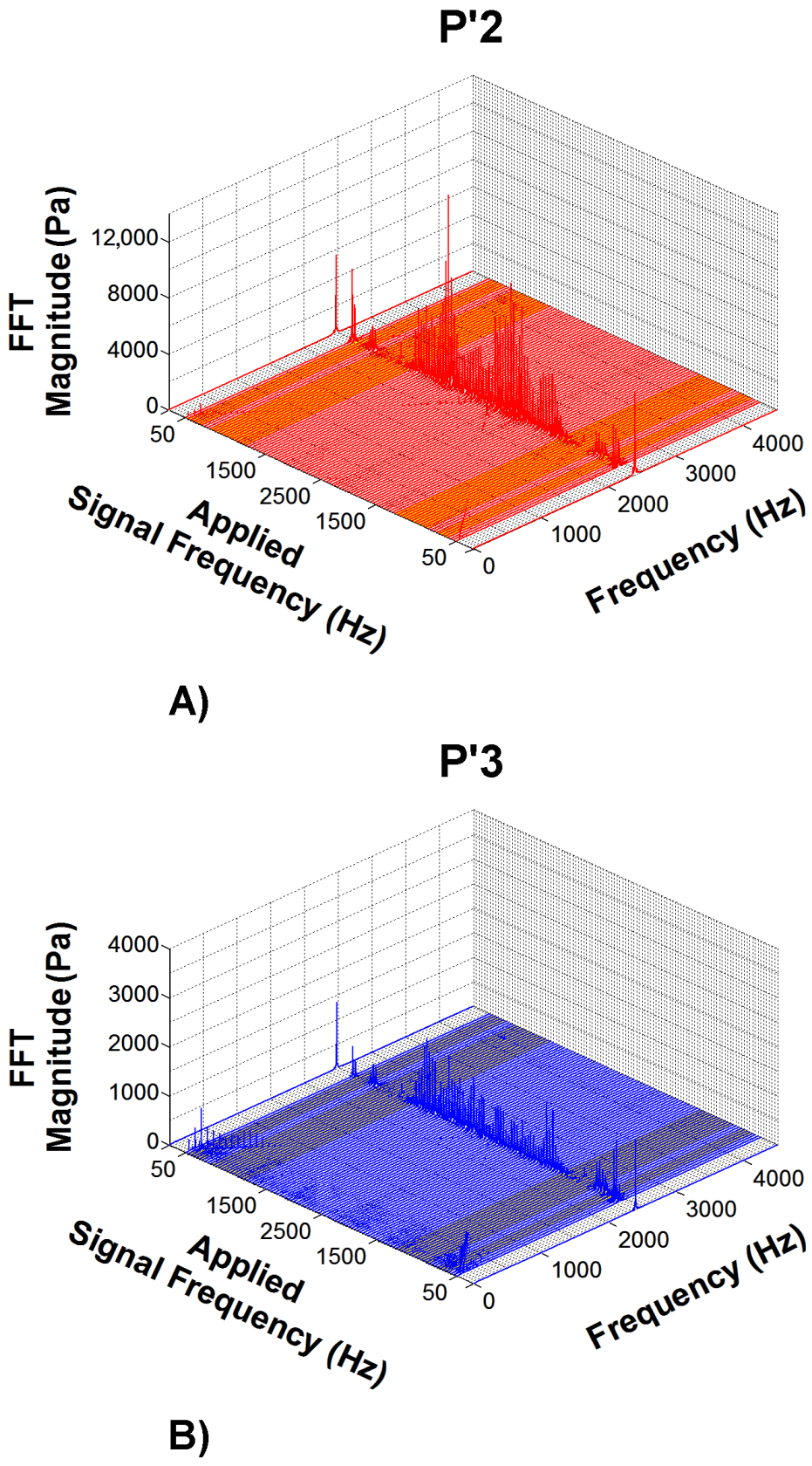

Figure B.6: Enlarged Waterfall Plots for Test 08-01-05: A) $P'2$ and B) $P'3$.

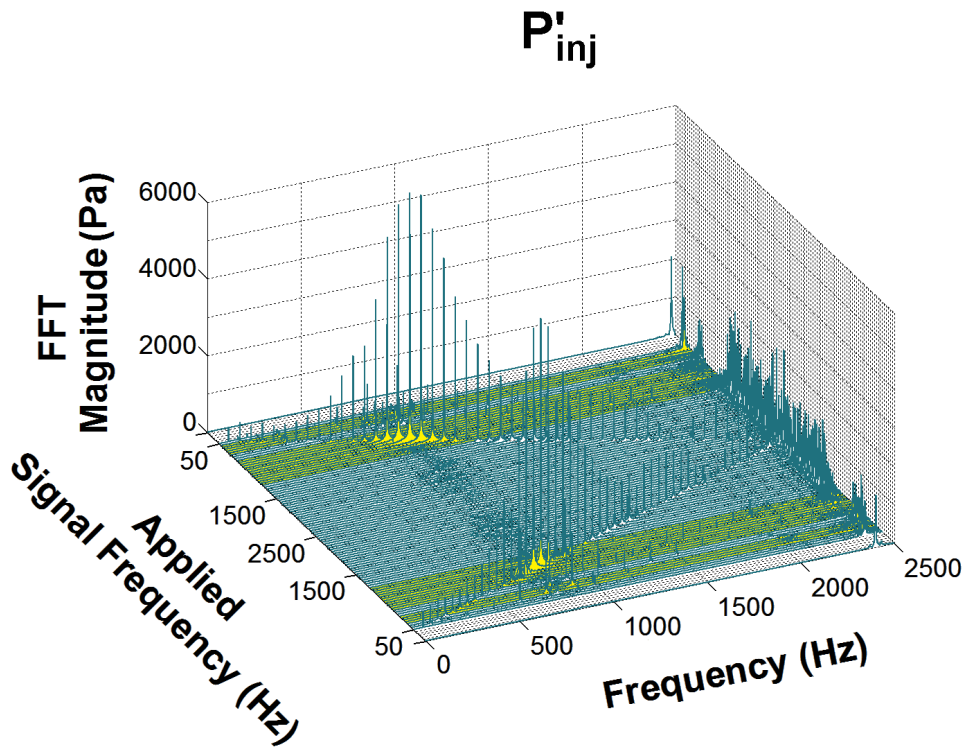

Figure B.7: Enlarged Waterfall Plot for Test 08-01-05: P'_{inj}.

B.2.4 Test 08-01-05: Maximum Normalized Instability Amplitude Response

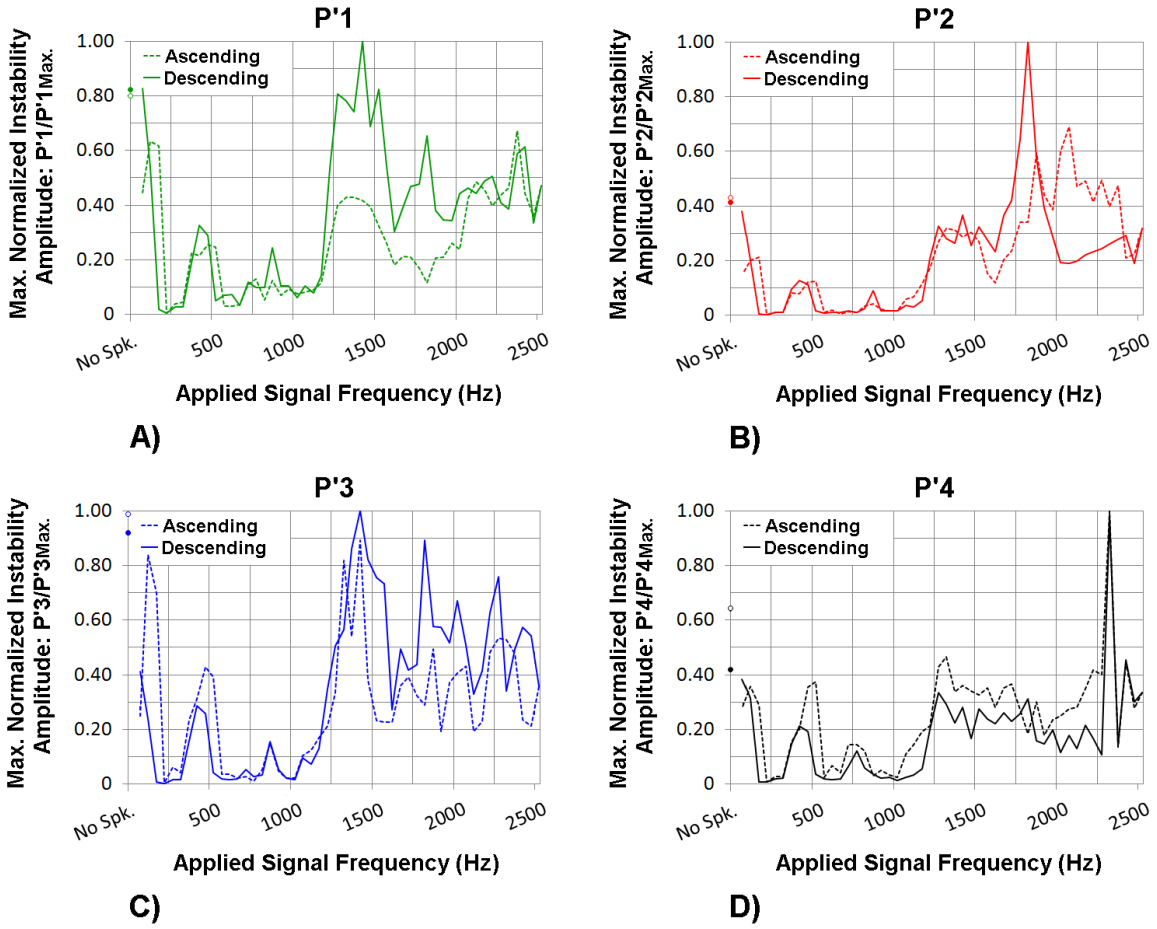

Figure B.8: Maximum Normalized Instability Amplitude Response from Test 08-01-05 for A) $P'1$, B) $P'2$, C) $P'3$ and D) $P'4$.

B.3 Band-Limited White Noise: Signal Amplitude Study

B.3.1 $P'3$ Waterfall Plot Supplement

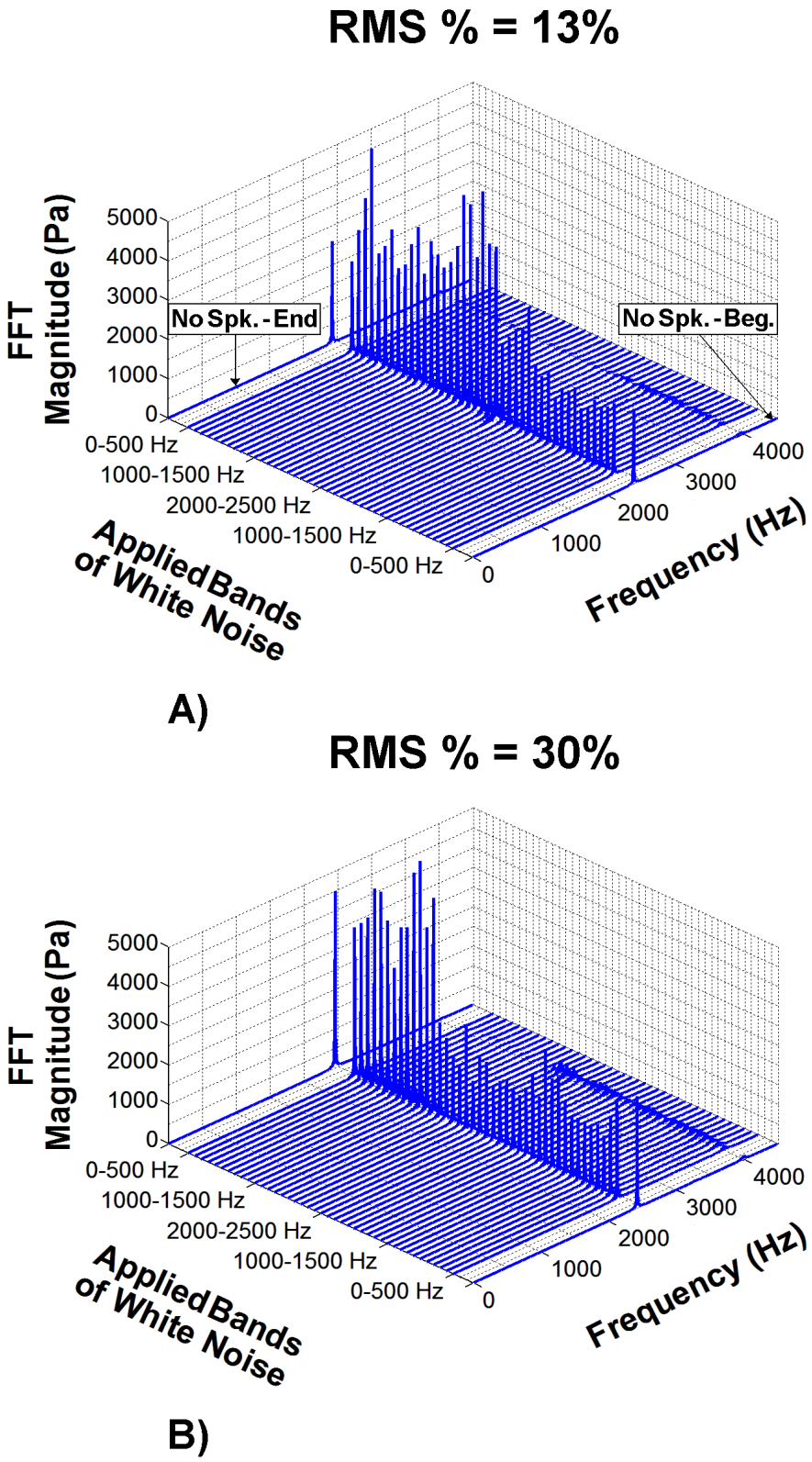

Figure B.9: Enlarged $P'3$ Waterfall Plots for the Band-Limited White Noise Signal Amplitude Study: A) 13% and B) 30% RMS.

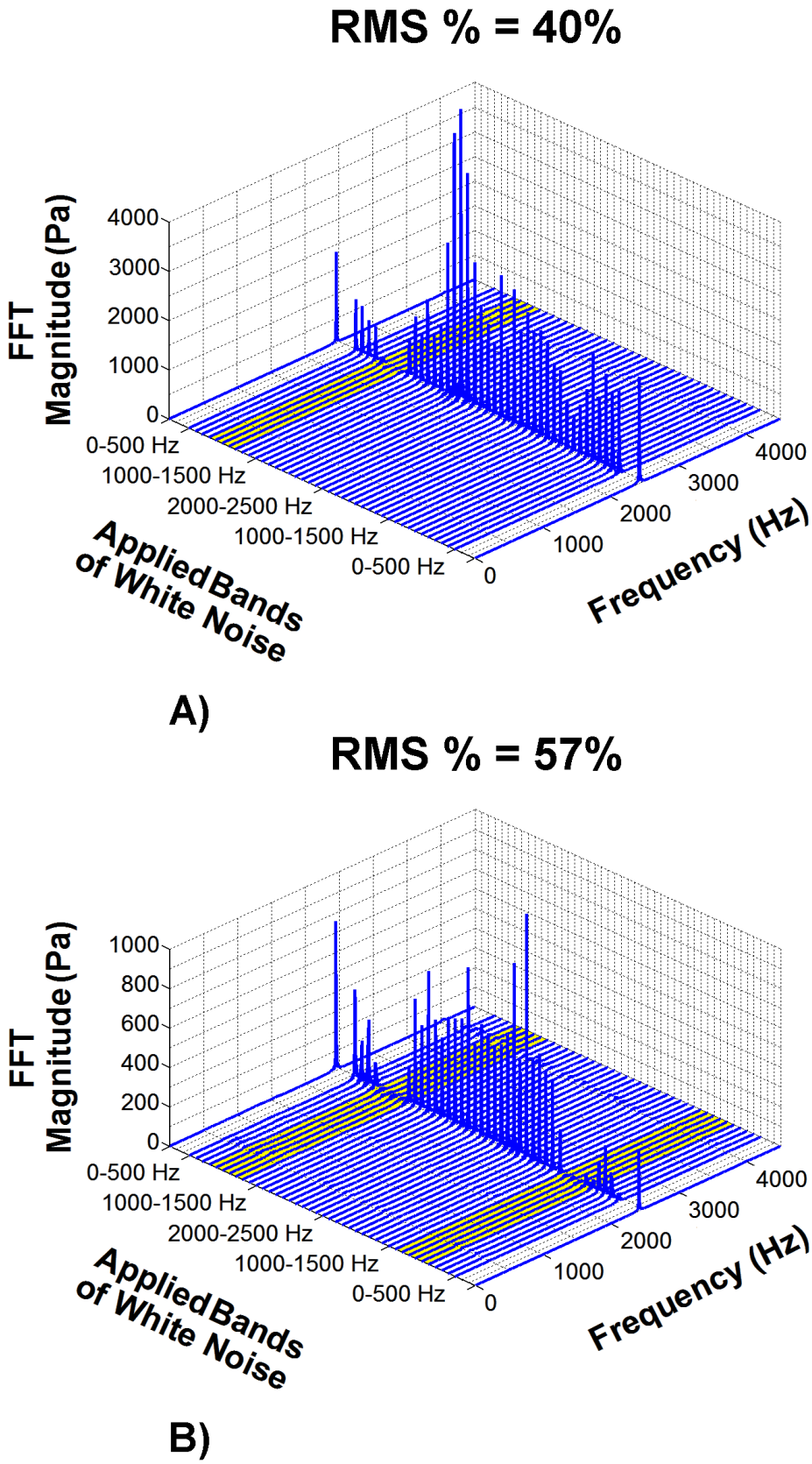

Figure B.10: Enlarged $P'3$ Waterfall Plots for the Band-Limited White Noise Signal Amplitude Study: A) 40% and B) 57% RMS.

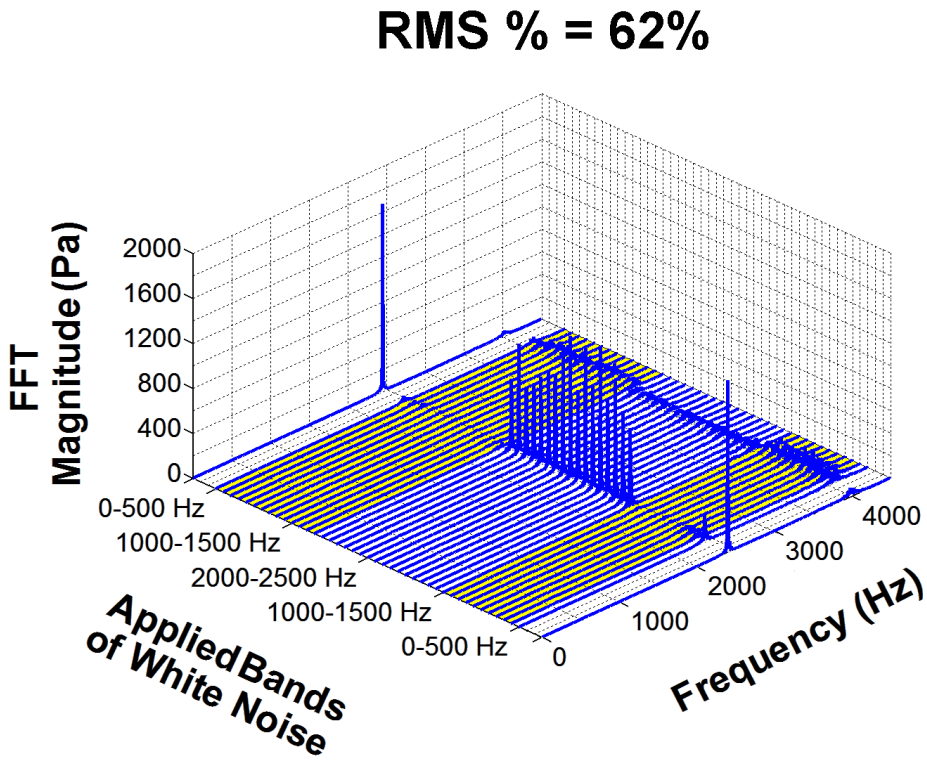

Figure B.11: Enlarged $P'3$ Waterfall Plot for the Band-Limited White Noise Signal Amplitude Study: 62% RMS.

B.3.2 P'_{inj} Waterfall Plot Supplement

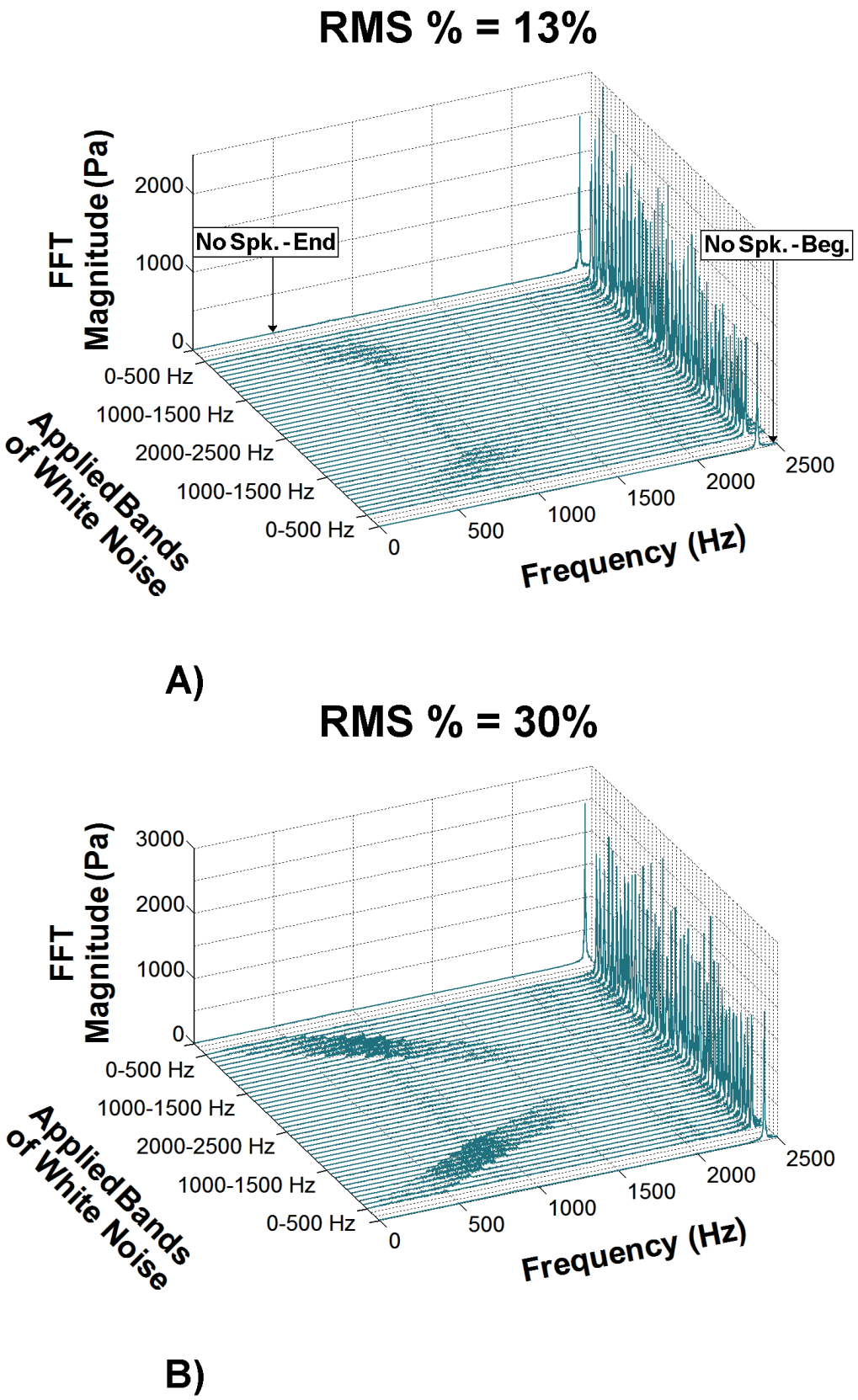

Figure B.12: Enlarged P'_{inj} Waterfall Plots for the Band-Limited White Noise Signal Amplitude Study: A) 13% and B) 30% RMS.

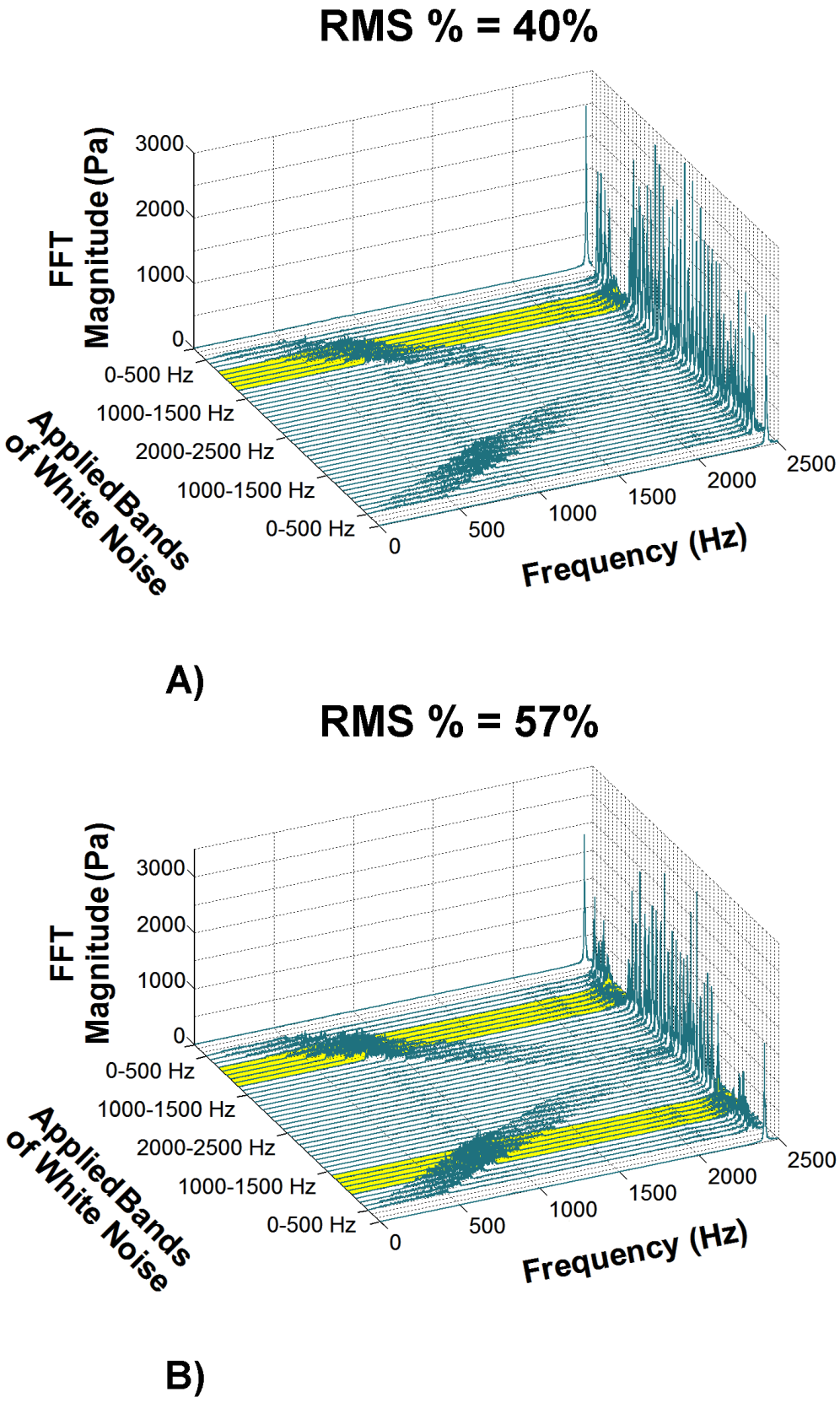

Figure B.13: Enlarged P'_{inj} Waterfall Plots for the Band-Limited White Noise Signal Amplitude Study: A) 40% and B) 57% RMS.

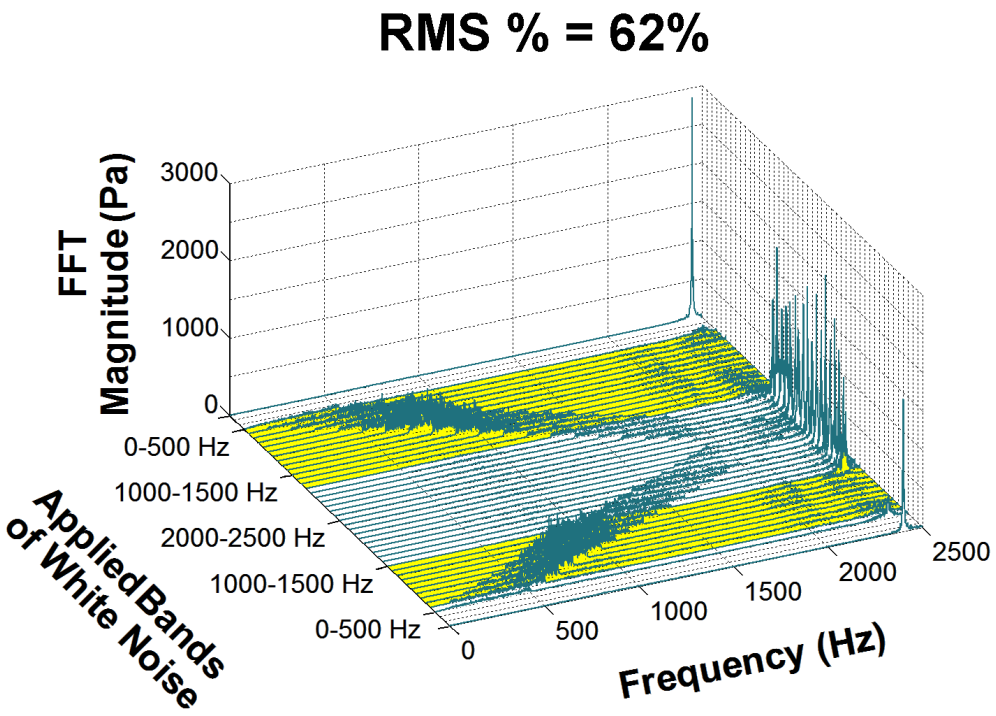

Figure B.14: Enlarged P'_{inj} Waterfall Plot for the Band-Limited White Noise Signal Amplitude Study: 62% RMS.

B.3.3 Maximum Normalized Instability Amplitude Response

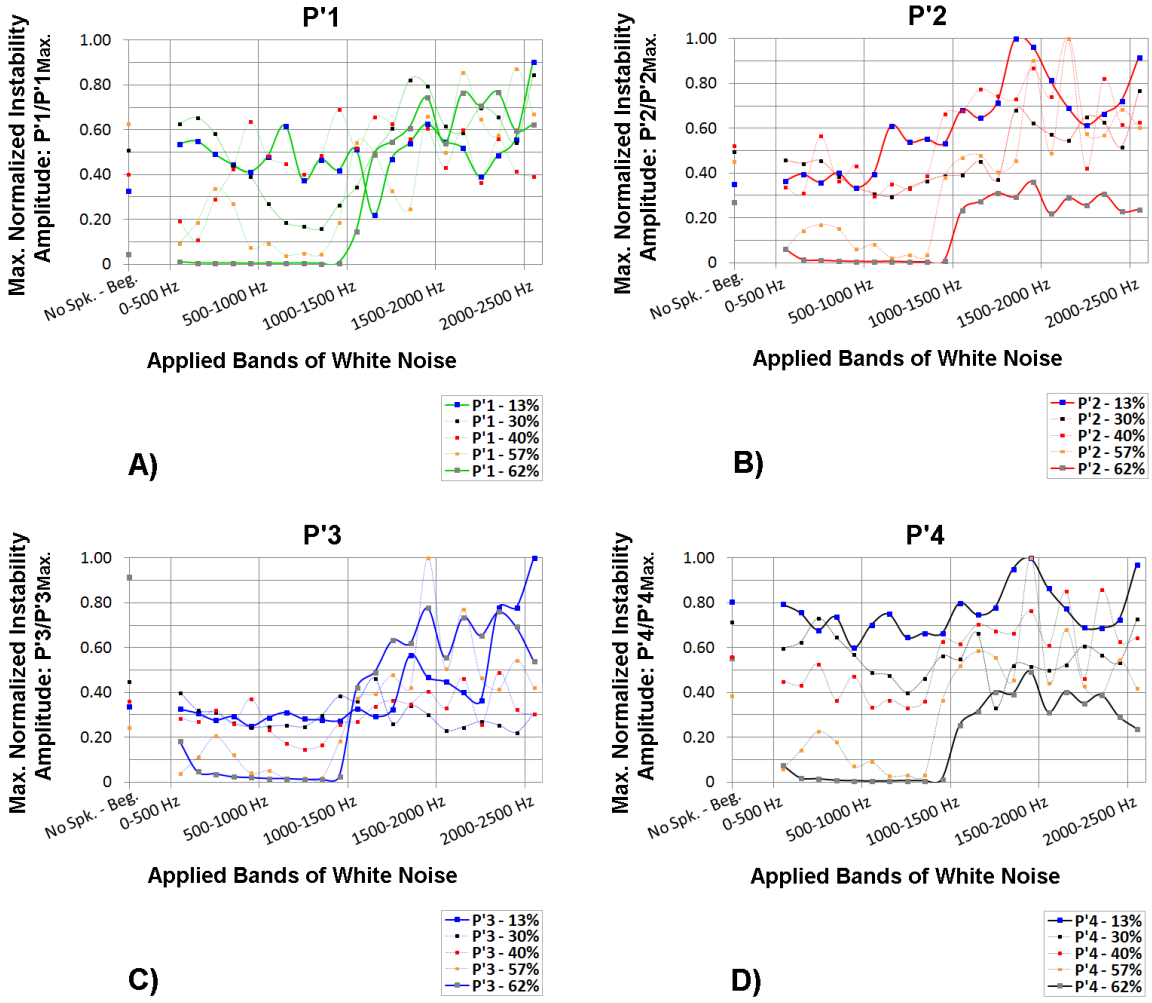

Figure B.15: Maximum Normalized Instability Amplitude Response in the Ascending Band-Limited White Noise Direction for A) $P'1$, B) $P'2$, C) $P'3$ and D) $P'4$.

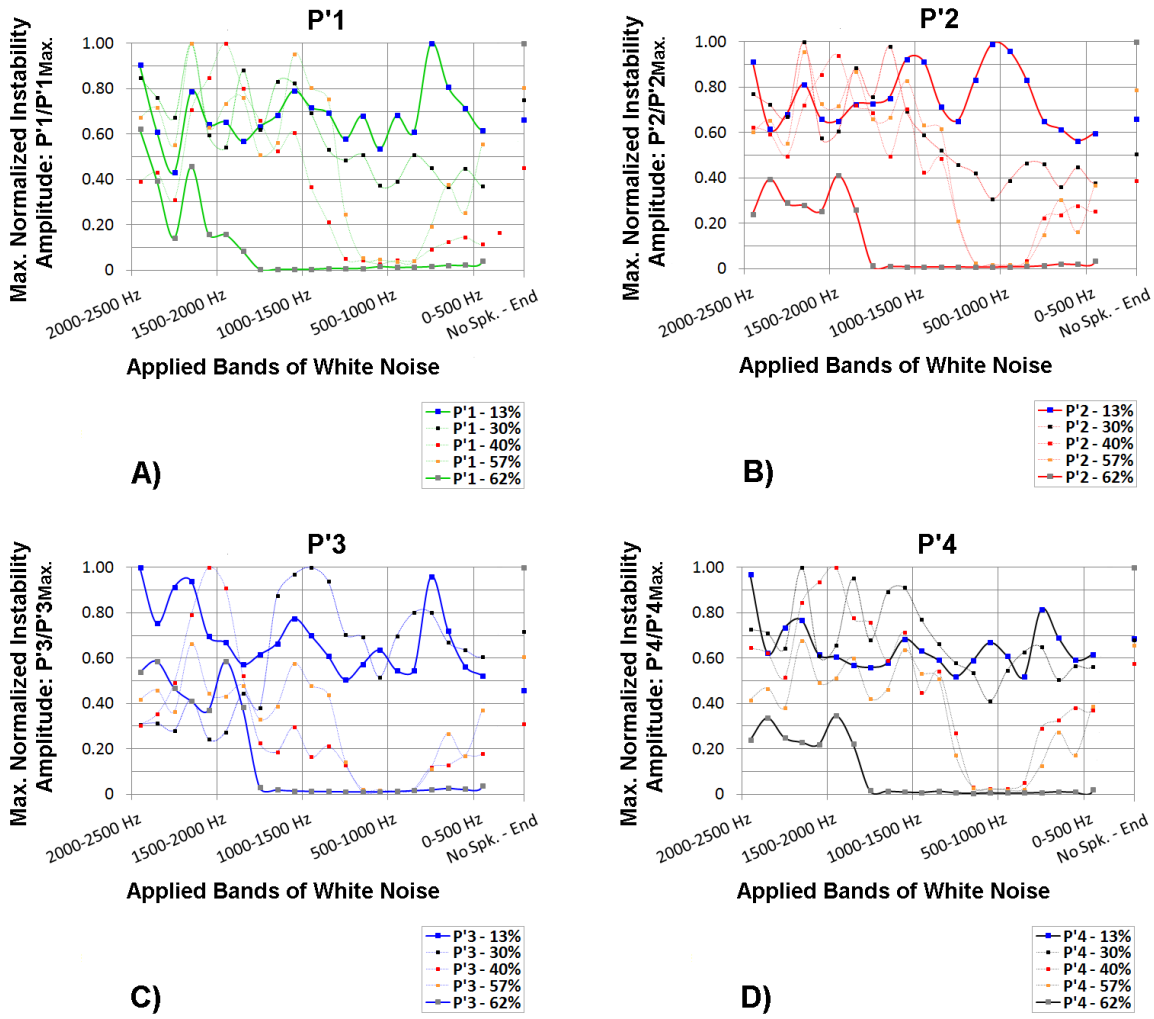

Figure B.16: Maximum Normalized Instability Amplitude Response in the Descending Band-Limited White Noise Direction for A) $P'1$, B) $P'2$, C) $P'3$ and D) $P'4$.

B.4 Single-Frequency Acoustic Modulation: Signal Amplitude Study

B.4.1 $P'1$ Waterfall Plot Supplement

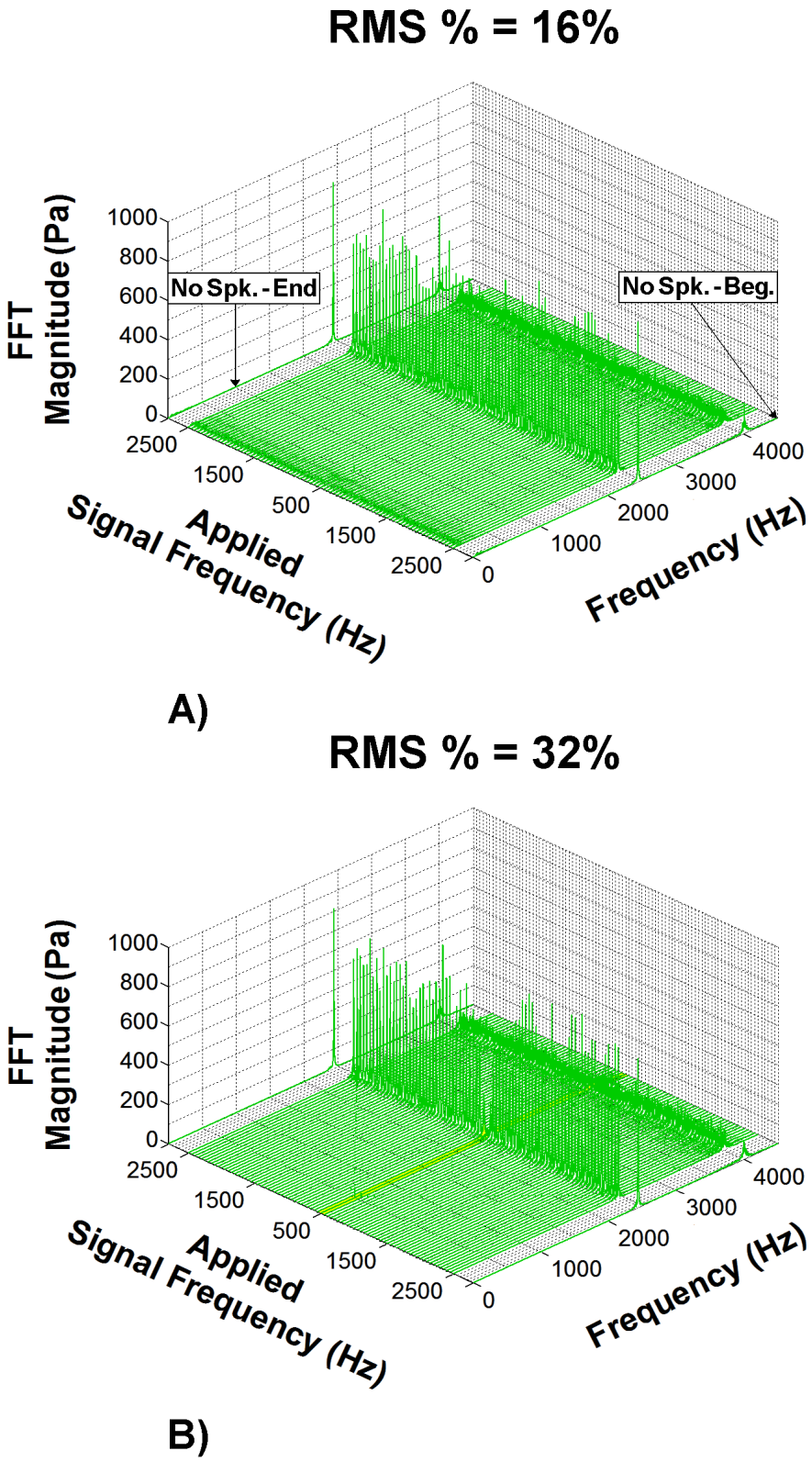

Figure B.17: Enlarged $P'1$ Waterfall Plots for the Single-Frequency Acoustic Modulation Signal Amplitude Study: A) 16% and B) 32% RMS.

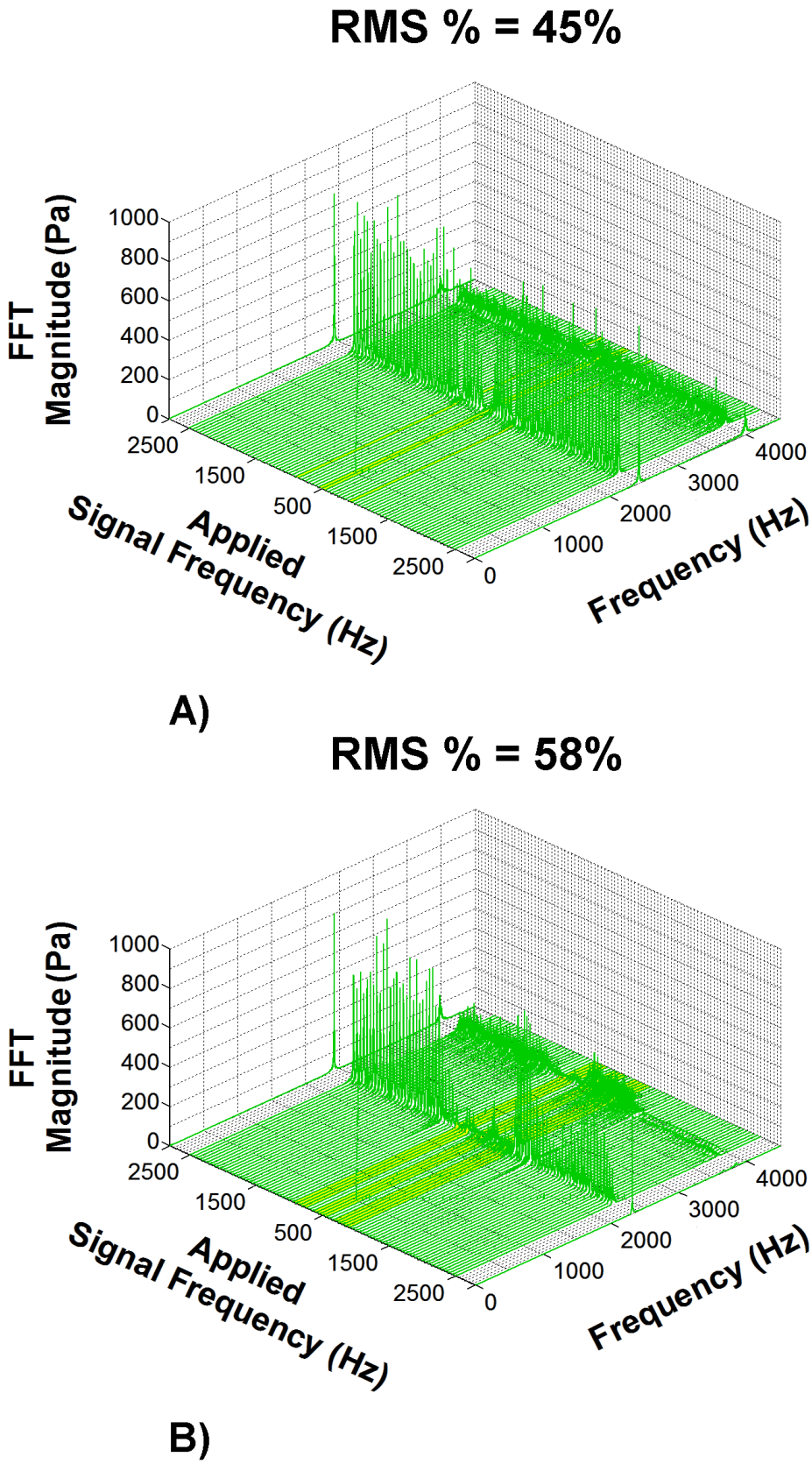

Figure B.18: Enlarged $P'1$ Waterfall Plots for the Single-Frequency Acoustic Modulation Signal Amplitude Study: A) 45% and B) 58% RMS.

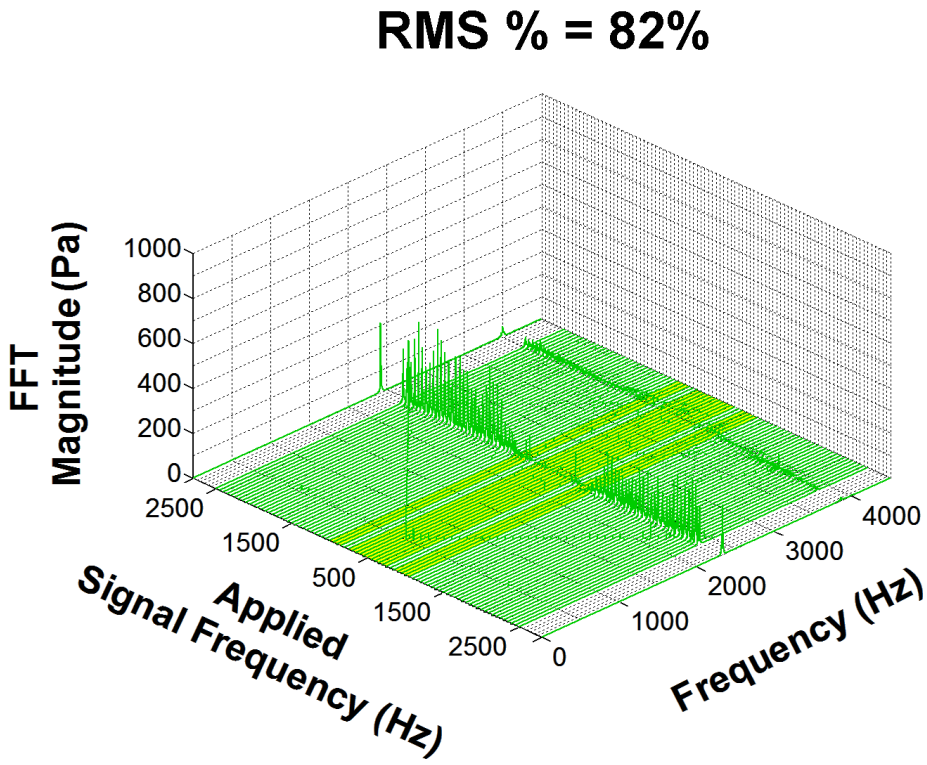

Figure B.19: Enlarged $P'1$ Waterfall Plot for the Single-Frequency Acoustic Modulation Signal Amplitude Study: 82% RMS.

B.4.2 P'_{inj} Waterfall Plot Supplement

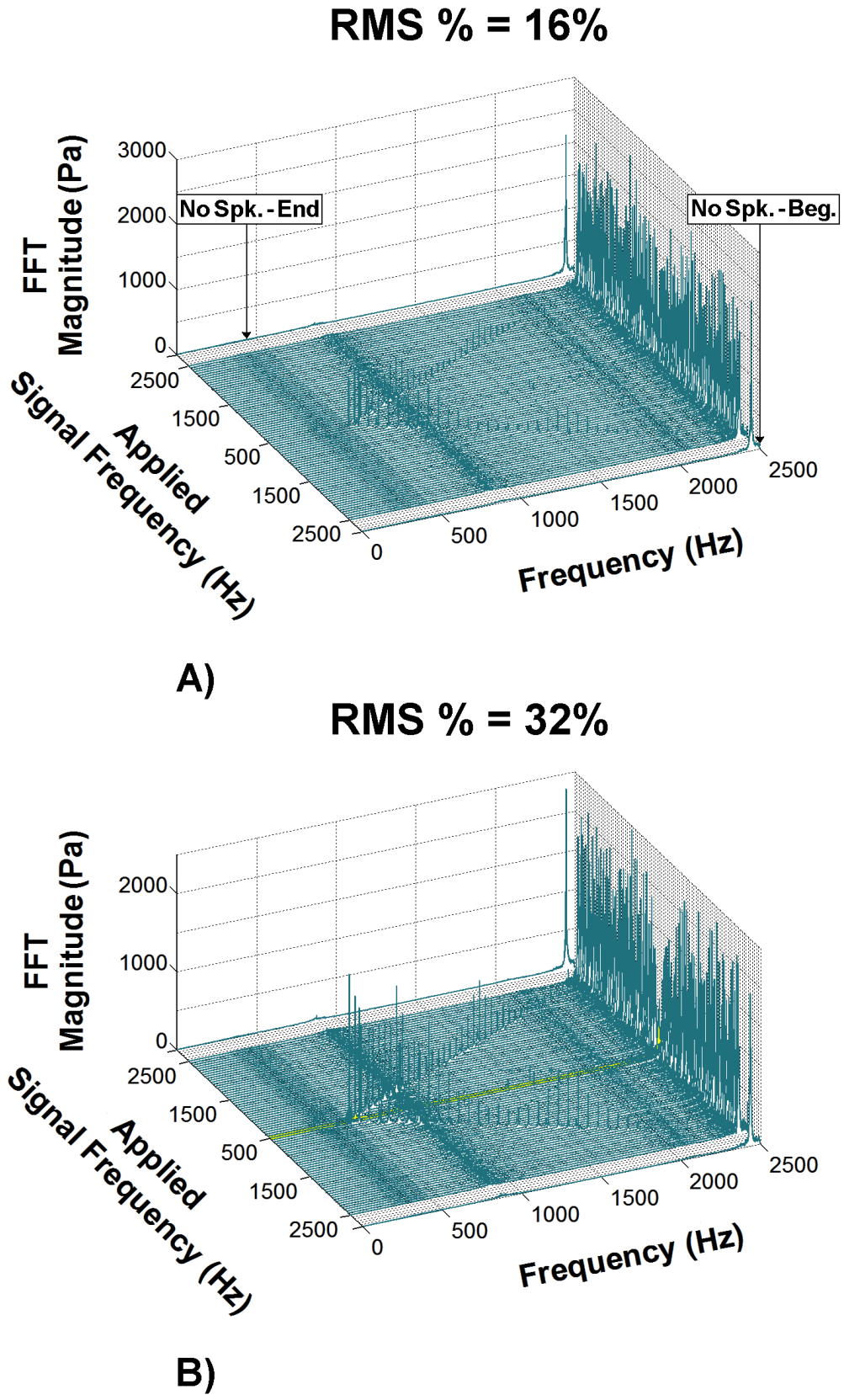

Figure B.20: Enlarged P'_{inj} Waterfall Plots for the Single-Frequency Acoustic Modulation Signal Amplitude Study: A) 16% and B) 32% RMS.

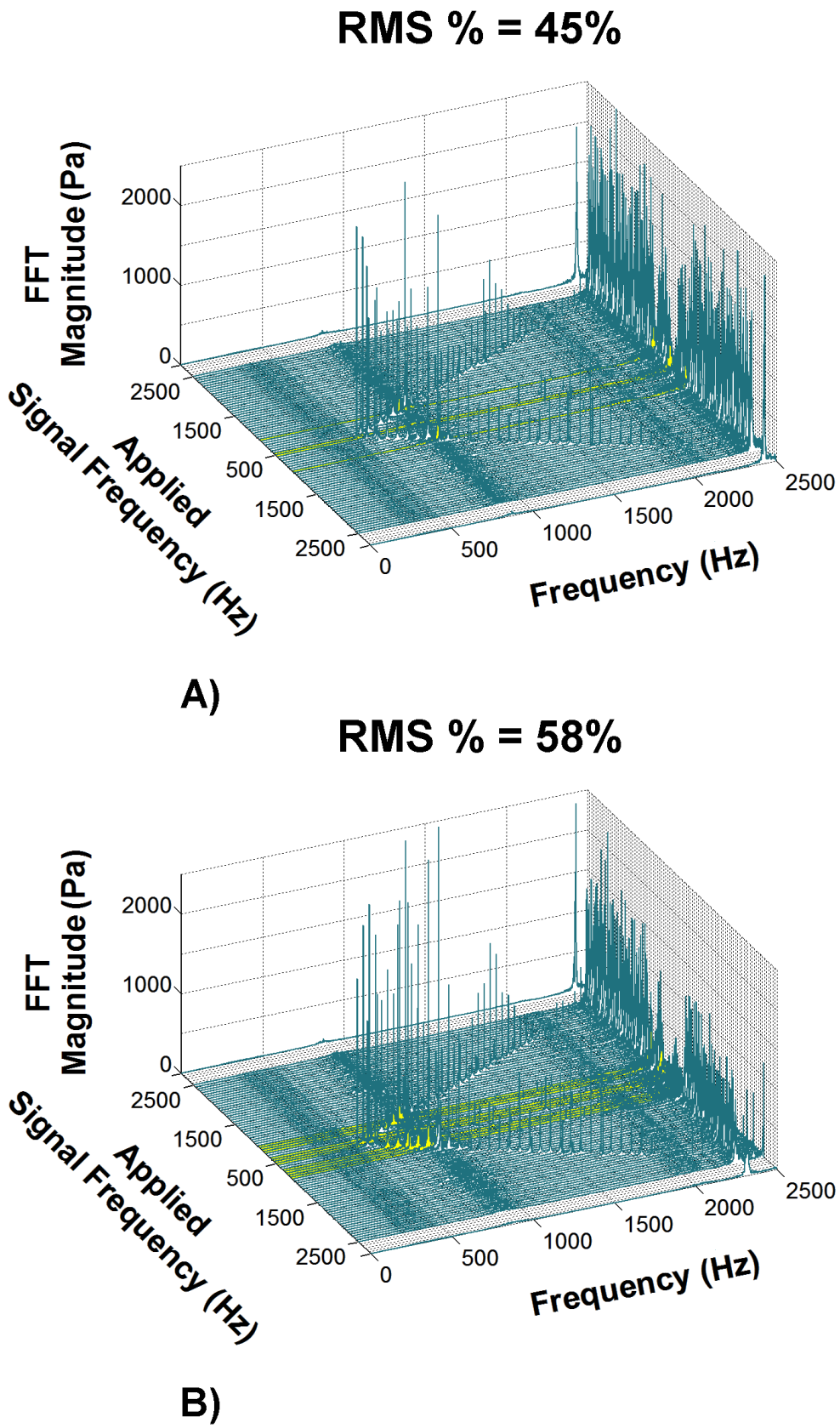

Figure B.21: Enlarged P'_{inj} Waterfall Plots for the Single-Frequency Acoustic Modulation Signal Amplitude Study: A) 45% and B) 58% RMS.

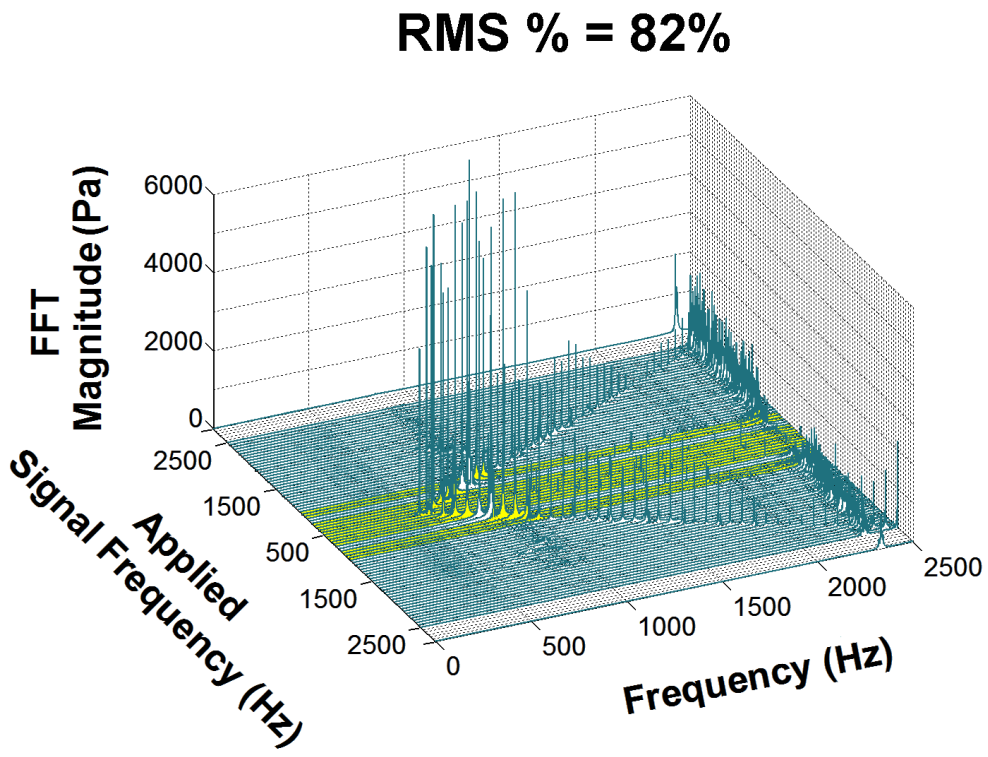

Figure B.22: Enlarged P'_{inj} Waterfall Plot for the Single-Frequency Acoustic Modulation Signal Amplitude Study: 82% RMS.

B.5 Band-Limited White Noise: Pure Acoustic Testing

B.5.1 $P'1$ Waterfall Plot Supplement

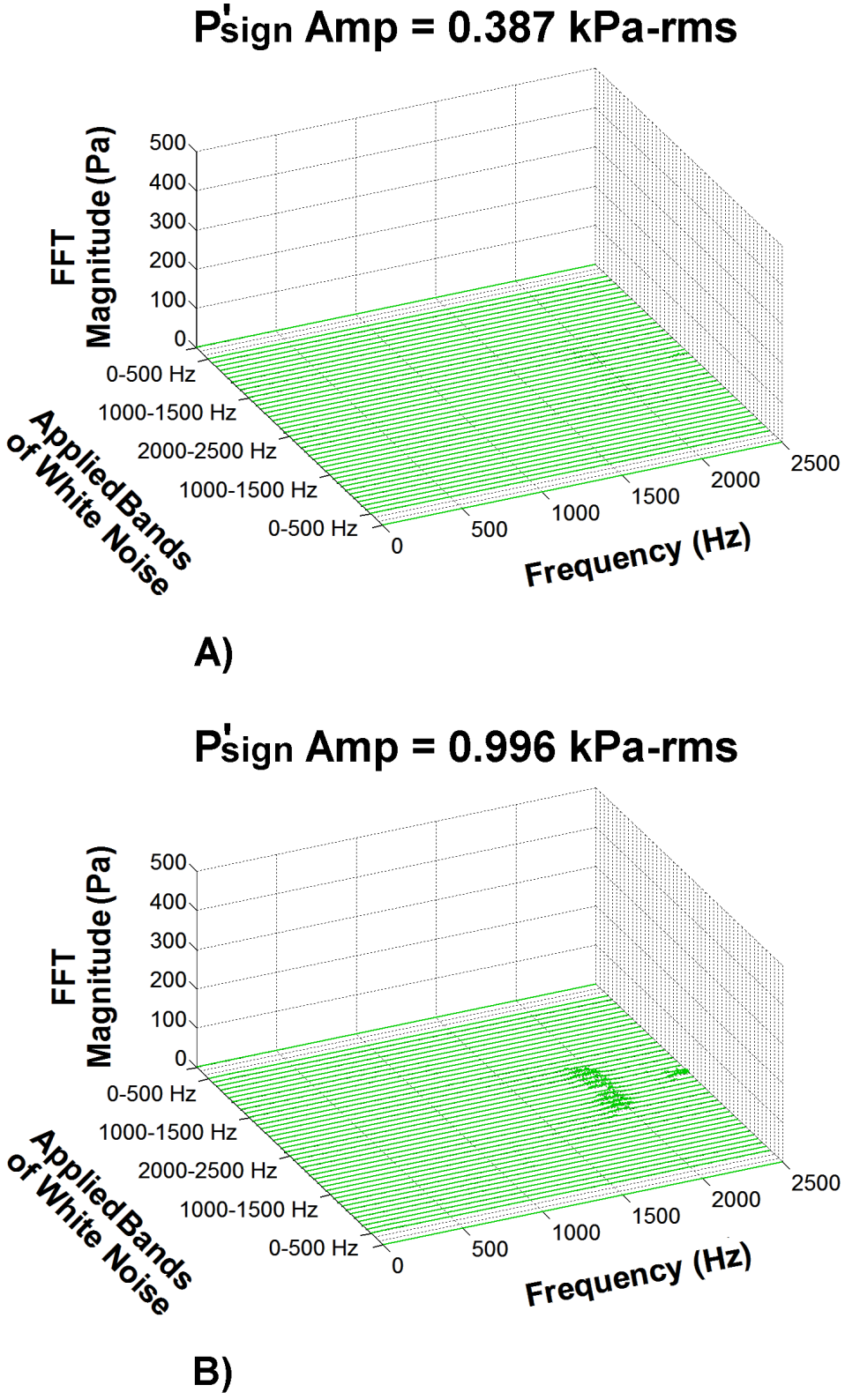

Figure B.23: Enlarged $P'1$ Waterfall Plots for the Band-Limited White Noise Pure Acoustic Tests: A) 0.387 kPa-rms and B) 0.996 kPa-rms.

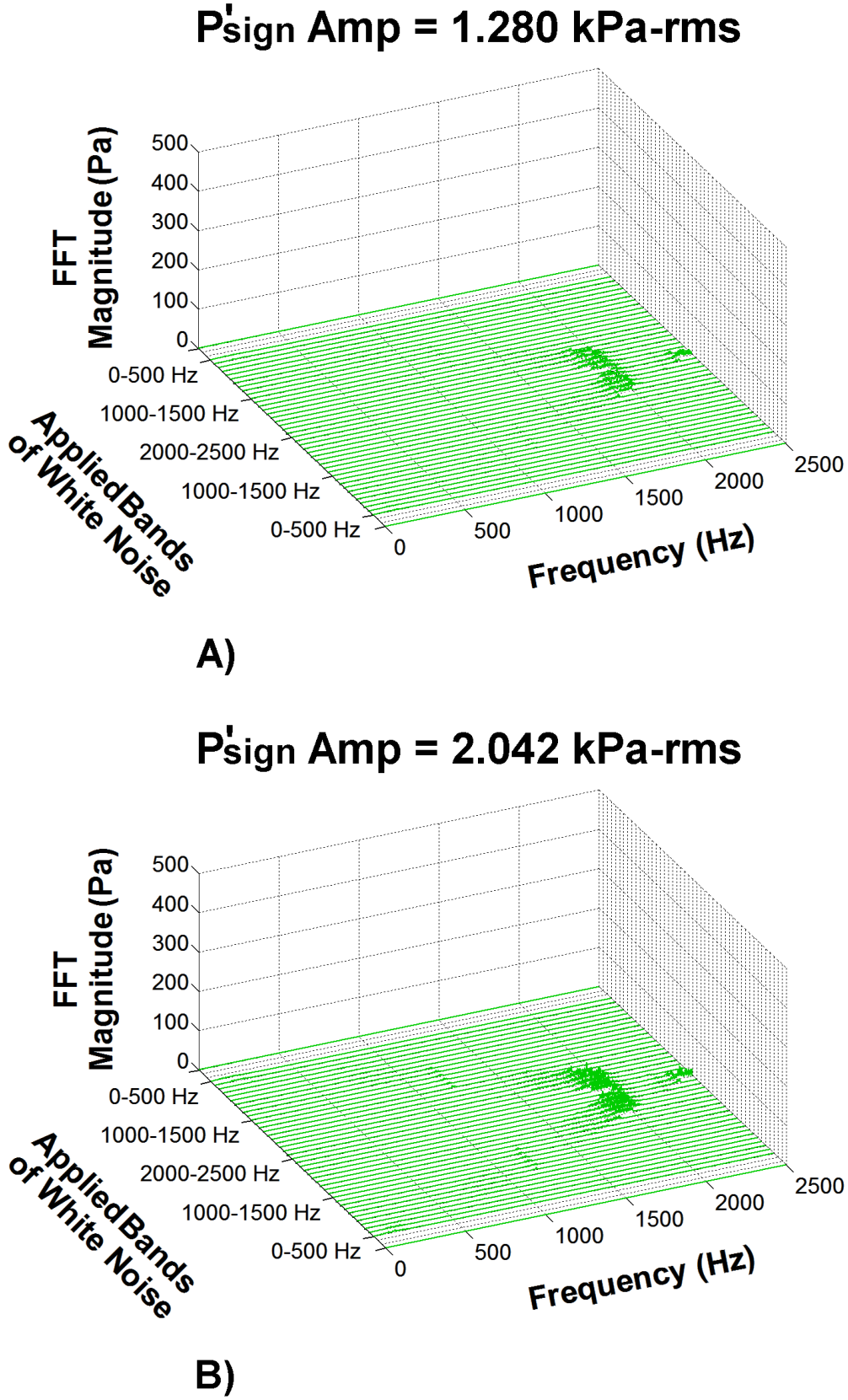

Figure B.24: Enlarged $P'1$ Waterfall Plots for the Band-Limited White Noise Pure Acoustic Tests: A) 1.280 kPa-rms and B) 2.042 kPa-rms.

B.5.2 $P'2$ Waterfall Plot Supplement

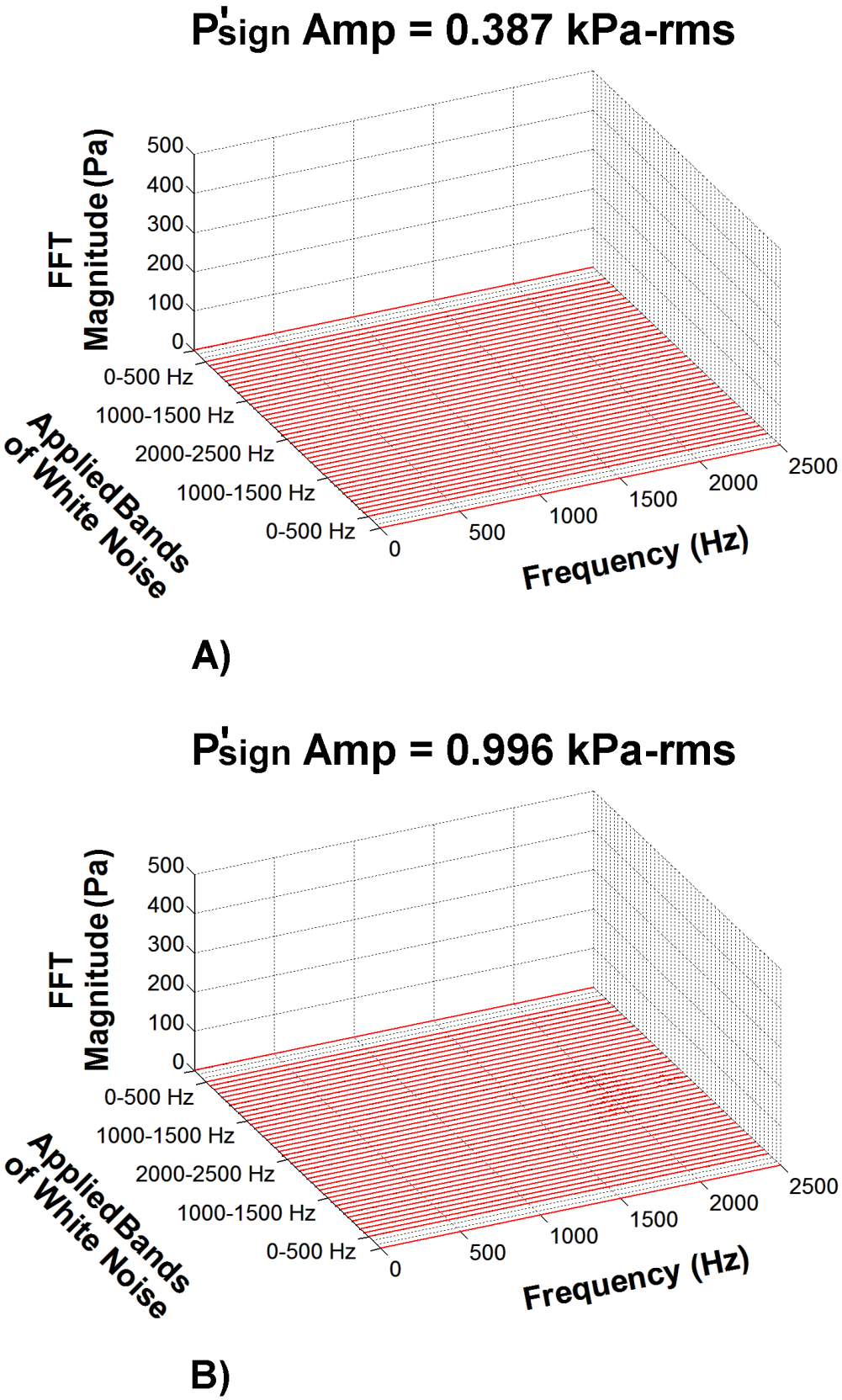

Figure B.25: Enlarged $P'2$ Waterfall Plots for the Band-Limited White Noise Pure Acoustic Tests: A) 0.387 kPa-rms and B) 0.996 kPa-rms.

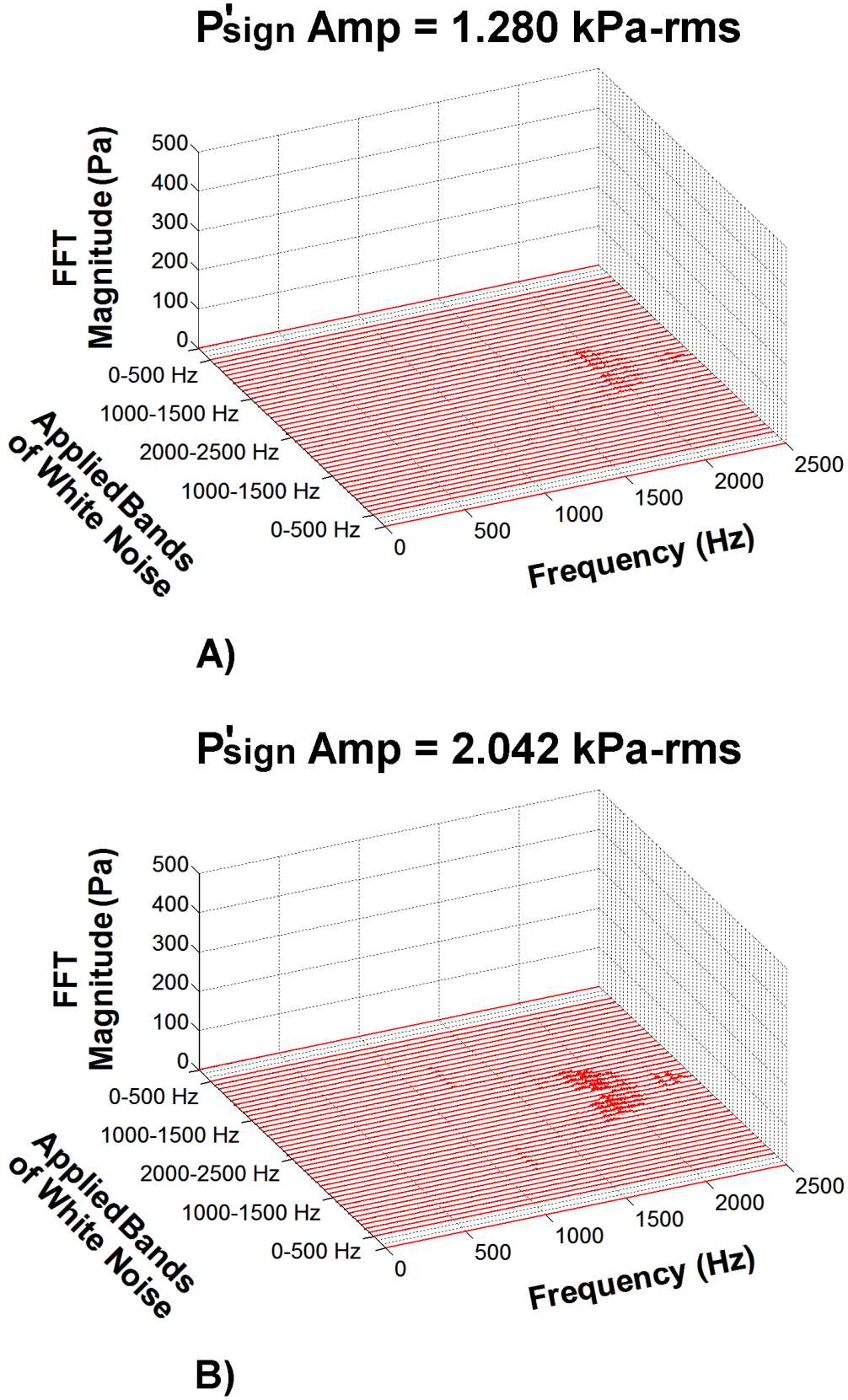

Figure B.26: Enlarged $P'2$ Waterfall Plots for the Band-Limited White Noise Pure Acoustic Tests: A) 1.280 kPa-rms and B) 2.042 kPa-rms.

B.5.3 $P'3$ Waterfall Plot Supplement

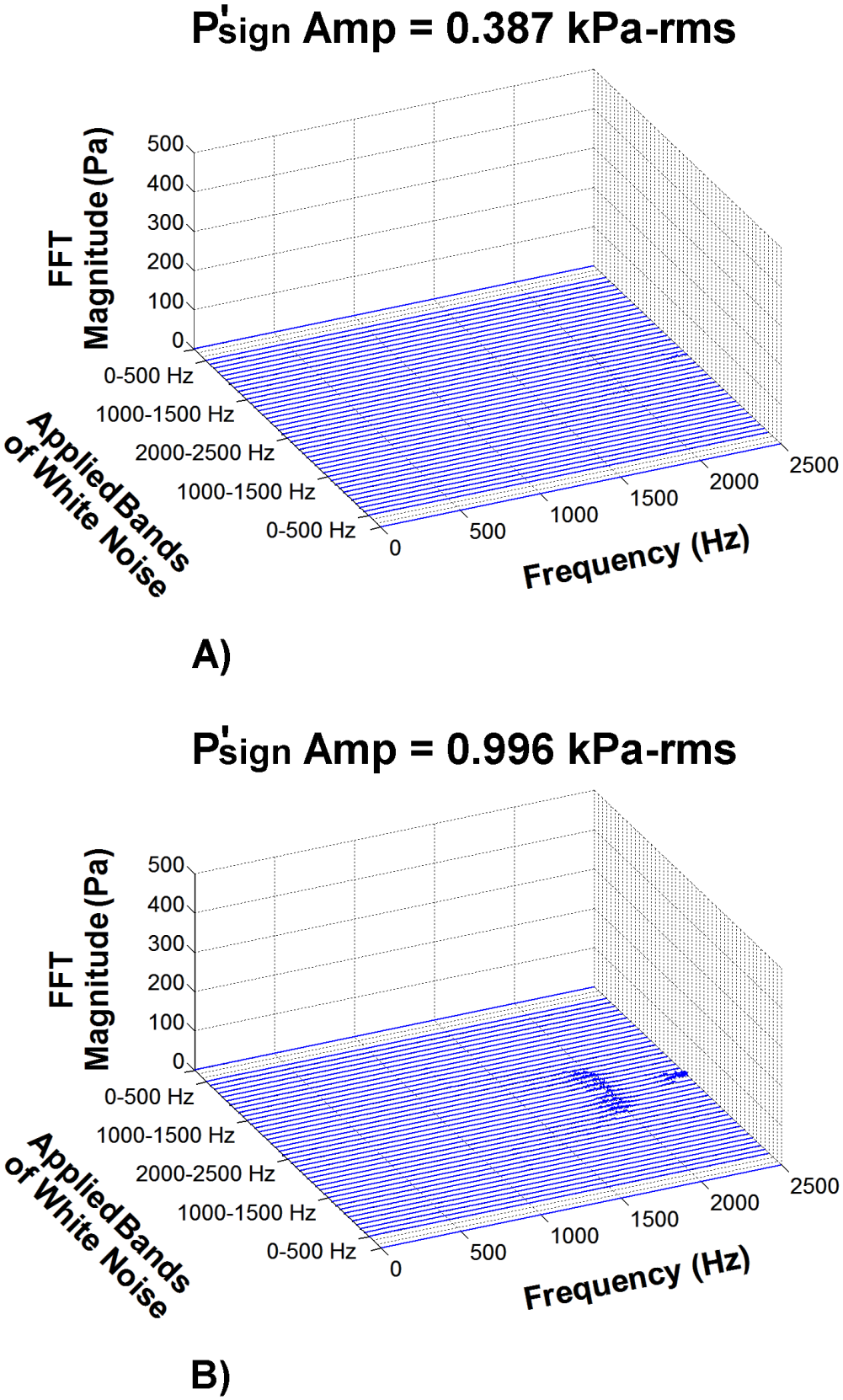

Figure B.27: Enlarged $P'3$ Waterfall Plots for the Band-Limited White Noise Pure Acoustic Tests: A) 0.387 kPa-rms and B) 0.996 kPa-rms.

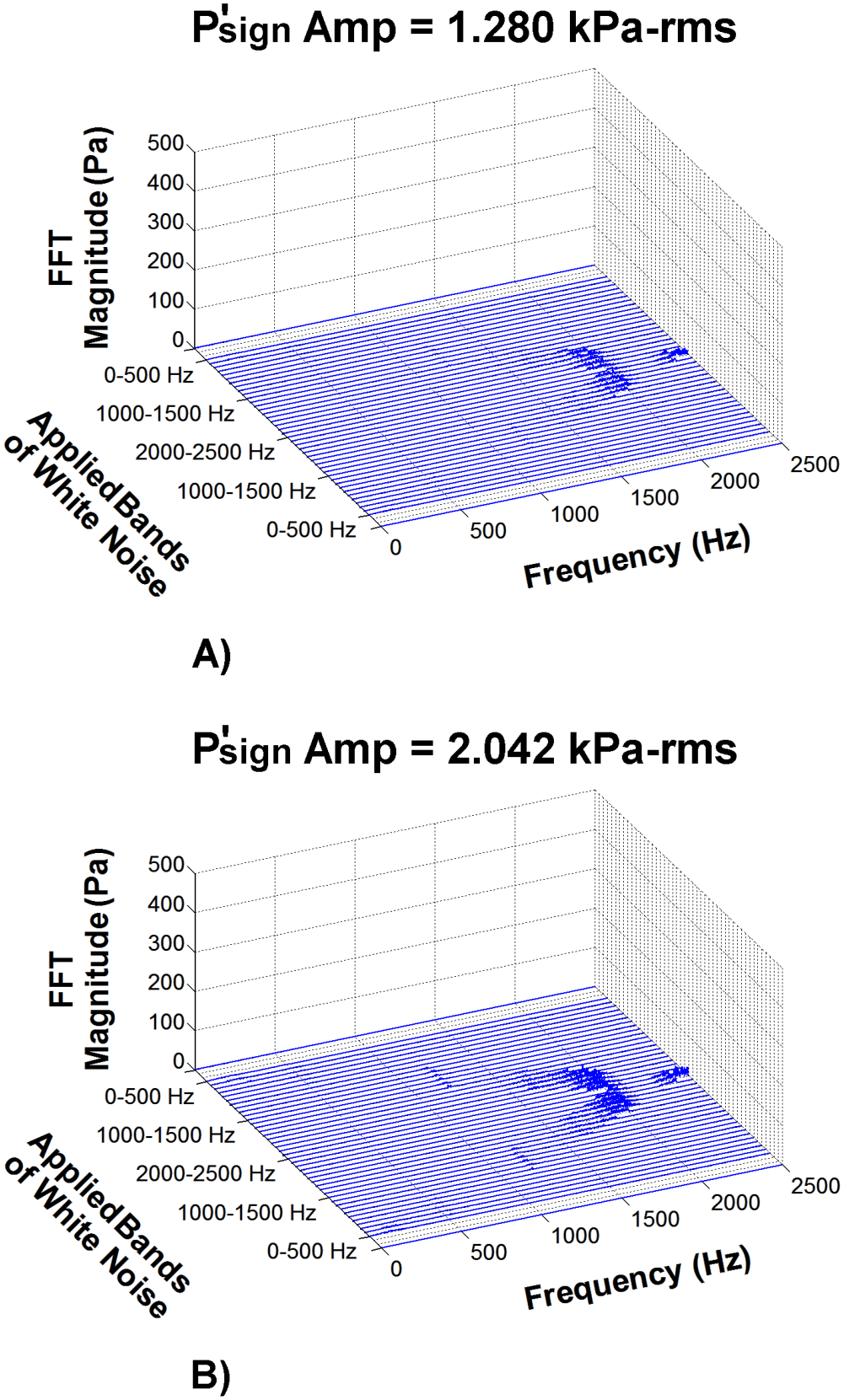

Figure B.28: Enlarged $P'3$ Waterfall Plots for the Band-Limited White Noise Pure Acoustic Tests: A) 1.280 kPa-rms and B) 2.042 kPa-rms.

B.5.4 P'_{inj} Waterfall Plot Supplement

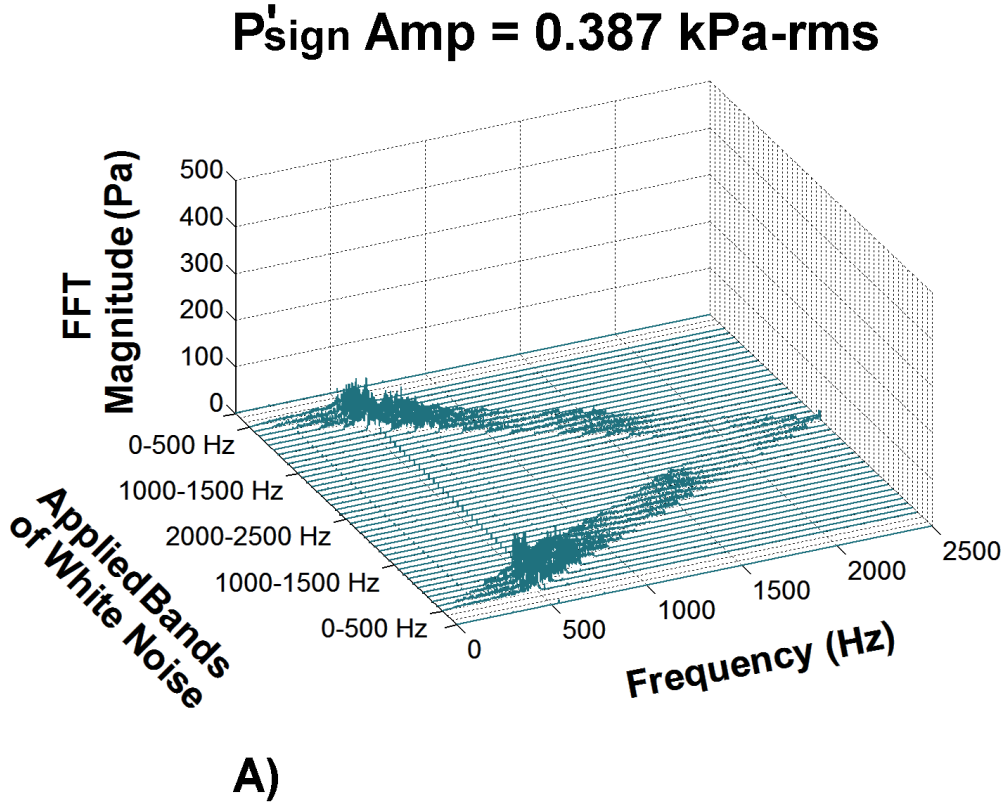

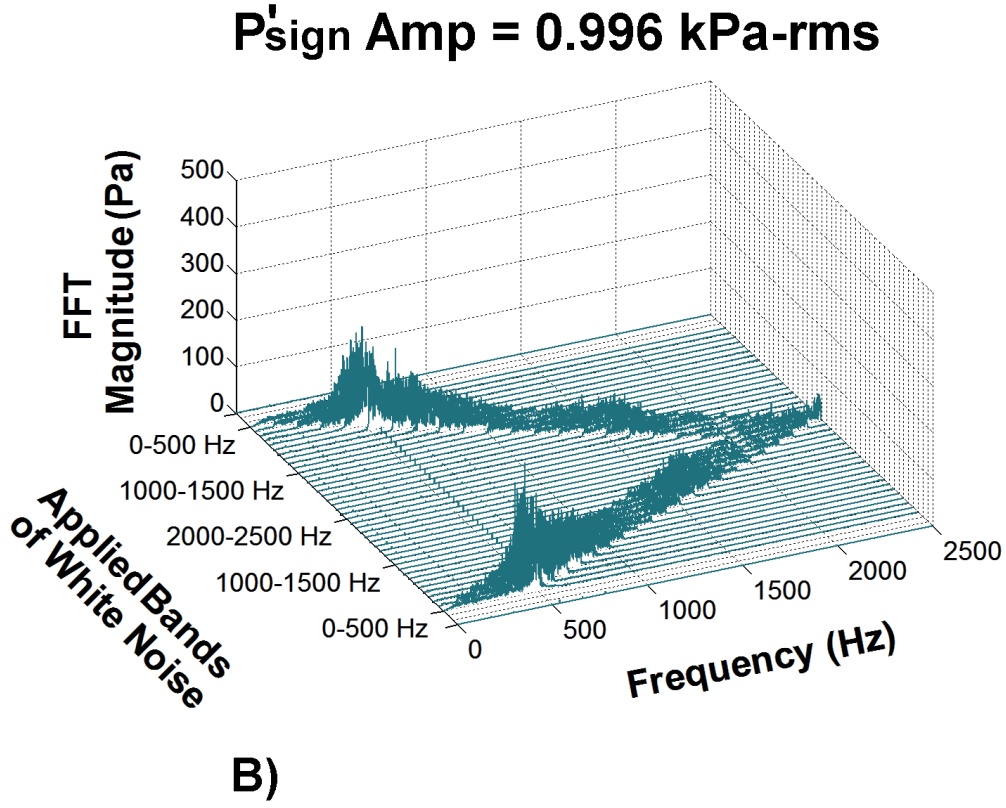

Figure B.29: Enlarged P'_{inj} Waterfall Plots for the Band-Limited White Noise Pure Acoustic Tests: A) 0.387 kPa-rms and B) 0.996 kPa-rms.

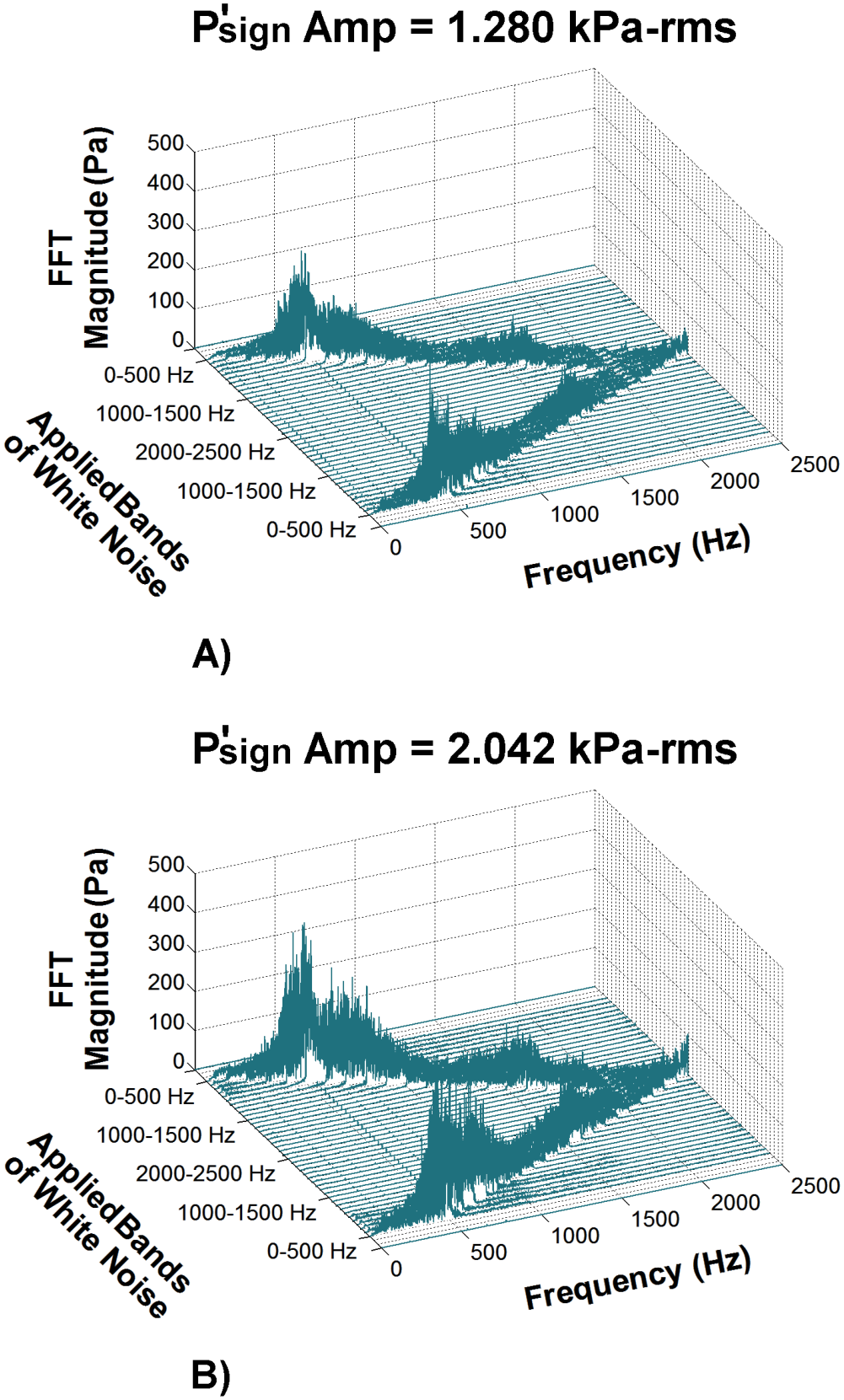

Figure B.30: Enlarged P'_{inj} Waterfall Plots for the Band-Limited White Noise Pure Acoustic Tests: A) 1.280 kPa-rms and B) 2.042 kPa-rms.

B.6 Single-Frequency Acoustic Modulation: Pure Acoustic Testing

B.6.1 $P'1$ Waterfall Plot Supplement

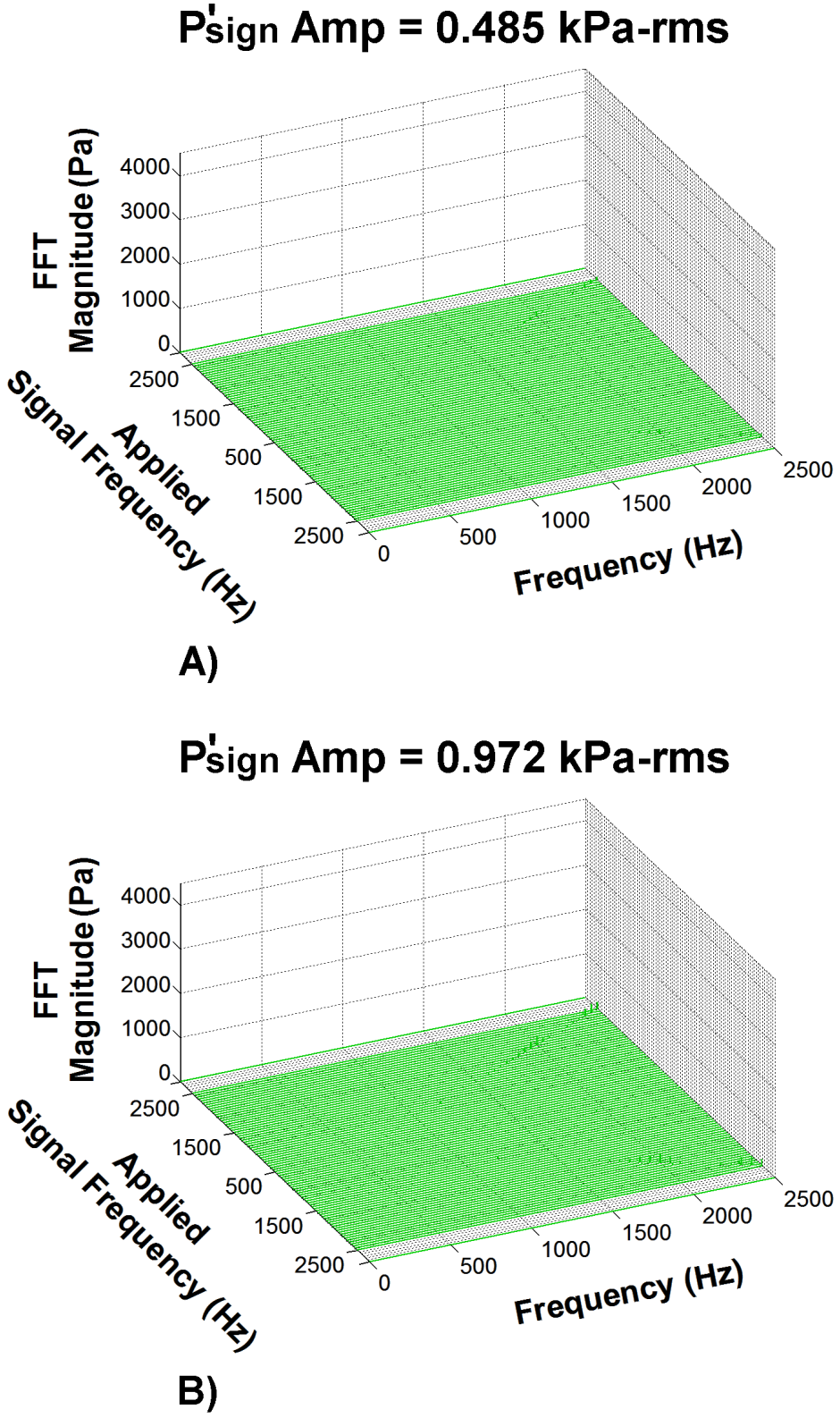

Figure B.31: Enlarged $P'1$ Waterfall Plots for the Single-Frequency Acoustic Modulation Pure Acoustic Tests: A) 0.485 kPa-rms and B) 0.972 kPa-rms.

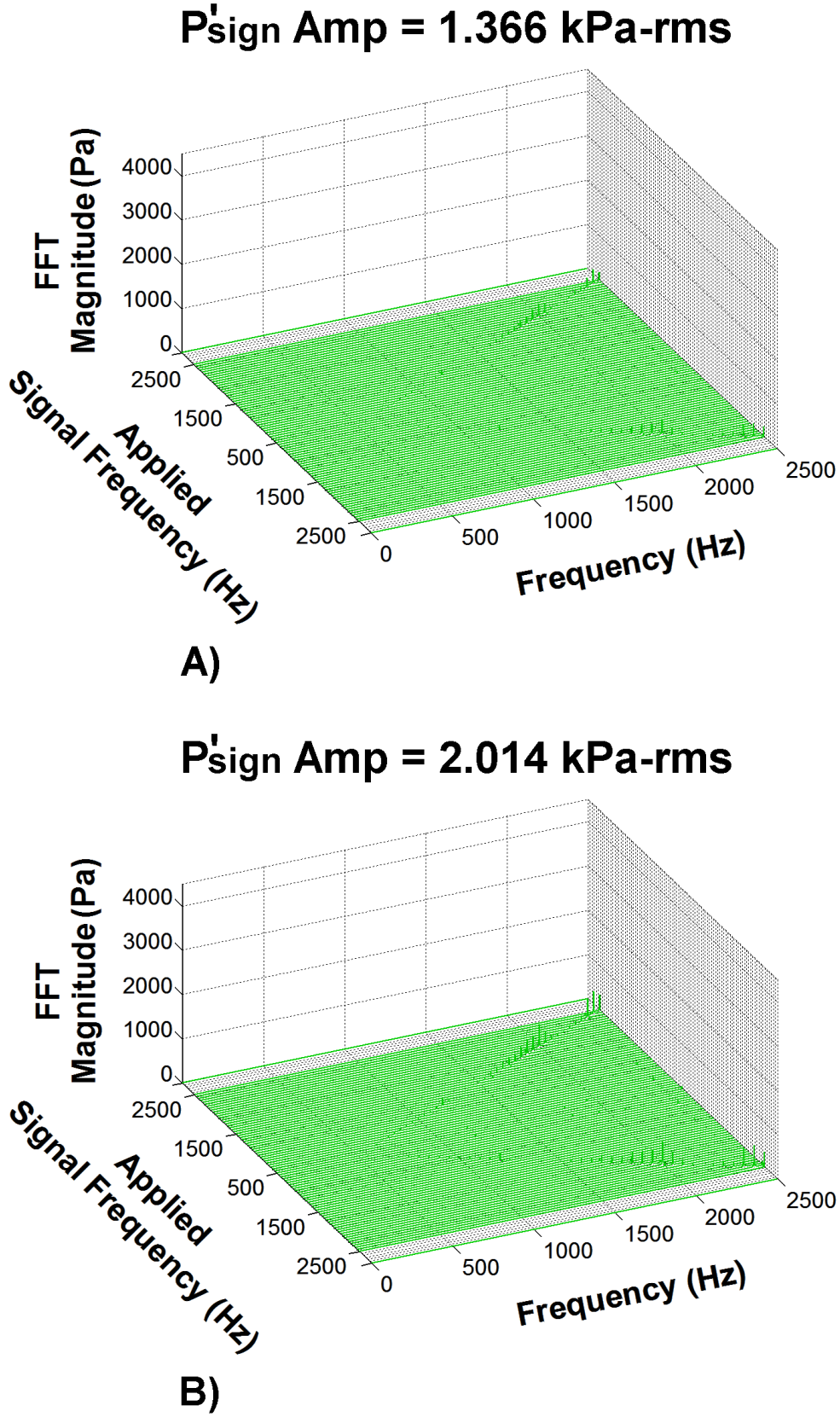

Figure B.32: Enlarged $P'1$ Waterfall Plots for the Single-Frequency Acoustic Modulation Pure Acoustic Tests: A) 1.366 kPa-rms and B) 2.014 kPa-rms.

B.6.2 $P'2$ Waterfall Plot Supplement

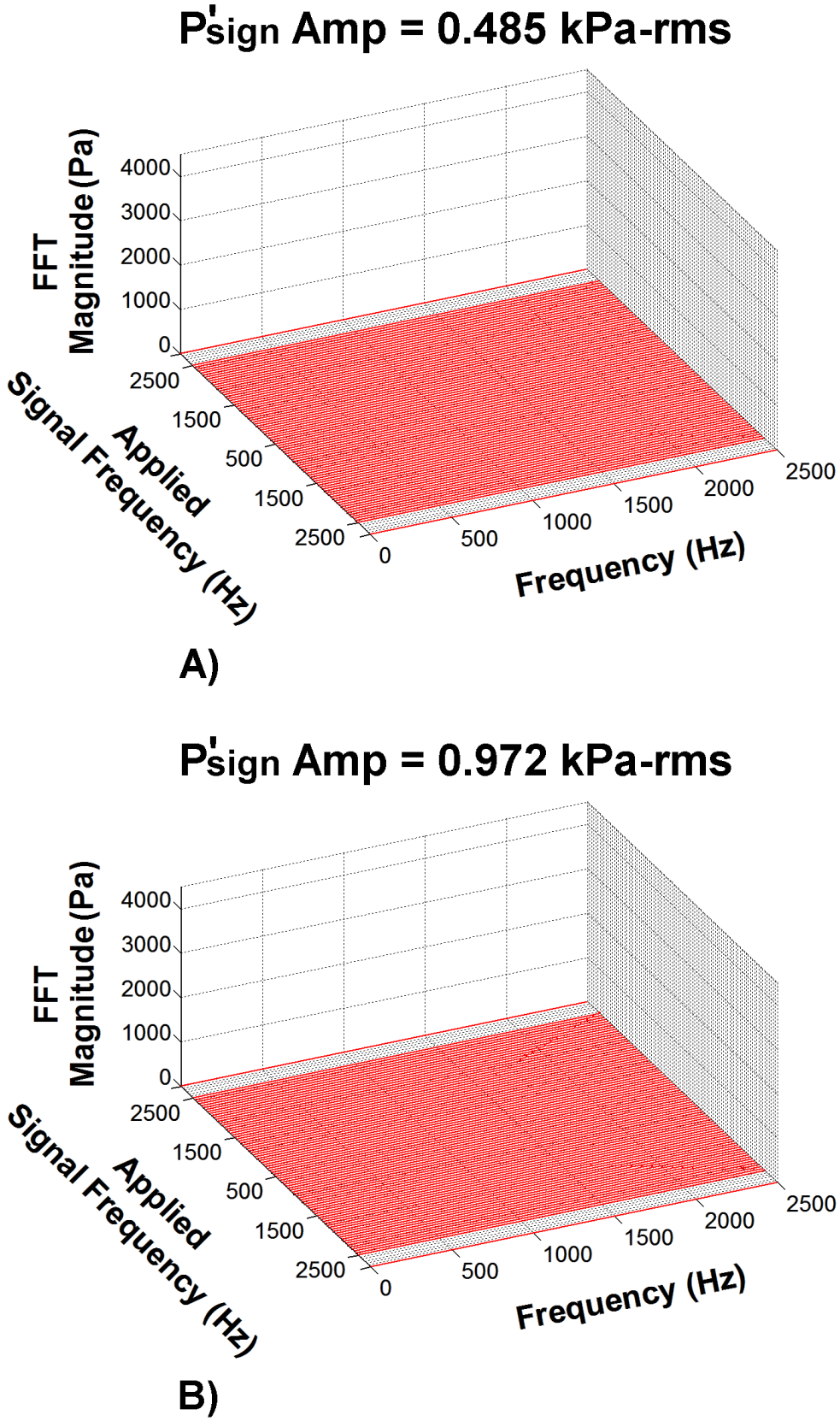

Figure B.33: Enlarged $P'2$ Waterfall Plots for the Single-Frequency Acoustic Modulation Pure Acoustic Tests: A) 0.485 kPa-rms and B) 0.972 kPa-rms.

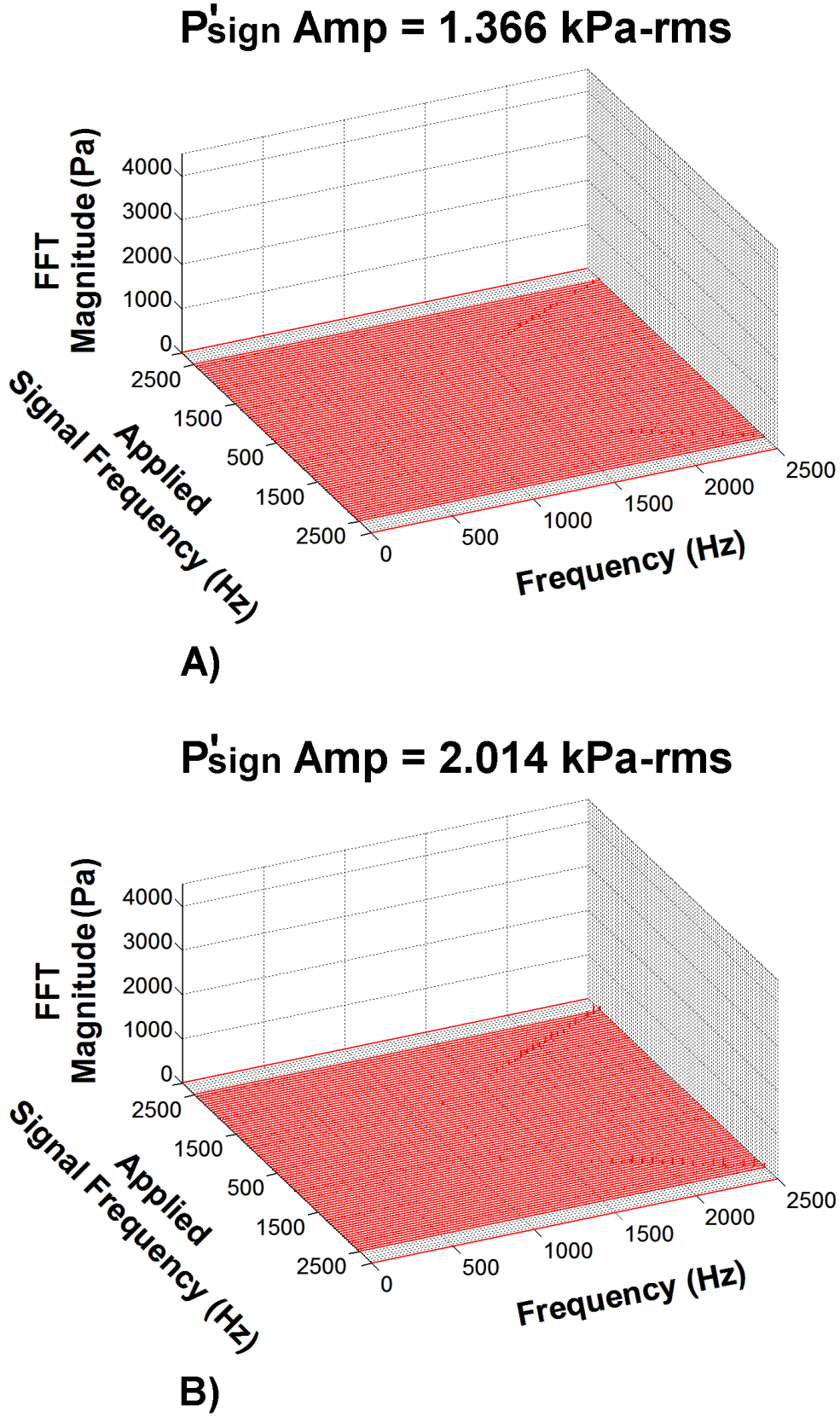

Figure B.34: Enlarged $P'2$ Waterfall Plots for the Single-Frequency Acoustic Modulation Pure Acoustic Tests: A) 1.366 kPa-rms and B) 2.014 kPa-rms.

B.6.3 $P'3$ Waterfall Plot Supplement

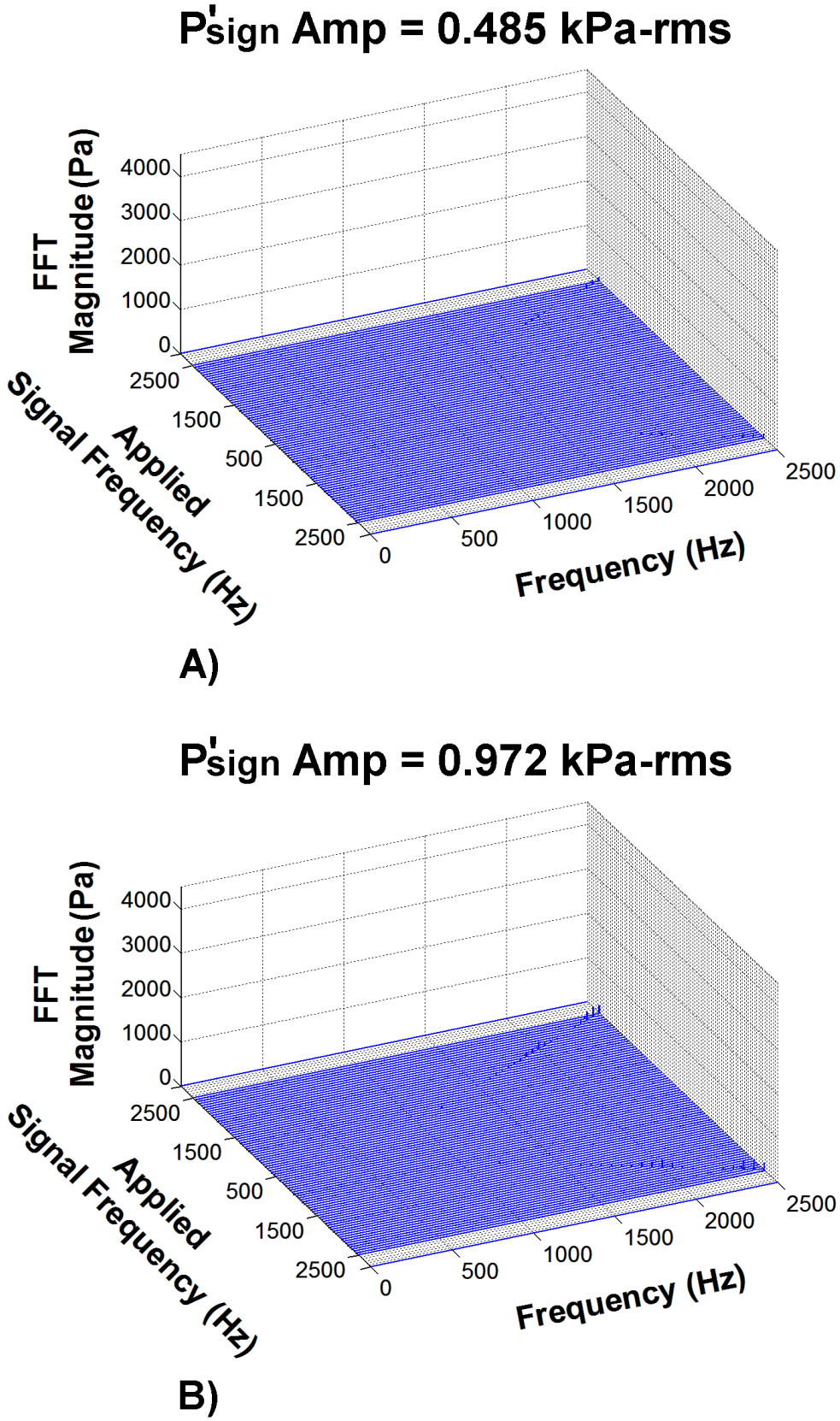

Figure B.35: Enlarged $P'3$ Waterfall Plots for the Single-Frequency Acoustic Modulation Pure Acoustic Tests: A) 0.485 kPa-rms and B) 0.972 kPa-rms.

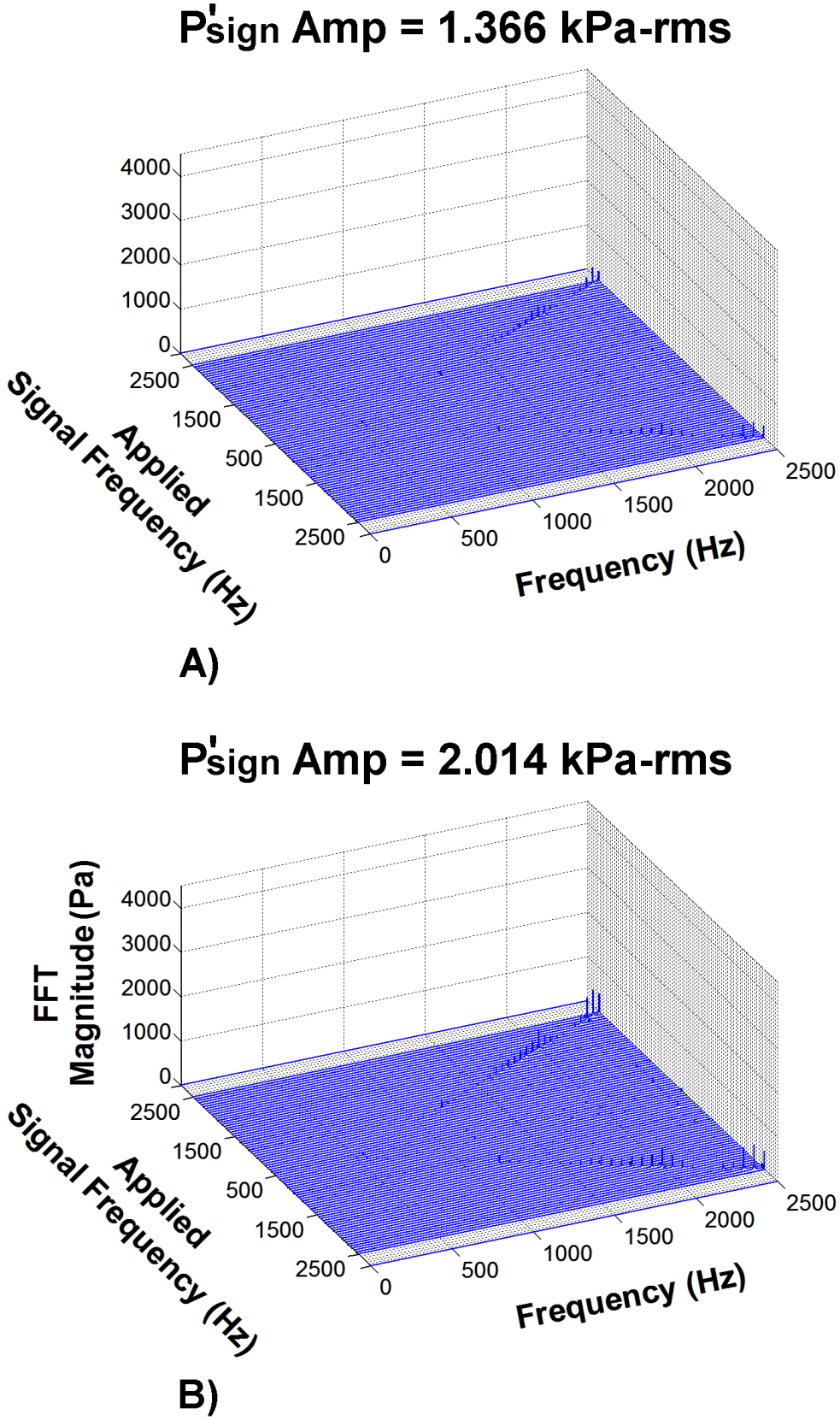

Figure B.36: Enlarged $P'3$ Waterfall Plots for the Single-Frequency Acoustic Modulation Pure Acoustic Tests: A) 1.366 kPa-rms and B) 2.014 kPa-rms.

B.6.4 P'_{inj} Waterfall Plot Supplement

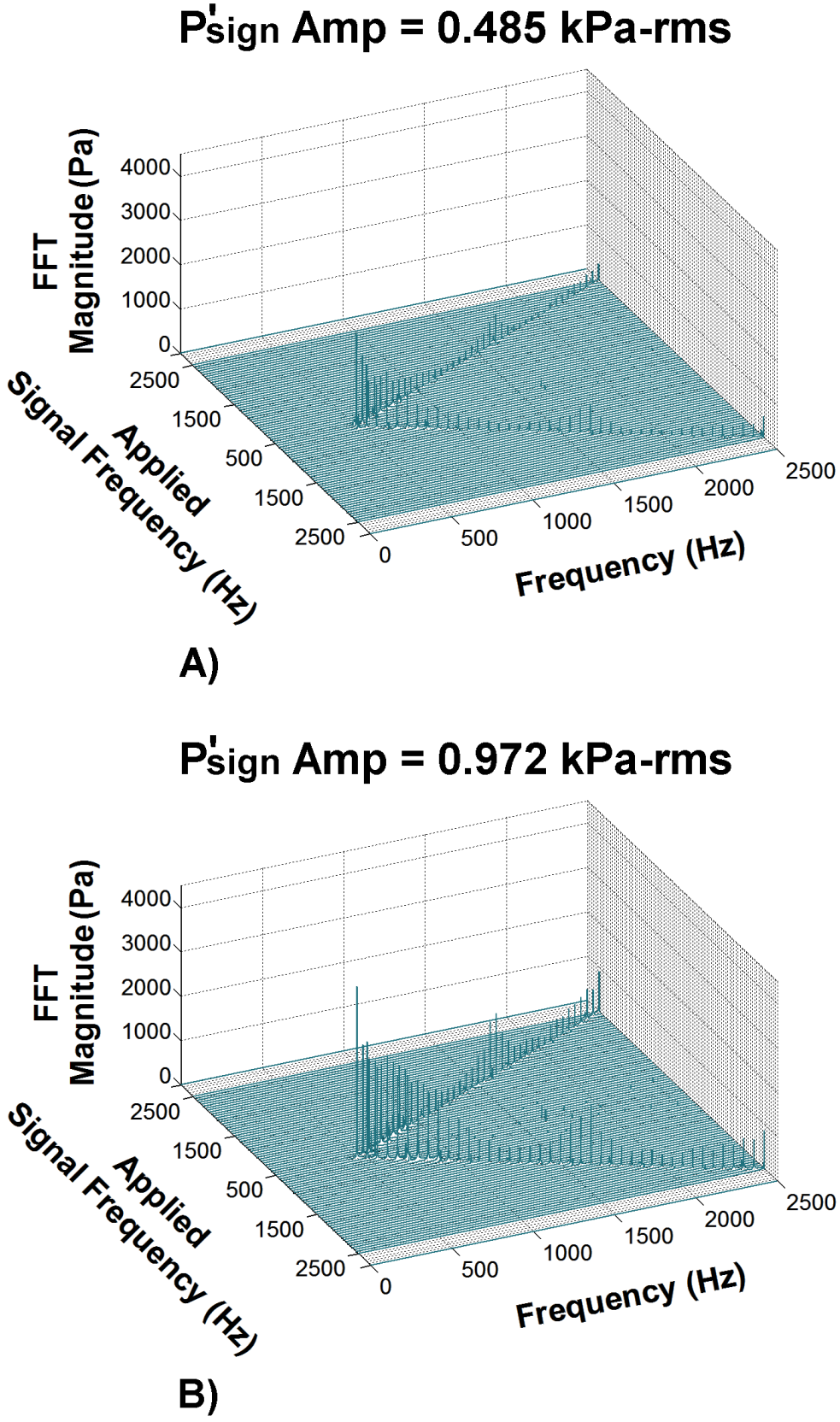

Figure B.37: Enlarged P'_{inj} Waterfall Plots for the Single-Frequency Acoustic Modulation Pure Acoustic Tests: A) 0.485 kPa-rms and B) 0.972 kPa-rms.

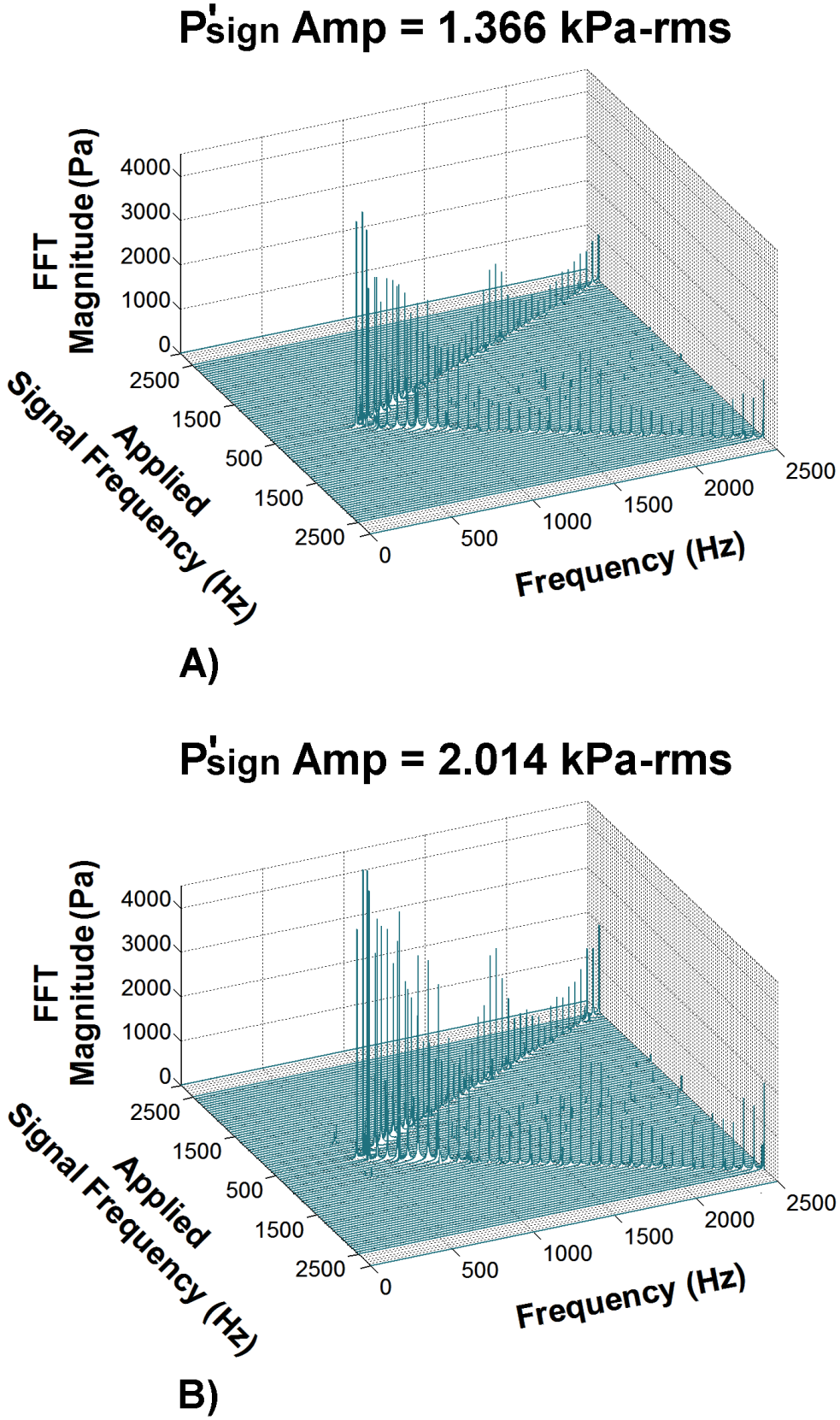

Figure B.38: Enlarged P'_{inj} Waterfall Plots for the Single-Frequency Acoustic Modulation Pure Acoustic Tests: A) 1.366 kPa-rms and B) 2.014 kPa-rms.

REFERENCES

[1] Yang, V. and Culick, F. E., "Overview of Combustion Instabilities in Liquid-Propellant Rocket Engines," *Progress in Astronautics and Aeronautics*, Vol. 169, 1995, pp. 3–37.

[2] Sutton, G. P. and Biblarz, O., *Rocket Propulsion Elements*, John Wiley & Sons, Inc., Hoboken, NJ, 8$^{\text{th}}$ ed., 2010.

[3] Hardi, J. S., "High Frequency Combustion Instability in LOx/H_2 Rocket Engines," Technical Report, University of Adelaide, School of Mechanical Engineering, 2008.

[4] Cavitt, R. C., *Experimental Methodology for Measuring Combustion and Injector Coupled Responses*, Master's Thesis, The University of Alabama in Huntsville, 2007.

[5] Byrd, R. E. and Frederick Jr., R. A., "Instability Characteristics of a Gasesous-Oxygen/Methane Pentad Injector," *Journal of Propulsion and Power*, Vol. 26, No. 4, July-August 2010, pp. 689–695.

[6] Mayer, W. O. and Hiroshi, T., "Propellant Injection in a Liquid Oxygen/Gaseous Hydrogen Rocket Engine," *Journal of Propulsion and Power*, Vol. 12, No. 6, November-December 1996, pp. 1137–1147.

[7] Mayer, W. O. and Smith, J. J., "Fundamentals of Supercritical Mixing and Combustion of Cryogenic Propellants," *Progress in Astronautics and Aeronautics*, Vol. 200, 2004, pp. 339–367.

[8] Sliphorst, M., *High Frequency Combustion Instabilities of LO_x/CH_4 Spray Flames in Rocket Engine Combustion Chambers*, Doctoral Dissertation, Institute of Space Propulsion, Lampoldshausen, 2011.

[9] Turns, S. R., *An Introduction to Combustion: Concepts and Applications*, McGraw-Hill Higher Education, Boston, MA, 8$^{\text{th}}$ ed., 2000.

[10] Glassman, I. and Yetter, R. A., *Combustion*, Elsevier, Burlington, MA, 4$^{\text{th}}$ ed., 2008.

[11] Sirignano, W., Delplanque, J., Chiang, C., and Bhatia, R., "Liquid-Propellant Droplet Vaporization: A Rate-Controlling Process for Combustion Instability," *Progress in Astronautics and Aeronautics*, Vol. 169, 1995, pp. 307–343.

[12] Oefelein, J. C. and Yang, V., "Comprehensive Review of Liquid-Propellant Combustion Instabilities in F-1 Engines," *Journal of Propulsion and Power*, Vol. 9, No. 5, September-October 1993, pp. 657–677.

[13] Pożarlik, A., *Vibro-Acoustical Instabilities Induced by Combustion Dynamics in Gas Turbine Combustors*, Doctoral Dissertation, University of Twente, 2010.

[14] Hubbard, H. H., "Aeroacoustics of Flight Vehicles: Theory and Practice," Technical Report WRDC-TR-90-3052, National Aeronautics and Space Administration, Langley Research Center, 1991.

[15] Lieuwen, T., *Investigation of Combustion Instability Mechanisms In Premixed Gas Turbines*, Doctoral Dissertation, Georgia Institute of Technology, 1999.

[16] Oyediran, A., Darling, D., and Radhakrishnan, K., "Review of Combustion-Acoustic Instabilities," 31^{st} *AIAA Joint Propulsion Conference & Exhibit*, No. AIAA 95-2469, American Institute of Aeronautics and Astronautics, San Diego, CA, 1995.

[17] Rayleigh, J., "The Explanation of Certain Acoustical Phenomena," *Nature*, Vol. 18, July 1878, pp. 319–321.

[18] Harrje, D. T. and Reardon, F. H., "Liquid Propellant Rocket Combustion Instability," Technical Report NASA SP-194, National Aeronautics and Space Administration, Washington D.C., 1972.

[19] Yang, V., Yoon, M., and Wicker, J., "Acoustic Waves in Baffled Liquid-Propellant Rocket Engines," Technical Report AD-A267-260, Air Force Office of Scientific Research, Bolling Air Force Base, 1993.

[20] Bennewitz, J. W., Lubarsky, E., Shcherbik, D., Bibik, O., and Zinn, B. T., "Asymmetric Injector Distribution for Passive Control of Liquid Rocket Engine Combustion Instabilities," 48^{th} *AIAA Aerospace Sciences Meeting & Exhibit*, No. AIAA 2010-1527, American Institute of Aeronautics and Astronautics, Orlando, FL, 2010.

[21] Hurlbert, E. A., Sun, J. L., and Zhang, B., "Instability Phenomena in Earth Storable Bipropellant Rocket Engines," *Progress in Astronautics and Aeronautics*, Vol. 169, 1995, pp. 113–143.

[22] Conrad, T., Bibik, O., Shcherbik, D., Lubarsky, E., and Zinn, B. T., "Control of Instabilities in Liquid Fuel Combustor by Modification of the Reaction Zone Using Smart Fuel Injector," 40^{th} *AIAA Joint Propulsion Conference & Exhibit*, No. AIAA 2004-4029, American Institute of Aeronautics and Astronautics, Fort Lauderdale, FL, 2004.

[23] Benedictis, M. D. and Ordonneau, G., "High Frequency Injection Coupled Combustion Instabilities - Study of Combustion Chamber / Feed System Coupling," 42^{nd} *AIAA Joint Propulsion Conference & Exhibit*, No. AIAA 2006-4721, American Institute of Aeronautics and Astronautics, Sacramento, CA, 2006.

[24] Kraemer, R. and Wheelock, V., *Rocketdyne: Powering Humans into Space*, American Institute of Aeronautics and Astronautics, Reston, VA, 2006.

[25] Dranovsky, M. L., Yang, V., Culick, F. E., and Talley, D. G., *Combustion Instabilities in Liquid Rocket Engines: Testing and Development Practices in Russia*, Progress in Astronautics and Aeronautics, Reston, VA, 2007.

[26] "Liquid Rocket Engine Combustion Stabilization Devices," Technical Report NASA SP-8113, National Aeronautics and Space Administration, Marshall Space Flight Research Center, 1974.

[27] Santana Jr., A., Silva, M., Lacava, P., and Góes, L., "Acoustic Cavities Design Procedures," *Engenharia Térmica (Thermal Engineering)*, Vol. 6, No. 2, December 2007, pp. 27–33.

[28] Lubarsky, E., Hadjipanayis, M., Shcherbik, D., Bibik, O., and Zinn, B. T., "Control of Tangential Instability by Asymmetric Baffle," 46^{th} *AIAA Aerospace Sciences Meeting & Exhibit*, No. AIAA 2008-955, American Institute of Aeronautics and Astronautics, Reno, NV, 2008.

[29] Lubarsky, E., Shcherbik, D., Bibik, O., and Zinn, B. T., "Active Control of Combustion Oscillations by Non-Coherent Fuel Flow Modulation," 9^{th} *AIAA/CEAS Aeronautics Conference & Exhibit*, No. AIAA 2003-3180, American Institute of Aeronautics and Astronautics, Hilton Head, SC, 2003.

[30] Schadow, K., Gutmark, E., and Wilson, K., "Active Combustion Control in a Coaxial Dump Combustor," 26^{th} *AIAA Joint Propulsion Conference & Exhibit*, No. AIAA 90-2447, American Institute of Aeronautics and Astronautics, Orlando, FL, 1990.

[31] Zinn, B. T. and Neumeier, Y., "An Overview of Active Control of Combustion Instabilities," *AIAA Aerospace Sciences Meeting & Exhibit*, No. AIAA 97-0461, American Institute of Aeronautics and Astronautics, Reno, NV, 1997.

[32] Yu, K. H., Ghosh, A., Ma, T., Diao, Q., Gers, D., and Lee, H. S., "Flame-Acoustic Interaction in Shear-Coaxial Injectors," *Grand Challenges in Propulsion Workshop*, National Institute for Rocket Propulsion Systems, Huntsville, AL, 2011.

[33] Diao, Q., Ghosh, A., and Yu, K. H., "Flame-Acoustic Interaction in a Shear-Coaxial Model Combustor Using H_2/CH_4 Fuel Mixture," *Grand Challenges in Propulsion Workshop*, National Institute for Rocket Propulsion Systems, Huntsville, AL, 2011.

[34] "JBL 2446 H/J Compression Driver Specifications, JBL Professional." 2005.

[35] "Setra 280E Specifications, Setra Sensing Solutions," 2012.

[36] "PCB Model 106B Specifications, PCB Piezotronics," 2008.

[37] "Omega KMQXL-062U-12 Thermocouple Specifications, Omega Engineering, Inc." 2012.

[38] Zucrow, M. J. and Hoffman, J. D., *Gas Dynamics Volume II: Multidimensional Flow*, John Wiley & Sons, Inc., New York, NY, 1977.

[39] Rani, V. K. and Rani, S. L., "An Acoustically Consistent Investigation of Combustion Instabilities in a Dump Combustor," *Journal of Propulsion and Power*, Vol. 31, No. 1, January 2015, pp. 298–308.

[40] Yu, Y. C., Sisco, J. C., Sankaran, V., and Anderson, W. E., "Effects of Mean Flow, Entropy Waves, and Boundary Conditions on Longitudinal Combustion Instability," *Combustion Science and Technology*, Vol. 182, 2010, pp. 739–776.

[41] Black, P., *Acoustic Transfer Functions Derived from Finite Element Modeling for Thermoacoustic Stability Predictions of Gas Turbine Engines*, Master's Thesis, Virginia Polytechnic Institute and State University, 2007.

[42] Quinlan, J. M. and Zinn, B. T., "Simulating Full-Scale Transverse Combustion Instabilities in a Lab-scale Facility," 49^{th} *AIAA Joint Propulsion Conference & Exhibit*, No. AIAA 2013-4019, American Institute of Aeronautics and Astronautics, San Jose, CA, 2013.

[43] Quinlan, J. M., Kim, Y. J., Dumitrache, C., Baroncelli, M., and Zinn, B. T., "Fundamental Processes that Drive Combustion Instabilities in Liquid Rocket Engines: 2011 - 2012 Annual Report," Technical Report, Air Force Office of Scientific Research, Bolling Air Force Base, 2012.

[44] Kinsler, L. E., Frey, A. R., Coppens, A. B., and Sanders, J. V., *Fundamentals of Acoustics*, John Wiley & Sons, Inc., New York, NY, 4^{th} ed., 2000.

[45] Atkinson, K. E., *An Introduction to Numerical Analysis*, John Wiley & Sons, Inc., New York, NY, 2^{nd} ed., 1989.